Modeling, Parametrization, and Diagnostics for Lithium-Ion Batteries with Automotive Applications

Dissertation

Presented in Partial Fulfillment of the Requirements for the Degree Doctor
of Philosophy in the Graduate School of The Ohio State University

By

James Marcicki, M.S.

Graduate Program in Graduate Program in Mechanical Engineering

The Ohio State University

2012

Dissertation Committee:

A.T. Conlisk, Co-Advisor

Giorgio Rizzoni, Co-Advisor

Marcello Canova

Yann Guezennec

Abstract

Lithium-ion (Li-ion) batteries are a promising source of electrical energy storage due to their improved energy and power densities coupled with potential cost savings compared to previous battery chemistries. However, significant research is needed to achieve a level of technical maturity that enables greater market pentration in the electrified vehicle segment. Energy density is currently an opportunity for improvement, and this shortcoming is compounded by the unavoidable aging process that shortens battery life by reductions in the energy and power that a battery can deliver.

Model-based analysis may be used to identify and suggest mitigation strategies for the performance limiting factors. Most battery models are macroscopic and ignore the presence of interfaces between the solid and liquid phases. In these regions, known as the electrical double layer, the ionic concentration and potential vary rapidly. A better understanding of the electrical double layer leads to improved models for interfacial charge transfer. The potential variation within the electrical double layer may also modify the rate of side reactions that occur in close proximity to the electrode surface, when compared with macroscopic models.

Model order reduction techniques applied to the partial differential equations of porous electrode theory leads to models that can be used for parameter estimation and large-scale aging simulations, but retain important aspects of electrochemistry. Since the developed models of lithium ion transport and potential variation across the battery unit cell are of low computational order, parameter estimation techniques may be incorporated to gain insight into the set of parameters that represent aging. Application of nonlinear least squares estimation is particularly powerful because the models exhibit dependence on electrochemical parameters that have physical meaning. Two case studies are presented for the reduced order modeling techniques that incorporate chemistry-specific phenomena.

Model-based diagnostics are useful to understand the aging process, since *in situ* methods for measuring the aging process are often not feasible due to the small spatial dimensions and long time scales involved. Diagnostic methods are applied to characterize the process of capacity loss for the two studied cell types. Once the performance limiting mechanisms are understood, predictive models can be developed. To address the instance where loss of cyclable lithium is deemed the dominant capacity fade mode, a capacity fade model is developed based on a novel interpretation of sold-electrolyte interphase (SEI) layer growth.

This dissertation contains the development of reduced-order models suitable for aging parameter estimation, an identification of the dominant capacity fade mechanisms via a model-based analysis for two types of commercially available Li-ion cells, a micro-scale model of the electrical double layer near each electrode, and a novel model of SEI growth. In future work, the SEI growth model can be integrated with improved understanding of the electrical double layer to provide high fidelity capacity fade prediction.

Acknowledgments

I am deeply grateful to my co-advisors, Professor Giorgio Rizzoni and Professor A. Terrence Conlisk. Their technical knowledge and commitment to producing high quality research was invaluable throughout my program, and beyond that, they promoted an atmosphere that made coming to work a joy each day. I will never forget their patience and kind support. I would also like to thank Professor Marcello Canova and Professor Yann Guezennec for being members of my Doctoral Examination Committee. Professor Canova's experience in model order reduction techniques proved to be invaluable, and Professor Guezennec's support of my experimental work is highly appreciated.

I would like to thank Ted Miller, Xiao Guang Yang, Kent Snyder, Dawn Bernardi, and all my colleagues at Ford Motor Company for the excellent learning experience as an intern in their department, and continued support of my research.

I would like to give special thanks to my family for their love and support throughout my program. The quality time I spent with my mother, father, grandmother, sister, brother-in-law, niece, and nephew made the stress of producing a dissertation much easier to bear. I would also like to thank all my friends who encouraged me and provided an outlet from my graduate studies, including new friends I met while in Columbus and old friends from Michigan.

Vita

April 27, 1986	Born - Royal Oak, Michigan
June 2004	Diploma, Adlai. E. Stevenson High School
April 2008	B.S. Mechanical Engineering Summa Cum Laude, University of Michigan
April 2009	M.S. Mechanical Engineering, University of Michigan
September 2009 - Present	Graduate Student, The Ohio State University

Publications

Research Publications

J. Marcicki, S. Onori, and G. Rizzoni, "Nonlinear Fault Detection and Isolation for a Lithium-Ion Battery Management System", Proceedings of the ASME Dynamic Systems and Control Conference, DSCC2010-4085, Cambridge, MA, Sept. 12 - 15 2010.

J. Marcicki, G. Rizzoni, A.T. Conlisk, and M. Canova, "A Reduced Order Electrochemical Model of Lithium-Ion Cells for System Identification of Battery Aging", Proceedings of the ASME Dynamic Systems and Control Conference, DSCC2011-6013, Arlington, VA, Oct. 31 - Nov. 2, 2011.

J. Marcicki, A.T. Conlisk, and G. Rizzoni, "Comparison of Limiting Descriptions of the Electrical Double Layer Using a Simplified Lithium-Ion Battery Model", ECS Transactions, 41 (14), 9 - 21, 2012.

J. Marcicki, F. Todeschini, S. Onori and M. Canova, "Nonlinear Parameter Estimation for Capacity Fade in Lithium-Ion Cells Based on a Reduced-Order Electrochemial Model", Proceedings of the 2012 IEEE American Control Conference, 1268, Montreal, Canada, June 2012.

J. Marcicki, M. Canova, A.T. Conlisk, and G. Rizzoni, “Design and Parametrization Analysis of a Reduced-Order Electrochemical Model of Graphite/LiFePO4 Cells for SOC/SOH Estimation”, Journal of Power Sources, 2013, (Accepted).

Fields of Study

Major Field: Mechanical Engineering

Studies in:

System Dynamics	Professor Giorgio Rizzoni
Mass Transfer and Electrokinetics	Professor A.Terrence Conlisk

Table of Contents

List of Tables

List of Figures

Figure **Page**

Chapter 1: Introduction and Overview

1.1 Introduction: Batteries in Automotive Applications

Batteries have an extensive history in stationary and mobile energy storage applications. In particular, the use of batteries in the automotive industry dates to the beginning of the 20th century. Originally batteries were conceived as the central source of propulsion power, but they did not gain widespread use due to low energy density and high cost. Instead, hydrocarbon-fueled combustion engines emerged as the universally accepted power system because they exhibit high specific power output as well as low cost. Additionally, the gas tank holding a hydrocarbon liquid fuel source is a far more energy dense storage system than a typical battery (Van Mierlo *et al.*, 2006). Thus, to provide the vehicle range that customers desire, the only battery featured in automotive applications for many years was a lead-acid unit that served as the power supply for the engine starter motor. The internal combustion engine was the sole source of propulsion.

In the late 1990's, automotive manufacturers began to investigate the use of nickel-metal hydride (Ni-MH) batteries for hybrid vehicle (HEV) applications (Snyder *et al.*, 2009; Karden *et al.*, 2007). A HEV provides superior fuel economy compared to a conventional vehicle by storing energy within that is usually wasted as heat during vehicle braking, then using the stored energy during periods of vehicle acceleration (Baumann *et al.*, 2000).

To accomplish this task many energy storage systems have been proposed, including hydraulic, pneumatic, or kinetic concepts, but the current technology of choice remains the electrochemical cell. In particular, the development of Ni-MH chemistry made the HEV concept feasible because it exhibited greater specific power than the already commonplace lead-acid chemistry. For approximately the next ten years, Ni-MH cells were the technology of choice for vehicle propulsion applications as HEV market acceptance steadily increased (Jenn *et al.*, 2012).

During the mid-to-late 2000's, consumers began to demand greater fuel economy due to economic and environmental influences. As one of many diverse technical solutions in response to this consumer preference, automakers pursued the option of increasing the energy storage capabilities of the typical HEV battery. To accomplish the task of increased energy storage within the stringent volume requirements of a typical light-duty vehicle, Li-ion cells were introduced (Srinivasan, 2008). This increased energy storage capability combined with increased specific power after switching from Ni-MH to Li-ion chemistry resulted in the ability to propel the vehicle by battery power alone. Moreover, adding the capability to charge the vehicle battery using household alternating current (AC) power created the plug-in hybrid electric vehicle (PHEV). The increased amount of battery energy and ability to charge from a household supply means that consumers do not need gasoline if operating the vehicle for a short distance, generally up to 40 miles. Trips farther than 40 miles will still use significantly less hydrocarbon fuel than a conventional vehicle due to the energy supplied by the battery in the charge-depleting initial phase of the trip. Once the battery energy has been depleted, the vehicle will operate as a charge-sustaining HEV. As Li-ion cells were developed to meet PHEV goals, they also replaced Ni-MH as the preferred technology for HEV applications due to their superior power density.

The ultimate stage of vehicle electrification is the battery electric vehicle (BEV or EV). This vehicle does not possess an internal combustion engine, relying solely on battery power for propulsion. Its range is directly dependent on the energy stored within the Li-ion battery pack. Since packs are typically size to address range concerns, they have more than adequate power capabilities to handle acceleration demands and rapid charging during braking.

Figure 1.1 summarizes the preceding discussion by use of a Ragone plot. Devices that exhibit higher values on the horizontal axis can provide faster acceleration in a vehicle application by supplying more energy within a specified time period. Those that demonstrate higher values along the vertical axis can provide greater vehicle range by supplying a specified amount of power for a longer time period. Each chemistry is plotted as a band along the chart, because engineering design changes can be made to tailor the technology for a specific power- or energy-oriented applications. As battery technology has progressed, it has become increasingly feasible for automotive applications. United States Department of Energy goals for HEV, PHEV, and EV battery performance have been made public by the United States Advanced Battery Consortium (USABC) (Anonymous, 2002, 2012*c*,*a*). These goals are specified on the Ragone plot, and it is evident that PHEV and HEV goals are met by current Li-ion technology. However, the EV goal is still beyond the current state of battery performance. Additionally the internal combustion engine and gasoline tank system has roughly an order of magnitude better specific energy storage than current Li-ion batteries.

A second way of assessing the technological progress of Li-ion batteries is the star chart shown in Figure 1.2. This plot has been developed with a focus on the PHEV application though results are essentially generalizable to the BEV and HEV applications as well. This

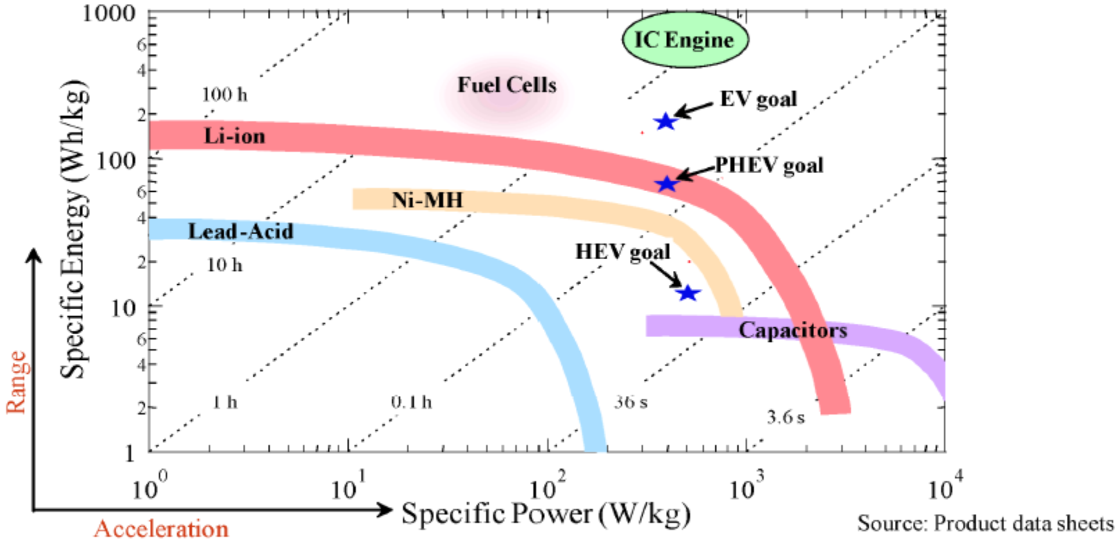

Source: Product data sheets

Figure 1.1: Ragone plot of specific power versus specific energy (Srinivasan, 2008) for various vehicle propulsion candidates.

figure gives a qualititative assessment of which battery perfromance traits are meeting the long-term technology goals, and which require further research. Overall, the base level of performance is adequate to meet the imposed power and energy demands. This reflects the fact that 40 miles of all-electric range is adequate for most customers when used in conjunction with an internal combustion engine that can extend the trip length if necessary. Further work is required in the areas of reducing system cost and ensuring that automotive battery packs will perform to customer expectations throughout their expected life. These areas are related, since one solution to enhance the usable life of the system is to design it to exceed the required performance at the beginning of life, so that performance goals are still met after significant performance degradation due to aging. Though this solution is feasible as a near-term, immediately implementable approach, it increases cost and long-term research should search for a more elegant approach to adequately satisfying life requirements.

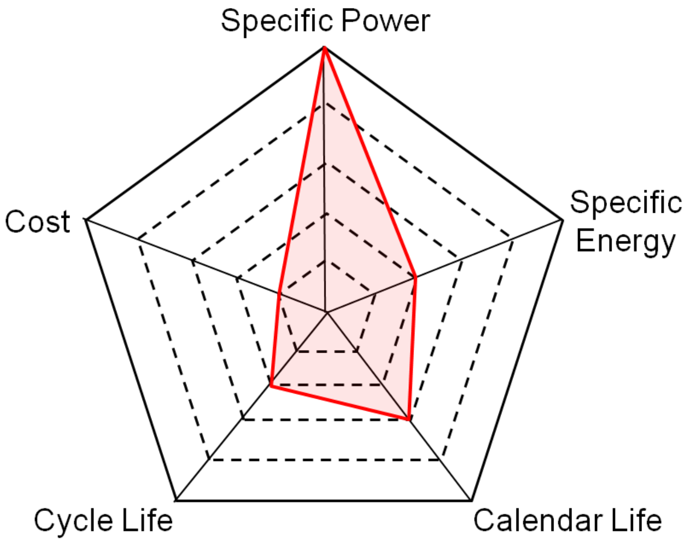

Figure 1.2: Star chart of battery performance characteristics (Srinivasan, 2008) compared with USABC goals for PHEVs (Howell, 2012).

This chapter provides context for the use of Li-ion batteries in automotive applications. The benefits of Li-ion technology compared with other chemistries and areas requiring further research are highlighted. A brief overview of how batteries work leads to the discussion of the physical structure and fabrication process of Li-ion batteries. Definitions of important terms that will be used throughout the rest of the dissertation are given, and finally the main objectives of the dissertation are stated.

1.2 How Batteries Work

Electrochemical batteries produce a useful electrical current, denoted by the symbol I throughout this dissertation, by converting stored chemical energy into electrical energy.

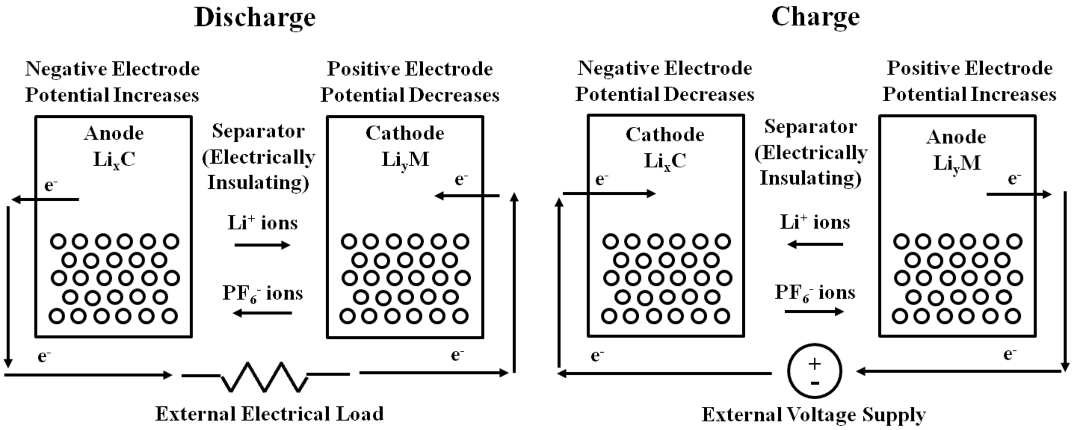

Figure 1.3: Schematic of the direction of ion and electron movement, and the labeling of anode and cathode, during battery discharge and charge.

The batteries considered for automotive applications consist primarily of a negative electrode, positive electrode, electrically insulating separator, and a solvent containing a dissolved lithium salt. The schematic of Figure 1.3 gives a view of the relative positions of the battery components.

The primary chemical reaction that drives all commonly used batteries is called an oxidation-reduction reaction. The reaction takes place via two half–reactions at two locations within the battery called electrodes. The anode, also called the negative electrode, is where ions are oxidized. Oxidation is a chemical process where a molecule (called the oxidized species) loses one or more electrons. Equation 1.1 shows a typical reaction for the negative electrode of a Li-ion battery

$$Li_xC_6 \rightleftharpoons Li^+ + e^- + C_6 \tag{1.1}$$

where $0 \leq x \leq 1$ is a fractional measure of the amount of lithium stored within the electrode, normalized by the saturation (maximum) value, and is referred to interchangeably as composition, degree of lithiation, or fractional occupancy. A carbon-based electrode has been assumed, hence the C reactant, though other materials can be substituted with minimal modifications. This reaction is not a true chemical reaction, rather it represents the process of intercalation by which lithium is stored in the solid portion of the electrode. The intercalation process is reversible and when lithium is removed from the electrode it is called de-intercalation.

The cathode, also called the positive electrode, is where ions are reduced. Reduction is a chemical process where a molecule (called the reduced species) gains one or more electrons. Equation 1.2 gives a typical reaction for the positive electrode of a Li-ion battery

$$Li^{+} + e^{-} + M \rightleftharpoons Li_{y}M \tag{1.2}$$

where y has the same definition as x used previously for the anode, but instead refers to the cathode, and M refers generally to a metal oxide or phosphate compound such as $FePO_4$, Mn_2O_4, or other compounds. Depending on whether the cell is being charged or discharged, either electrode can be the anode or cathode at a given instant. However, the ‘positive’ or ‘negative’ electrode labels do not change depending on the direction of current flow. The ‘positive’ label always refers to the electrode with higher potential, and the ‘negative’ lablel to the electrode with lower potential. Throughout this work, the discharge convention is chosen such that the term negative electrode is used interchangeably with the term anode, and positive electrode is used interchangeably with cathode.

The schematic of Figure 1.3 illustrates the path of electrons and lithium ions for charge and discharge. In between the half–reaction taking place at each electrode, the electrons traverse an external circuit and provide useful energy in the form of electricity if the battery is being discharge. During charging, energy must be supplied to the cell to drive current from the positive electrode to the negative electrode. A separator that is permeable to ions but not electrons lies between the electrodes to prevent an electrical short circuit. A liquid or gel solvent, containing a dissolved salt known as electrolyte, permeates the entire cell volume and enables ion transfer between the electrodes.

As a specific example, consider the lithium-ion battery illustrated in Figure 1.3. During discharge, lithium ions are removed from the negative electrode and deposited into the liquid solvent. The ions diffuse within the liquid, through the separator region, to the cathode where they are accepted into the solid material. Transport of lithium ions into the cathode solid material completes the oxidation-reduction reaction. During charging, the process is repeated in reverse.

1.3 Physical Structure and Fabrication of Li-Ion Batteries

The physical structure of the battery and each of its components is now discussed in greater detail. The cells that will be examined throughout this dissertation are either of a cylindrical format constructed via the “jelly-roll” method, or a pouch format constructed via folding and/or stacking of rectangular unit cell layers. A unit cell refers to the combination of two electrodes and the separator. Figure 1.4 gives a visual overview of these cell designs. Cylindrical cells were originally favored because they theoretically offer better protection against environmental contaminants. However, the pouch or prismatic format has gained acceptance in recent years due to better volumetric energy density when incorporating cells into a pack. Prismatic cells can be stacked more efficiently with minimal gaps as compared to cylindrical cells.

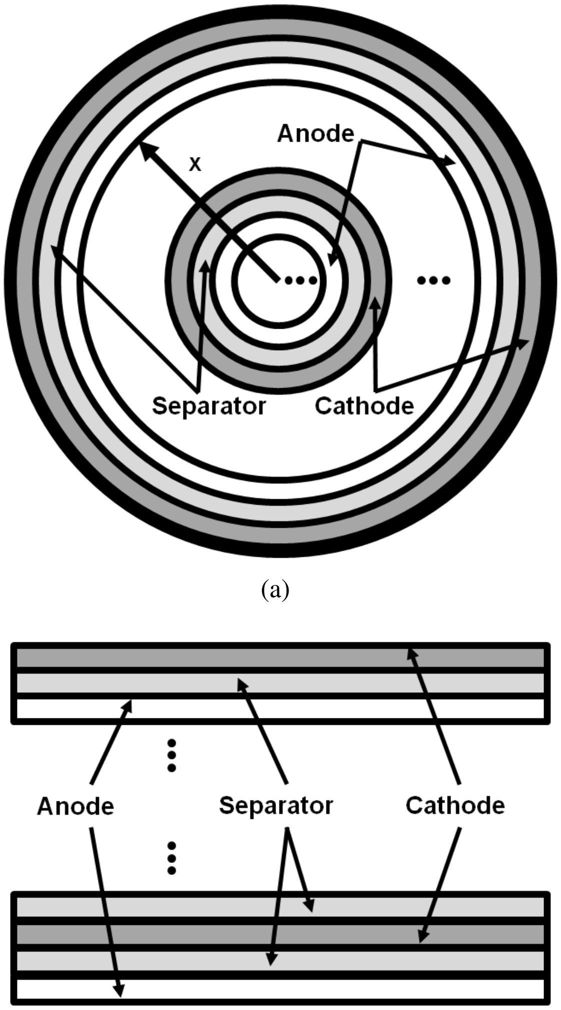

(a)

(b)

Figure 1.4: Unit cell orientation within a) cyclindrical and b) pouch cell geometry.

1.3.1 Electrodes

The construction of each electrode begins with an active material powder, that is a collection of roughly spherical or ellipsoid active material particles of a diameter ranging from nanometers to micrometers. This powder is mixed with a mixture of conductive carbon filler material and polyvinylidene fluoride (PVDF) glue that immobilizes the particles known as a binder. The completed mixture forms a thick slurry or paste that does not flow but is still conformable. To construct each electrode, the active material paste is deposited in a thin layer onto a long strip of metal foil, the width of which is roughly equal to the diameter of the cylindrical battery casing. The metal foil is called the current collector, because it transports the generated electrical current to the external battery tabs. Metal foil must be used due to its very high conductivity. It is typically made of copper for the anode and aluminum for the cathode. The active material paste in each electrode contains compounds that are carefully chosen to drive the overall chemical reaction of the cell, which produces a useful electrical current. The electrodes are referred to as "porous" electrodes because they consist of a packing of active material particles with liquid–filled pores throughout. The general properties of porous electrodes that are common between the anode and cathode are summarized in Table 1.1, and Figure 1.5 shows scanning electron microscopy (SEM) images of common anode and cathode structures. Figure 1.6 shows a three-dimensional rendering obtained from the reconstruction of X-ray tomography data (Shearing *et al.*, 2010).

At this point the properties of the active material compounds typically used for Li-ion cell anodes are discussed. The most common present technology is a lithium/graphite compound, generally referred to as Li_xC_6 for the rest of this dissertation. The formulations of this graphite compound exhibit different degrees of graphite crystalline structure based

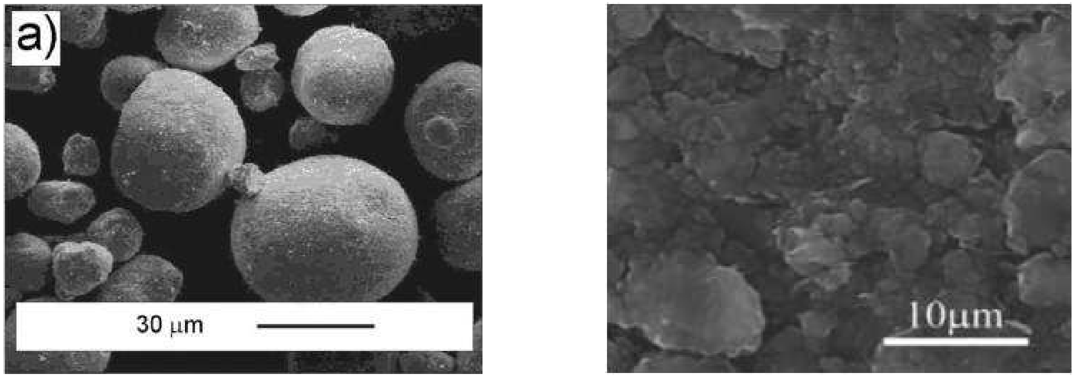

(a) (b)

Figure 1.5: Scanning electron microscopy images of electrode structures for a) $Li_yMn_2O_4$ positive electrode (Deiss *et al.*, 2001) and b) Li_xC_6 negative electrode (Safari & Delacourt, 2011*b*). Individual active material particles are clearly visible as large spheres in image (a), and have a more flake-like structure in image (b).

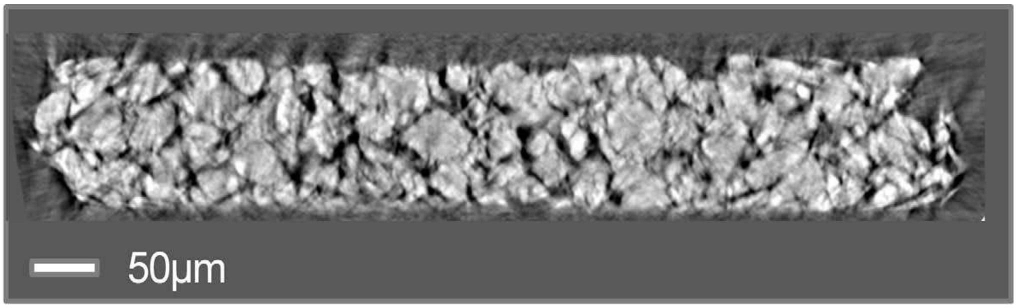

Figure 1.6: A slice of negative electrode from a tomography reconstruction process (Shearing *et al.*, 2010). Electrode thickness is in the vertical direction.

Property	Value
Binder volume fraction	5 - 10 %
Porosity	30 - 40 %
Mean Active Material Particle Radius	$10^{-9} - 10^{-6}\ m$
Thickness	$50 - 100 \times 10^{-6}\ m$

Table 1.1: Typical properties of porous electrodes.

on their formation processes, which leads to slight variations of electrochemical properties. For instance, (Lee *et al.*, 2002) analyzed two different types of mesocarbon microbead (MCMB) carbon electrodes, formed by heat treating at different temperatures. It is shown that the samples treated to higher temperatures ($2800°C$ compared with $1000°C$) exhibited larger mean particle diameter (25 μm compared with 6 μm). It appears that greater amounts of heat treatment can cause greater ordering of the graphite structure, as shown by well-defined voltage plateaus in the open-circuit voltage for the samples treated at $2800°C$. In general the lithium/carbon anodes have a specific capacity of approximately $372\ mAh/g$ (Ohzuku *et al.*, 1993), which is usually higher than their cathode partner. They often exhibit higher electrical conductivity than the cathode, usually on the order of 100 S/m (Levi & Aurbach, 1997).

There are other anode chemistries that have matured beyond the research stage, such as titanate oxide (Nakahara *et al.*, 2003). This chemistry exhibits excellent cycle life due to the minimization of side reactions that are comparatively more destructive for carbon-based electrodes. This mitigation of side reactions is possible due to the elevated potential relative to Li/Li^+ of around 1.5 V. However, they are not commonly used due to this high voltage characteristic which leads to a significant reduction in specific energy when incorporated within a cell as the negative electrode.

The cathode paste also consists of a conductive filler, binder, and active material, but replaces the Li_xC_6 compound with a lithium metal oxide or phosphate of general chemical formula Li_yM, where M is a metallic compound. The specific capacity is typically in the range of $100 - 200\ mAh/g$ (Ohzuku & Brodd, 2007), which requires thicker electrodes to achieve the same capacity as compared with anodes. The electrical conductivity is lower than for carbon-based electrodes and takes a value anywhere between $10^{-3} - 10^{1}\ S/m$ (Ohzuku & Brodd, 2007) depending on the additives incorporated in the electrode slurry.

1.3.2 Separator

When the cell sandwich is manufactured, an electrically non-conducting layer must be placed between the anode and cathode to prevent short circuits. It may either be held in place with adhesive or left floating within the sandwich. Typically the "float" method is more common due to less time and cost involved. This layer is referred to as the separator, and may consist of a single or multiple layers of porous polyethylene or polypropylene. Although its purpose is to serve as an electrical barrier between the electrodes, it must also be porous to allow for the transport of lithium ions dissolved in the liquid solvent. The porosity may vary depending on the manufacturer, but generally falls between 0.3 and 0.7 (Zhang, 2007). Dimensional stability with respect to mechanical stresses and shrinking is a very important separator characteristic. Consistent tortuosity is also important to prevent dendrite growth that can cause a short circuit between electrodes (Anonymous, 2012*b*).

A separator that is generally representative of those used throughout industry, and has been used in the half-cell experiments of this dissertation, is Celgard® 2400. The dimension that serves as separation between the electrodes is 25 μm. The material is a single layer of microporous, polypropylene membrane designed for low temperature lithium batteries. Celgard claims it has excellent resistance to acids and bases, uniform pore structure with high chemical and thermal stability, zero shrinkage to reduce the possibilities of internal shorting, and oxidation resistance. Its technical data is summarized in Table 1.2. Other

Property	Value
Thickness	25 μm
Porosity	41 %
Average Pore Diameter	0.043 μm
TD Shrinkage @ 363 K / 1 hour	0 %
MD Shrinkage @ 363 K / 1 hour	5 %
Puncture Strength	450 g
Tensile Strength, MD	1420 kg/cm^2
Tensile Strength, TD	140 kg/cm^2

Table 1.2: A listing of separator technical properties. Transverse direction is denoted by TD and machine direction is denoted by MD.

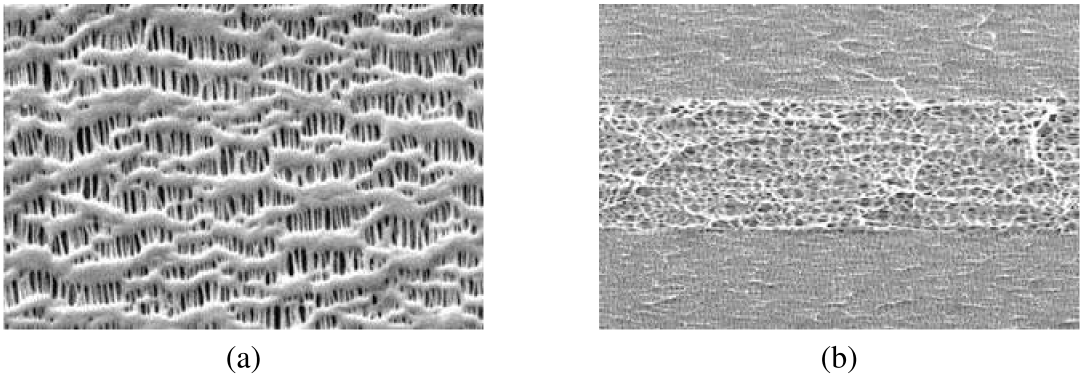
(a) (b)

Figure 1.7: (a) Uni-layer separator SEM image and (b) tri-layer separator SEM image (Anonymous, 2011).

separators, known as tri-layer separators, contain a three layer sandwich of polypropylene-polyethylene-polypropylene (PP-PE-PP). The polypropylene layers provide oxidation resistance for better long term cycling performance while the polyethylene inner layer provides faster shutdown due to melting upon overheating (Venugopal *et al.*, 1999; Troffkin *et al.*, 1993). This is possible because the melting point of polyethylene is approximately 105 - 130°C, while that of polypropylene is 130 - 170°C. An SEM image of a mono-layer separator, courtesy of Celgard, is shown in Figure 1.7a, while a tri-layer separator is shown in Figure 1.7b. The uni-layer picture has the direction across the unit cell (from anode to cathode) as into the page. The tri-layer picture is a side-view where the direction across the unit cell runs vertically.

1.3.3 Assembly

At this point, it should be reiterated that the three main components of the cell sandwich are porous, disregarding the metal foil current collectors that serve as a substrate for the active material. This allows the electrolyte solution to permeate throughout the electrodes and separator and provides a transport mechanism for the lithium ions produced from the reactions at the electrodes. The electrolyte solvent is generally a mixture of carbonates such as ethylene carbonate (EC), dimethyl carbonate (DMC), or diethyl carbonate (DEC). The electrolyte salt may be any of several salts containing Li, though a common example is $LiPF_6$. The salt concentration is usually near 1.0 M because the liquid conductivity is a strong function of the salt concentration and usually exhibits a maximum near this concentration.

To complete the cell fabrication, the entire cell sandwich is assembled by rolling, folding, or stacking and placed within a hermetically sealed casing that is filled with electrolyte solution. Quite often, the amount of liquid electrolyte solution added is small so that only the pores of the solid matrix are wetted an no free liquid can visibly be observed. The best analogy of this situation is a minimally damp sponge that contains some amount of liquid, but so little that none can be removed by squeezing it. The porous nature of both electrodes will generally result in a need to account for ion transport within both the solid and liquid phases.

1.4 General Definitions

This section details the general terms that form the foundational knowledge used throughout this dissertation.

A **Faradaic current** is defined as the electrical current produced by the intended oxidation and reduction reactions that occur at each electrode. Other terms such as **external current**, **main current**, or **current demand** may be used interchangeably with this term throughout this dissertation. The **sign convention** for current is that a discharge current is positive (energy supplied by the cell) and a charge current is negative (energy supplied to the cell).

The **open-circuit voltage** (OCV) of an electrochemical cell is defined as the voltage measured across the cell terminals after the system has been allowed to reach equilibrium. This means that there is no current being passed and that all macroscopic concentration gradients within the solid and liquid phases are negligible. For Li-ion batteries, the OCV is a strong function of the total charge throughput history of the cell. Specifically, as the cell is discharged, the OCV will decrease as the amount of charge removed increases. The OCV is the potential difference of the two electrodes.

The **capacity** of an electrochemical cell is defined as the amount of charge stored within the cell between specific voltage limits that are defined by the cell manufacturer. It is typically measured using a cell charged to 100% SOC and allowed to reach equilibrium followed by discharging the cell to the lower voltage limit using a constant current. Upon reaching the lower voltage limit, capacity is defined as the integral of current,

$$Q = \int_0^{t_f} I(t)\, dt \tag{1.3}$$

The upper voltage limits for commercially available Li-ion cells are usually from 3.6 to 4.2 V, while the lower voltage limits vary from 2.0 to 2.8 V depending on the cell chemistry. Consideration of the voltage limits is an important facet of calculating the cell capacity, because these limits place a constraint on the final time t_f, defined as the elapsed time since the start of the test when the lower voltage limit is reached. In this sense, Eq. (1.3) is misleading, because the final time is not arbitrarily chosen but instead it is the time when a voltage limit is reached. A voltage range must be specified because harmful side reactions or catastrophic fires can occur outside the voltage limits. The capacity of a cell is directly related to the mass of **active material** it contains, where active material is defined as a component of the electrode solid phase that can store lithium. **Inactive material** refers to all other solid components such as the conductive additives and binder.

The **C-rate** is a current magnitude specified as a multiple of the cell capacity. For instance, a 1C rate is the current required to fully discharge the cell in a period of one hour. A 2C rate would take 1/2 hour to discharge, while a C/2 rate would take two hours to discharge.

The cell **state-of-charge** (SOC) is defined as the amount of charge stored within the cell at any instant in time, normalized by the maximum amount of charge that may be stored by the cell within the voltage limits specified by the cell manufacturer. Operationally, it is defined as

$$SOC(t) = SOC(0) - \frac{100}{Q} \int_0^{t_f} I(t)dt \tag{1.4}$$

where Q is the nominal cell capacity and the initial condition $SOC(0)$ is usually specifed as equal to 100% after charging the cell to the upper voltage limit, and then executing a constant voltage hold for several minutes to hours depending on the desired precision of the initial condition, since current tapers towards zero with time at constant voltage. At zero current the system is at equilibrium. The factor of 100 is included as a conversion factor to a percentage basis, but SOC can alternatively be defined as $0 < SOC < 1$.

The **internal resistance** of an electrochemical cell defines the immediate deviation from the equilibrium voltage that occurs when a current is passed. The **overpotential** of a cell is defined as the total voltage deviation from the equilibrium value at any point in time. An illustration of the effects of the internal resistance after passing a discharge current is shown in Figure 1.8, where an initial overpotential, ΔV_0, and a current input, I, are used to define an initial resistance $R_0 = \frac{\Delta V_0}{I}$. The initial resistance is the sum of ohmic and kinetic contributions that are discussed in more detail in Chapter 2. These contributions have time scales of around 1 kHZ and 10 Hz respectively (Barsoukov & Macdonald, 2005), so it appears to be an instantaneous response when viewing system-level voltage and current measurements. At longer time scales of 1 Hz to the 1 mHz range, other electrochemical processes contribute to the additional observed overpotential defined as ΔV_1.

The process of **aging** for an electrochemical cell is defined as performance degradation that evolves over a time scale that is much longer than that of the voltage dynamics. The

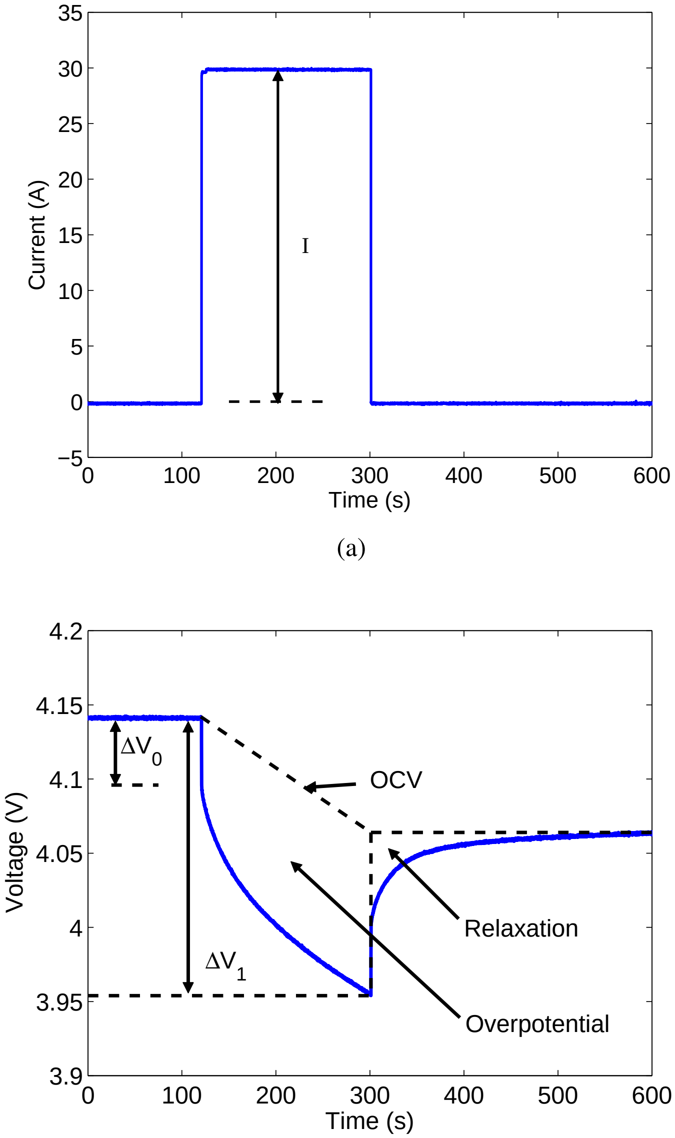

(a)

(b)

Figure 1.8: Definition of internal resistance after passing a discharge current. a) The current passed by the cell and b) the voltage response. The internal resistance during a charge current causes the voltage to rise above the equilbrium value.

mechanisms for aging are numerous and will be discussed in the following chapters of this dissertation. The system-level effects caused by aging are a reduction of cell power and energy capabilities that are caused by increased internal resistance and reduced capacity. A **side reaction** is any chemical reaction that occurs within the cell that is not associated with the Faradaic current, and side reactions are a common cause of aging.

1.5 Thesis Objectives

The objectives of this dissertation are the following:

- Develop a first-principles model of electrical double layer effects in Li-ion batteries.
- Develop reduced-order models that retain a parametric dependence on electrochemical and physical parameters.
- Use these models as a tool to interpret experimental aging data and identify fundamental mechanisms for capacity fade.
- Based on the knowledge gained from the previous two objectives, develop a predictive capacity fade model that is based on first principles.

Chapter Two discusses the fundamental equations needed to develop models of the potential and concentration dynamics during Li-ion battery charge/discharge processes. Beginning with the fundamentals of electrochemistry, governing equations are derived and solution methods are discussed, beginning with computationally complex models and ending with low-order realizations.

Chapter Three presents a model of the electrical double layer in Li-ion batteries. Accounting for this region that exists within nanometers of each electrode surface can lead to different local potential prediction. This potential can be linked to the rate of side reactions in close proximity to the electrode surface.

Chapter Four applies model-order reduction techniques to the partial differential equations of ionic transport. A low-order model is derived and parameterized to predict the experimentally measured battery voltage for a wide range of temperature, SOC, and current inputs. Then, the model is compared with experimental data from an aging campaign and the parameters responsible for capacity fade during battery aging are estimated using nonlinear least squares.

Chapter Five extends the model structure developed in Chapter Four to a cell featuring an electrode that is a composite mixture of active materials. After validating the model with experimental data, it is compared with data from an aging study to examine the mechanisms for capacity fade. Once loss of lithium is established as the dominant mode of capacity fade, a model of solid-electrolyte interphase (SEI) growth is used to explain the lithium loss. Then, capacity fade is simulated for the conditions of the aging experiments, and the simulated capacity fade is compared with experimental data.

Chapter Six is a summary of the main points from each chapter. Future work is suggested that builds upon the results presented in this dissertation.

Chapter 2: Mathematical Modeling of Li-Ion Batteries

2.1 Introduction

This chapter introduces the governing equations used to model the ionic concentration and potential dynamics within Li-ion batteries. The overall goal of the battery models presented in this dissertation is to predict battery terminal voltage while revealing information about the internal electrochemical processes of the cell. First the governing equations of electrochemistry are introduced, then they are applied specifically to the Li-ion battery problem. A hierarchical approach is used to present a number of modeling techniques, ranging from distributed parameter models towards lumped, low-order models. A number of solution methods are discussed with a focus on methods that are commonly utilized to avoid the complexity of a numerical solution. Then, common battery aging mechanisms are reviewed along with a set of diagnostic techniques used to assess the effects of aging on battery performance.

2.2 Governing Equations for Electrochemical Systems

The field of electrochemistry consists of thermodynamics, interfacial kinetics, and mass transport. Each plays an important role in determining the time-varying voltage of an electrochemical cell. Thermodynamics defines the maximum achievable power and/or energy for the cell, whereas kinetics and transport represent deviations from the thermodynamic ideal that act to reduce cell performance.

2.2.1 Thermodynamics

Recall from Chapter 1 that the open-circuit voltage (OCV) of the cell is defined as the potential difference between electrodes that would be reached for a given state-of-charge, if the cell is at thermodynamic equilibrium. By applying the principles of thermodynamics, the physical meaning of the OCV can be identified. For the following discussion, chemical and thermodynamic reversibility is assumed since thermodynamics deals with systems at equilibrium, and reversibility is a result of that requirement. This corresponds to the condition that no current flows within the cell, so that by definition any side reaction currents responsible for the aging process are neglected as well. The Gibbs free energy, G, is defined generally as (Moran & Shapiro, 2004)

$$G = H - TS = U + p\bar{V} - TS \tag{2.1}$$

where H is enthalpy, T is temperature, S is entropy, U is internal energy, p is pressure, and $\bar{V}$ is volume. The change in Gibbs free energy is

$$\Delta G = \Delta U + \bar{V}\Delta p + p\Delta\bar{V} - T\Delta S - S\Delta T \tag{2.2}$$

However, a Li-ion cell operates at constant pressure, and for this analysis constant temperature is also assumed so that terms involving change of pressure or temperature can be neglected. Furthermore, the change of internal energy for a system with these assumptions while undergoing a chemical reaction is

$$\Delta U = T\Delta S - p\Delta\bar{V} - n_e F\phi \tag{2.3}$$

where n_e is the number of electrons that are lost or gained during the chemical reaction, and F is Faraday's constant. The reduction (oxidation) potential ϕ is also referred to as the OCV and given the symbol U throughout the remainder of this dissertation, but in this instance U already refers to internal energy. The reduction potential is treated as a known quantity since it can be measured experimentally by assembling a cell with the electrode of interest as the working electrode with a lithium counter/reference electrode. It is defined as a potential where reactants are reduced, gaining an electron. Substituting the definition of internal energy into Eq. (2.2) gives

$$\Delta G = -n_e F \phi \tag{2.4}$$

When reactions occur at non-standard conditions, the activity of the reaction constituents must be accounted for. In a non-standard case, the Gibbs free energy is calculated as

$$\Delta G = \Delta G^0 + \bar{R}T ln \left(\frac{\Pi a_{products}}{\Pi a_{reactants}} \right) \tag{2.5}$$

where G^0 represents the Gibbs free energy change at standard conditions, $\bar{R}$ is the universal gas constant, T is temperature, a represents the activity of a species, and the symbol Π means multiplication of terms. For instance, $\Pi a_{products}$ means multiplication of the activity coefficient of all products. Applying Eq. (2.4) to the Gibbs free energy at standard conditions gives $\Delta G^0 = n_e F \phi^0$. Substituting this expression into Eq. (2.5) gives the definition of the reduction potential for non-standard conditions as

$$\phi = \phi^0 - \frac{\bar{R}T}{n_e F} ln \left(\frac{\Pi a_{products}}{\Pi a_{reactants}} \right) \tag{2.6}$$

Equation 2.6 is known as the Nernst equation and it is used to define the electrochemical potential, or the open-circuit voltage (OCV) of an electrode. The full cell OCV is equal to the difference of ΔG quantities for the reaction that produces a Faradaic current associated with each of the two electrodes. Therefore, the cell voltage is found by taking the difference of Eq. (2.6) for the positive electrode and the negative electrode.

It should be noted that in virtually all cases, the intercalation reaction contains several unknown steps that are neglected when writing intercalation reactions in the standard form, such as Eq. (1.2), repeated here for convenience

$$Li_xC_6 \rightleftharpoons Li^+ + e^- + C_6 \tag{2.7}$$

The unknown steps associated with the intercalation process make calculating the Gibbs free energy difficult. Additionally, the potentials vary dramatically as a function of the amount of lithium contained within the electrode due to the effect of ion-ion interactions (Verbrugge & Koch, 1996) on ionic activity, since the concentrations are typically much greater than in a dilute solution.

At ths point, the concentration of lithium present in the electrodes is discussed to motivate the need to include the activity coefficient term within the Nernst equation. Typical concentrations are on the order of 20–30 M depending on the active material of the electrodes and the electrode state-of-charge. There is a well-defined relationship between the saturation capacity of lithium within the electrode solid phase c_{max}, the specific capacity of the electrode active material q, Faraday's constant F, and the active material density ρ.

$$c_{max} = \frac{q\rho(1000)(3.6)}{F} \tag{2.8}$$

Saturation capacity values are usually reported as mol/m^3, so the conversion factor of 1000 is used to change to units of mAh/g to mAh/kg, and 3.6 is used to change from coulombs to Ah. It is constructive to calculate the saturation capacity for common materials such as graphite in the anode and iron phosphate, manganese oxide, and a nickel transition metal oxide in the cathode. The parameter values are shown in Table 2.1.

	LiC_6	$LiFePO_4$	$LiMn_2O_4$	$LiNi_{1/3}Co_{1/3}Al_{1/3}O_2$
$q\left(\frac{mAh}{g}\right)$	370	170	105	135
$\rho\left(\frac{kg}{m^3}\right)$	2250	2550	4220	4710
$c_{max}\left(\frac{mol}{m^3}\right)$	30500	16320	16530	23640

Table 2.1: Parameter values and resulting saturation concentrations for typical electrode materials.

Due to the high concentrations involved in the solid phase of each electrode, the Nernst equation (Eq. (2.6)) applied within Li-ion battery modeling usually requires a model of the activity coefficients of the involved species. The inclusion of the activity coefficient model can be accounted for by considering an excess free energy, G^E. Several models are available for the excess Gibbs function (Conlisk, 2011; Taylor & Kooijman, 1991; Taylor & Krishna, 1993) and a detailed analysis of all the models is outside the scope of this dissertation. One model (Wohl, 2004; Verbrugge & Koch, 1996) that has been applied to Li-ion negative electrodes writes the excess free energy as

$$G^E = \sum_{k=2}^{n_E} \Omega_k x^k \tag{2.9}$$

where the fractional occupancy or composition, $x = c/c_{max}$ for a negative electrode and $y = c/c_{max}$ for a positive electrode, has been substituted for concentration and n_E is the number of fitting terms needed to provide arbitrarily good agreement with experimental data. The terms Ω_k are a set of empirical coefficients that define the effect of ion-ion interactions on the activity coefficient. The activity coefficients, f, of each species are related to the excess Gibbs free energy by

$$f = exp\left(\frac{1}{\bar{R}T}\frac{\partial}{\partial n_m}\left(n_m G^E\right)\right) \tag{2.10}$$

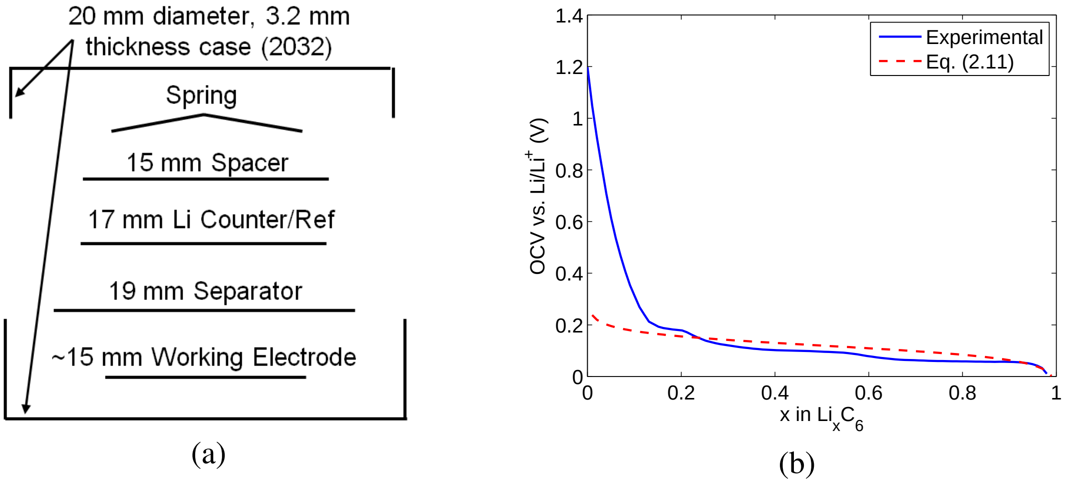

Figure 2.1: (a) Exploded side-view of a two electrode coin cell setup used to measure OCV and (b) experimental data for a graphite negative electrode, along with the prediction of Eq. (2.11) without inclusion of the excess Gibbs term.

where n_m is the number of moles of the species. Substituting Eq. (2.9) into Eq. (2.10), and then substituting that result into Eq. (2.5) gives a logical fitting function for the OCV of a non-ideal solid solution electrode (Verbrugge & Koch, 1996) as

$$\phi = \phi^0 + \frac{\bar{R}T}{n_e F} ln\left(\frac{1-x}{x}\right) - \sum_{k=2}^{n_E} k\Omega_k x^{k-1} \tag{2.11}$$

Though this approach is theoretically closer to the true meaning of the OCV, since only the unknown coefficients Ω_k are left to be identified, it is not often employed, since it nonetheless relies on empirical coefficients. Any general expression for the reduction potential versus x or y that provides agreement with the experimental data is acceptable. Often, a simple experimentally-based interpolation table is utilized for modeling purposes after sufficient filtering of the data to remove noise.

Typically, the electrode of interest is assembled as the working electrode in a two or three electrode setup, with the two electrode setup illustrated in Figure 2.1a. Lithium metal is used as the counter and reference electrode. Between the lithium metal and the working electrode a layer of insulating separator material is placed. The case thickness and number of springs or spacers must be designed so that electrical contact is maintained between the cell case and the electrodes.

Figure 2.1b indicates the result obtained for a graphite electrode, where a constant current discharge of C/20 is used to discharge/charge the cell between voltage limits of 10 mV to 1.2 V. A current this small serves as an approximation to the true OCV, since the resistive effects are small. As the amount of intercalated lithium approaches the saturation capacity of the active material, the potential relative to lithium metal approaches 0 V. The prediction of Eq. (2.11) without inclusion of the excess Gibbs term is also plotted, to demonstrate the need for activity coefficient models. The voltage predicted by Eq. (2.11) without the excess Gibbs term has as high as 60% error for the range $0.6 < x < 0.9$ and it also does not predict the sharp rise in voltage for $x < 0.2$.

As a final note on thermodynamic considerations, the Gibbs free energy of a reaction such as Eq. (2.7) can also be written in terms of the sum of electrochemical potentials, μ. Electrochemical potentials account for the change in chemical energy as well as electrostatic potential, so they are frequently needed when charged ions are considered in a chemical reaction. The relationship between Gibbs free energy and electrochemical potential is $G = \sum_{i=1}^{n} \mu_i n_{m,i}$, where n is the number of species, so that the preceding discussion of thermodynamics could have been written in terms of electrochemical potential. Though it was not needed for the general discussion of electrode OCV, the electrochemical potential will be revisited in a later section to derive the potential variation for a liquid concentrated solution.

The amount of time-varying deviation from the OCV is defined as the overpotential of the cell and may be associated with ohmic sources, charge transfer kinetics, or concentration polarization. These factors are described in detail in the following sections.

2.2.2 Ohmic Factors

The ohmic overpotential is the result of several sources, namely the imperfect electrical contact between the slurry coating and the metallic current collectors, weld joints between the current collectors and external battery tabs, conduction of electrons through the depth of the porous electrode in the solid phase, and ionic conduction in the liquid phase. Of all the sources of overpotential, it is the simplest to model because it requires only a straightforward application of Ohm's law

$$\frac{d\phi}{dx} = \frac{I}{\sigma A} \tag{2.12}$$

where I is current, A is the area available for conduction, ϕ is potential, σ is the conductivity, and x is the coordinate along the conduction path. The conductivity is a material property, that is often a function of temperature, and defines the ability of the material to transport electrons and therefore transfer an electrical current. It relates the gradient of electrical potential to the current density, I/A, traveling in the medium. In general current is a vector, but in one-dimension the vector symbol ($\rightarrow$) is not included to simplify the notation.

The integral form of Eq. (2.12) is commonly applied when the prediction of the potential as a function of the spatial coordinate is not needed, but rather only the difference in potential between two points is required. If the conductivity is not a function of space, then

$$V = \phi(x_2) - \phi(x_1) = IR \tag{2.13}$$

where the potential difference $\phi(x_2) - \phi(x_1)$ is now denoted as a voltage V, $R = (x_2 - x_1)/(\sigma A)$, and the distance between x_2 and x_1 defines the total conduction length. Figure 2.2 illustrates the potential and voltage for a situation with $A = 1$ m^2, $I = 1$ A, and $R = 0.25\ \Omega$.

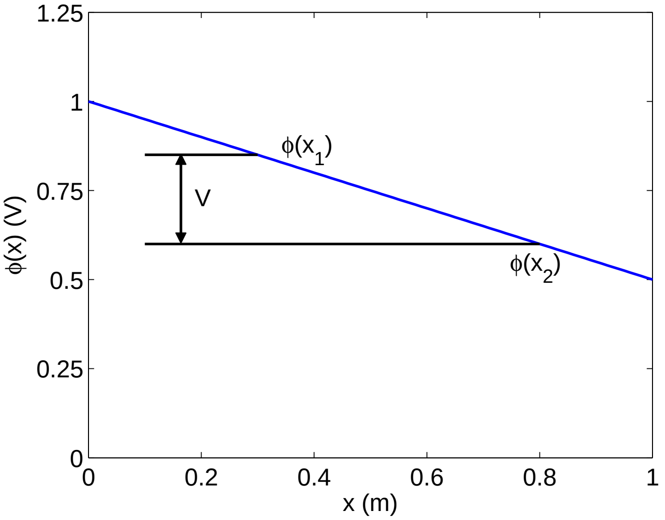

Figure 2.2: Demonstration of the potential and voltage for Eq. (2.13), with $A = 1\ m^2$, $I = 1\ A$, and $R = 0.25\ \Omega$.

2.2.3 Kinetics

In Li-ion electrochemistry, kinetic theory is used to study the rate of the oxidation-reduction reaction that transfers ions across the interface between the solid electrode and liquid electrolyte. It is also used to model the irreversible side reactions responsible for the formation of the solid-electrolyte interphase layer. At equilibrium, both the forward and backward directions of a reversible reaction, such as the process of inserting lithium into the solid host structure, occur at an equal rate. The kinetic overpotential of the reaction

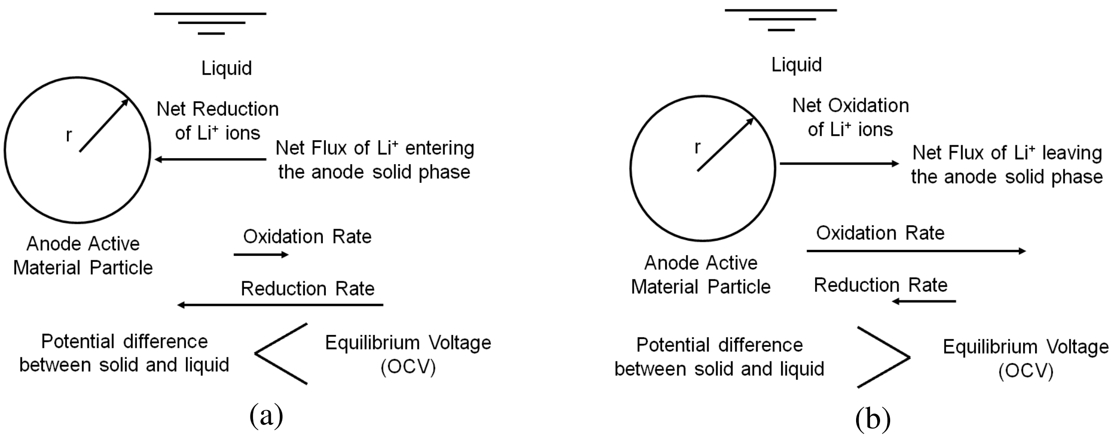

Figure 2.3: Reaction rate bias during a) charge and b) discharge.

results from the finite overpotential, or voltage beyond the equilibrium value, needed to bias the oxidation-reduction reaction in the desired discharge or charge direction. This aspect is illustrated by Figure 2.3.

In Figure 2.3a, the reaction occurs at a voltage that is less than that of the OCV for a representative active material particle of a negative electrode. This results in an increase of the rate of Li^+ ion reduction, and a decrease in the rate of Li oxidation. The net effect is a flux of Li^+ ions leaving the liquid phase and entering the solid phase, in a process known as intercalation.

In Figure 2.3b, the case of de-intercalation is considered, where the reaction occurs at a voltage that is greater than the OCV. This causes the reduction reaction to occur at a reduced rate, and the oxidation rate to increase. The net effect is a flux of Li^+ ions leaving the solid phase and entering the liquid phase, in a process known as de-intercalation.

Butler-Volmer Kinetics

The following gives a derivation of the kinetic expression typically used in Li-ion battery modeling for the calculation of reaction rates, which relies on an equilbrium voltage function. Much of the derivation is taken from (Newman & Thomas-Alyea, 2004).

Before any modeling of reaction kinetics can begin, the chemical reactions being studied must obviously be specified. Until this point, the oxidation-reduction reaction has only been discussed in general terms. Consider the processes that occur during discharge, though the processes that occur during charge are not difficult to determine simply by reversing the direction of current flow in the cell and following the order of events backwards. For instance, during charge, the left arrow (backward direction) of Eqs. (2.14) and (2.15) would occur. For the purposes of this discussion, lithium is assumed to exist in its atomic form in the solid phase of each electrode, though the exact valence of intercalated Li$^+$ is still an active topic of research. When Li de-intercalates from the host matrix and enters the liquid phase, it loses an electron and thus becomes a lithium ion with valence equal to one. This process creates an open site in the host matrix which the lithium atom once occupied. The reaction is summarized for the negative electrode in Eq. (2.14).

$$Li_xC_6 \rightleftharpoons Li^+ + e^- + C_6 \tag{2.14}$$

where a carbon-based electrode has been assumed, hence the compound C_6, though other materials can be substituted with minimal modifications. The convention for all reactions in this work will be to have the forward direction indicate cell discharge. The atomic lithium in the anode solid phase is represented by the left-hand side term Li_xC_6, the lithium ions in the liquid phase are represented by Li^+, and the open site in the anode solid phase created by de-intercalation is given by C_6. The reason six carbon atoms are required for each lithium atom is that the lithium atom fills the intersticial space in the material structure left between six carbon atoms. In the cathode, the lithium ions from the liquid phase intercalate into the solid phase, and an open site that was once available is now occupied by a lithium atom. The cathode half reaction is described by (2.15), where again the right arrow indicates the direction of the reaction during discharge

$$Li^{+} + e^{-} + M \rightleftharpoons Li_{y}M \tag{2.15}$$

where M refers generally to a metal oxide or phosphate compound such as iron phosphate ($FePO_4$) or manganese oxide (Mn_2O_4). The lithium ions in the liquid phase are represented by Li^{+}, the open site within the cathode solid phase is given by M, and the atomic lithium in the cathode solid phase is defined by $Li_{y}M$.

Next, Le Chatelier's principle is applied to quantitatively describe the reaction rate as a function of the reactant concentrations. This principle states that when a chemical system at equilibrium experiences a change in operating conditions such as reactant concentrations or temperature, the equilibrium will shift to counteract the change and a new equilibrium will be established. First we apply it to Eq. (2.14). An increase in $Li_{x}C_{6}$ will cause the rate of the forward reaction to increase, whereas an increase in Li^{+} or C_6 will cause the rate of the reverse reaction to increase. For Eq. (2.15), an increase in Li^{+} or $FePO_4$ will increase the rate of the forward reaction while an increase in $Li_{y}FePO_4$ will increase the rate of the backward reaction.

At this point, we begin to use the notation described in Table 2.2 to be consistent with the notation of the model development later in this dissertation. A bit of discussion on why the quantities $c_{A,an,max} - c_{A,an}$ and $c_{A,ca,max} - c_{A,ca}$ are introduced is required. The symbol C_6 represents an open site in the solid. The number of open sites is equal to the total number of sites, c_{max}, minus the number of occupied sites, $c_{A,an}$. Therefore the symbol C_6

Table 2.2: Notation equivalency between reaction equations and symbols used for model development.

Model Symbols	Reaction Equation Symbols
c_A	Li^+
$c_{A,an,max} - c_{A,an}$	C_6
$c_{A,ca,max} - c_{A,ca}$	M
$c_{A,an}$	Li_xC_6
$c_{A,ca}$	Li_yM

is equivalent to the quantity $c_{max} - c_{A,an}$. A similar discussion applies in the cathode for the relationship between $c_{A,ca,max} - c_{A,ca}$ and the symbol $FePO_4$.

The net rate of a reaction is equal to the difference between the rate of the forward reaction and the rate of the backward reaction, written as

$$\frac{i}{n_eF} = k_f c_R exp\left(\frac{(1-\alpha)n_eF}{\bar{R}T}\phi\right) - k_b c_O exp\left(-\frac{\alpha n_eF}{\bar{R}T}\phi\right) \tag{2.16}$$

where i is current density in A/m^2, k_f and k_b are rate constants for the forward and backward reactions, respectively, and c_R and c_O are the concentrations of the reduced and oxidized reactants, respectively. Here we use the term reduced and oxidized reactants loosely to mean any reactant on the same side of the reaction equation as a reduced or oxidized species, so that c_O and c_R can actually represent multiple species. The combination of the k values along with the exponential dependence on potential represent rate constants with potential-dependent activation energies. The dependence on temperature is Arrhenius, which is the term given to the dependence on temperature of the form $exp(1/T)$. The quantity $\phi n_eF/\bar{R}T$ is referred to as the "energy" of the reaction. It is assumed that the chemical reaction of interest produces electrons, so that it is appropriate to use current density to define the reaction rate.

The units of the rate constants depend on the number of reactants included in the c_R and c_O terms as well as the order of the reaction. As an example, consider the case of a first order reaction with one reactant. Current density has units of A/m^2, and the reactant has units of mol/m^3. Thus, the rate constant must have units of m/s. Other situations involving more than one reactant will have different rate constant units.

The parameter α is called the reaction symmetry factor. It defines the fraction of applied potential that contributes to the forward ($1 - \alpha$) and backward (α) reaction rates. It takes values between zero and one, with the most common assumption as $\alpha = 0.5$. Still, the limiting cases provide insight into the parametric effects of this constant. For instance, if α is equal to zero, we have

$$\frac{i}{n_e F} = k_f c_R exp\left(\frac{n_e F}{\bar{R}T}\phi\right) - k_b c_O \tag{2.17}$$

In this specific case, the backward reaction rate is a function solely of k_b and c_O and has no dependence on the potential. It essentially reduces the backward reaction rate to a first-order chemical reaction, instead of an electrochemical reaction. Next consider α equal to one,

$$\frac{i}{n_e F} = k_f c_R - k_b c_O exp\left(-\frac{n_e F}{\bar{R}T}\phi\right) \tag{2.18}$$

With this assumption, the forward reaction rate is a function solely of k_f and c_R and has no dependence on the potential. Both of these cases ($\alpha = 0$ and $\alpha = 1$) are not physically relevant when considering the intercalation process within lithium-ion batteries, though they may have some relevance when considering side reactions. To identify the exact value of α, one would need to perform potentiostatic sweeps in a half-cell setup and consider whether

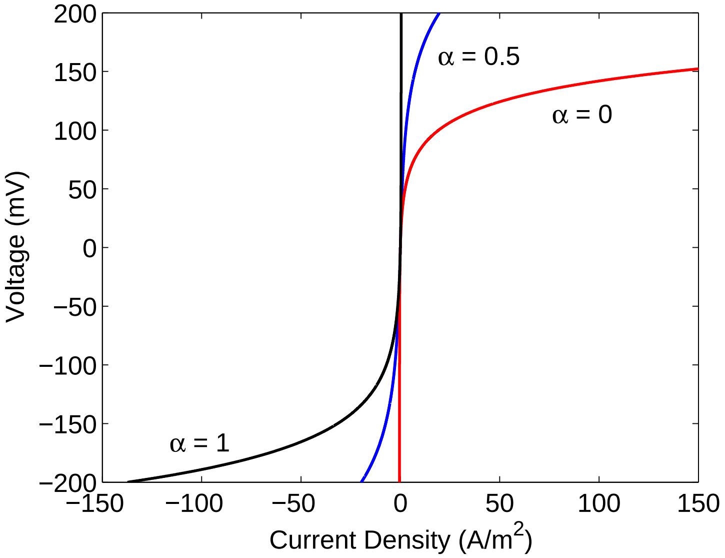

Figure 2.4: Demonstration of the effects of the symmetry factor on the current-voltage relationship of charge transfer.

the voltage-current plot is symmetric. Figure 2.4 gives an illustration of the dependence of the current-voltage relationship on α.

For the limiting cases of $\alpha = 0$ and $\alpha = 1$, the current reaches a saturation value in one direction. Symmetry about the origin of this plot indicates $\alpha = 0.5$. The system-level result of this fundamental parameter is that it determines whether the electrode polarization is dependent on the direction of current. In other words, the electrode resistance is not dependent on the direction of the current for $\alpha = 0.5$. Since this is the behavior observed from the cell-level current-voltage relationship of the cells studied in this dissertation, the assumption that both negative and positive electrodes have α equal to 0.5 is used throughout the model development of later sections. However, the rest of the derivation will proceed without this assumption to maintain generality.

The equations describing the rate of Eq. (2.14) and Eq. (2.15) are respectively

$$\frac{i}{n_eF} = k_f c_{A,an} exp\left(\frac{(1-\alpha)n_eF}{\bar{R}T}\phi_{an}\right) - k_b c_A (c_{A,an,max} - c_{A,an}) exp\left(-\frac{\alpha n_e F}{\bar{R}T}\phi_{an}\right) \tag{2.19}$$

$$\frac{i}{n_eF} = k_f c_A (c_{A,ca,max} - c_{A,ca}) exp\left(\frac{(1-\alpha)n_eF}{\bar{R}T}\phi_{ca}\right) - k_b c_{A,ca} exp\left(-\frac{\alpha n_e F}{\bar{R}T}\phi_{ca}\right) \tag{2.20}$$

Equation (2.19) is the rate equation at the anode while Eq. (2.20) is the rate equation of the cathode. Note that $i_{an} = i_{ca}$ in order to achieve a closed electrical circuit and conserve charge.

As discussed previously, the equilibrium potential is the value of the potential difference between each electrode and the liquid phase, at which the rates of the forward reaction and the backward reaction will become equal. This value of potential is called U, the equilibrium potential, and is highly material-dependent. Previous discussion used U for internal energy, but from this point forward it represents equilibrium potential, or OCV.

The following derivation focuses on Eq. (2.19), though the method can be applied at either the anode or the cathode with minimal modifications. Setting $i_{an} = 0$ such that the forward and backward rates are equal gives

$$k_f c_{A,an} exp\left(\frac{(1-\alpha)n_eF}{\bar{R}T}U_{an}\right) = k_b c_A (c_{A,an,max} - c_{A,an}) exp\left(-\frac{\alpha n_e F}{\bar{R}T}U_{an}\right) \tag{2.21}$$

Solving for U_{an} gives

$$U_{an} = \frac{\bar{R}T}{n_eF} ln\left(\frac{k_b c_A (c_{A,an,max} - c_{A,an})}{k_f c_{A,an}}\right) \tag{2.22}$$

Now, replace ϕ_{an} with $\eta_{an} = \phi_{an} - U_{an}$ in Eq. (2.14), where η is referred to as the applied overpotential with the subscript indicating the electrode of interest. Substituting this and

Eq. (2.22) into Eq. (2.19) gives

$$\begin{aligned}\frac{i_{an}}{n_eF} =&k_fc_{A,an}exp\left[\frac{(1-\alpha)n_eF}{\bar{R}T}\eta_{an}+(1-\alpha)ln\left(\frac{k_bc_A(c_{A,an,max}-c_{A,an})}{k_fc_{A,an}}\right)\right]\\ &-k_bc_A(c_{A,an,max}-c_{A,an})exp\left[-\frac{\alpha n_eF}{\bar{R}T}\eta_{an}-\alpha ln\left(\frac{k_bc_A(c_{A,an,max}-c_{A,an})}{k_fc_{A,an}}\right)\right]\end{aligned} \tag{2.23}$$

Further algebraic simplifications can be obtained by removing the natural logarithm terms from the exponential

$$\begin{aligned}\frac{i_{an}}{n_eF} =&k_fc_{A,an}exp\left[\frac{(1-\alpha)n_eF}{\bar{R}T}\eta_{an}\right]\left(\frac{k_bc_A(c_{A,an,max}-c_{A,an})}{k_fc_{A,an}}\right)^{(1-\alpha)}\\ &-k_bc_A(c_{A,an,max}-c_{A,an})exp\left[-\frac{\alpha n_eF}{\bar{R}T}\eta_{an}\right]\left(\frac{k_bc_A(c_{A,an,max}-c_{A,an})}{k_fc_{A,an}}\right)^{-\alpha}\end{aligned} \tag{2.24}$$

Then, distributing the exponent (α or $1-\alpha$) throughout all the terms gives

$$\begin{aligned}\frac{i_{an}}{n_eF} =&k_f^{\alpha}k_b^{1-\alpha}c_{A,an}^{\alpha}(c_A(c_{A,an,max}-c_{A,an}))^{1-\alpha}\\ &\cdot\left(exp\left[\frac{(1-\alpha)n_eF}{\bar{R}T}\eta_{an}\right]-exp\left[-\frac{\alpha n_eF}{\bar{R}T}\eta_{an}\right]\right)\end{aligned} \tag{2.25}$$

The exchange current density for the anode is defined as

$$i_0 = n_eFk_f^{\alpha}k_b^{1-\alpha}c_{A,an}^{\alpha}(c_A(c_{A,an,max}-c_{A,an}))^{1-\alpha} \tag{2.26}$$

Then, with the assumption of α equal to 0.5, setting $n_e = 1$ because one lithium ion is intercalated per electron, lumping all k_i's into one k, and writing the difference in exponentials as hyperbolic sine, we have the final form typically used in Li-ion battery modeling literature

$$i_{an} = 2i_0sinh\left(\frac{F}{2\bar{R}T}\eta_{an}\right) \tag{2.27}$$

with $i_0 = Fk_{an}\sqrt{c_{A,an}c_A\left(c_{A,an,max}-c_{A,an}\right)}$. Again, the derivation process could be repeated for the cathode following similar steps.

If the electrodes are metallic, and therefore not limited by a saturation capacity as in electrodes that operate via intercalation, then there is no dependence on sites within the host matrix as a reactant. This is because the plating/stripping process on a metallic electrode is a fundamentally different process than intercalation. The rate equation based on Eq. (2.16), but for a metal electrode, is

$$\frac{i}{n_e F} = k_f c_R exp\left(\frac{(1-\alpha)n_e F}{\bar{R}T}\phi\right) - k_b c_m exp\left(-\frac{\alpha n_e F}{\bar{R}T}\phi\right) \tag{2.28}$$

The concentration $c_m = \rho_m / M_m$ is the molar density of the metal used to fabricate the electrode, with ρ_m as the metal density and M_m as the metal molecular weight. Note that this approach implies that c_m is a constant, meaning diffusion is not limiting for the process. Following the procedure of the previous section to obtain an exchange current density via algebraic manipulations gives

$$i_0 = n_e F k_f^{\alpha} k_b^{1-\alpha} c_R^{\alpha} c_m^{1-\alpha} \tag{2.29}$$

For lithium metal, the exchange current density tends to be large because $c_m = 76900$ mol/m^3 when taking $\rho = 0.534$ g/cm^3 and $M_m = 6.94$ g/mol. This situation results in low overpotentials when lithium metal is used as a counter/reference electrode, making a two-electrode setup sufficient in most cases involving lithium. Equation (2.29) does not have a dependence on available sites within the solid, as Eq. (2.26) does.

Tafel Kinetics

Beginning from Eq. (2.27), simplifications may be introduced when the applied overpotential η is large. This results in the reaction proceeding predominantly in the forward or backward direction depending on the sign of the overpotential. Quantitatively this implies

$$i = i_0 exp\left(\frac{\alpha F}{\bar{R}T}\eta\right) \quad \text{or} \quad i = -i_0 exp\left(-\frac{(1-\alpha)F}{\bar{R}T}\eta\right) \tag{2.30}$$

Julius Tafel made the experimental observation that the current density varies exponentially with the overpotential for large overpotentials (Burstein, 2005), so Eq. (2.30) is called the

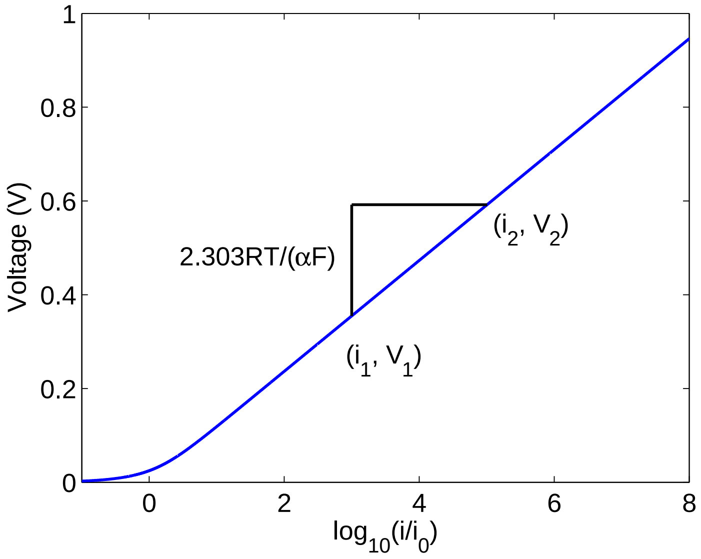

Figure 2.5: Plot of Eq. (2.30) that demonstrates the Tafel slope (Burstein, 2005) for large overpotentials.

Tafel approximation of the Butler-Volmer law (van Schalkwijk & Scrosati, 2002). Figure 2.5 shows the linear trend of the current-voltage relationship for large overpotentials, when plotting on a semi-log plot. The Tafel slope between points (i_1, V_1) and (i_2, V_2) is labeled as $2.303\frac{\bar{R}T}{\alpha F}$ for the linear portion of the plot. The factor of $2.303 = ln(10)$ comes from computing the slope of voltage versus decade of current rather than voltage versus current. Since it is typical in battery modeling literature to assume $\alpha = 0.5$, the value of the Tafel slope lies in using it to estimate the exchange current density. The current and voltage are experimentally measured quantities, so the exchange current density is estimated as

$$i_0 = i \cdot 10^{\left(-\frac{\eta\alpha F}{2.303\bar{R}T}\right)} \tag{2.31}$$

Typically many points would be used to obtain an average estimate of the exchange current density in order to reduce the experimental uncertainty of the calculation.

Low-Field Kinetics

If the overpotential η is small, a linearized form of the Butler-Volmer kinetics may be applied. This approach is called the "low-field" approximation. Taking the derivative of Eq. (2.27) gives

$$\frac{di}{d\eta} = \frac{i_0 \alpha F}{\bar{R}T} \left[exp\left(\frac{\alpha F}{\bar{R}T}\eta \right) - exp\left(-\frac{\alpha F}{\bar{R}T}\eta \right) \right] \tag{2.32}$$

The term within brackets is equal to $cosh\left(\frac{\alpha F}{\bar{R}T}\eta\right)$, which equals one when its argument equals zero. For $\eta \ll \bar{R}T/(\alpha F)$, the term within brackets can be taken as approximately one. Applying this simplification gives

$$\frac{di}{d\eta} = \frac{i_0 \alpha F}{\bar{R}T} \tag{2.33}$$

Comparing this expression with the typical manifestation of Ohm's law, $V = IR_{ct}$, suggests that for Butler-Volmer kinetics $R_{ct} = \frac{\bar{R}T}{\alpha F i_0}$, a quantity that is called the charge-transfer resistance. It may be extracted from electrochemical impedance spectroscopy experiments (Barsoukov & Macdonald, 2005) since these inherently use a small signal.

2.2.4 Transport

The transport of species within a Li-ion cell is an important fundamental process because transport limitations occuring in both the solid and liquid phases will affect the cell voltage. The Poisson Nernst-Planck equations are used to model the concentration of ionic species as well as the potential field. These equations are general enough to be applied to either the solid or liquid phase within a Li-ion cell, though different sets of assumptions apply for each. The Poisson Nernst-Planck equations are accurate for dilute solutions that do not exhibit significant interaction between ions; in many situations involving the chemistries commonly used in Li-ion batteries, concentrated solution theory provides improved agreement with experimental data. For this reason, concentrated solution theory is also discussed.

The Poisson Nernst-Planck Equations

The Poisson Nernst-Planck (PNP) equations are used to model the transport of ionic species. The conservation of mass for an arbitrary ion *i* is given by

$$\frac{\partial c_i}{\partial t} + \nabla \cdot \vec{N}_i = -\tilde{R}_i(t) \tag{2.34}$$

where the ionic concentration is denoted as c_i, the ionic flux as N_i, and the local production (or depletion) of ions due to a chemical reaction as $\tilde{R}_i$. In the separator region of a Li-ion battery, $\tilde{R}_i = 0$, while in the electrodes it is determined through a nonlinear coupling of the solid and liquid phases by the Butler-Volmer law. In the general case, the flux contains contributions from diffusion, migration, and convection (Conlisk, 2011). However in a Li-ion battery there is no fluid convection, so the flux is

$$\vec{N}_i = -D_i \nabla c_i + \frac{D_i}{\bar{R}T} z_i F c_i \vec{E} \tag{2.35}$$

in which the diffusion coefficient is D_i, z_i is the valence of the ion, F is Faraday's constant, $\vec{E}$ is the electric field, $\bar{R}$ is the universal gas constant, and T is the cell temperature. In the general case temperature can be a function of space and time.

The potential must also be defined since it is a factor in determining the ionic flux due to migration. The potential and electric field are related by Maxwell's equation (Fleisch, 2008) such that

$$\vec{E} = -\nabla \phi \tag{2.36}$$

In a dilute solution, where the electrostatic potential dominates, the potential ϕ satisfies Poisson's equation such that

$$-\nabla \cdot \bar{\epsilon}_e \nabla \phi = \rho_e \tag{2.37}$$

where $\bar{\epsilon}_e$ is the electrical permittivity of the medium in which transport occurs, which is often assumed to be invariant of space for a uniform medium. By performing a simple summation over the number of species n, the charge density per unit volume, ρ_e, is defined as

$$\rho_e = F \sum_{i=1}^{n} z_i c_i \tag{2.38}$$

Combining Poisson's equation (2.37), the charge density definition (2.38), and the electric field definition (2.36) gives the final dimensional form of the equation for potential

$$\nabla^2 \phi = -\frac{F}{\bar{\epsilon}_e} \sum_{i=1}^{n} z_i c_i \tag{2.39}$$

The definition of the electrical current density in a flowing electrolyte solution having concentration gradients is derived in a similar fashion to the charge density, by summing over all charged constituents

$$\vec{J} = F \sum_{i=1}^{n} z_i \vec{N}_i \tag{2.40}$$

Equations (2.34) and (2.39) are a complete set of $N+1$ equations, where N is the number of ionic species in the solution, that can be solved for the N ionic concentrations and potential distribution after specification of appropriate boundary conditions.

An alternate form of Eq. (2.35), written in terms of the current density rather than the potential gradient (Taylor & Krishna, 1993), can be useful since batteries are often operated with a controlled current instead of a controlled voltage. It is convenient for the following analysis to define the electrical conductivity, κ_i, of species i as

$$\kappa_i = \frac{F^2}{\bar{R}T} c_i z_i^2 D_i \tag{2.41}$$

as well as the equivalent electrical conductivity of the mixture, κ, which is the sum of all species conductivities

$$\kappa = \frac{F^2}{\bar{R}T} \sum_{i=1}^{n} c_i z_i^2 D_i \tag{2.42}$$

The transference number, t_i, is defined as the ratio of the species conductivity to the mixture conductivity

$$t_i = \frac{\kappa_i}{\kappa} \tag{2.43}$$

These parameters are purely algebraic expressions that do not require any assumptions for their definition at this point. They clearly depend on the ionic concentrations, which vary in space, so in later analysis if they are moved outside a gradient operator there is an implicit assumption of negligible concentration gradients. Inserting the flux definition of Eq. (2.35) into Eq. (2.40) and solving for the potential gradient while making use of the conductivity definitions gives

$$\nabla\phi = -\frac{\vec{i}}{\kappa} - \frac{F}{\kappa} \sum_{i=1}^{n} z_i D_i \nabla c_i \tag{2.44}$$

Now substituting Eq. (2.44) into Eq. (2.35) gives the flux in terms of the ionic current density

$$\vec{N}_i = -D_i \nabla c_i + \frac{t_i}{z_i F}\vec{i} + \frac{t_i}{z_i} \sum_{i=1}^{n} z_j D_j \nabla c_j \tag{2.45}$$

where the definition of the transference number has also been utilized. This expression may be simplified even further by grouping all terms that involve a concentration gradient and thereafter defining an effective diffusion coefficient

$$D_{i,eff} = D_i - \frac{t_i}{z_i} \sum_{i=1}^{n} z_j D_j \frac{\nabla c_j}{\nabla c_i} \tag{2.46}$$

which, upon substitution into Eq. (2.45) yields (Taylor & Krishna, 1993)

$$\vec{N}_i = -D_{i,eff} \nabla c_i + \frac{t_i}{z_i F}\vec{i} \tag{2.47}$$

This is the dilute form of the flux that is commonly applied in Li-ion battery literature, since the convection term $c_i v_i$ has been neglected.

The discussion to this point has considered the most general case of a three-dimensional geometry and no negligible flux terms. Further simplifications can be made in several instances relevant to Li-ion battery modeling. For example, a one-dimensional geometry is often considered to be sufficient based on a dimensional analysis of the unit cell geometry, illustrated in Figure 2.6. The unit cell components (negative electrode, separator, positive electrode) have length and width on the order of several centimeters to meters. Their thickness, however, is on the order of 10^{-4} m. This results in the gradients in the y and z directions to be negligible compared to the x direction.

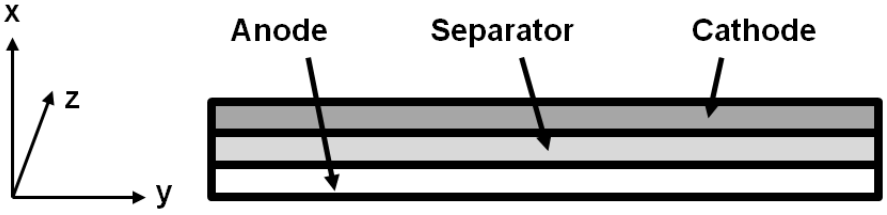

Figure 2.6: Unit cell geometry where x dimension is O(10^{-4}) m, while y and z (into the page) dimensions are O(10^0) m.

The convective flux within the liquid phase has been neglected because volume changes in the electrodes are not considered. If galvanostatic charge or discharge is being considered, the time derivative on the left-hand side of Eq. (2.34) is zero based on the time scale of discharge (hours) compared with the time scale of transport (several seconds).

Further simplifications depend on the condition of electroneutrality, which states that there is no charge separation over a macroscopic distance (Newman & Tiedemann, 1975).

If the liquid phase is assumed to be electroneutral for the bulk region, where the term bulk referes to any region that is a sufficient distance away from the interface between solid and liquid, and the galvanostatic case is considered, then an analytical solution to the set of Eqs. (2.34) and (2.39) is possible.

In the solid phase, other simplifications are possible. Again, the convection flux may be neglected if volume expansion effects are negligible. Migration is not applicable for two reasons. First, significant variations in potential do not exist within an active material particle. This is a generally accepted assumption due to the small size of active material particles and the conductive carbon coating that is typically applied to enhance their conductivity. Second, it may be assumed that there is a net zero charge in the solid phase due to fast electron transport relative to lithium diffusion. The resulting transport equation for the solid phase is a diffusion equation,

$$\frac{\partial c_i}{\partial t} = \nabla \cdot (D_i \nabla c_i) \tag{2.48}$$

The solid phase transport process is important because the concentration of lithium at the active material particle surface determines several of the important thermodynamic and kinetic characteristics discussed in previous sections.

The dynamics of the cell voltage after the initial overpotential are driven primarily by increasing concentration polarization. This aspect is illustrated by Figure 2.7. A representative graphite electrode particle has been used for this discussion, but the explanation applies equally well to most presently utilized Li-ion chemistries. Due to diffusion limitations, the surface concentration of lithium, $c_n(R_n, t)$, may be significantly different than the average concentration contained within the active material particle. The average concentration indicates the concentration level that the would be reached if the current were interrupted and the cell were allowed to come to equilibrium. The difference between the

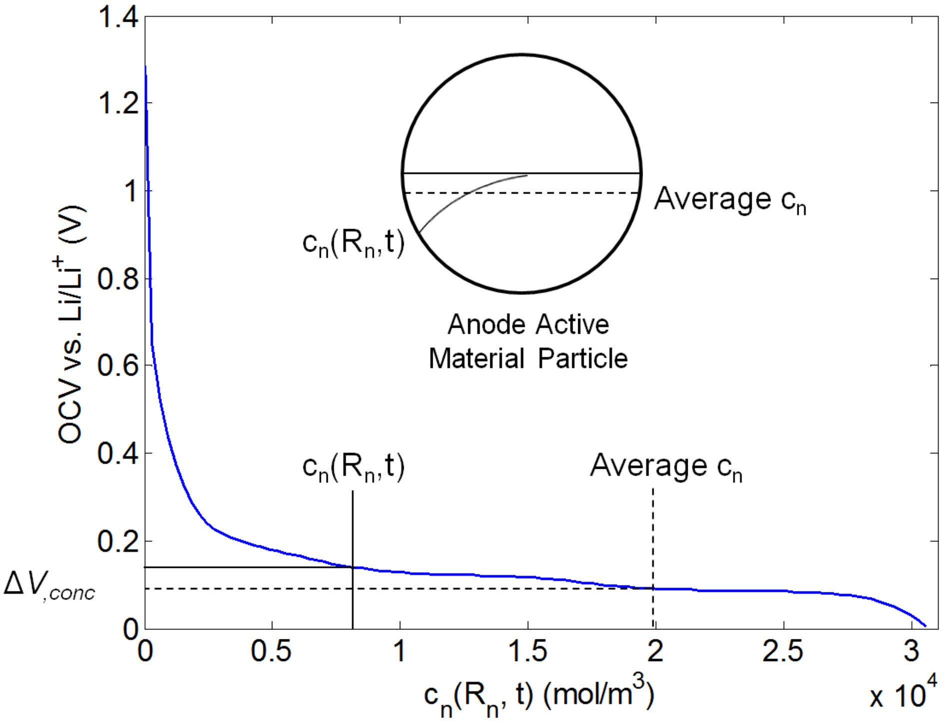

Figure 2.7: Concentration overpotential due to difference between mean concentration and surface concentration. Difference between solid and dashed lines indicating voltage on the vertical axis gives concentration overpotential.

two concentrations is represented by the solid and dashed lines indicating points along the x-axis, and this variation leads to a variation in the OCV indicated along the y-axis. This variation is referred to as solid concentration overpotential.

Concentrated Solution Theory

The term concentrated solution refers to an electrolyte/solvent mixture in which there are important interactions between ionic species that require modification of the flux description (Newman & Chapman, 1973). In the dilute solution development, the species are assumed to interact only with the solvent, while in the concentrated solution development interactions between all species are considered. Transport properties in the dilute solution section contained only one subscript because it is clear that the species interact only with the solvent. In this section, a dual subscript such as D_{ij} indicate the transport property resulting from the interaction of species i with species j.

The definition of the flux, Eq. (2.35), from dilute solution theory can be replaced by the multicomponent transport equation (Newman & Thomas-Alyea, 2004)

$$c_i \nabla \mu_i = \bar{R}T \sum_{j=1}^{n} \frac{c_i c_j}{c_T D_{ij}} \left(\vec{v}_j - \vec{v}_i \right) \tag{2.49}$$

where μ_i is the electrochemical potential of species i, n is the number of species in the solution, $K_{ij} = \bar{R}T \frac{c_i c_j}{c_T D_{ij}}$ is a friction coefficient characterizing species interactions, D_{ij} is the diffusion coefficient based on interactions between species i and species j, and $\vec{v}_i$ is the average velocity of species i such that $\vec{N}_i = c_i \vec{v}_i$. For each index i, the index j denotes the interaction between species i and the species indicated by j. The total concentration within the solution is $c_T = \sum_{i=1}^{n} c_i$.

For this analysis, a two ion system is considered since most current cases of interest for Li-ion batteries consist of a salt composed of a single positive and single negative ion. Additionally, further analysis requires the inversion of Eq. (2.49) to obtain the flux as a function of the driving electrochemical potential μ_i, and the inversion procedure is simplest for a two ion system. Denoting properties of the positive ion with a subscript $+$, and those of the negative ion with $-$, the two independent flux equations that emerge from Eq. (2.49) are

$$\begin{aligned} \vec{N}_+ &= -\frac{\nu_+ \bar{D}}{\nu \bar{R}T} \frac{c_T}{c_0} c \nabla \mu_e + \frac{\vec{i} t_+^0}{z_+ F} \\ \vec{N}_- &= -\frac{\nu_- \bar{D}}{\nu \bar{R}T} \frac{c_T}{c_0} c \nabla \mu_e + \frac{\vec{i} t_-^0}{z_- F} \end{aligned} \tag{2.50}$$

where c_0 refers to the solvent concentration, and in general in this section the subscript 0 refers to solvent properties, $\mu_e = \nu_+\mu_+ + \nu_-\mu_-$, and the ν values are determined by the stoichiometry of the electrolyte salt dissociation reaction. As an example consider the complete dissociation of lithium hexaflourophosphate ($LiPF_6$) into positive and negative ions

$$LiPF_6 \rightleftharpoons Li^+ + PF_6^- \tag{2.51}$$

Here there is one positive and one negative ion produced per salt molecule. Thus, $\nu_+ = 1$, $\nu_- = 1$, and $\nu = \nu_+ + \nu_- = 2$. Note that the ν_+ and ν_- quantities are defined in the same manner as stoichiometric coefficients. However, when later defining the potential of a concentrated solution there will be a reference electrode reaction in addition to the salt dissociation reaction of Eq. (2.51). Therefore, the ν symbol is used to distinguish electrolyte dissociation quantities from those of the reference electrode. There is no dependence on the composition, x or y, as was observed for the intercalation reactions specified in Eqs. (2.14) and (2.15) respectively.

Prior discussion featured a diffusion coefficient, D, that relates the ionic flux to the concentration gradient. The term $\bar{D}$ is a diffusion coefficient for the entire salt based on the gradient of electrochemical potential, which is the true thermodynamic driving force, and its definition

$$\bar{D} = \frac{D_+ D_- \left(z_+ - z_-\right)}{z_+ D_+ - z_- D_-} \tag{2.52}$$

emerges from the algebraic manipulations required when inverting Eq. (2.49) (Newman & Thomas-Alyea, 2004). This relationship between $\bar{D}$ and D, is used to relate the gradient of chemical potential of the electrolyte in terms of the concentration gradient of salt

$$\frac{\bar{D}}{\nu \bar{R} T}\frac{c_T}{c_0} c \nabla \mu_e = D \left(1 - \frac{d\ln c_0}{d\ln c}\right) \nabla c \tag{2.53}$$

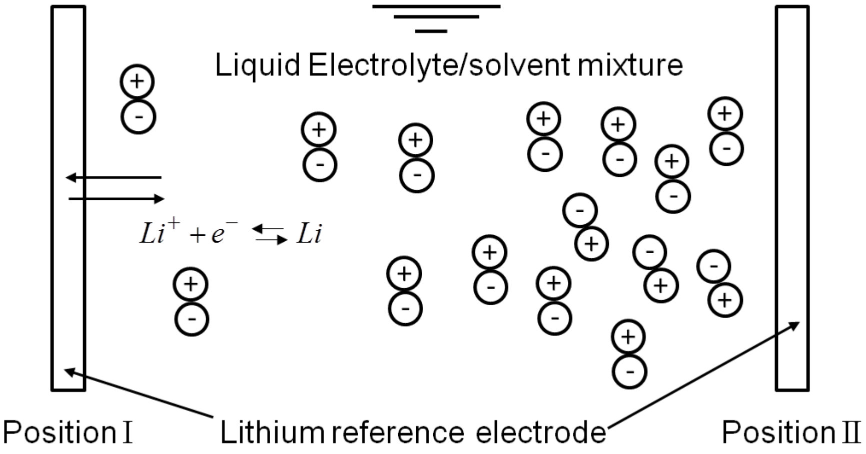

Figure 2.8: Hypothetical reference electrode used to develop the equations describing potential in a concentrated solution. Position II exhibits a greater electrochemical potential than Position I.

Using Eq. (2.53) to substitue the electrochemical potential for the concentration gradient into the general flux definition gives

$$\vec{N} = D\left(1 - \frac{d\ln c_0}{d\ln c}\nabla c\right) - \frac{\vec{i}t_+^0}{z_+\nu_+F} \tag{2.54}$$

Comparing Eq. (2.54) with Eq. (2.35), there are many similarities. The convective flux term is unchanged, as is the migration term. If the variation of the solvent concentration with respect to the salt concentration is small, so that $\frac{d\ln c_0}{d\ln c} \ll 1$, then the flux expressions are equivalent. Physically this implies that the change of the solvent/solute system volume with addition of the solute is negligible.

The potential must also be modified when considering concentrated solution theory. To develop the equations describing the variation of potential in an electrolytic solution, consider the situation of Figure 2.8 where a reference electrode is immersed in a liquid electrolyte solution (van Schalkwijk & Scrosati, 2002). A general reaction equation for a reference electrode immersed in electrolyte is (Newman & Thomas-Alyea, 2004)

$$s_-\mu_- + s_+\mu_+ + s_0\mu_0 = -n_e F\phi \tag{2.55}$$

Figure 2.8 shows the specific case where $s_0 = 0$ and $s_- = 0$, which will often be the case for Li-ion batteries, but the rest of the derivation proceeds with the general form. Since this is a reference electrode, the current passed by the electrode is negligible and the electrode/electrolyte system is in equilibrium. An alternative analysis that reaches the same conclusions as the reference electrode considers a junction of two dissimilar liquids (Bard & Faulkner, 2001).

Next, consider moving the electrode from on spatial Position I to spatial Position II, indicated in Figure 2.8. There is a variation in electrochemical potential due to the variation in salt concentration between Position I and Position II. This variation could also be due to a variation in the electrostatic potential, though a concentration gradient is easier to visualize as an exemplary case. Note that the presence of a concentration gradient in this sense does not violate the requirement of equilibrium conditions as discussed in the thermodynamics section, since equilibrium refers to the electrode/electrolyte interface and not to the entire electrolyte system in this sense. Thus the gradient between Position I and Position II of Eq. (2.55) is

$$s_-\nabla\mu_- + s_+\nabla\mu_+ + s_0\nabla\mu_0 = -n_e F\nabla\phi \tag{2.56}$$

At this point, the individual electrochemical potentials will be replaced by the current density and the chemical potential by algebraic manipulations (Newman & Thomas-Alyea, 2004). This is desirable since the chemical potential is related to the ionic concentration of salt by Eq. (2.53). To accomplish this task, the flux expressions of Eqs (2.50) are substituted into the multicomponent diffusion equation, Eq. (2.49) to give

$$\frac{1}{z_-}\nabla\mu_- = -\frac{F}{\kappa}\vec{i} - \frac{t_+^0}{z_+\nu_+}\nabla\mu_e \tag{2.57}$$

Here κ is still the conductivity of the solution, but has a new definition because interactions between all species are now considered rather than only interactions between the species and solvent

$$\frac{1}{\kappa} = \frac{-\bar{R}T}{c_T z_+ z_- F^2}\left(\frac{1}{D_{+-}} + \frac{c_0 t_-^0}{c_+ D_-}\right) \tag{2.58}$$

The consideration of interactions in this two-ion system gives an additional term, $1/D_{+-}$. If more species were present there would be additional interaction terms. The quantity μ_0 can be eliminated from Eq. (2.56) by means of the Gibbs-Duhem equation, $c_0 d\mu_0 + cd\mu_e = 0$ (Moran & Shapiro, 2004). Then combining terms that are multiplying the gradient of electrochemical potentials and noting that $s_+z_+ + s_-z_- = -n_e$ gives

$$s_+\mu_+ + s_-\mu_- = \frac{s_+}{\nu_+}\nabla\mu_e - \frac{n_e}{z_-}\nabla\mu_- \tag{2.59}$$

Substituting this result into the equilibrium condition, Eq. (2.55), gives

$$-F\nabla E = \left(\frac{s_+}{n_e\nu_+} - \frac{s_0 c}{n_e c_0}\right)\nabla\mu_e - \frac{1}{z_-}\nabla\mu_- \tag{2.60}$$

The potential is now defined in terms of the electrochemical potential and the current density by

$$\nabla\phi = \frac{\vec{i}}{\kappa} - \frac{\kappa}{F}\left(\frac{s_+}{n_e\nu_+} + \frac{t_+^0}{z_+\nu_+} - \frac{s_0 c}{n_e c_0}\right)\nabla\mu_e \tag{2.61}$$

where s is the stoichiometry coefficient of the reference electrode reaction, for example given in Figure 2.8, t_+^0 is the transference number, and z is the ion valence, and ν is the number of moles of ions each mole of salt contains. Since the electrochemical potential is related to the concentration gradient, which is typically of more interest, it is preferable to insert the concentration dependence

$$\nabla\phi = \frac{\vec{i}}{\kappa} - \frac{\nu\bar{R}T}{F}\left(\frac{s_+}{n_e\nu_+} + \frac{t_+^0}{z_+\nu_+} - \frac{s_0 c}{n_e c_0}\right)\left(1 - \frac{d\ln c_0}{d\ln c}\right)\left(1 + \frac{d\ln f}{d\ln c}\right)\nabla c \qquad (2.62)$$

In summary, Eq. (2.54) and (2.62) of concentrated solution theory may be used in place of Eq. (2.35) and (2.39).

2.3 Hierarchy of Modeling Techniques for Li-Ion Batteries

There are many techniques that are capable of modeling lithium-ion battery performance, where performance modeling is defined as predicting the battery voltage in response to current and temperature inputs. A performance modeling literature review is now conducted by organizing the contributions into a hierarchical framework that allows for a unique comparison of the various model structures, functionalities and potential applications. The hierarchical arrangement displayed in Figure 2.9 gives an introduction to the various model structures that will be discussed. This arrangement is viewed as a family of models that predict the performance of battery systems, but with application-specific complexity. The hierarchy separates into two distinct branches representing two fundamentally different modeling methods. The starting point for the right side of the hierarchy is the porous electrode model structure (Newman & Tiedemann, 1975; Doyle *et al.*, 1993; Newman & Thomas-Alyea, 2004). This model is useful in cell design studies and for developing an understanding of the fundamental processes that occur during battery operation. The left branch represents models that apply the equivalent circuit analogy to predict the electrical dynamics of batteries using an empirical approach that provides limited information about internal processes. Both branches achieve simplifications by reducing the number of spatial dimensions that are modeled. Model order reduction techniques can also be applied, as discussed in more detail in a later section of this chapter. Model order reduction refers

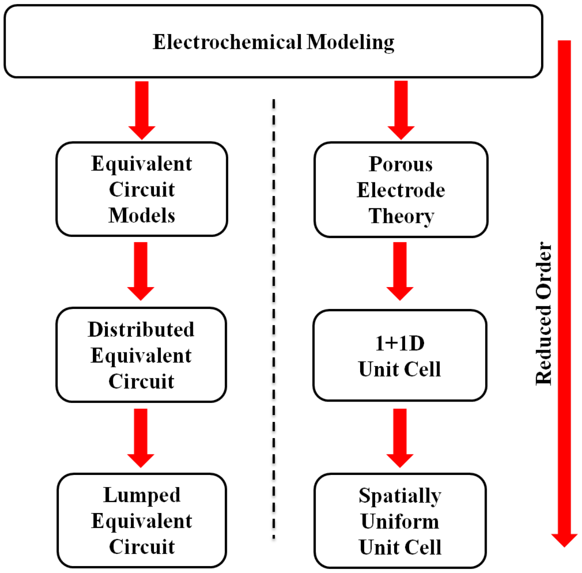

Figure 2.9: Hierarchical arrangement of various approaches for modeling electrochemical systems.

to the process of applying mathematical or phenomenolgical simplifications to a physical problem to reduce the number of differential and algebraic equations that must be solved.

In order to model battery performance, the system is considered to be a collection of unit cells, comprised of a negative electrode, separator, and positive electrode, as illustrated in Figure 2.10. If the battery temperature is uniform, then typically one unit cell is used to represent the performance of the entire battery. Consideration of multiple, coupled unit cell models to model spatially non-uniform heat generation within a Li-ion cell can lead to improved cell design strategies (Kim *et al.*, 2011). However, for the cell geometry and discharge rates considered in this dissertation, non-uniform thermal effects are not prevalent and one unit cell is considered sufficient.

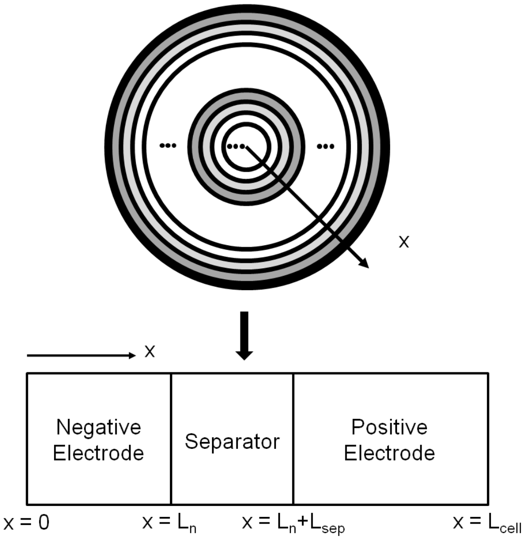

Figure 2.10: Schematic of unit cell as a cross-section along x. Ellipsis implies repeated unit cells.

2.3.1 Porous Electrode Models

Porous electrode models predict the concentration and potential in the liquid and solid phases of an electrochemical cell using the superposition approach illustrated in Figure 2.11. The porous electrode is a complex, tortuous mixture of particles held together by binder and conductive coating. Porous electrode models take a macroscopic approach and assume electroneutrality. The main outcome of electroneutrality is the current density based on the projected current collector area is constant, implying $\nabla \cdot \vec{i} = 0$, where $\vec{i}$ is the current density. However, current can be conducted in either the solid, $\vec{i}_s$, or the liquid, $\vec{i}_e$, phase such that $\vec{i} = \vec{i}_e + \vec{i}_s$ and

$$\nabla \cdot \vec{i}_s + \nabla \cdot \vec{i}_e = 0 \tag{2.63}$$

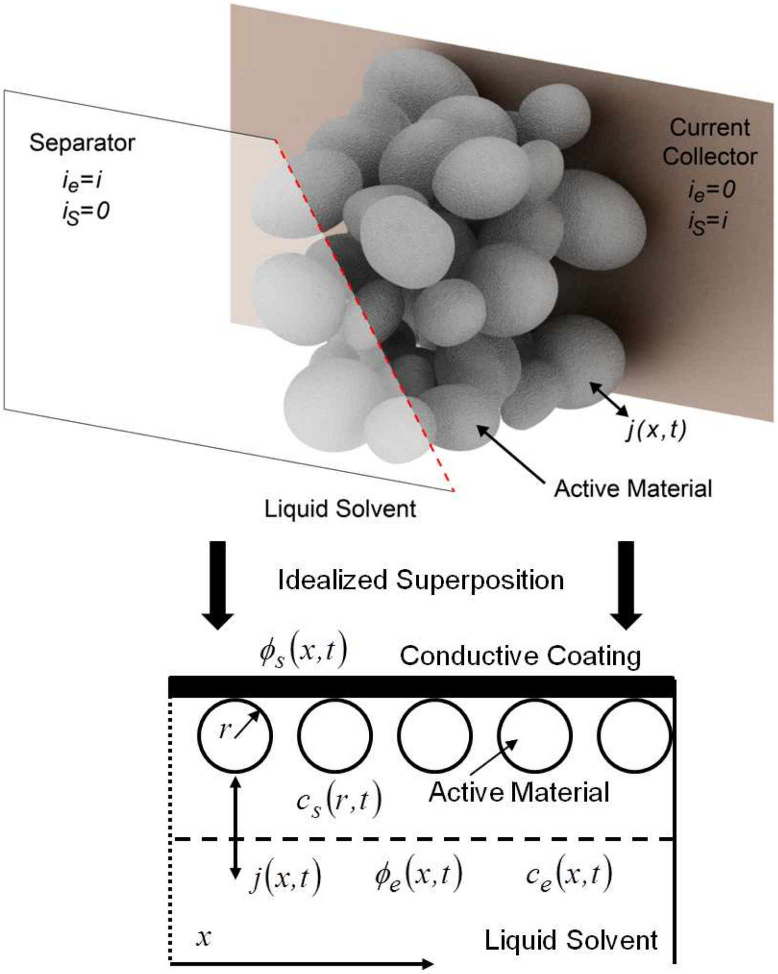

Figure 2.11: Representation of the porous electrode geometric complexity (top) and the idealized modeling approach using superposition (bottom).

At the current collector, electrons carry the current and the flux of lithium ions is zero because the current collector is a solid metal film. This is indicated in Figure 2.11, where $\vec{i}_e = 0$ and $\vec{i}_s = \vec{i}$ at the current collector. At the separator, no electronic current can flow since the separator is electrically insulating. Thus $\vec{i}_s = 0$ and $\vec{i}_e = \vec{i}$. These considerations will serve as useful boundary conditions for modeling.

The transfer current density, j, defines the rate of current divergence within each phase, or equivalently the amount of current transmitted between the phases at each x coordinate

$$\nabla \cdot \vec{i}_s = -\nabla \cdot \vec{i}_e = a_i j(x,t) \tag{2.64}$$

where $a_i = 3\epsilon_i / R_i$ is the surface area of the electrode per unit volume, ϵ_i is the electrode active volume fraction, and R_i is the active particle radius. The parameter a_i takes $i = n$ for x values in the negative electrode and $i = p$ for x values in the positive electrode. The quantity j is a function of space and time, since it depends on lithium concentration and potential. While j has the same units as $\vec{i}$, it is a current density based on actual active surface area of the electrode rather than projected current collector area.

If we discretize the partial differential equations into a number of discrete x nodes, the superposition approach leads to considering one active material particle at each node point. The transport equations of concentrated solution theory derived in the previous section are utilized in each phase, and the transfer current is modeled using Butler-Volmer kinetics. All transport and conductivity properties are treated as effective values, rather than using values that apply for a pure, uniform material. The Bruggeman coefficient, $brug$, is used to modify the electronic conductivity and diffusion coefficient based on the tortuosity of the conduction or diffusion path respectively (Patel *et al.*, 2003). This parameter accounts for the empirical observation that transport is slower and electronic conductivity is lower than predicted by merely accounting for the volume fraction of the porous media, giving effective values $\sigma_{eff} = \sigma\epsilon^{brug}$ and $D_{eff} = D\epsilon^{brug}$ respectively. The quantity ϵ is the volume fraction of the phase of interest. Since $\epsilon < 1$, inclusion of the Bruggeman coefficient always gives a lower effective property value. In order to simplify the model notation, properties are treated as effective values when discussing porous electrode theory even though the eff subscript is not carried throughout the model discussion.

To begin, consider the potential in the solid phase. This is current in the form of electrons flowing in a conductive medium, which is governed by Ohm's law, Eq. (2.12). Based on the approximation introduced by Figure 2.11, only one spatial dimension is modeled and therefore the vector notation for current density is removed. Differentiating this expression once with respect to x leads to

$$\frac{\partial^2 \phi_s}{\partial x^2} = \frac{j(x,t)}{\sigma_s} \quad \text{with } \phi = \phi_{rel} \text{ at } x = 0 \text{ and } \frac{\partial \phi_s}{\partial x} = \frac{i}{\sigma_s} \text{ at } x = L_{cell} \tag{2.65}$$

Only potential differences between the positive and negative electrode are relevant, so ϕ_{rel} is actually arbitrary. It is usually convenient to either set $\phi_{rel} = 0$, and this convention is used unless explicitly stated otherwise.

Next, conservation of charge for the liquid phase is modeled using the potential for a concentrated solution. Beginning from Eq. (2.62) in one-dimension, simplifying assumptions are made. Considering a two-ion electrolyte and the dissociation reaction of Eq. (2.51) with the reference electrode reaction of Figure 2.8, $\nu = 2$, $\nu_+ = 1$, $s_0 = 0$, $n_e = 1$, and $\nu_+ = 1$. Additionally, assume negligible variation of the solvent concentration with respect to the salt concentration, which amounts to neglecting volume change of the solvent as additional solute is added, so that $\frac{\mathrm{d}\ln c_0}{\mathrm{d}\ln c} \ll 1$. Differentiating the result with respect to x

gives

$$\frac{\partial^2\phi_e}{\partial x^2} - \frac{2\bar{R}T}{F}\frac{\partial}{\partial x}\left(\left(1+\frac{dln(f)}{dln(c_e)}\right)\frac{\partial lnc_e}{\partial x}\right) = -\frac{j(x,t)}{\kappa} \quad with\ \tfrac{\partial\phi_e}{\partial x} = 0\ at\ x = 0, L_{cell} \tag{2.66}$$

Next, lithium transport in the solid phase is modeled using Eq. (2.48), applied to the spherical particle geometry.

$$\frac{\partial c_s}{\partial t} = \frac{D_s}{r^2}\frac{\partial}{\partial r}\left(r^2\frac{\partial c_s}{\partial r}\right) \quad \text{with } \tfrac{\partial c_s}{\partial r} = 0 \text{ at } r = 0 \text{ and } \tfrac{\partial c_s}{\partial r} = \tfrac{-j(x,t)}{DF} \text{ at } r = R \tag{2.67}$$

The boundary condition links the tranfer of lithium ions between the solid and liquid phases.

Equation (2.34) is used to model the concentration of lithium ions in the liquid phase, with the flux defined in Eq. (2.54) and the reaction term as $j(x,t)$

$$\epsilon_e\frac{\partial c_e}{\partial t} = \frac{\partial}{\partial x}\left(D_e\frac{\partial c_e}{\partial x}\right) - a_i\frac{\left(1-t_0^+\right)}{F}j(x,t) \quad \text{with } \tfrac{\partial c_e}{\partial x} = 0 \text{ at } x = 0, L_{cell} \tag{2.68}$$

The surface area per unit volume, a_i, converts the surface flux from active material particles into a volumetric source/sink in the liquid phase.

The transfer current density is a function of the local concentration and potential

$$j(x,t) = i_0\left(e^{\frac{\alpha F}{\bar{R}T}\eta} - e^{-\frac{(1-\alpha)F}{\bar{R}T}\eta}\right) \tag{2.69}$$

with $i_0 = Fk\sqrt{c_s(R,t)c_e(x,t)\left(c_{max}-c_s\right)}$ and $\eta = U - \phi_s - \phi_L$. The battery terminal voltage is is defined as the difference betwen the solid phase potential evaluated at the current collector boundaries

$$V(t) = \phi_s(L_{cell},t) - \phi_s(0,t) - R_cI(t) \tag{2.70}$$

The quantity R_c is a contact resistance that accounts for the ohmic losses in the current collectors and at weld joints between the current collectors and external battery tabs.

This basic model structure has seen numerous applications and chemistry-specific variations. It was applied to the $LiFePO_4$ electrode in order to understand the low power capability of the material (Srinivasan & Newman, 2004*b*,*a*) and its interesting response of increasing resistance with respect to depth of discharge during current pulses Thomas-Alyea (2008). It has been used to study the effects of modeling a particle size distribution (Darling & Newman, 1997; Stephenson *et al.*, 2007) on rate capabilities and overall power output. It has been applied to high current pulse modeling (Bernardi & Go, 2011; Fang *et al.*, 2009) since it accounts for the spatially non-uniform transfer current that occurs in such situations. The formulation is general enough to allow for a high amount of modeling complexity, such as the inclusion of a thermal energy balance to study temperature transients during high current operation (Bernardi *et al.*, 1985; Rao & Newman, 1997; Srinivasan & Wang, 2002; Smith & Wang, 2006*a*), materials that exhibit phase change during intercalation (Christensen *et al.*, 2006), or mixed active material electrodes (Albertus *et al.*, 2009).

2.3.2 Uniform Utilization Models

The porous electrode equations, Eq. (2.65) to Eq. (2.68), are distributed, coupled differential equations. The numerical solution methods required make them difficult to solve in real-time. For real-time applications involving estimation or control with a microprocessor that would be common in an embedded application such as an electric vehicle, a lumped model is needed. Such a model can be derived by assuming the transfer current has no spatial dependence, leading to the term ‘uniform utilization” since lithium is added and removed to the electrode uniformly with respect to the x coordinate of the unit cell in Figure 2.10. and instead the total current is averaged over the entire active surface area to compute an average transfer current density

$$j_i(t) = \frac{I(t)}{AL_i a_i} \tag{2.71}$$

where $i = p, n$ to indicate the positive or negative electrode. Equation (2.67) is solved subject to this boundary condition. This amounts to considering a single, average particle with lithium transport that represents the electrode. The liquid phase is only considered as an ohmic resistance. This approach is often called the *single particle* model and it was first developed for Ni-MH batteries Haran *et al.* (1998). The system may be conceptualized as in Figure 2.12. The kinetic overpotential, η, is modeled by inverting the Butler-Volmer law,

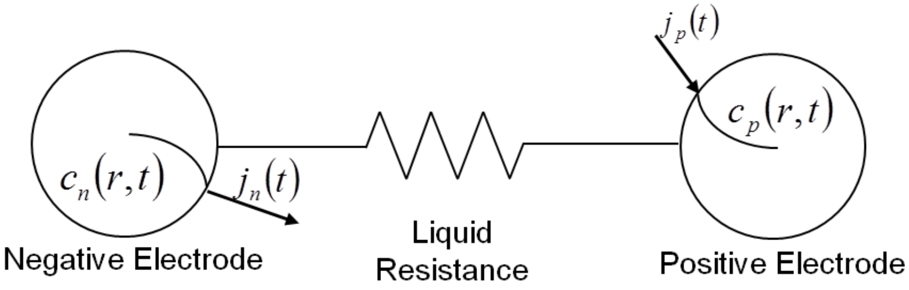

Figure 2.12: Single particle model conceptual representation.

Eq. (2.69), to yield

$$\eta = \frac{\bar{R}T}{\alpha F} sinh^{-1}\left(\frac{j(t)}{2i_0}\right) \tag{2.72}$$

The resulting battery terminal voltage is

$$V(t) = (U_p(t) - U_n(t)) - (\eta_p(t) - \eta_n(t)) - R_c I(t) \tag{2.73}$$

if we exclude complex effects such as hysteresis or resistive-reactant overpotential. Since the transfer current density is assumed to be known, and the liquid phase transport is not considered, the coupling between these equations is eliminated, the computational requirements are considerability reduced, and real-time estimation is possible. A number of papers (Di Domenico *et al.*, 2008*a*,*b*; Speltino *et al.*, 2009; Santhanagopalan & White, 2006) have successfully applied this model structure to the problem of SOC estimation during pulse operation. Cycling results for this model have been presented alongside porous electrode and polynomial approximation models (Santhanagopalan *et al.*, 2006) to illustrate their utility for low current rates. As mentioned previously, this approach does not allow for concentration gradients in the liquid phase, whose relaxation effects are observable in the cell voltage during following interruption of a charge or discharge current (see Figure 1.8). An approach which does include relaxation effects is pursued in Chapter 4.

2.3.3 Analogy–Based Models

This branch of the hierarchy is not discussed in detail as it is not the main focus of this proposal. It should be noted that systematic methods of parameterization have been applied more frequently to equivalent circuit models than to electrochemical models. For instance, the extended Kalman Filter (EKF) has been used to perform dual state and parameter identification for a fourth order equivalent circuit model (Plett, 2004*a*,*b*,*c*). Subspace methods have been used (Hu & Yurkovich, 2011; Hu *et al.*, 2009) to parameterize a linear parameter-varying model to account for the temperature and SOC dependence of battery resistance (Hu *et al.*, 2011). Offline nonlinear methods have been used to identify the relevant parameters for ohmic and charge transfer resistance (Juang *et al.*, 2011).

2.4 Selected Solution Methods for the Governing Equations

This section gives some potential solution methods for the governing equations. Numerical methods are briefly discussed, but are not emphasized. Instead, more focus is placed on methods that result in a small number of algebraic or ordinary differential equations, since these are more suitable for design of battery management systems.

2.4.1 Numerical

Popular numerical solution methods include the finite difference method (Ciarlet & Lions, 1990) and finite volume method (West & Fuller, 1996). Solving sets of coupled differential equations with either method is a standard problem (Parker *et al.*, 1980). An excellent review of these numerical solution methods for convective-diffusion equations has been conducted (Botte *et al.*, 2000).

2.4.2 Model Order Reduction

In this section, a comparison of model order reduction (MOR) techniques will be presented for a model problem to demonstrate the effectiveness of a particular MOR approach known as the Pade approximate method. The model problem is diffusion in a one-dimensional cartesian coordinate system, with the domain pictured in Figure 2.13. The governing equation for diffusion in the domain of Figure 2.13 is

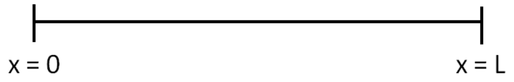

Figure 2.13: Modeling domain for model order reduction example calculations.

$$\frac{\partial c^*}{\partial t^*} = D\frac{\partial^2 c^*}{\partial x^{*2}} \tag{2.74}$$

where c^* is a salt concentration, and D is the salt diffusion coefficient. The imposed boundary conditions are

$$\left.\frac{\partial c^*}{\partial x^*}\right|_{x^*=0} = 0, \qquad D\left.\frac{\partial c^*}{\partial x^*}\right|_{x^*=L} = -N \tag{2.75}$$

where N is the flux of salt at the boundary, and would be defined by the current density of Eq. (2.69) in the case of solid diffusion in a Li-ion cell. The initial condition is $c^*(x^*, 0) = c_0 c_{max}$ where $0 < c_0 < 1$.

To reduce the number of arbitrary parameters, the equations are non-dimensionalized according to $x = x^*/L$, $c = c^*/c_{max}$, and $t = t^* D/L^2$. Note that in this section, the $*$ superscript indicates dimensional quantities and all other quantities are non-dimensional. Additionally define the parameter $\psi = \frac{NL}{Dc_{max}}$ to simplify the non-dimensional boundary condition. The resulting governing equation and boundary conditions are

$$\frac{\partial c}{\partial t} = \frac{\partial^2 c}{\partial x^2} \tag{2.76}$$

$$\left.\frac{\partial c}{\partial x}\right|_{x=0} = 0, \qquad \left.\frac{\partial c}{\partial x}\right|_{x=1} = -\psi \tag{2.77}$$

The nondimensional initial condition is $c(x, 0) = c_0$. In order for the following model order reduction techniques to be effective, a key assumption is that the only desired solution of the problem is the concentration at a specific x location. In this instance, that location is $x = 1$, but the technique applies equally well for any location within the domain.

Analytical Solution for Steady Boundary Flux

An analytical solution is obtained by the separation of variables method for a steady flux. Normally in non-homogeneous problem, a steady solution would be defined that satisfies the corresponding boundary conditions. However, with the prescribed boundary conditions of this problem, there is no steady solution because the salt concentration within the modeling domain continually increases in time. Instead, the solution is broken into three parts (Crank, 1975)

$$c(x,t) = u(x) + w(x,t) + \bar{c}(t) \tag{2.78}$$

corresponding to a steady term $u(x)$ that defines the shape of the long-time response, but not its magnitude; a transient term $w(x,t)$ that defines the difference between $u(x)$ and the actual solution at time t; and $\bar{c}(t)$, the time-varying mean concentration. The transient term $w(x,t) \to 0$ for large t. First the solution for the mean concentration is computed by integrating Eq. (2.76)

$$\int_0^1 \frac{\partial c}{\partial t} dx = \left.\frac{\partial c}{dx}\right|_{x=1} - \left.\frac{\partial c}{dx}\right|_{x=0} \tag{2.79}$$

which after substituting known terms results in

$$\frac{d\bar{c}}{dt} = -\psi \tag{2.80}$$

The integration gives $\bar{c}(t) = -\psi t + 0.2$, where 0.2 corresponds to the initial condition. Next, the proposed solution of Eq. (2.78) is substituted into Eq. (2.76) to obtain

$$\frac{\partial w}{\partial t} + \frac{d\bar{c}}{dt} = \frac{\partial^2 w}{\partial t^2} + \frac{d^2 u}{dx^2} \tag{2.81}$$

Requiring that $w(x,t)$ satisfies Eq. (2.76) individually, and substituting for $\bar{c}(t)$ yields

$$\frac{d\bar{c}}{dt} = \frac{d^2 u}{dx^2} \tag{2.82}$$

This expression is integrated twice to give $u(x) = -\psi \frac{x^2}{2} + c_1 x + c_2$ where c_1 and c_2 are arbitrary constants that are identified using the boundary conditions. From the first condition of Eq. (2.77), $c_1 = 0$. The second boundary condition is satisfied automatically, so an additional condition is required, utilizing the previously described constraint that $w(x,t) \to 0$ for large t. This leaves $c = \bar{c} + u$, which upon integration reveals that

$\int_0^1 u(x)dx = 0$, since $\int_0^1 cdx = \int_0^1 \bar{c}dx$. Using this integral to solve for the remaining constant gives $c_2 = \psi/6$.

Now, solutions have been obtained for $\bar{c}(t)$ and $u(x)$, leaving only $w(x,t)$ to solve via Eq. (2.76) with homogeneous, zero flux boundary conditions. This is a straightforward separation of variables problem, which requires the assumption of $w(x,t) = T(t)X(x)$, and the solution is given by Crank (1975)

$$w(x,t) = \sum_{n=1} -\frac{2(-1)^n}{(n\pi)^2} cos(n\pi x)e^{-(n\pi)^2 t} \tag{2.83}$$

The total solution obtained by substituting the solutions of $w(x,t)$, $\bar{c}(t)$, and $u(x)$ into Eq. (2.78) is now

$$c(x,t) = c_0 + \psi\left(\frac{1}{6} - \frac{x^2}{2} - t\right) - 2\sum_{n=0} \frac{(-1)^n}{(n\pi)^2} cos(n\pi x)e^{-(n\pi)^2 t} \tag{2.84}$$

Keep in mind that this solution requires a steady boundary flux. In order to compare the frequency response of the analytical PDE solution to various MOR techniques, a solution in the Laplace domain is required.

Analytical Solution in the Laplace Domain

The Laplace transform is defined as

$$F(s) = \int_0^\infty e^{-st} f(t)dt \tag{2.85}$$

where $f(t)$ is any function that is locally integrable on $[0, \infty]$, and here $s = -jw$ with $j = \sqrt{-1}$. Capital symbols are used to indicate the Laplace transform of lower case symbols. Applying this operator to Eq. (2.76) gives

$$sC(x,s) - \frac{\partial^2 C}{\partial x^2} = 0 \tag{2.86}$$

Treating s as a parameter, this is a second-order ordinary differential equation in $C(x)$, which can be solved by the characteristic equation method (Boyce & DiPrima, 2009). Applying the boundary conditions of Eq. (2.77), and evaluating the solution at the location of interest ($x = 1$) gives

$$\frac{C(1,s)}{\Psi(s)} = \frac{e^{\sqrt{s}} + e^{-\sqrt{s}}}{\sqrt{s}\left(e^{\sqrt{s}} - e^{-\sqrt{s}}\right)} \tag{2.87}$$

Pade Approximation of the Frequency Response

To obtain a reduced-order representation of the boundary concentration dynamics, the coefficients of a low-order transfer function are identified using moment matching. The approximate transfer function of order N for the system of Eqs. (2.76) and (2.77) is given by

$$P(s) = \frac{a_0 + a_1 s + \cdots + a_{N-1} s^{N-1}}{s\left(1 + b_2 s + \cdots + b_N s^{N-1}\right)} \tag{2.88}$$

where the coefficients are to be identifed as a function of the boundary conditions and dimensional parameters. The identification procedure requires evaluating the limit as $s \to 0$ of Eq. (2.87) and its derivatives. A single coefficient of the approximate transfer function can be identifed for each limit that is computed. As an example, consider a second order transfer function. First evaluate the limit of Eq. (2.87)

$$\lim_{s\to 0} s\frac{C(1)}{\Psi(s)} = 1 \tag{2.89}$$

noting that Eq. (2.87) is actually undefined at zero, so it is first multiplied by s, and then the limit is computed. Next, the limit of the second-order realization of Eq. (2.88), after multiplying by s so that the limit actually exists, is

$$\lim_{s\to 0} sP(s) = a_0 \tag{2.90}$$

Equating Eq. (2.89) with Eq. (2.90) gives $a_0 = 1$. Next, the limit of the derivative of (2.76) is evaluated

$$\lim_{s\to 0} \frac{d}{ds}\left(s\frac{C(1)}{\Psi}\right) = \frac{1}{3} \tag{2.91}$$

Next, the limit of the derivative of the second-order realization of Eq. (2.88) is evaluated

$$\lim_{s\to 0} \frac{d}{ds}\left(sP(s)\right) = a_1 - b_2 a_0 \tag{2.92}$$

To complete the coefficient identification process for the second-order realization, the limit of the second derivative of both the analytical solution and the approximate transfer function must be computed.

$$\lim_{s\to 0} \frac{d^2}{ds^2}\left(s\frac{C(1)}{\Psi}\right) = -\frac{2}{45} \tag{2.93}$$

$$\lim_{s\to 0} \frac{d^2}{ds^2}\left(sP(s)\right) = 2b_2\left(a_0 b_2 - a_1\right) \tag{2.94}$$

By equating Eq. (2.89) and Eq. (2.90), Eq. (2.91) and (2.92), and Eq. (2.93) and (2.94), a system of three equations with three unknowns is established

$$\begin{aligned} &a_0 = 1 \\ &a_1 - b_2 a_0 = \frac{1}{3} \\ &2b_2\left(a_0 b_2 - a_1\right) = -\frac{2}{45} \end{aligned} \tag{2.95}$$

The solution of the system in Eq. (2.95) gives the approximate traansfer function coefficients. The process is repeated for third and fourth order approximations, but two additional derivatives are required for an increase of one in the approximation order. The approximations for orders one through four are summarized in Table 2.3.

Polynomial Approximation

The polynomical approximation assumes that the concentration profile at any time is given by a polynomial of arbitrary order. Usually a second-order polynomial is used to give

Table 2.3: Pade approximate transfer functions (TFs) up to fourth order for Eq. (2.87).

Order	1st	2nd	3rd	4th
TF	$\frac{1}{s}$	$\frac{1+\frac{2}{5}s}{s\left(1+\frac{1}{15}s\right)}$	$\frac{1+\frac{4}{9}s+\frac{1}{63}s^2}{s\left(1+\frac{1}{9}s+\frac{1}{945}s^2\right)}$	$\frac{1+\frac{6}{13}s+\frac{10}{429}s^2+\frac{4}{19305}s^3}{s\left(1+\frac{5}{39}s+\frac{2}{715}s^2+\frac{1}{135135}s^2\right)}$

a parabolic profile. To begin let

$$c_p(x,t) = c_{p,1}(t) + c_{p,2}(t)x^2 \tag{2.96}$$

This satisfies the first boundary condition of Eq. (2.77) automatically. The second boundary condition yields

$$2c_{p,2}(t) = -\psi \tag{2.97}$$

or $c_{p,2}(t) = -\psi/2$. To identify $c_{p,1}(t)$, compute the volume-averaged concentration via Eq. (2.76) and Eq. (2.96), and equate the results

$$\int_0^1 c_{p,1}(t) + c_{p,2}(t)x^2 dx = c_{p,1}(t) + \frac{c_{p,2}(t)}{3} \tag{2.98}$$

$$\int_0^1 \frac{\partial c}{\partial t} dx = \int_0^1 \frac{\partial^2 c}{\partial t^2} dx \tag{2.99}$$

$$\frac{d\bar{c}}{dt} = \left.\frac{\partial c}{\partial x}\right|_{x=1} - \left.\frac{\partial c}{\partial x}\right|_{x=0} \tag{2.100}$$

$$\bar{c} = -\psi t + c_0 \tag{2.101}$$

Then solving for $a(t)$ gives $a(t) = -\psi t + c_0 + \psi/6$. Evaluating this result at $x = 1$ gives

$$c_p(1,t) = t + c_0 + 1/3 \tag{2.102}$$

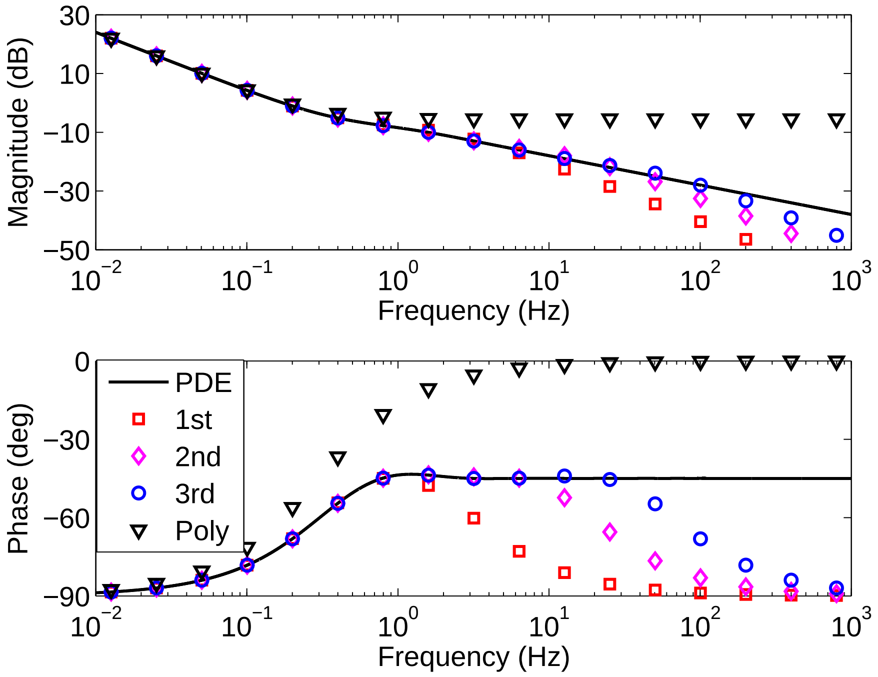

Figure 2.14: Frequency response of analytical solution to PDE and Pade approximations of various order of truncation.

Frequency Response and Step Response Predictions

All results in this section use $\psi = 1$, and $c_0 = 0.2$, but the results are generalizable for any value of ψ and c_0. Figure 2.14 compares the frequency response of the analytical solution, given by Eq. (2.87), the family of Pade approximate models, and the polynomial model. The results show that each Pade approximation to the analytical solution matches well for low frequencies. As the frequency increases, error is introduced due to the neglect of high frequency poles during the Pade approximation procedure. As the approximation order increases, both the magnitude and the phase exhibit better agreement for higher frequencies. To select the best model for an application, information about the frequency

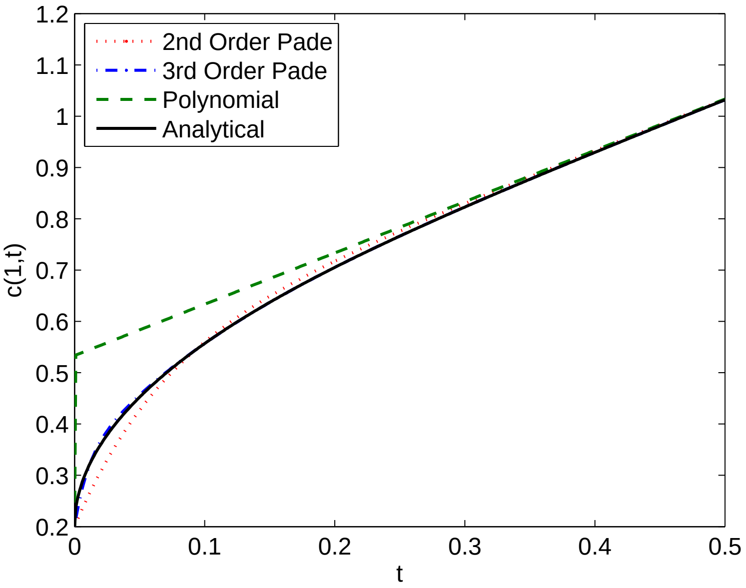

Figure 2.15: Step response of analytical solution to PDE, Pade approximations of various order, and polynomial approximation.

content of the input signal is used to decide a cutoff frequency, above which the dynamics are unimportant. Then the lowest order Pade approximation that matches the frequency response up to the cutoff frequency is selected.

The polynomial approximation exhibits the poorest agreement of all the models because it greatly overpredicts the response magnitude for high frequency. Although it matches at low frequency similar to the Pade approximations, it begins to depart from the PDE solution at a lower frequency.

Figure 2.15 compares the step response in the time domain of the analytical solution to the Pade approximations of various order and the polynomial approximation. The responses for Pade approximations higher than third order are not shown because they exhibit no appreciable difference compared to the third order response. The initial response to the step input is more accurate for the third order Pade approximation than the second order approximation. However, both are significantly more accurate than the polynomial approximation, which does not include the transient dynamics at short times. In the context of a battery model, this means that the polynomial method is incapable of modeling the voltage transients that occur during initiation or interruption of current as illustrated in Chapter 1. The Pade method is capable of representing these dynamics.

2.5 The Effects of Battery Aging

This section begins by reviewing common battery aging mechanisms and their sytem-level effects. Then, diagnostic techniques that are used to assess the aging process and may be performed during battery operation, meaning without diassembling the cell, are presented.

2.5.1 Review of Battery Aging Mechanisms

The following are a collection of cell aging mechanisms discussed in the lithium-ion battery literature. The effects of each mechanism are ultimately combined to characterize performance degradation at the cell level.

Agglomeration of Solid Electrode Particles

Agglomeration is defined as a process where smaller electrode particles combine with one another to form particles with a larger mean radius. Agglomeration of electrode particles has been characterized experimentally (Nagpure *et al.*, 2010), resulting in increased electrode porosity, decreased specific surface area, and possible de-bonding of particles from the substrate. The authors also refer to the process as grain coarsening, since the

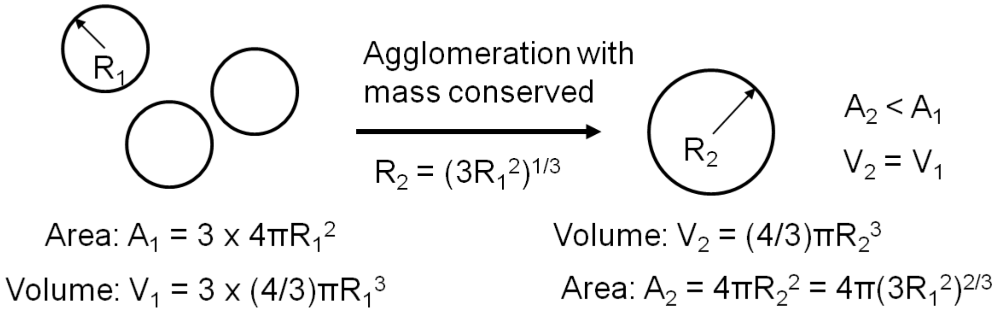

Figure 2.16: Demonstration of decreasing surface area while holding active material volume constant. The example uses three particles but the result holds for any number of particles.

fine (small radius) particles at the beginning of life become coarse (large radius) agglomerates as the battery ages. Scanning spreading resistance microscopy is used to visually confirm this mechanism in aged lithium-ion cell cathode material. No mechanism has been proposed yet for the driving force behind the observed particle coarsening. Particle agglomeration could be linked in two ways to increased resistance.

First, the electrode surface area per unit volume may change as a result of coarsening. If mass is conserved and connections to the electronic matrix are maintained, combining a group of particles into a single, larger particle does not necessarily reduce active material of the electrode. However, it does reduce the total electrochemically active surface area of the electrode. Figure 2.16 shows an example of this effect, where constant density has been assumed so that active material mass and volume are proportional.

Reducing the available surface area for Faradaic current production will cause a higher apparent current density for the cell surface area, leading to greater overpotential with charge transfer being the most affected. Therefore, as the process continues and the mean particle radius increases, the resistance of the cell rises.

Second, electronic contact loss can occur between carbon particles, the current collector and carbon, the binder and carbon, or between binder and current collector (Vetter *et al.*, 2005) as part of the agglomeration process. Removal of the physical connections between these areas manifests itself as an increase in the battery impedance due to decreasing solid phase conductivity. Also, several studies mention that as structural changes continue, internal stresses increase and cracks in the particles may develop, which could impact electronic connectivity. While mechanical stresses during intercalation have been modeled (Renganathan *et al.*, 2010), they have only been related to aging in the context of solid-electrolyte interphase (SEI) layer growth (Deshpande *et al.*, 2012).

Formation of the Solid-Electrolyte Interphase Layer

Chemical reactions between the electrolyte and active material, termed a solvent decomposition reaction, form a deposit over both the cathode and anode surfaces (Vetter *et al.*, 2005; Arora & White, 1998), though the anode is favored due to its low potential relative to Li/Li^{+}. This side reaction occurs simultaneously with the faradaic current that is normally present during battery operation, and is widely considered among the dominant aging effects that must be considered to accurately predict battery life. The effects of SEI growth that are observed at the system-level are impedance rise and capacity fade.

Several electrolyte decomposition reactions have been proposed (Arora & White, 1998). The most relevant reactions are those that contain carbonate solvent reduction, such as propylene carbonate (PC), dimethyl carbonate (DMC), and diethyl carbonate (DEC). Of these, the most commonly considered reaction is the ethylene carbonate (EC) reduction and subsequent formation of SEI products, because EC is a widely used electrolyte solvent and molecular dynamics simulations have indicated that it is likely to undergo reduction at voltages common to Li-ion batteries (Goers *et al.*, 2011; Markle *et al.*, 2011; Bedrov *et al.*, 2012). The proposed electrolyte decomposition reaction for EC is proposed as a two-step process (Arora & White, 1998; Safari & Delacourt, 2011*c*; Safari *et al.*, 2009) that involves the one-electron reduction of EC molecules

$$EC + e^{-} \rightleftharpoons EC^{-} \tag{2.103}$$

$$2EC^{-} + 2Li^{+} \rightleftharpoons (CH_2OCO_2Li)_2 + C_2H_4 \tag{2.104}$$

The primary SEI product is dilithium ethylene dicarbonate, $(CH_2OCO_2Li)_2$. The reactions that result in SEI production have both a voltage and temperature dependence. Increased temperature accelerates the rate of SEI growth (Vetter *et al.*, 2005) as does high charging voltages corresponding to low negative electrode potential.

It has been proposed that this mechanism causes capacity fade during storage periods (Broussely *et al.*, 2005, 2001), and a parabolic capacity fade expression in time was derived from kinetic and transport principles for the storage case. This parabolic expression comes from the integrating a diffusion-limited transport expression with the assumption of constant potential. Capacity fade that results from film growth in a variety of operation modes has been included in a single particle model of the battery dynamics (Safari *et al.*, 2009; Ning *et al.*, 2006; Santhanagopalan *et al.*, 2006). Results indicate that there is a change in the rate of capacity fade as aging progresses (Safari *et al.*, 2009), with the authors attributed to diffusion in the SEI layer. They presented simulation results, validated with experimental data, for both potentiostatic rest and cycling. However, they required different sets of reaction rate constants to match the experimental data for each capacity fade mode.

The classical view of SEI growth posits that the thickness of the layer steadily increases as the number of moles of product increases. Surface area coverage of the SEI is assumed to be uniform throughout the electrode. The increase of SEI thickness is generally viewed

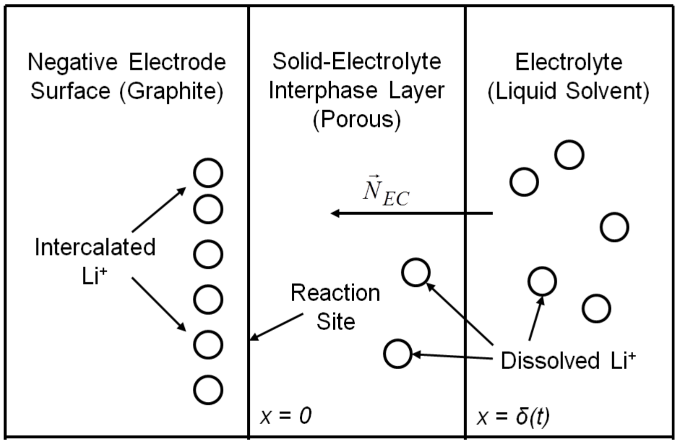

Figure 2.17: Diagram of the classical view of SEI growth, where $\delta(t)$ increases as additional moles of SEI layer are produced.

as either kinetic-limited or diffusion-limited. The diffusion-limited rate of SEI growth decreases with increasing layer thickness. This phenomenon is widely attributed to poor diffusion of solvent molecules through the SEI layer, such that reactants of the side reaction cannot reach the graphite surface to produce additional SEI product as the layer thickness increases. A schematic outline of the classical view of SEI growth is given in Figure 2.17.

Insight regarding this classical view may be obtained by applying a time scale analysis to the equation describing solvent transport, based on the diffusion time scale through the SEI layer. The time scale of transport through the SEI thickness is $\tau_D = L_{SEI}^2/D_{EC}$, where L_{SEI} is the characteristic maximum SEI thickness and D_{EC} is the solvent diffusion coefficient. A typical free diffusion coefficient of Li^+ through carbonate solvent is 1.5×10^{-10} m^2/s (Valoen & Reimers, 2005). Though the solvent molecules are clearly larger than a proton, they exhibit similar diffusion coefficients within carbonate solvents (Hayamizu, 2012). Considering a maximum SEI layer thickness of $L_{SEI} = 10\ nm$ gives a diffusion time constant of much less than one second for transport of either molecule through the SEI.

However, it is well known from the literature that aging takes place on a much longer time scale characteristic of the kinetics of side reactions. The time scale of aging is

$$\tau_a = \frac{Q}{dQ/dt} \tag{2.105}$$

where Q is the cell capacity, and dQ/dt is its time derivative. The initial calendar capacity fade rate is approximately 0.5% per month. Inserting $Q = 15\ Ah$ gives $\tau_a \approx 10^8\ s$. This further allows an estimate of the side reaction current density based on $dQ/dt = i_{SEI} a_n A_n L_n \epsilon_n / F$. Using $a_n = 3/R_n$, $R_n = 2 \times 10^{-6}\ m$, $A = 0.877\ m^2$, $L_n = 50 \times 10^{-6}\ m$, and $\epsilon_n = 0.5$ gives $i_{SEI} \approx 1.0 \times 10^{-4}\ A/m^2$. The disparity between the time scales of capacity fade and diffusion through the SEI layer removes any diffusion limitations associated with the side reaction current and predicts that the solvent concentration at the graphite surface is equal to the bulk value for all time. It follows that the SEI growth will be kinetically limited for any reasonable thickness of the SEI and solvent diffusion coefficient, a result which contradicts previously proposed diffusion-limitations (Safari *et al.*, 2009; Safari & Delacourt, 2012).

Here the $*$ superscript is used to indicate dimensional variables, and all others are non-dimensional. The typical transport equation for the solvent within the SEI region is pure diffusion, since these molecules are not charged. Transforming to non-dimensional form gives

$$\frac{\partial c_{EC}}{\partial t} = \frac{\tau D_{EC}}{L_{SEI}^2} \frac{\partial^2 c_{EC}}{\partial x^2} \tag{2.106}$$

where c_{EC} is the solvent concentration and the scales are $c_{EC} = c_{EC}^*/c_0$ and $x = x^*/L_{SEI}$ with τ as either the diffusion or aging time scale. The boundary conditions are based on a side reaction flux at the electrode surface and equating the bulk concentration to the concentration just inside the SEI layer

$$\frac{D_{EC}\partial c_{EC}}{\partial x} = \vec{N}_{EC} \,\text{at}\, x = 0, \quad c_{EC} = \frac{\rho_{EC}}{M_{EC}} \,\text{at}\, x = L(t) \tag{2.107}$$

where $\vec{N}_{EC}$ is the flux of EC molecules determined by the side reaction rate such that $N_{EC} = \frac{i_{SEI}L_{SEI}\rho_{EC}}{FD_{EC}M_{EC}}$, M_{EC} is the molar mass of EC, and ρ_{EC} is the density of EC. The interpretation of Eqs. (2.106) and (2.107) depends on how the time scale is chosen and the magnitude of the side reaction current density.

To have a diffusion-limited mechanism, where the time scale of diffusion is roughly the same order of magnitude as the time scale for aging, requires that the diffusion coefficient is approximately $1.0 \times 10^{-22}\ m^2/s$. This value is much less than typical self-diffusion values for EC in carbonate solvent (Hayamizu, 2012). Even applying the common Bruggeman coefficient correction $D = D(\epsilon_L)^{brug}$ for diffusion through tortuous, porous media (Patel *et al.*, 2003) does not produce diffusion coefficients small enough for a non-trivial solution of Eq. (2.106). A typical Bruggeman coefficient of 4.0 and assuming a porosity of 50% gives a hindered diffusion coefficient of $9 \times 10^{-12}\ m^2/s$, still several orders of magnitude too low for diffusion-limited SEI.

The correct order of magnitude is not obtained unless it is assumed that the SEI layer has porosity of $< 1\%$ combined with a Bruggeman coefficient of 4.0. In this cases, it is questionable whether Li^+ intercalation could still proceed without drastic overpotentials that would be observable from system-level voltage and current measurements.

Lithium Metal Deposition (Plating)

Lithium metal deposition refers to the process of lithium precipitating from the liquid solvent onto the electrode surface (Vetter *et al.*, 2005; Broussely *et al.*, 2001), resulting in capacity fade. Lithium plating occurs on electrodes that operate near the open-circuit potential of pure lithium, which includes most carbon anodes in commercially available cells. The precipitation occurs when the threshold of 0 V relative to Li/Li^+ is crossed, and occurs at a rate proportional to the overpotential relative to the 0 V equilibrium (Harris *et al.*, 2010).

Most carbon electrodes exhibit low overpotential during normal operation. Since the overpotential is generally low, plating is not a problem at room temperature despite maintaining an open-circuit potential that is less than 100 mV relative to Li/Li^+. At temperatures less than room temperature, the intercalation of Li^+ into the carbon electrode begins to require more overpotential to maintain a given net current due to the Arrhenius dependence of the rate constant. Lithium deposition occurs when the desired phenomena, intercalation becomes too slow, and the plating potential threshold of 0 V is reached. Increasing overpotential makes reaching the 0 V threshold more likely. From the standpoint of mitigating this mechanism, maintaining a moderate temperature (near room temperature) is beneficial (Broussely *et al.*, 2001). However, higher temperatures result in faster SEI film growth (generally described by an Arrhenius dependence) and aggravate other corrosion mechanisms within the cell. Combined modeling and experiments with a 3-electrode cell are performed in (Fang *et al.*, 2010) to illustrate the temperature dependence of the overpotential in the negative electrode.

Mechanical Cracking Due to Fatigue Stress

Mechanical stresses in the solid phase of the anode and cathode have been modeled recently. Initial work used the typical solid-solution active material as a representative example (Renganathan *et al.*, 2010; Verbrugge & Cheng, 2008; Zhao *et al.*, 2010; Christensen & Newman, 2006) and the assumption of static equilibrium (Cheng & Verbrugge, 2010*b*), with the main conclusion that the stress profile within an active material particle is roughly proportional to the concentration profile. This relationship is due to the non-negligible volume displaced by Li^+ ions as they intercalate into the host matrix, with the displacement they cause representing a strain to the active material. The authors of (Cheng & Verbrugge, 2010a) used Hasselmans crack propagation model to establish a criterion for crack propagation in spherical electrode particles as a function of the intercalation rate and parameters such as the diffusion coefficient and saturation concentration. Non-ideal geometries are examined in (Zhang *et al.*, 2007), leading to the conclusion that particle morphology plays a significant role in predicting stress, and shaping particles as ellipsoids may have a theoretical benefit in reducing intercalation stresses. Finally, (Deshpande *et al.*, 2011) looked at the effects of mechanical stresses within materials that undergo a phase change during intercalation. Concentration discontinuities at phase boundaries result in stress discontinuities, which the authors propose as a mechanism for cracking.

Active Material Dissolution

For some positive electrode chemistries, active material dissolution into the electrolyte solvent is a prominent aging effect. Though it is present to some extent for many olivine (Iltchey *et al.*, 2003), layered (Sclar *et al.*, 2009), and spinel (Huang *et al.*, 1999) structures, it is particularly severe for lithium manganese oxide, $LiMn_2O_4$. This mechanism was proposed after testing variations of electrode and electrolyte composition and correlating improved capacity retention with the amount dissolved Mn measured in the electrolyte (Gummow *et al.*, 1994; Jang *et al.*, 1996; Amatucci *et al.*, 1999). These initial results lead to the proposed dissolution reaction

$$2Mn^{3+} \rightarrow Mn^{4+} + Mn^{2+} \tag{2.108}$$

and the realization that a shuttling mechanism causes additional capacity fade at graphite negative electrodes exposed to dissolved Mn. A common approach to analyzing this mechanism is to construct coin cells with $LiMn_2O_4$ positive electrodes and either Li or some form of carbon as a negative electrode. Fabricating electrodes with varying degrees of surface area showed that decreased surface area led to decreased capacity fade, confirming a reaction-based degradation mechanism (Xia *et al.*, 2000).

An extensive study for multiple temperatures and positive electrode chemistries while retaining a graphite counter electrode confirmed that negative electrode capacity is also significantly degraded when dissolved Mn is present (Tsunekawa *et al.*, 2002). This data, when combined with measurements of the concentration of Mn ions in solution and reference electrode measurements of negative electrode impedance (Amine *et al.*, 2004), gives evidence that Mn ions migrate to the carbon negative. There they either catalyze the solid electrolyte interphase reaction or replace lithium ions in the host matrix (Wohlfahrt-Mehrens *et al.*, 2004; Tsujikawa *et al.*, 2011; Cho *et al.*, 2010).

Many experimental techniques have been applied to gain insight into this degradation mechanism. Qualitatively, imaging techniques such as scanning electron microscopy and transmission electron microscopy are common. To evaluate electrochemical performance, researchers have used galvanostatic cycling, cyclic voltammetry, and electrochemical impedance spectroscopy. X-ray diffraction, X-ray photoelectron spectroscopy, and energy dispersive spectroscopy are often used to characterize the crystal structure and chemical composition of electrodes before and after inducing dissolution. Differential pulse polarography (Jang *et al.*, 1996) has been used to measure the concentration of dissolved manganese within the electrolyte solution by performing measurements at specified intervals after cycling. The dissolution reaction has also been studied by thermogravimetric analysis and differential thermal analysis (Xia *et al.*, 2000). Precise quantitative measurements of the amount of dissolved manganese on the counter electrode have been made with an inductively coupled plasma optical emission spectrometer (Tsujikawa *et al.*, 2011) or an atomic absorption spectrophotometer (Tsunekawa *et al.*, 2002).

On the modeling front, there are fewer numbers of prior work. The dissolution process has been linked to the decrease of secondary active volume, and therefore capacity fade, in the positive electrode (Park *et al.*, 2011; Cai *et al.*, 2013). The presented dissolution models depends on electrode potential and temperature, however they are not validated with experimental data. Furthermore, the authors did not model the interaction of dissolved manganese ions and the negative electrode.

2.5.2 Aging Diagnostic Methods

There are many ways to assess the aging process in Li-ion batteries. These include detailed *ex-situ* characterization, *in-situ* performance measurements, and model-based characterization. Of these techniques, only *in-situ* performance measurements and model-based characterization are considered in this dissertation. This is because these methods are non-disruptive and can be applied with minimal intrusiveness during an aging campaign.

Hybrid Pulse Power Characterization Test

The hybrid pulse power characterization (HPPC) test (Anonymous, 2010) is used to assess the internal resistance of an electrochemical cell. As a side benefit, it also furnishes information related to the OCV of the cell. Figure 2.18 shows an overview of experimental data for an entire HPPC test.

The procedure consists of ten-second duration, high current inputs followed by rest periods to allow the cell to return to equilibrium before the next high current input. The

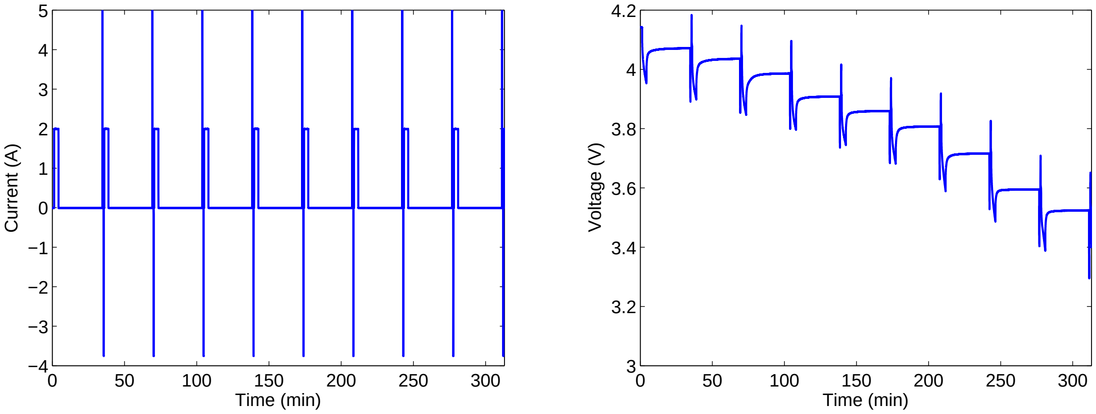

(a) (b)

Figure 2.18: Demonstration of the (a) current and (b) voltage during a standard HPPC test.

exact current is determined by the nominal battery voltage and the battery size factor. The procedure for calculating these procedures is given in (Anonymous, 2010).

Capacity Test

Capacity assessments are performed by charging the cell using the protocol recommended by the manufacturer, then discharging at constant current to the lower voltage limit. Once the lower voltage limit is reached, the capacity is defined as

$$Q = \int_0^{t_f} I(t)\, dt \tag{2.109}$$

where I is the cell current. Figure 2.19 illustrates the current and voltage during a capacity test, as well as the calculation of the capacity from the raw data. The horizontal axis is scaled in terms of time and also capacity. Plotting the voltage versus units of capacity is more effective than time since small variations in current can lead to significant variations in discharge time, but the effects on capacity remain small. In this example, the capacity value at t_f is 15 Ah.

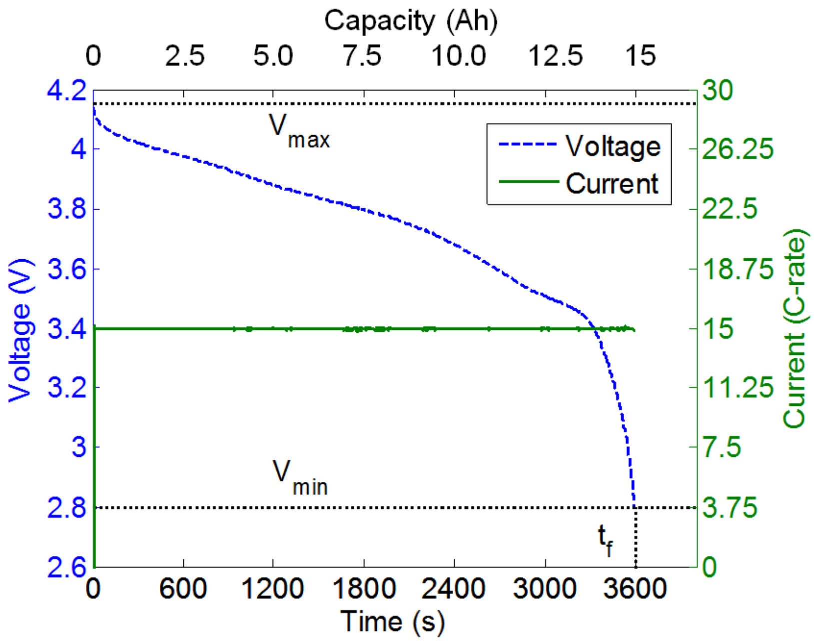

Figure 2.19: Demonstration of the current and voltage during a capacity test.

Differential Voltage (Capacity) Technique

The differential voltage technique has gained interest from battery researchers after recently being utiilized within aging studies conducted by the United States national laboratories (Bloom *et al.*, 2005a,b, 2006, 2010). It requires galvanostatic data for its application, and generally works best for low rate (C/10 or less) discharge or charge. Low rates are preferred for two reasons. First, testing the cell at a low rate ensures that only thermodynamic effects are being observed and the changes in the transport or kinetic parameters that occur with aging do not affect the measurement. Second, the signal can be more aggressively filtered if the rate is low. Filtering is important because the technique relies on the derivative of the measured signal, which contains high-frequency noise. Since there is an upper limit on the sampling rate, usually 10 to 100 Hz, extending the duration of the experiment effectively gives more samples per experiment to apply filtering. The differential voltage is defined as

$$Q_{max}\frac{dV}{dQ} = f(Q) \tag{2.110}$$

where V is the cell voltage, Q_{max} is the measured capacity at the lower voltage limit which serves as a normalization factor for the quantity dV/dQ, and Q is the incremental capacity gained at each time. The function $f(Q)$ depends on the cell voltage during discharge and must be obtained experimentally. Alternatively, the differential capacity is defined as the reciprocal of dV/dQ.

Both quantities are generally plotted versus cell voltage to show the amount of charge being stored at each voltage. Hence, they provide a measure of the incremental charge that may be stored as a function of cell voltage, and increased differential voltage (decreased differential capacity) indicates that the cell is storing less charge at a given voltage. Usually the differential voltage is preferred since the derivatives of the half-cell voltages may be summed in a straightforward manner, instead of being inverted as in differential capacity. This is apparent from $V = U_p - U_n$, which after differentiation gives $dV = dU_p - dU_n$.

The theory supporting the differential analysis of aging mechanisms is that each degradation mode will affect the cell voltage in a unique manner. Simulation results can be used to confirm this hypothesis for a fictitious graphite (C) and $Ni_{1/3}Co_{1/3}Mn_{1/3}O_2$ (NMC) cell. Figure 2.20a shows the individual half cell OCVs as well as the full cell OCV, which can be used as an approximation for a low-rate discharge since they represent the limit of the voltage response to an infinitesimally small discharge current. The capacity loss due to loss of cyclable lithium and loss of active volume (sites) is set to an identical 20$\%$ in each case, and the voltages in each scenario differ by a maximum of only 15 mV at any point.

Thus, it is difficult to determine from the cell voltage measurement what the degradation mechanism is.

Figure 2.20b shows the derivatives of the half cell voltages and the full cell voltage, which is the sum of the half cell contributions. The middle plot of Figure 2.20b contains several peaks that correspond to the transitions between plateaus of the negative electrode voltage. The lower plot has labeled these peaks for each scenario. By examining the shift of these peaks, as well as the distance between each peak, the aging mechanism can be identified. A change in the amount of cyclable lithium does not affect the distance between peaks because the electrode has not lost capacity, it only contains less lithium; however, a loss of active material means that the electrode itself contains less capacity, regardless of the amount of available lithium. This causes the distance between peaks to become closer as the capacity decreases. In summary if considering only the distance along the horizontal axis then

$$|P1 - P2|_{BOL} = |P1 - P2|_{x_0} > |P1 - P2|_{\epsilon_n} \tag{2.111}$$

and the distinction between loss of cyclable lithium and loss of active material can be made from cell-level voltage measurements.

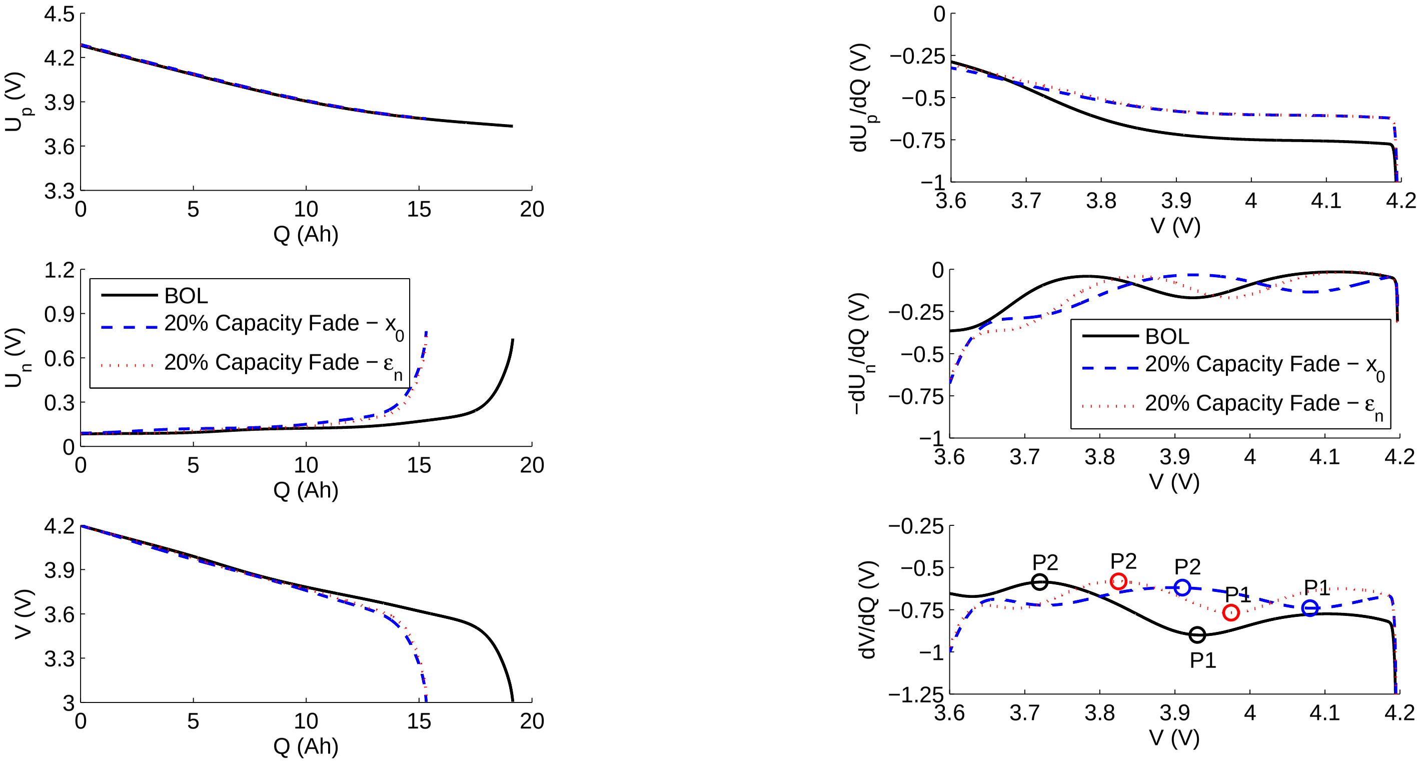

(a)

(b)

Figure 2.20: Effects of a 20% capacity reduction caused by an active volume reduction in the negative electrode or loss of cyclable lithium. (a) Positive electrode, negative electrode, and cell voltage simulations demonstrating difficulty in distinguishing between capacity reduction modes. (b) Differential voltage of positive electrode, negative electrode, and cell. Peaks indicated by P1 and P2 are used to distinguish between capacity reduction modes.

2.6 Summary

In this chapter, the governing equations of electrochemistry have been presented in the context of Li-ion batteries. The principles describing thermodynamics, kinetics, ohmic losses, and transport are reviewed. Then, the modeling conventions needed to apply these equations to voltage and lithium concentration predictions for a battery cell are reviewed along with relevant literature. After presenting the equations of porous electrode theory, a simplified modeling approach is also reviewed based on the assumption that the transfer current density is uniform with respect to electrode thickness. Selected solution methods are reviewed with a focus on model order reduction techniques that require less computation than numerical methods.

After reviewing the modeling approaches that describe the beginning-of-life concentration and potential dynamics, aging mechanisms are introduced. Several prominent aging mechanismsm are reviewed, along with their effects on battery performance characteristics. A brief set of system-level diagnostics that may be used to analyze battery performance during aging conclude the chapter, with a focus placed on tests that do not require disassembly of the cell such that battery usage can continue after completion of the test.

Chapter 3: Effects of the Electrical Double Layer Within a Simplified Li-Ion Battery Model

3.1 Introduction

Modeling is extremely important to advancing the science of electrochemical energy storage. Direct and dynamic measurements of concentration and electric potential profiles within a Lithium-ion (Li-ion) cell are currently not possible due to the micro-scale physical dimensions of the battery electrodes and separator. As a result, researchers have relied on modeling as a means of understanding the complex processes governing electrochemical cells. As discussed in the previous chapter, there have been a number of fundamental studies of Li-ion battery operation based on porous electrode theory (Newman & Tiedemann, 1975). With this methodology, detailed knowledge of the surface morphology of electrodes and separator, which is difficult to obtain and computationally prohibitive to model, is not required. However, the separation of solid and liquid phases is somewhat arbitrary, and models based on porous electrode theory present a macroscopic interpretation of battery electrochemistry.

Since porous electrode models compute averaged quantities over a region that is small with respect to the overall electrode dimensions but large compared to the pore structure

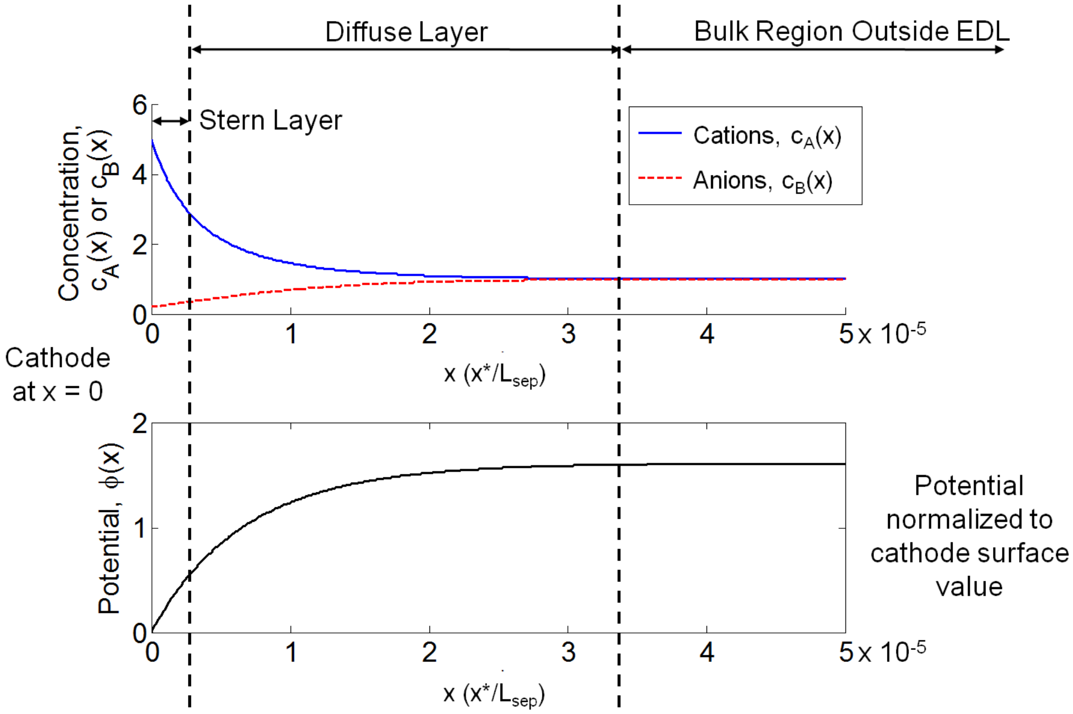

Figure 3.1: Illustration of the electrical double layer for the equilibrium case with zero current. Concentrations and potential vary rapidly within the electrical double layer and are constant outside.

(Newman & Tiedemann, 1975), Li-ion battery modeling literature typically applies the assumption of electroneutrality within commonly used non-aqueous liquid electrolytes. This assumption is justified based on the assertion that charge separation over a macroscopically significant distance (the volume averaging distance) would require a prohibitively large electric field (Newman & Thomas-Alyea, 2004). However at the boundary between the liquid and solid phases, an interfacial region known as the electrical double layer (EDL) exists where the assumption of electroneutrality no longer holds (Newman, 1965). This region is pictured in Figure 3.1. The diffuse layer contains mobile charges. Charge separation begins in this layer due to interaction between the ions in the liquid and the potential of the solid phase. The Stern layer is very narrow, only one to two ions thick, and contains immobilized charge.

The EDL in its most simplifed representation is a region that stores charge. A method of accounting for capacitive effects of the EDL in cell terminal voltage has previously been presented (Ong & Newman, 1999), but the scope of that research did not encompass some important features of the EDL such as the coupling between ion concentration and potential described in several classical works (Bazant *et al.*, 2005; Smyrl & Newman, 1967; Chu & Bazant, 2005; Dukhin *et al.*, 2005). Given the general lack of literature pertaining to the EDL as it applies to Li-ion batteries, it is appropriate to examine this feature in greater detail.

A more accurate understanding of the EDL is important for its impact on interfacial charge transfer. Porous electrode models postulate that charge transfer kinetics are governed by the potential difference between the solid phase and the electroneutral portion of the liquid outside the EDL (Newman & Thomas-Alyea, 2004). This assumption is made implicitly in the application of Butler-Volmer kinetics, which is treated as a semi-empirical relationship (though possessing fundamental origins) between the local intercalation current and the potential difference between solid and liquid relative to the open-circuit voltage versus a hypothetical lithium reference electrode. However, the Stern layer is the location of the reaction plane and the potential difference across it represents the actual activation energy barrier for the intercalation reaction (Bazant *et al.*, 2005). Thus it is of fundamental interest to consider only the Stern layer potential difference when examining the current-voltage relationship of electrode kinetics. A complete methodology for dividing the potential difference of the EDL between the diffuse layer and the Stern layer is discussed in (Bazant *et al.*, 2005) in relation to a micro-battery, and for galvanic cells in (Biesheuvel *et al.*, 2005). Results are presented for a range of kinetic rate constants selected to examine various limits of battery operation with no particular system studied. For an intercalation battery, the effective rate constant changes over the course of discharge due to the change in exchange current density driven by the degree of intercalation within active material. This change is governed by the composition ranges of the electrodes chosen by the manufacturer and the cell state of charge (SOC), and provides a physical mechanism for alteration of the effective rate constants over the course of discharge.

The objectives of this research are to gain insight into electrical double layer modeling through comparisons with experimental data from a commercially available intercalation battery, and to do so using a purely analytical model structure. The presented model structure accounts for the potential difference in the electroneutral liquid within the separator pores, as well as a microscopic interpretation of the EDL, which leads to a novel view of electrode kinetics. The model development is presented first, the Poisson Nernst-Planck equations are used to model liquid phase transport and solve a representative solid diffusion problem in each electrode. Two limiting descriptions of the EDL are used to examine the impact of the EDL potential on the cell overpotential. After obtaining analytical solutions for all variables of interest the experimental procedure for gathering data from commercially available cells is discussed. The case study uses a graphite anode and iron phosphate cathode, and electrolyte composed of 1 M $LiPF_6$ dissolved in a 1:1 mixture of ethylene carbonate and dimethyl carbonate. Model results are compared with galvanostatic discharge data and the areas impacted by the microscopic hypotheses of the EDL are discussed. Additional dynamics that are related to the resistive reactant nature of the cathode are introduced, and finally conclusions and areas for future work are given.

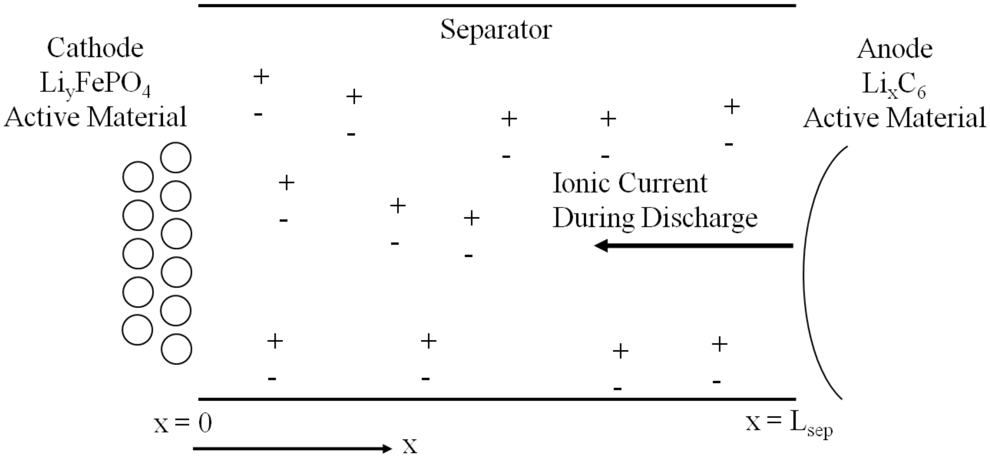

Figure 3.2: Modeling domain showing a separator pore connecting solid portions of anode and cathode and spatial coordinate definition. Dimensions are not to scale.

3.2 Model Development

To develop a model suitable for comparing microscopic hypotheses of the EDL we consider the transport of ions that occurs along a single liquid-filled pore of the separator that terminates at solid faces of the anode and cathode. Throughout this chapter, the $(*)$ superscript is used to indicate a dimensional quantity, and the terms without superscripts are dimensionless. Figure 3.2 shows the modeled domain of this work in the context of the full unit cell typically modeled in literature.

3.2.1 Separator Liquid Phase

The assumptions used to derive the governing equations are as follows. First, significant concentration and potential gradients occur only in the direction through the thickness of a unit cell, indicated by x in Figure 3.2. Second, bulk convection of the electrolyte solvent is neglected. Third, the external current is independent of time. Finally, the liquid phase ionic transport occurs via steady state conditions since the time scale of liquid transport is much less than the duration of the capacity test.

The Poisson Nernst-Planck (PNP) equations are used to model transport of charged species in dilute solutions. The simplicity that dilute solution theory offers compared with concentrated solution theory is a benefit when interested in factors such as the limiting cases of the EDL discussed in the introduction. In dimensional form, the simplified equations that result from the previously listed assumptions are

$$D_i \frac{\partial^2 c_i^*}{\partial x^{*2}} + \frac{D_i z_i F}{\bar{R}T} \left(\frac{\partial c_i^*}{\partial x^*} \frac{\partial \phi^*}{\partial x^*} + c_i^* \frac{\partial^2 \phi^*}{\partial x^{*2}} \right) = 0 \tag{3.1}$$

where c_i^* gives the ionic concentration with $i = A$ corresponding to Li$^+$ ions and $i = B$ denoting PF_6^- ions, D and z are the diffusion coefficient and valence respectively of the ion indicated via subscripts, and ϕ^* is the electric potential in the liquid phase. Conceptually, Eq. (3.1) states that the sum of fluxes due to diffusion and migration are balanced at steady state. The electric potential is governed by Poisson's equation

$$\bar{\epsilon}_e \frac{\partial^2 \phi^*}{\partial x^{*2}} = -F(z_A c_A^* + z_B c_B^*) \tag{3.2}$$

where $\bar{\epsilon}_e$ is the permittivity of the liquid solvent taken to be an average of the two main solvent components, ethylene carbonate (EC) and dimethyl carbonate (DMC). This is a differential formulation of Gauss's Law, which states that the electric field is proportional to the net enclosed charge within a differential control volume.

Specifying the boundary conditions of Eq. (3.2) is a non-trivial task due to the lack of direct knowledge of the potential at the solid surfaces of each electrode. However the boundary conditions for Eq. (3.1) are readily drawn from the physical consideration that there is no flux of PF_6^- ions into the solid phase; that is, consider the active material at either electrode as a permselective membrane that only allows passage of Li^+ ions. Setting the PF_6^- flux equal to zero gives

$$\frac{\partial c_B^*}{\partial x^*} + \frac{F c_B^* z_B}{\bar{R}T}\frac{\partial \phi^*}{\partial x^*} = 0 \quad \textit{at } x^* = 0, L_{sep} \textit{ for all } t \tag{3.3}$$

where $x^* = 0$ denotes the surface of the cathode, and $x^* = L_{sep}$ is the coordinate for the anode surface. Furthermore, the flux of Li$^+$ ions is fixed by the cell current density i^*

$$\frac{\partial c_A^*}{\partial x^*} + \frac{F c_A^* z_A}{\bar{R}T}\frac{\partial \phi^*}{\partial x^*} = \frac{i^*}{D_A F} \quad \textit{at } x^* = 0, L_{sep} \textit{ for all } t \tag{3.4}$$

The discussion of boundary conditions for Eq. (3.2) is deferred until a later section of this chapter because Eq. (3.2) is not solved explicitly. Instead the dimensionless form is used to justify the division of the problem into electroneutral and non-electroneutral regions and the resulting simplified problem is solved analytically.

Next the governing equations for the liquid phase are converted to dimensionless form. To begin the spatial coordinate x is scaled as

$$x = \frac{x^*}{L_{sep}} \tag{3.5}$$

where L_{sep} is the separator thickness. The liquid phase concentrations are scaled based upon the nominal electrolyte concentration

$$c_A = \frac{c_A^*}{c_{A,0}} \text{ and } c_B = \frac{c_B^*}{c_{B,0}} \tag{3.6}$$

where $c_{A,0} = c_{B,0} = c_0$ since the liquid is macroscopically electroneutrality, and c_0 is the average electrolyte concentration. The classical definition of the potential scale is employed where

$$\phi = \phi^* \frac{F}{\bar{R}T} \tag{3.7}$$

The potential scale is equal to 26 mV at a temperature of 298 K, which is the condition describing all results in this work. The dimensionless current density i is defined as

$$i = \frac{i^*}{i_D} \tag{3.8}$$

where i_D is the diffusion-limited current density,

$$i_D = \frac{Dc_0F}{L_{sep}} \tag{3.9}$$

which takes a value of approximately 630 A/m^2. This quantity is equal to one-fourth the value of the current that would cause the electroneutral electrolyte concentration to approach zero at the electrode where reduction occurs.

The dimensionless liquid phase governing equations may now be readily derived. The conservation of mass equations for either the anion or cation are

$$\frac{\partial^2 c_i}{\partial x^2} + z_i \left(\frac{\partial c_i}{\partial x}\frac{\partial \phi}{\partial x} + c_i \frac{\partial^2 \phi}{\partial x^2} \right) = 0 \tag{3.10}$$

where both concentration and potential are dimensionless. The dimensionless boundary conditions become

$$\frac{\partial c_B}{\partial x} + c_B z_B \frac{\partial \phi}{\partial x} = 0 \quad at\ x = 0, 1\ \textit{for all t} \tag{3.11}$$

$$\frac{\partial c_A}{\partial x} + c_A z_A \frac{\partial \phi}{\partial x} = i \quad at\ x = 0, 1\ \textit{for all t} \tag{3.12}$$

where the dimensionless current density has been introduced. The dimensionless potential equation is

$$\epsilon^2 \frac{\partial^2 \phi}{\partial x^2} = -(z_A c_A + z_B c_B) \tag{3.13}$$

where again both concentration and potential are dimensionless. The parameter $\epsilon = \frac{\lambda}{L_{sep}}$ arises from converting Eq. (3.2) to dimensionless form. The parameter λ is defined as

$$\lambda = \sqrt{\frac{\bar{\epsilon}_e \bar{R} T}{F^2 c_0}} \tag{3.14}$$

and called the Debye length. It is directly related to the thickness of the equilibrium EDL, which is typically described as $O(\epsilon)$. Using typical parameter values for the system of this work, the Debye length is 0.33 nm and ϵ value is $O(10^{-5})$. These parameters indicate a very small EDL thickness relative to all other dimensions of the system. Again, Eq. (3.10) and 3.13 are steady due to the constant boundary conditions and the liquid phase time constant being much smaller than total elapsed time during a capacity test.

3.2.2 Electrode Solid Phase

The diffusion dynamics in the active material of each electrode play an important role in determining the cell output voltage. It is assumed that the intercalation process occurs as diffusion into a single phase in both graphite and lithium iron phosphate. This approach has been shown to work well in a previous study (Safari & Delacourt, 2011*b*) and the exact physics of the two-phase nature of iron phosphate are still openly debated (Singh *et al.*, 2008; Srinivasan & Newman, 2004*b*,*a*). Furthermore, the EDL structure is the focus of this chapter and a less complex treatment of the solid phase is acceptable. The time-varying concentration of cations in the solid phase of either electrode is described in terms of the ionic flux. The convective term normally associated with ionic transport may be assumed zero if volume changes in the active material are neglected, and migration may be neglected if significant variations in potential do not exist (van Schalkwijk & Scrosati, 2002). Graphite is a good electronic conductor and therefore the assumption of negligible potential variation within a particle, and thus negligible migration, is applied to the anode. Though iron phosphate is a poor conductor, this assumption is also applied to the cathode due to the small size of cathode particles leading to insignifcant variation of potential within a particle. It is assumed that a sufficient amount of electrons are present to ensure a net zero charge within the solid, but their presence is not actively modeled.

The solid transport equation resulting from the previous assumptions is

$$\frac{\partial c^*_{A,j}}{\partial t^*} = D_j \frac{\partial^2 c^*_{A,j}}{\partial x^{*2}_j} \tag{3.15}$$

where D_j is the solid phase diffusion coefficient which takes different values in the anode ($j = an$) and cathode ($j = ca$). The boundary conditions are

$$\frac{\partial c^*_{A,j}}{\partial x^*_j} = 0 \; at \; x^*_j = 0, \quad D_j \frac{\partial c^*_{A,j}}{\partial x^*_j} = \frac{i^*_j}{\epsilon_j F} \; at \; x^*_j = L_j \tag{3.16}$$

where ϵ_j denotes the volume fraction of active material within the electrode, and L_j is the effective diffusion length. The inactive material encompasses conductive additives, polymer binder, and void volume, all of which is incapable of allowing lithium intercalation. Note that x^*_j is defined locally within the solid phase such that $x^*_j = 0$ refers to the interface between the current collector and the active material slurry and $x^*_j = L_j$ denotes the interface between the active material slurry and the separator. For simplicity, the same coordinate system is maintained for both electrodes, though in reality the electrodes would mirror each other.

At the interface between the current collector and the electrode, there can be no flux of ions because the current collector consists of a solid metal film, which corresponds to the first of Eqs. 3.16. The boundary condition at the interface between the electrode and the separator, the second of Eqs. 3.16, has a non-zero flux related to the ionic current in the cell which must be scaled based on the volume fraction of active material. A minus sign would be needed when considering the cathode, to account for the fact that a discharge current causes a flux of ions into the active material. This information is summarized in the schematic of Figure 3.3.

The initial conditions of the solid diffusion problem are directly related to the range of lithiation incurred by the electrodes, which is typically a design parameter of Li-ion cells that must be determined empirically. Again referring to the conditions for a capacity test, we assume the cell is fully charged initially to the upper voltage limit of 3.6 V which corresponds to 100 % SOC as specified by the manufacturer. The initial degree of lithiation

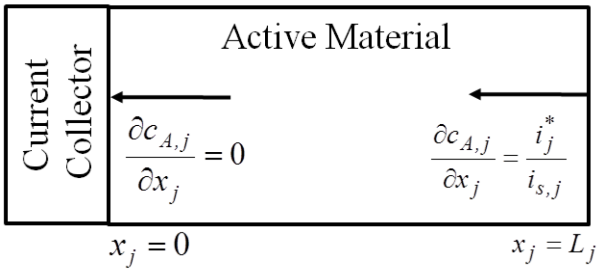

Figure 3.3: Summary of the boundary conditions for solid diffusion within electrode active material, presented in general form for either the anode or the cathode.

is approximately

$$c^*_{A,an}(x,0) = 0.80c_{A,an,max} \quad c^*_{A,ca}(x,0) = 0.025c_{A,ca,max} \tag{3.17}$$

where $c_{A,an,max}$ and $c_{A,ca,max}$ are the saturation concentrations of the anode and cathode active material respectively. To determine these initial conditions, the work of (Safari & Delacourt, 2011*b*) is referenced as an initial starting point followed by empirical modifications to achieve agreement with experimental data.

Unlike the liquid phase governing equations, the solid phase cannot be assumed to be in steady state, because the amount of lithium in each electrode is unsteady. Thus a time scale needs to be introduced based on the characteristic time of diffusion for cations within the solid phase,

$$t_j = t^* \frac{D_j}{L_j^2} \tag{3.18}$$

where t^* indicates the dimensional time. The spatial variable is scaled by the total electrode thickness

$$x_j = \frac{x_j^*}{L_j} \tag{3.19}$$

The concentration scale in the solid phase is based upon the saturation concentration according to

$$c_{A,j} = \frac{c^*_{A,j}}{c_{A,j,max}} \tag{3.20}$$

The governing equation becomes

$$\frac{\partial c_{A,j}}{\partial t_j} = \frac{\partial^2 c_{A,j}}{\partial x_j^2} \tag{3.21}$$

The boundary conditions are

$$\frac{\partial c_{A,j}}{\partial x_j} = 0 \; at \; x_j = 0, \quad \frac{\partial c_{A,j}}{\partial x_j} = \frac{L_j}{D_j c_{A,j,max}} \frac{J^*}{\epsilon_j F} = \frac{i^*}{i_{D,s,j}} \; at \; x = 1 \tag{3.22}$$

During the process of converting to dimensionless equations, the boundary flux is scaled by the quantity $i_{D,s,j}$. The solid and liquid phases have been presented as if they are self-contained problems. In reality the coupling between them is enforced by the continuity of the ionic current and its inclusion in their boundary conditions. This ionic current must remain continuous across the EDL to conserve mass.

3.2.3 Reaction Kinetics

The procedure described in Chapter 2 is used to develop the kinetic expressions. For the chemistry of interest, the anode reaction is given by

$$Li_xC_6 \rightleftharpoons Li^+ + e^- + C_6 \tag{3.23}$$

where atomic lithium in the anode solid phase ($c_{A,an}$) is represented by the left-hand side term Li_xC_6, the lithium ions in the liquid phase (c_A) are represented by Li^+, and the open site in the anode solid phase created by de-intercalation ($c_{A,an,max} - c_{A,an}$) is given by C_6. The cathode reaction is defined by

$$Li_yFePO_4 \rightleftharpoons Li^+ + e^- + FePO_4 \tag{3.24}$$

where the lithium ions in the liquid phase are again represented by Li^+, the open site within the cathode solid phase ($c_{A,ca,max} - c_{A,ca}$) is given by $FePO_4$, and the atomic lithium in the cathode solid phase ($c_{A,ca}$) is defined by Li_yFePO_4. These reactions govern the charge/discharge process with the right arrow indicating oxidation and the left arrow indicating reduction. Oxidation corresponds to a positive reaction current and reduction to a negative reaction current in both electrodes.

For the procedure of applying Le Chatelier's principle (Atkins, 1993), the reader is again referred to Chapter 2. The resulting rate equations are

$$i_j^* = k_{o,j}^* c_{A,j}^* e^{\frac{(1-\alpha)F}{RT}\Delta\phi_{s,j}^*} - k_{r,j}^* c_{A,\infty,j}^* (c_{A,j,max} - c_{A,j}^*) e^{-\frac{\alpha F}{RT}\Delta\phi_{s,j}^*} \tag{3.25}$$

where each k^* is a reaction rate constant which relates the conditions of the reaction to the net reaction rate, $\Delta\phi_{s,j}^*$ is the Stern layer potential difference which will be discussed in greater detail in the following sections, and $c_{A,\infty,ca}^* = c_A^*(0)$ for the cathode and $c_{A,\infty,an}^* = c_A^*(1)$ for the anode is the concentration of Li^+ ions at the interface between the EDL and the electroneutral liquid. The parameter α is referred to as a symmetry factor or transfer coefficient, as discussed in Chapter 2. These rate equations will be used to derive an analytical current-voltage relationship for a steady current. They are similar to the relationships presented by (Bazant *et al.*, 2005), but with the addition of the dependence on filled and open sites in the active material matrix.

Equation (3.25) is of the same form as Eqs. (2.19) and (2.20). However, in this chapter solutions are presented for the concentration and potential in the EDL region, so these local solutions are used in place of the bulk values of Chapter 2.

As stated previously, the Stern layer voltage is only part of the entire potential drop within the EDL in the general case. In fact the entire potential difference of the EDL, $\Delta\phi_{EDL,j}$, is equal to the sum of the Stern layer and diffuse layer potentials such that

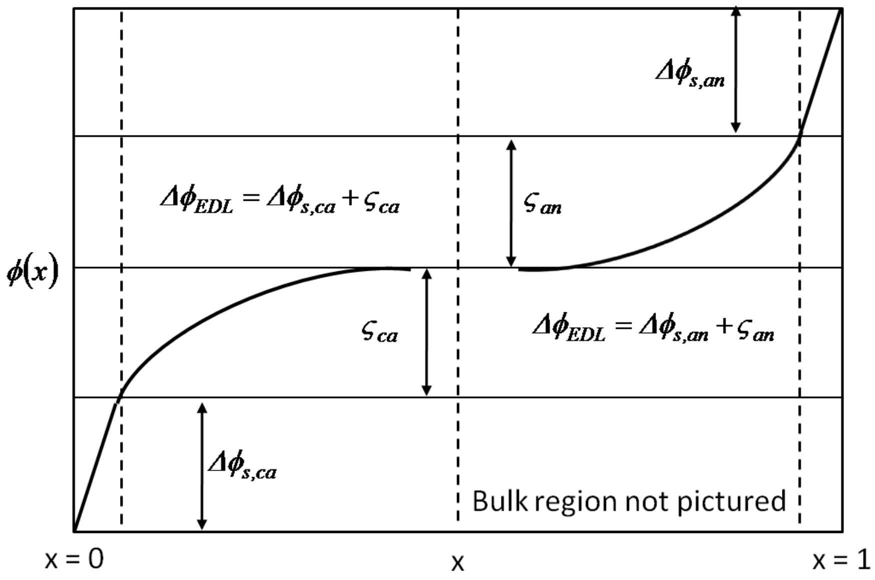

Figure 3.4: Definition of potential differences in the electrical double layer at anode and cathode. The potential profile in the bulk is omitted.

$\Delta\phi_{EDL,j} = \Delta\phi_{s,j} + \zeta_j$, where we use ζ_j to represent the diffuse layer potential and refer to it as the zeta potential. Visually, we represent the assignment of the total EDL potential difference to the Stern layer and the diffuse layer in Figure 3.4. A positive current with $i > 0$, directionally from the anode to the cathode, requires a positive potential difference across the anode EDL ($\Delta\phi_{EDL,an} = \phi_{an} - \phi(1) > 0$) and a negative potential difference across the cathode EDL ($\Delta\phi_{EDL,ca} = \phi_{ca} - \phi(0) < 0$). Imposing $i > 0$ also corresponds to discharging the cell in the sign convention of this work, which requires $i_{an} >$ and $i_{ca} < 0$ to match the oxidation/reduction sign convention. We present Eq. (3.25) in dimensionless form by dividing both sides by the diffusion-limited current density. We also recognize that the arguments of the exponential terms are in fact dimensionless to give the final dimensionless form as

$$i_j = k_{o,j} c_{A,j} e^{(1-\alpha)\Delta\phi_{s,j}} - k_{r,j} c_{A,\infty,j} (1 - c_{A,j}) e^{-\alpha\Delta\phi_{s,j}} \tag{3.26}$$

where i is used to denote the dimensionless current density, as was discussed previously in the boundary conditions for solid and liquid transport. The diffusion-limited current density is utilized in the process of converting to non-dimensional form because it yields an expression that has all terms of order unity except for the arbitrary reaction rate constants. From this point forward, we omit subscripts unless absolutely necessary and note that for a positive (discharge) current, $i^*_{an} = i^*$ and $i^*_{ca} = -i^*$ due to the sign convention associated with oxidation and reduction currents. The individual concentrations and rate constant are still dimensional, but their product is dimensionless. This does not pose any mathematical difficulties because the two terms appear as a product for the rest of the analysis in this work. The pre-multipliers of the exponential terms are directly related to the state of charge of each electrode. As stated in the introduction this provides a physical mechanism for altering the values of the rate constants during the discharge process, or in this instance the product of the rate constant and the reactants.

3.3 Solution of the Governing Equations

This section details the solution of the previously derived governing equations. First the solution of the electroneutral liquid phase is presented. Next, the separation of variables method is used to solve for the lithium concentration in each electrode solid phase. Finally, the solutions for ionic concentration and potential are derived for the two limiting descriptions of the EDL. These sets of solutions are utilized by the polarographic relationships in the Helmholtz and Gouy-Chapman limit, which conclude the section.

3.3.1 Solutions in the Separator

At this point, an analytical solution to the governing equations is derived. Equations (3.10) and (3.13) with corresponding boundary conditions comprise a system of three coupled ordinary differential equations when considering the ionic concentrations independently. The coupling is stiff due to the introduction of the ϵ parameter. In order to make the system mathematically tractable, the analysis is divided to deal with the electroneutral region (commonly referred to as the 'bulk') and the EDL separately. To develop an equation for the bulk solution it is first noted that in the bulk, the ionic concentrations are equal ($c_A(x) = c_B(x) = c(x)$) everywhere to establish electroneutrality. Then the equations for each individual ionic concentration are summed and integrated with i constant to obtain

$$i = 2\frac{\partial c}{\partial x} \tag{3.27}$$

Equation (3.27) will be solved directly via integration. The constant of integration must be determined by applying conservation of mass for the anion

$$\int\limits_0^1 c_B(x)dx = 1 \tag{3.28}$$

This conservation of mass condition comes from the constraint that there is no flux of PF_6^- ions into the solid portion of either electrode, which implies that the total number of anions within the liquid must be constant. Integrating Eq. (3.27) and applying Eq. (3.28) gives

$$c(x) = \frac{i}{2}\left(x - \frac{1}{2}\right) + 1 \tag{3.29}$$

To obtain an equation for the electric potential the equation describing the ionic concentration of the anion is subtracted from that of the cation, and the result is integrated to yield

$$i = 2c\frac{\partial \phi}{\partial x} \tag{3.30}$$

Since an expression for the bulk concentration has already been derived, it may be substituted and integration performed again to obtain

$$\phi(x) = ln\left(1 + \frac{i}{2}\left(x - \frac{1}{2}\right)\right) \tag{3.31}$$

3.3.2 Solutions in the Electrode Solid Phase

The solution to the solid transport problem is found by the same method as presented for Eq. (2.74). Doing so yields the solution

$$c_{A,j}(x_j, t_j) = c_{A,j}(x_j, 0) + \frac{i^*}{i_{D,s,j}}\left(t_j + \frac{3x_j^2 - 1}{6} - \frac{2}{\pi^2}\sum_{n=1}^{\infty}\frac{(-1)^n}{n^2}e^{-n^2\pi^2 t_j}cos\left(n\pi x_j\right)\right) \tag{3.32}$$

Even for small t, the solution of Eq. (3.32) does not change appreciably by including more than five terms from the infinite series. For large t, the infinite series is inconsequential due to the exponential term and the solution becomes linearly increasing with respect to t and parabolic in the spatial coordinate x. If the external current density i is constant then the solution for the bulk, steady state, liquid concentration and potential, as well as the time-varying solid concentration in each electrode, is given for all time.

3.3.3 Solutions in the Electrical Double Layer

The solution in the EDL depends on the limiting assumption being applied, which corresponds to either the Helmholtz limit or the Gouy-Chapman limit. In the Helmholtz limit, all the potential difference associated with the EDL is assumed to be present across the Stern plane. As a result, no diffuse charge exists in the EDL and no solution describing the concentration of anions and cations in the diffuse layer of the EDL is required. If it is assumed that the entire potential difference of the EDL occurs across the Stern layer, then $\Delta\phi_{EDL,j} = \Delta\phi_{s,j}$, and the solution for $\Delta\phi_{s,j}$ is found starting from Eq. (3.26) with the assumption that $\alpha = 0.5$. Using symbolic algebra software gives

$$\Delta\phi_{s,j} = ln\left(\frac{1}{2}\frac{i_j + \sqrt{i^2 + 4k_{o,j}c_{A,j}k_{r,j}c_{\infty,j} - 4k_{o,j}c_{A,j}^2k_{r,j}c_{\infty,j}}}{k_{o,j}c_{A,j}}\right) \tag{3.33}$$

In the Gouy-Chapman limit it is assumed that the potential difference across the Stern layer is zero and the diffuse layer accounts for all of the double layer potential. This limit allows for the presence of diffuse charge in the EDL and requires an inner solution that is valid within a region of width $O(\epsilon)$ at $x = 0$ and $x = 1$. The full solution is then equal to the sum of the solutions within the EDL and the electroneutral region with the common part subtracted. This methodology applies to both concentration and potential. Previously it was stated that the Stern layer potential difference is the actual driving force for the electrochemical reaction. However, this is inconsistent with the current assumption that the potential difference across the Stern layer is zero. Thus in this instance the more common approach is used where the entire double layer potential difference is the driving force for the reaction. The rate equation, Eq. (3.26), becomes

$$i_j = k_{o,j}c_{A,j} - k_{r,j}c_{\infty,j}(1 - c_{A,j})e^{-\zeta_j} \tag{3.34}$$

Equation (3.34) is solved for ζ_j, resulting in

$$\zeta_j = ln\left(\frac{k_{r,j}c_{A,\infty,j}(1 - c_{A,j})}{k_{o,j}c_{A,j} - i_j}\right) \tag{3.35}$$

This gives the total potential difference across the EDL, such that $\Delta\phi_{EDL,j} = \zeta_j$. We apply the Boltzmann distribution for ionic concentration which is valid for equilibrium conditions

$$c_i(y) = c_{\infty,j}e^{-z_i\phi(y)} \tag{3.36}$$

where $c_{\infty,j}$ is the concentration at the interface between the EDL and the electroneutral liquid as x tends to zero or one, $y = \frac{x}{\epsilon}$ is the inner solution spatial variable, and $\phi(y)$ is the inner potential. The solution for potential in the EDL is found by solving Poisson's equation subject to the previously applied Boltzmann distribution of ionic concentration

$$\frac{d^2\phi}{dy^2} = sinh(\phi) \tag{3.37}$$

To solve Eq. (3.37), multiply by $2\frac{d\phi}{dy}$ and integrate twice to obtain

$$\phi_{EDL,j}(y) = 4tanh^{-1}\left(tanh\left(\frac{\zeta_j}{4}e^{-y}\right)\right) \tag{3.38}$$

Equations 3.36 and 3.38 are collectively referred to as the Poisson-Boltzmann distribution for the classical EDL.

3.3.4 Polarographic Relationships

The entire liquid phase solution, encompassing solutions in the electroneutral portion as well as the EDL, may be viewed in terms of a polarographic relationship for the case of a steady external current. The term polarographic refers to the steady state relationship between current and voltage which defines the amount of overpotential required to sustain a given current through the liquid phase, and this overpotential manifests itself as a deviation from the cell open circuit voltage. This is an important component of predicting the cell voltage during a charge or discharge.

Helmholtz Limit

We note that in general the voltage difference across the separator (referred to interchangeably as the liquid voltage, V_L) is given by the sum of the voltage difference in the electroneutral liquid and that of each EDL

$$V_L(t) = \Delta\phi_{EDL,an} + 2tanh^{-1}(i) + \Delta\phi_{EDL,ca} \tag{3.39}$$

where the inverse hyperbolic tangent term arises from the potential difference in the electroneutral separator liquid, and the other two terms are associated with the potential difference across the electrical double layer. Upon substitution of Eq. (3.33) into Eq. (3.39), the current voltage relationship becomes

$$V_L(t) = 2tanh^{-1}(i) + ln\left(\frac{k_{o,ca}c_{A,ca}}{k_{o,an}c_{A,an}}\frac{i+\sqrt{i^2+4k_{o,an}c_{A,an}k_{r,an}c_A(1)(1-c_{A,an})}}{-i+\sqrt{i^2+4k_{o,ca}c_{A,ca}k_{r,ca}c_A(0)(1-c_{A,ca})}}\right) \tag{3.40}$$

The first term, $2tanh^{-1}(i)$, defines the voltage in the electroneutral liquid. The natural logarithm term represents the voltage of the EDLs at the anode and cathode.

The current-voltage relationship must be modified to account for the use of an equilibrium potential during model development. Typical open-circuit voltages for the anode and cathode are empirically obtained using half-cell measurements, where the working electrode is assessed relative to a lithium metal counter/reference electrode. The zero current EDL potential is inherently included in the measured data, so the EDL voltage value at zero current is subtracted from the measured open-circuit voltage. The overall process is similar for either the Helmholtz limit or the Gouy-Chapman limit of the following section, with the only difference being a change in the form of the polarographic expression. Mathematically, the preceding discussion is accomplished as

$$\widetilde{V_L}(t) = V_L(t) - V_L(t)|_{i=0} \tag{3.41}$$

where $V_L(t)$ on the right-hand side is defined in Eq. (3.40) and $\widetilde{V_L}(t)$ on the left-hand side accounts for only the non-equilibrium portion of the EDL potential.

Gouy-Chapman Limit

Before presenting the polarographic relationship, the complete solutions for potential and concentration are given. The complete solution for potential is equal to the electroneutral solution plus the inner solution, minus their common part

$$\begin{aligned}\phi(x) =&ln\left(\frac{\frac{i}{2}\left(x-\frac{1}{2}\right)+1}{\left(1-\frac{i}{4}\right)\left(1+\frac{i}{4}\right)}\right)+4tanh^{-1}\left(tanh\left(\frac{\zeta_{ca}}{4}\right)e^{-\frac{x}{\epsilon}}\right)\\ &+4tanh^{-1}\left(tanh\left(\frac{\zeta_{an}}{4}\right)e^{-\left(\frac{1-x}{\epsilon}\right)}\right)\end{aligned} \tag{3.42}$$

where the common part is equal to the bulk value at $x = 0$ and $x = 1$. Following a similar methodology, the complete solution for concentration is

$$c_i(x) = 1+\frac{i}{2}\left(x-\frac{1}{2}\right)+\left(1-\frac{i}{4}\right)\left(e^{-z_i(\phi(x))}-1\right)+\left(1+\frac{i}{4}\right)\left(e^{-z_i(\phi(x))}-1\right) \tag{3.43}$$

where $\phi(x)$ is defined in Eq. (3.42). Noting that $\phi_{EDL,ca} = -\zeta_{ca}$ due to the convention of Figure 3.4 where the zeta potential is defined relative to the bulk liquid potential, and substituting the result from Eq. (3.35), the current voltage relationship of Eq. (3.39) becomes

$$V_L(t) = 4tanh^{-1}(i)+ln\left(\frac{k_{r,an}(1-c_{A,an})}{k_{o,an}c_{A,an}-i}\frac{k_{o,ca}c_{A,ca}+i}{k_{r,ca}(1-c_{A,ca})}\right) \tag{3.44}$$

The electroneutral portion of the EDL voltage, $2tanh^{-1}(i)$, remains as discussed previously. However an additional $2tanh^{-1}(i)$ and natural logarithm term are associated with the EDL voltage in the Gouy-Chapman limit. Again Eq. (3.41) must be applied to account for only the non-equilibrium portion of the EDL in the cell voltage. This is different from the expression derived using the assumption that the entire potential difference of the EDL occurs in the Stern layer. We will further explore the similarities and differences between Eq. (3.40) and 3.44 in the Results and Discussion section, including comparing models using each hypothesis to experimental data. The aim of this comparison is to understand if one model more accurately describes the nano-scale physics of a commercially available Li-ion cell. As discussed in (Bazant *et al.*, 2005), there is an infinite number of possibilities for division of the entire EDL potential across the Stern layer and the diffuse layer determined by the capacitance of each layer. However in the Results and Discussion it is noted that the results are ultimately quite similar when comparing the two extremes discussed here, so further investigtion of the intermediate cases is outside the scope of this paper. A result of the preceding sections is that the overpotential required in the EDL is determined in closed form by the battery SOC, the current, and the solution of the fully electroneutral portion of the liquid in both limiting cases.

3.4 Results and Discussion

In this section, results obtained from the solution of the governing equations for a galvanostatic capacity test are presented. The applicability of the limiting descriptions of the EDL in view of system-level considerations and experimental data is also discussed, and finally empirical modifications to the theoretical current-voltage relationship are introduced.

3.4.1 Definition of Cell Terminal Voltage

The output voltage is obtained by moving from cathode to anode and summing the voltages encountered, recalling that $\widetilde{V_L^*}(t)$ contains the effects of both the electroneutral liquid as well as the EDL

$$V^*(t) = U^*_{ca}\left(c_{ca}(L,t)\right) - U^*_{an}\left(c_{an}(L,t)\right) - \widetilde{V_L}^*(t) - R_c i^*(t) \tag{3.45}$$

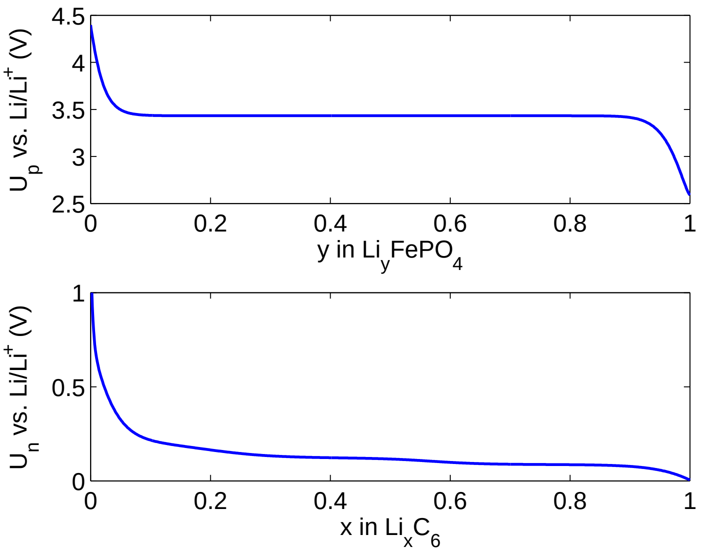

Figure 3.5: Open-circuit voltage curves for cathode and anode.

An ohmic resistance R_c accounts for the initial ohmic polarization that is not due to the bulk liquid. The quantity R_c is the sum of ohmic losses from the solid phase of the electrode, poor contact between iron phosphate particles and the conductive matrix (Safari & Delacourt, 2011*b*; Srinivasan & Newman, 2004*b*), and conduction through the current collectors. The sum of voltage losses is treated as a deviation away from the open-circuit voltage between electrodes given by the difference of U^*_{ca} and U^*_{an}.

The difference in the open-circuit voltages is taken as the thermodynamic maximum voltage that can be achieved under ideal conditions during discharge (Bernardi & Go, 2011), though the concentration overpotential in the solid phase is embedded in these functions through their dependence on the surface concentration rather than the mean solid concentration. These functions for the anode and cathode are defined in Figure 3.5.

The parameter values used to produce the simulation results of the following section are documented in Table 3.1. The source of each parameter is defined by the superscript next to the parameter definition. For measured parameters, AFM and SEM images from the Center for Automotive Research and the Nanoprobe Laboratory for Bio- and Nanotechnology and Biomimetics were examined using image analysis software. Active material volume fractions were tuned based on the measured electrode volumes to match the composition range of the electrodes given by (Safari & Delacourt, 2011a). Since the anode is the capacity-limiting electrode during discharge in this instance, its diffusion coefficient was estimated

Table 3.1: Summary of model parameters used for simulation results. Sources are: a) measured, b) estimated from available experimental data, c) from literature.

Parameter	Definition	Value
ϵ_{an}	anode active material volume fraction^b	0.44
ϵ_{ca}	cathode active material volume fraction^b	0.36
$\bar{\epsilon}_e$	liquid permittivity^c	46 F/m
A	current collector area^a	0.19 m^2
$c_{A,max,an}$	saturation concentration of Li^+ in anode active material^c	30500 mol/m^3
$c_{A,max,ca}$	saturation concentration of Li^+ in cathode active material^c	16300 mol/m^3
$c_{an}(x_{an},0)$	initial degree of anode intercalation^c	0.80
$c_{ca}(x_{ca},0)$	initial degree of cathode intercalation^c	0.025
c_0	electroneutral concentration^c	1000 mol/m^3
D	effective liquid phase diffusion coefficient^c	1.7 $\times 10^{-10}$ m^2/s
D_{an}	anode solid phase diffusion coefficient^b	4.0 $\times 10^{-14}$ m^2/s
D_{ca}	cathode solid phase diffusion coefficient^c	8.0 $\times 10^{-18}$ m^2/s
L_{an}	anode effective diffusion length^b	3.4 μm
L_{ca}	cathode effective diffusion length^b	31 nm
L_{sep}	separator thickness^c	25 μm
$k_{o,an}$	anode oxidation rate constant^b	2.5 $\times 10^{-3}$ $A \cdot m/(mol \cdot s)$
$k_{o,ca}$	cathode oxidation rate constant^b	4.0 $\times 10^{-7}$ $A \cdot m/(mol \cdot s)$
$k_{r,an}$	anode reduction rate constant^b	2.5 $\times 10^{-3}$ $A \cdot m^4/(mol^2 \cdot s)$
$k_{r,ca}$	cathode reduction rate constant^b	4.0 $\times 10^{-7}$ $A \cdot m^4/(mol^2 \cdot s)$
R_c	contact resistance^b	26 $\times 10^{-3}$ Ωm^2
T	temperature	298 K

using the capacity difference between capacity tests of varying current magnitude. Specifically, the value was adjusted to account for the difference in capacity between the C/3 and C/1.2 tests reported in the Experimental section.

The rate constants are adusted using the following process. First the experimentally measured voltage for the C/3 rate is subtracted from the cell open-circuit voltage defined by the first two terms of Eq. (3.45). This gives the amount of overpotential experienced by the cell over the course of a discharge cycle. Then the rate constant values and contact resistance are adjusted so that the last two terms of Eq. (3.45) give an adequate fit to the voltage losses. Since there are four values of the rate constant, assumptions are made to simplify the fitting process. The forward and backward rate constants are assumed to be equal. The anode rate constant values are set high enough to give minimal contribution to the overpotential, since this is generally the case for graphite electrodes operating near room temperature. This leaves only the cathode rate constant and contact resistance to fit the observed overpotential. The rate constant values are identified only for the lowest current and then used to predict the voltage at higher currents. To add another set of data to test the predictive nature of the model, 3C capacity test data from (Safari & Delacourt, 2011*b*) is also plotted.

3.4.2 Analytical Predictions

The steady state profiles for concentration using each of the limiting hypotheses are plotted in Figure 3.6. The profiles computed using the Gouy-Chapman limit will be largely the same as those for the Helmholtz limit, except for a small region of $O(10^{-5})$ near either solid boundary. Since the liquid phase transport reaches steady-state quickly compared to the total discharge time, the concentration in the liquid is a function of only space and

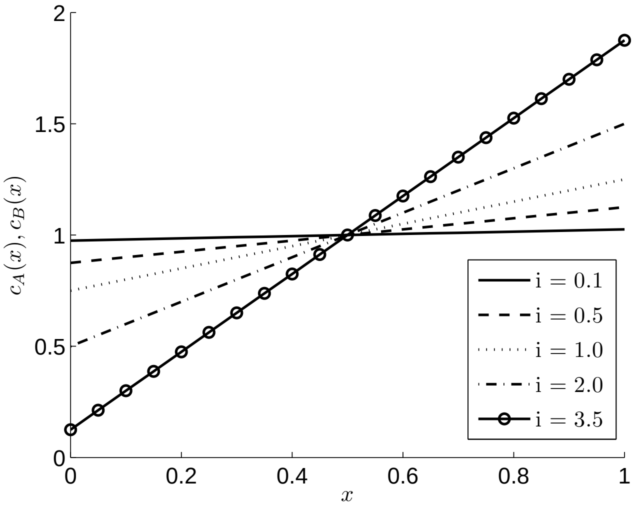

(a)

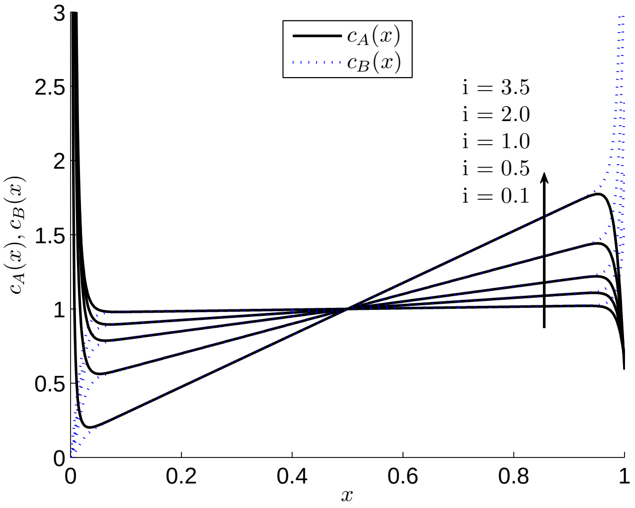

(b)

Figure 3.6: Steady state dimensionless concentration profiles in the liquid obtained from Eq. (3.29) for varying dimensionless current density. (a) The Helmholtz limit which neglects the presence of diffuse charge and corresponding variation in potential near $x = 0$ and $x = 1$. (b) The Gouy-Chapman limit with $\epsilon = 10^{-2}$ (artificially large only to enhance EDL visibility) assuming 50% SOC. Note the presence of diffuse charge within an *O(ϵ)* layer at $x = 0$ and $x = 1$.

current density. As the limiting discharge current ($i = 4$) is approached the concentration at the cathode surface goes to zero. During a charge condition, the steady-state concentration near the anode would approach zero for currents close to the limiting value.

The solution for potential is plotted in Figure 3.7, showing it is logarithmic with respect to the spatial coordinate. The total potential difference is non-linear with respect to the current and this non-linearity influences the concentrations at the Stern plane as well. The potential difference between the electrodes approaches zero as the current approches its limiting value. From cell level measurements one could expect a large magnitude of overpotential for currents near the limit, though in reality this limit is not easily approached before other limitations such as ohmic overpotential or solid diffusion become prohibitive.

Figure 3.8a gives a comparison of the polarographic expression relating current and steady state voltage in the liquid for the Helmholtz and Gouy-Chapman limits. Recall that this is a sum of the potential difference within the electroneutral liquid and the overpotential of the EDL. To produce Figure 3.8a, the solid concentration values are set to their corresponding values for each SOC of interest. Then the current is swept from zero to the limiting value while holding all other variables constant to give a polarographic curve for the liquid between electrodes. The plotted curves resulting from each limiting description of the EDL are fairly similar in several respects. First, both curves tend to shift upward or downward as the cell SOC is varied. However the Helmholtz limit exhibits symmetry about 50% SOC in its polarographic curves whereas the Gouy-Chapman limit does not. The polarographic curves of the Gouy-Chapman limit also tend to shift by a larger amount as the cell state of charge varies.

A final interesting point of Figure 3.8a is the voltage response at low current density. Due to the high value of the diffusion limited current density in this case, operation in the

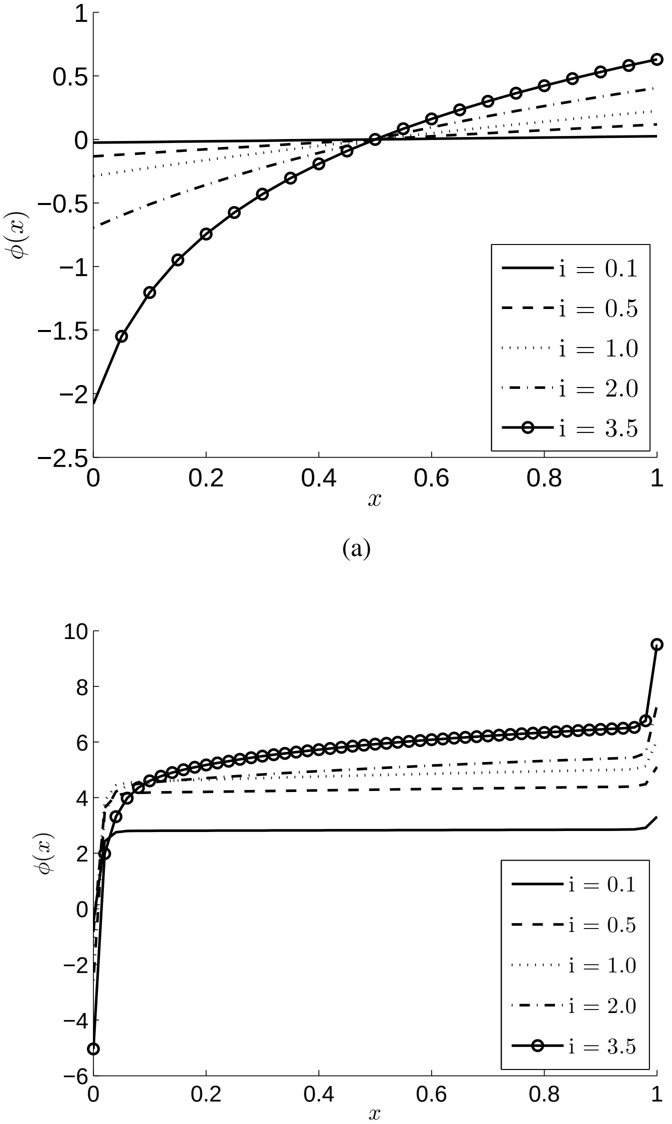

(a)

(b)

Figure 3.7: Steady state dimensionless potential profiles in the liquid obtained from Eq. (3.31) for varying dimensionless current density, using (a) the Helmholtz limit and (b) the Gouy-Chapman limit. Gouy-Chapman results use $\epsilon = 10^{-2}$ (artificially large only to enhance EDL visibility) and assume 50% SOC. The presence of diffuse charge modifies the total potential difference shown in (b) compared to (a).

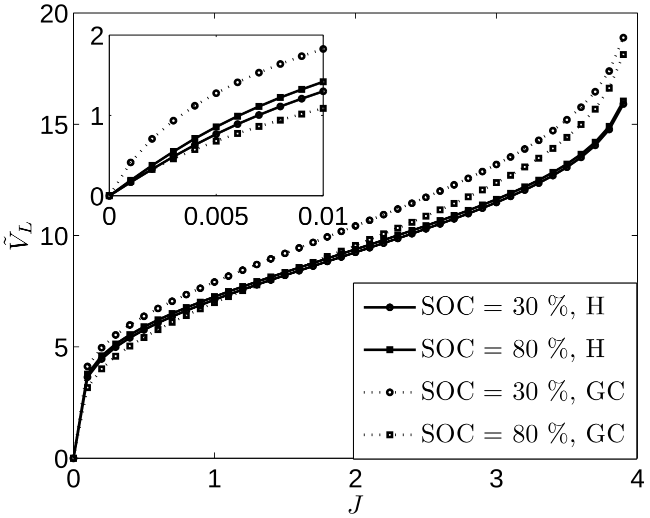

(a)

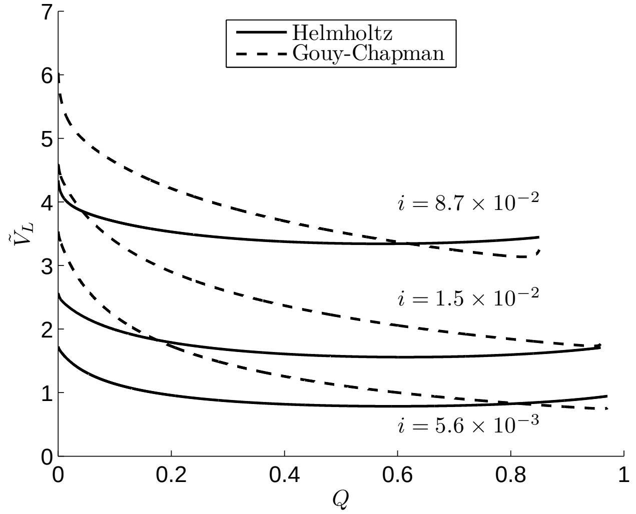

(b)

Figure 3.8: (a) Steady state relationship between dimensionless current and voltage from Eqs. (3.40) and (3.44) for varying cell state of charge. Parameter values are taken from Table 3.1. (b) Comparison of kinetic losses due to EDL and electroneutral liquid from Eqs. (3.40) and (3.44) for a range of current values. Full discharge cycle is simulated. Discharge time, and hence total charge passed, is normalized based on the value predicted for the lowest current rate.

region $|i| > 0.5$ is not expected. Furthermore for current rates of less than or equal to 1C, $|i| \leq 0.02$, and this corresponds to the region displayed in the inset of Figure 3.8a. In the context of lithium ion battery literature, the double layers are assumed to be thin and the Butler-Volmer kinetic law is applied based on concentration and potential values in the bulk. Reflecting on the solutions, this essentially implies that battery literature employs the Helmholtz limit for the EDL and neglects the possibility of diffuse charge caused by a non-negligible zeta potential.

To continue the comparison between the two models, the overpotential due to charge transfer in the Helmholtz limit is plotted in Figure 3.8b along with the overpotential according to the Gouy-Chapman limit. The comparison is made at the C/3, C/1.2, and 4.8C rates which corresponds to $i = 5.6 \times 10^{-3}$, 1.5×10^{-2}, and 8.7×10^{-2} respectively. This differs from the results of Figure 3.8a because here a current is fixed and the resulting time-varying response of concentration and potential is computed. The curves show qualitative similarity but the Gouy-Chapman limit exhibits significantly greater variation in voltage over the course of discharge. Additionally the Gouy-Chapman limit at the highest current level shows the beginning of an increase in overpotential near the end of discharge that could be associated with a voltage knee if it were larger in magnitude.

Finally the solid phase diffusion solution is examined. The spatial distribution of Li^+ concentration within the solid phase of each electrode is plotted at various times during a discharge at 4.8C rate in Figure 3.9. This current is chosen because it is large enough to highlight the spatial gradients that occur, which tend to be less apparent at lower rates. Since the cathode actually exhibits a phase change, solving the diffusion equation is an empirical method of accounting for rate effects.

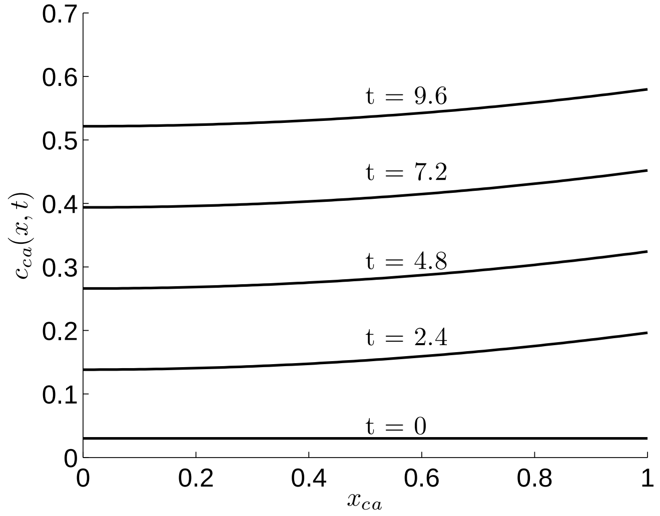

(a)

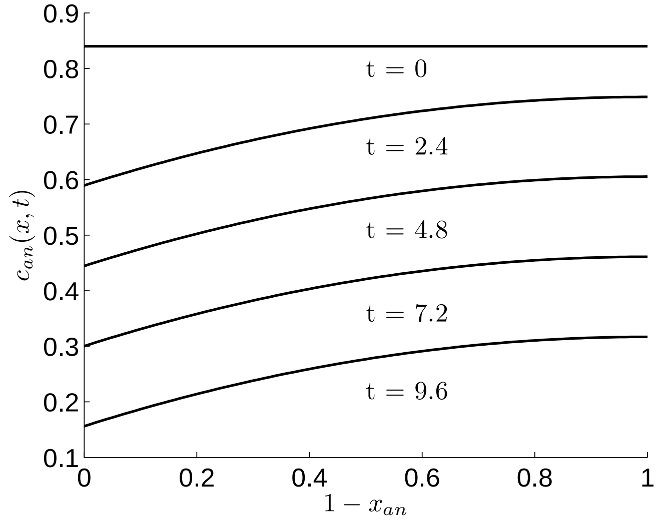

(b)

Figure 3.9: Concentration of Li^{+} within (a) cathode and (b) anode given by Eq. (3.32) for a full discharge cycle with $i = 8.7 \times 10^{-2}$ and parameter values from Table 3.1. Current collector is positioned at $x_{ca} = 0$ and $x_{an} = 1$, while the interface between electrode and separator is at $x_{ca} = 1$ and $x_{an} = 0$. Time scale shown is based on the anode, since it limits discharge capacity.

3.4.3 Experimental

Data obtained from a cylindrical graphite/iron phosphate cell with can dimensions of 26 mm diameter by 65 mm height (26650) are used for comparative purposes and to examine the validity of the double-layer assumptions. Galvanostatic capacity tests are performed at current rates of C/3, C/1.2, and 4.8C. Data is collected at 10 Hz and current is commanded using a PLA800-60-300 power load and supply from American Reliance, Inc. Temperature is fixed at $25°\mathrm{C}$ using an AC-027 Peltier junction from TE Technology, Inc. along with sufficient insulation to prevent excessive power draw by the Peltier junction. The lower voltage limit is 2.5 V while the upper limit is 3.6 V, as defined by the manufacturer. During charging, constant voltage is enforced at the upper voltage limit for 30 minutes.

Comparison of Theoretical Model Structure with Experimental Data

The model output using the Helmholtz limit is compared with experimental data in Figure 3.10 for multiple current rates. There is generally good agreement between the steady-state model using the Helmholtz limit of the EDL and the experimental data gathered at low current. The model results diverge from the experiment for the highest discharge rates. This is to be expected however, because several factors are neglected in developing this simplified model that would have a growing impact as the current rate increases. These factors include the neglect of the non-uniform reaction rate with respect to the thickness of the electrode, neglect of thermal effects, and neglect of the resistive reactant nature of lithium iron phosphate (Thomas-Alyea, 2008; Safari & Delacourt, 2011*a*). Given that the model overpredicts the cell voltage compared to the experimental data at the highest current, the most likely factor to improve the model predictions is inclusion of the time-varying resistance of the cathode that results from the resistive reactant effects.

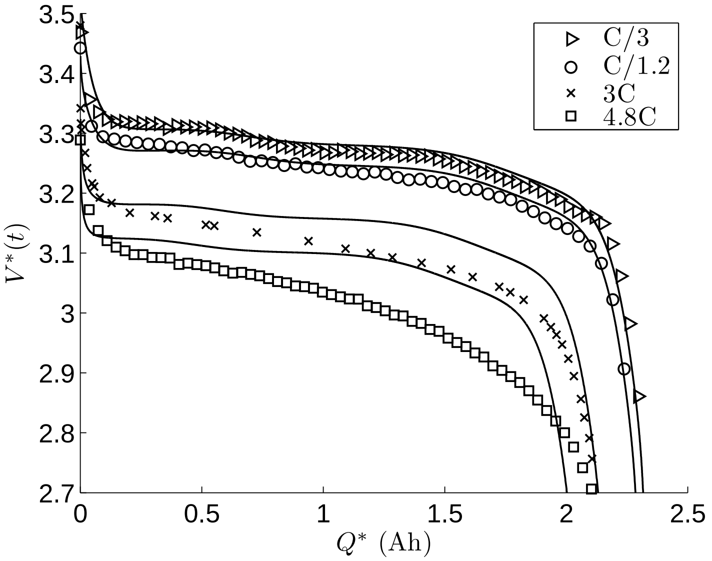

Figure 3.10: Comparison of model output (lines) and experimental data (symbols) for a range of current rates using Helmholtz limit. The charge values along the x axis are obtained as the integral of the constant current rate magnitude with respect to time. Parameter values are taken from Table 3.1, and error magnitude for experimental data is $\pm$ 5 mV.

The model output using the Gouy-Chapman limit is compared with experimental data in Figure 3.11 for multiple current rates. Recall that the Gouy-Chapman hypothesis allowing for mobile charge in the diffuse layer gives a wider variation in the kinetic overpotential over the course of the discharge. The wide variation in the overpotential magnitude leads to the non-physical phenomena of the voltage actually increasing during the course of discharge. The comparison between limiting cases of the EDL is made using equivalent rate constants for each case. It remains an open issue whether different rate constants could be selected for the Gouy-Chapman limit that would provide better agreement with experimental data. Whether these results are an indication that the double layer structure within the battery studied for this work tends to have more immobile charge in the Stern layer than

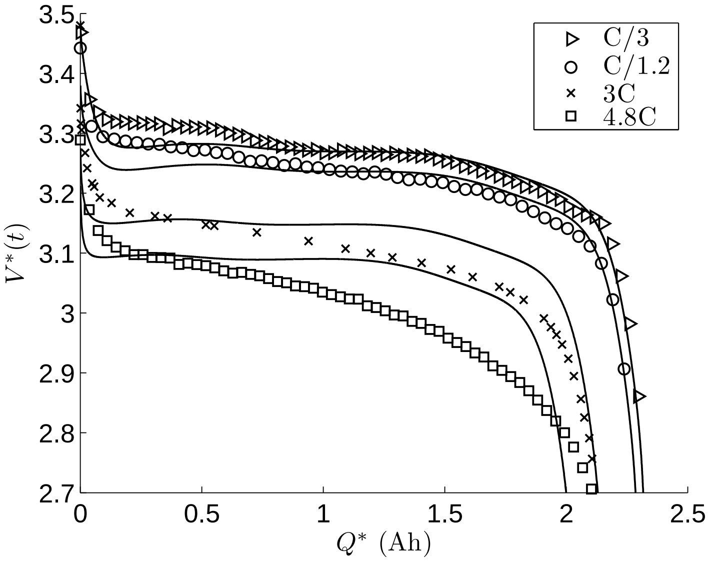

Figure 3.11: Comparison of model output (lines) and experimental data (symbols) for a range of current rates using Gouy-Chapman limit. The charge values along the x axis are obtained as the integral of the constant current rate magnitude with respect to time. Parameter values are taken from Table 3.1 and error magnitude for experimental data is ± 5 mV.

mobile charge in the diffuse layer is left as an interpretation for the reader. The Gouy-Chapman results also diverge from the experimental data for the 4.8C current for the same reasons discussed in the context of the Helmholtz limit.

Empirical Inclusion of Resistive Reactant Effects

It is clear from the preceding results that some effects which may be important for accurately predicting cell terminal voltage during high discharge currents have not been included in the theoretical development of the model. As discussed previously, the resistive reactant nature of iron phosphate results in increasing overpotential with respect to depth of discharge. The difference between model output and experimental data is plotted in

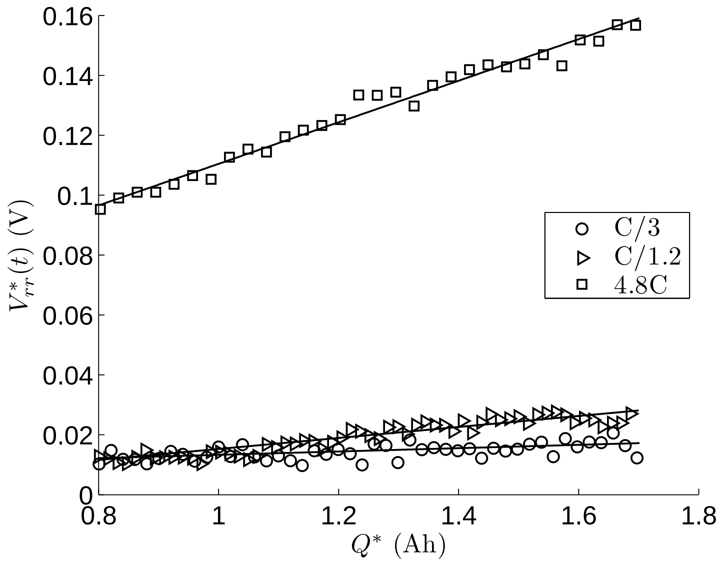

Figure 3.12: Fit of the resistive reactant overpotential after comparison of model developed from theory and experimental data. Increasing overpotential is modeled as a linear function of depth of discharge.

Figure 3.12, for the range of 0.8 to 1.8 Ah during discharge (roughly the middle third of the discharge curve). It is proposed that this difference between model and experiment is due solely to resistive reactant effects, and is hereafter referred to as the resistive reactant overpotential, V_{rr}.

In constructing a semi-empirical model of the resistive reactant effects, the region for parameter identification is restricted to the plotted region of 0.8 and 1.8 Ah. This is because the middle portion of the discharge curve is less prone to errors from the effects of incorrect initial conditions that may cause large errors in predicted voltage at the beginning and end of the discharge process. These potentially large errors arise because the open-circuit voltage varies rapidly with respect to SOC in these regions. As one may observe from Figure 3.12, the resistive reactant overpotential is roughly linear with respect to charge

Table 3.2: Summary of empirical corrections to account for resistive reactant nature of cathode material.

C-Rate	$\frac{d(V)}{dAh}$ (V/Ah)	$\frac{dR_r}{dAh}$ (Ωm^2/Ah)
C/3	5.6×10^{-3}	40×10^{-3}
C/1.2	1.84×10^{-2}	49×10^{-3}
4.8C	6.94×10^{-2}	32×10^{-3}

removed. The slope of the unmodeled overpotential is of use as a fitting parameter, so a linear least squares problem is formulated as

$$\vec{V}_r - V_{r,0} = V_{r,1}\vec{Q} \tag{3.46}$$

where $V_{r,0}$ is the initial unmodeled overpotential (the value at $Q = 0.8\ Ah$), and $V_{r,1}$ is the constant slope of the overpotential versus capacity. When solving the least squares problem, $\vec{V}_r - V_{r,0}$ is a vector of values corresponding to the difference between the experimental data and model predicted voltage and $\vec{Q}$ is a vector of capacity values. The solution to the least squares problem is given by

$$\vec{V}_{r,1} = \left(\vec{V}_r - V_{r,0}\right)\vec{Q}^T(\vec{Q}\vec{Q}^T)^{-1} \tag{3.47}$$

where the slope $V_{r,1}$ is in terms of $Volts/Ah$. Dividing by the magnitude of the discharge current density gives a slope in terms of $\Omega m^2/Ah$, as documented in Table 3.2. When comparing the unmodeled overpotential on a voltage basis, there is a wide discrepancy between the various discharge rates reported in Table 3.2. However when the rate of voltage change is scaled based upon the magnitude of the discharge current, the values for each discharge rate show much less variation. Based on the analysis outlined in Figure 3.12 and

Table 3.2, a resistance that varies with respect to depth of discharge is included in the model as

$$R_r = 32 \times 10^{-3} Q \tag{3.48}$$

where the value of the overpotential slope from the 4.8C discharge, 32×10^{-3}, has been used, and Q is measured from an initial value of zero at the beginning of discharge to the final capacity value at the end of discharge. The value from the 4.8C rate is used because it tends to have the largest overpotential and thus the greatest signal to noise ratio, which is a benefit during the parameter identification process. The overpotential slopes for the C/3 and C/1.2 are more likely to be corrupted by the presence of noise in the data, which was discussed previously in relation to the magnitude of error for Figure 3.10 and Figure 3.11.

The resistance R_r is added to the original contact resistance R_c in Eq. (3.45). The comparison between model and experiment when the resistive reactant effect of iron phosphate is included is shown in Figure 3.13. In general the agreement is improved for all the discharge rates, although the capacity at the 4.8C rate is still underpredicted due to neglect of thermal effects. Most likely internal heating has raised the cell core temperature enough to cause an elevated diffusion coefficient and enable improved utilization of active material. Another potential factor is the use of only one representative effective diffusion length (analagous to particle size). The inclusion of multiple particle sizes could improve model accuracy for higher rates as discussed in (Srinivasan & Newman, 2004*b*).

3.5 Summary and Conclusions

A simplified model structure that uses analytical expressions for the electroneutral liquid concentration and potential, kinetic overpotential, and solid lithium concentration in each electrode has been presented. The primary conclusion is that the presence of diffuse

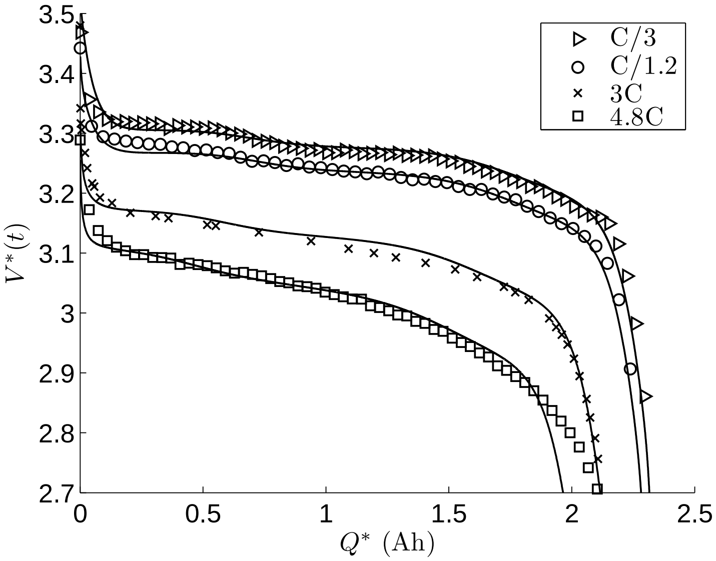

Figure 3.13: Comparison of model output (lines) and experimental data (symbols) for a range of current rates using Helmholtz limit with resistive reactant effect included. The charge values along the x axis are obtained as the integral of the constant current rate magnitude with respect to time. Parameter values are taken from Table 3.1.

charge in the EDL causes greater initial overpotential and greater variation of overpotential with respect to battery state of charge when modeled in an intercalation battery. This conclusion is derived from the inclusion of aspects of interfacial physics that have been negelected in prior work and the comparison between limiting cases of the EDL. This analysis also provides insight for understanding the Butler-Volmer representation of interfacial charge transfer typically applied within battery models. Rather than interpreting the Butler-Volmer law as a relationship between bulk properties of the solid and liquid, it may be conceptualized as governing the relationship between the reaction rate and the Stern layer voltage if diffuse charge is not present.

Furthermore, modifications have been proposed to the theoretical current-voltage relationship of the EDL and electroneutral liquid. It has been shown that a single resistance value that increases with depth of discharge improves the agreement with experimental data for a range of galvanostatic discharge experiments from C/3 to 4.8C. The model presented in this chapter captures essential features describing capacity such as the amount of cyclable lithium, active material volume fraction, and rate limitations. Its main advantage is the computational simplicity it offers while still providing agreement with galvanostatic discharge data.

In Chapter 5, a model of solid-electrolyte interphase growth is presented. This model depends on the potential in close proximity to the electrode surface. Inclusion of the effects of the EDL may lead to different predictions of the rate of SEI growth due to modification of the local potential.

Chapter 4: Reduced-Order Model Design, Parametrization, and Aging Analysis for Graphite / LiFePO$_4$ Cells

4.1 Introduction

As stated in Chapter 1, Li-ion batteries are a key technology for enabling the electrification of the automobile, due to their improved energy and power density, and potential cost savings compared to previous battery chemistries (Karden *et al.*, 2007; Snyder *et al.*, 2009; Sioshansi & Denholm, 2009). Chapter 2 established that considerable efforts are directed to modeling Li-ion battery performance, specifically predicting the output voltage in response to current and ambient temperature input conditions.

In this chapter, a novel modeling approach bridges the gap between the complex multiscale models based on the porous electrode theory and the models based on the single particle approximation discussed in Chapter 2. The objective is to develop a reduced-order electrochemical model for Li-ion battery cells that reduces the partial differential equations (PDEs) or lithium transport to a mathematical structure amenable for estimation and control purposes, namely as a low-order system of linear ordinary differential equations (ODEs). The model should accurately predict the cell output voltage dynamics in a broad range of C-rate conditions and retain a parametric dependence on electrochemical quantities that are measurable. The proposed model takes advantage of a formal model-order reduction method based on Pade approximation, as presented in Chapter 2.

The model is identified using a systematic procedure that utilizes experimental data which exercises only a subset of the sysem dynamics. Each phase of parametrization incorporates previously identified parameters to reduce the number of unknown values being identified by any one procedure and to ensure that the identified values retain their physical interpretation. The model is extensively validated via comparison with current profiles ranging from constant current pulses to the United States Department of Energy PHEV charge depleting (CD) profile (Anonymous, 2010), each for operating temperatures ranging from 5°C to 55°C.

Following the model design and parametrization, the advantages of the developed model are demonstrated by applying the model to estimation of electrochemical parameters during a battery aging campaign. The approach can be considered a formal procedure for understanding degradation mechanisms in a cell that has unknown causes for aging. It also provides a pathway to create model-based state-of-health (SOH) estimators.

Before beginning with the model design, it is useful to review model-order reduction (MOR) techniques that have been presented in literature. Most current efforts have focused on reducing the simulation time associated with electrochemical models by reducing the order and dimensionality of the equations describing the mass diffusion in the solid phase of the electrodes. The polynomial approximation reviewed in Chapter 2 is a common technique, (Subramanian *et al.*, 2005; Santhanagopalan *et al.*, 2006; Subramanian *et al.*, 2001), as well as the finite volume discretization (Smith & Wang, 2006*b*), and the Pade approximation methods (Forman *et al.*, 2011). Proper orthogonal decomposition has also been applied as a MOR approach (Cai & White, 2009, 2010), and semi-analytical solutions have been presented, in some cases allowing for a variable diffusion coefficient in the solid phase (Santhanagopalan & White, 2008).

Other research has focused on model reformulation (Subramanian *et al.*, 2009; Ramadesigan *et al.*, 2010; Subramanian *et al.*, 2007; Northrop *et al.*, 2011; Subramanian *et al.*, 2004) or obtaining an impedance-based model through residue grouping (Smith *et al.*, 2008, 2007). These methods allow one to deduce a model that is simple enough for parameter (Boovaragavan *et al.*, 2008) or state-of-charge (SOC) (Smith *et al.*, 2010) estimation. A set of numerical eigenvalues for the PDEs of lithium transport is generated for a particular model and parameter set, but as the battery parameters change due to aging, such as reduced electrode porosity or loss of active material, it is difficult to interpret how the eigenvalues will respond. This limits the applicability of these methods for real-time, long term life estimation with moderate to severe levels of battery power or energy degradation.

Most of the above methods pose several limits in their application, as they either require *a priori* knowledge of the system inputs, or still involve the solution of nonlinear, coupled ODEs respectively. Furthermore, most applications of MOR methods to electrochemical models (for instance, see (Forman *et al.*, 2011), (Santhanagopalan *et al.*, 2006)) focus on simplifying the porous electrode PDEs for reducing the computational burden. In this sense, there is considerable interest today in the application of MOR techniques to extract extremely low-order battery cell models oriented to model-based control or estimation, particularly in relation with aging and life-cycle prediction.

Another potential option is to augment single particle models with a representation of the liquid phase diffusion dynamics. One approach is to account for relaxation gradients in the liquid phase by empirically fitting relaxation data to an ODE-based model (Schmidt *et al.*, 2010*a*) that resulted from a modal transform approach. This model has been used SOH estimation (Schmidt *et al.*, 2010*b*). However, the liquid phase model of (Schmidt

Table 4.1: Cell internal physical dimensions.

Parameter	Definition	Value
L_n	negative electrode thickness	$50 \times 10^{-6}\ m$
L_{sep}	separator thickness	$25 \times 10^{-6}\ m$
L_p	positive electrode thickness	$98 \times 10^{-6}\ m$
R_n	negative active particle radius	$3.5 \times 10^{-6}\ m$
R_p	positive active particle radius	$50 \times 10^{-9}\ m$
A	current collector area	$1.9 \times 10^{-1}\ m^2$

et al., 2010*a*) is still not parametric in the sense that it is not obtained from physically measurable parameters such as the salt diffusion coefficient, component porosities, or component thicknesses. The model presented in this chapter retains parametric dependence on physically measurable properties.

4.2 Experimental Setup

In this chapter, a cylindrical cell of diameter 26 mm and height of 65 mm (26650) is considered with nominal capacity of 2.3 Ah and nominal voltage of 3.3 V. The cell electrolyte is assumed to be 1.0 M LiPF_6 in a 1:1 mixture of EC:DMC, and the negative/positive electrode couple is Li_xC_6/Li_yFePO_4. The relevant internal geometric dimensions of the cell are summarized in Table 4.1. With the exception of the negative active particle radius, which is fixed to a typical literature value, each of these measurements were obtained from microscopy imaging techniques or basic measurements performed on a disassembled cell.

Data for model validation, including the cell terminal voltage, current, and temperature are recorded using a sample frequency of 10 Hz. Current demands are controlled at a frequency of 100 Hz using a Kepco load and Lambda supply with a Labview interface to

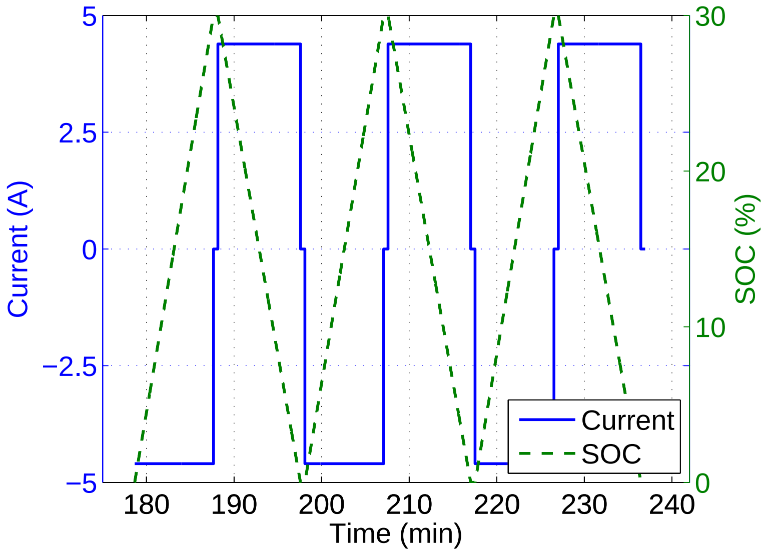

Figure 4.1: Current and SOC profile during aging campaign of cell cycled at 2C current between 0% and 30% SOC.

a standard PC. Thermoelectric temperature control is achieved using a Peltier junction that is in direct contact with the aluminum cell fixture.

The aging campaign uses a design-of-experiments to evaluate system-level capacity and power fade. The aging campaign conducted on the cells consists of charge/discharge cycling while controlling the cell surface temperature at $55°C$. This elevated temperature is chosen to accelerate the degradation process while ideally maintaining the same degradation mode as typical automotive operating conditions. Depth-of-discharge and current rate are varied using a full factorial DOE approach to investigate the effect of each factor on the performance degradation rate. State of charge information is obtained by post-processing the measured current throughput of the cell, and the duty cycle current is controlled to produce a triangular SOC waveform between selected maximum and minimum SOC values.

The SOC levels are 0–10 %, 0–20%, and 0–30%. The current rates used are 2C, 4C, and 8C. This gives 9 total experiments based on the possible permutations of these two factors. An example of the input current profile and the calculated SOC for the cell aged with 2C current and 0–30% SOC is plotted in Figure 4.1.

4.3 Model Development

Figure 4.2 provides a schematic description of the model considered in this study, showing the solid and liquid phase computation domains as well as the subscript $i = p$ or n to indicate the positive or negative electrode respectively. The proposed model structure stems from the single particle principle (Haran *et al.*, 1998), with the introduction of two novel extensions. First, a time-varying resistance that accounts for the resistive reactant nature of the Li_yFePO_4 electrode (Thomas-Alyea, 2008) is included. Second, the concentration overpotential from the liquid phase is modeled by applying the assumption of uniform intercalation current density to generate a solution for the liquid diffusion PDE. While the time-varying resistance is specific to systems with low solid phase electronic conductivity, the liquid phase model is applicable to all porous Li-ion electrodes.

The model description begins with the definition of the cell output voltage $V(t)$, which results from subtracting the overpotential arising from several electrochemical phenomena from the time-varying open circuit voltage (OCV)

$$\begin{aligned} V(t) =& (U_p(t) - U_n(t)) - (\phi_e(L_c, t) - \phi_e(0, t)) \\ & - (\eta_p(t) - \eta_n(t)) - (R_r(t) + R_c)\, I(t) - V_h(t) \end{aligned} \tag{4.1}$$

As discussed in (Roscher & Sauer, 2011), a significant path dependence of the OCV for both Li_yFePO_4 and Li_xC_6 has been observed, leading to hysteresis. Hysteresis refers to the behavior when the OCV at a specified SOC is different depending on the current

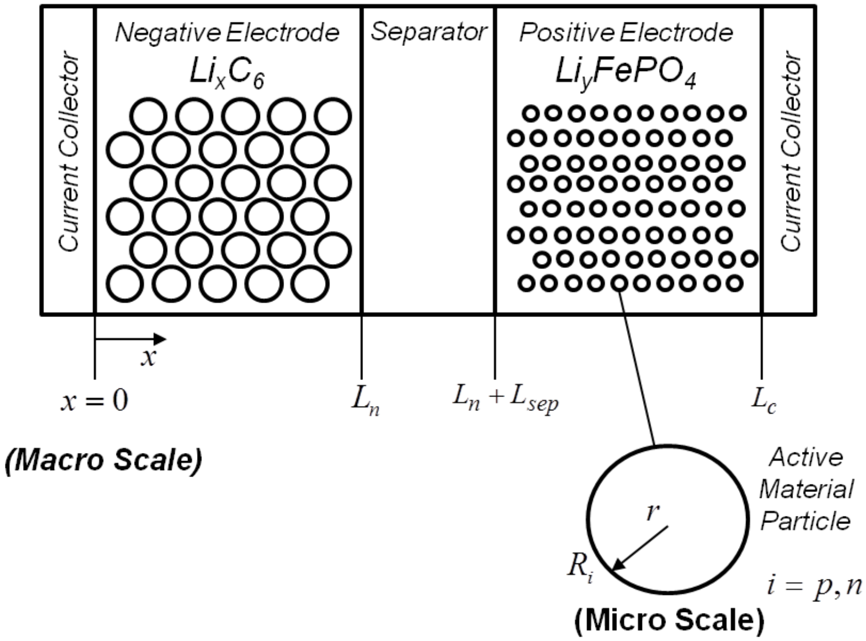

Figure 4.2: Schematic of unit cell idealized geometry with solid (r) and liquid (x) diffusion domains.

history used to reach that SOC. This phenomenon is modeled as a first order system with gain H and hysteresis transition factor Γ (Hu *et al.*, 2011)

$$\frac{dV_h}{dt} = |I|\Gamma(T)\left(H(T, SOC) - V_h\right) \tag{4.2}$$

The quantity V_h determines the deviation in the OCV at the specified SOC. Upon inspection, if the current is zero, the hysteresis voltage does not change. As explained in (Roscher & Sauer, 2011) there are actually some relaxation phenomena that may be a result of hysteresis that occur on the time scale of seconds following the interruption of current, but Eq. (4.2) models only the hysteresis effect that remains after large duration rest periods.

Deviations from the thermodynamic OCV when passing current may be attributed to ohmic, kinetic, and concentration overpotential, where each can occur in the solid or liquid phase. While the ohmic overpotential may be neglected in the negative electrode due to the high conductivity of Li_xC_6 (≈100 S/m), it is a significant loss in the positive electrode. Though the exact source of increasing ohmic resistance with respect to depth of discharge is unknown, a likely explanation is the Li_yFePO_4 electrode selectively charging or depleting the active material in an ohmically dominated fashion, such that the current density moves from areas with higher conductivity to lower.

Some authors have proposed that the current density moves through the electrode thickness from the current collector to the separator (Srinivasan & Newman, 2004b). Others have suggested that the local current density shifts from particles with low electronic contact resistance to the conductive carbon coating to those with higher contact resistance as low-resistance sites are depleted (Safari & Delacourt, 2011a). The same phenomena has also been interpreted as a current density that is non-uniform along the particle surface in the polar and asimuth coordinates, which in theory requires a three-dimensional solution though the authors retained the one-dimensional spherical model (Thomas-Alyea, 2008).

The first approach requires the solution of the fully coupled set of porous electrode PDEs. A particle size distribution is required for the second approach, which may add a prohibitive number of model states while also requiring an iterative procedure to solve. Each of these aspects are undesirable for control or estimation applications. To avoid these difficulties, the resistive reactant effect is conceptualized here as a pure integrator, causing an increasing resistance with respect to depth-of-discharge during a current pulse response

$$R_r(t) = \frac{R_p L_{cond}(t)}{3 L_p A \epsilon_p} \frac{1}{\sigma_p} \tag{4.3}$$

where R_p is the particle radius, L_p is positive electrode thickness, A is the current collector area, ϵ_p is the active material volume fraction, and σ_p is the electrical conductivity. The conduction length $L_{cond}(t)$ is computed by considering the path for current along a spherical active material particle. If current needed to travel along the entire half-circumference of an active material particle to reach the conductive matrix, then the total conduction length would be πR_p. Thus the actual conduction length increases in time at a rate proportional to the current according to

$$\frac{dL_{cond}}{dt} = \frac{\pi R_p |I|}{F c_{max,p} L_p A \epsilon_p} \tag{4.4}$$

where $c_{max,p}$ is the saturation concentration. The ohmic loss from this resistance is referred to as the resistive reactant or time-varying ohmic overpotential. It is added to a similar loss arising from the contact resistance R_c, also referred to as the initial ohmic overpotential, as shown in Eq. (4.1).

Concentration overpotential in the solid phase occurs due to the limited ability of lithium ions to diffuse through the active material. This phenomenon is modeled by solving the mass diffusion equation describing transport within a representative spherical particle of active material

$$\frac{\partial c_i}{\partial t} = \frac{D_i}{r^2} \frac{\partial}{\partial r} \left(r^2 \frac{\partial c_i}{\partial r} \right) \tag{4.5}$$

where c represents the concentration of lithium, and D is the diffusion coefficient. The imposed boundary conditions are:

$$\left. \frac{\partial c_i}{\partial r} \right|_{r=0} = 0 \quad , \quad D_i \left. \frac{\partial c_i}{\partial r} \right|_{r=R_i} = -\frac{j_i(t)}{F} \tag{4.6}$$

representing symmetry at the center of the particle and a prescribed flux at the particle surface. The surface value of lithium concentration, $c_i(R_i, t)$ governs many facets of the electrochemical behavior of the cell. For instance, concentration overpotential results from the variation between the mean concentration and the surface value.

The intercalation current density $j_i(x, t)$ has been assumed constant with respect to the direction x along the unit cell thickness

$$j_i(x, t) = j_i(t) = \frac{I(t)}{a_i A L_i} \tag{4.7}$$

where a_i is the surface area per unit volume defined as $3\epsilon_i/R_i$. The kinetic overpotential, η_i, is governed by the Butler-Volmer law. Inverting the Butler-Volmer law leads to the expression for the kinetic overpotential

$$\eta_i = \frac{\bar{R}T}{\alpha F} sinh^{-1}\left(\frac{j_i(t)}{2i_{0,i}}\right) \tag{4.8}$$

with the exchange current density $i_{0,i}$ defined as:

$$i_{0,i} = Fk_i\sqrt{c_i(R_i)c_{e,i}(c_{max,i} - c_i(R_i))} \tag{4.9}$$

Increased values of the kinetic rate constants k_i will lead to decreased kinetic overpotential. As the surface concentration c_i approaches the saturation value $c_{max,i}$, or tends to zero, the kinetic overpotential increases.

The liquid phase contains ohmic and concentration sources of overpotential according to the concentrated solution theory presented in Chapter 2. The governing equation of transport within the liquid is given by

$$\epsilon_e \frac{\partial c_e}{\partial t} = D_e \frac{\partial^2 c_e}{\partial x^2} + \frac{a_i\left(1 - t_0^+\right)}{F} j_i(t) \tag{4.10}$$

where ϵ_e is the liquid phase volume fraction and t_0^+ is the transference number. Based on the assumption introduced by Eq. (4.7), uniform intercalation current within each electrode, the intercalation current $j_i(t)$ is assumed as piecewise constant in the positive and negative electrode, and zero in the separator region. The imposed boundary conditions at each end of the unit cell are

$$\left.\frac{\partial c_e}{\partial x}\right|_{x=0,L_c} = 0 \tag{4.11}$$

Additionally, the ion flux and concentration must be matched at the boundaries between each domain

$$\begin{aligned}
&D_{e,n}\frac{\partial c_e}{\partial x}\bigg|_{x=L_n^-} = D_{e,sep}\frac{\partial c_e}{\partial x}\bigg|_{x=L_n^+}\\
&c_e\bigg|_{x=L_n^-} = c_e\bigg|_{x=L_n^+}\\
&D_{e,sep}\frac{\partial c_e}{\partial x}\bigg|_{x=((L_{sep}+L_n)^-)} = D_{e,p}\frac{\partial c_e}{\partial x}\bigg|_{x=((L_{sep}+L_n)^+)}\\
&c_e\bigg|_{x=((L_{sep}+L_n)^-)} = c_e\bigg|_{x=((L_{sep}+L_n)^+)}
\end{aligned} \tag{4.12}$$

The potential is dependent upon the concentration according to

$$\frac{\partial \phi_e}{\partial x} = -\frac{i_e(t)}{\kappa} + \frac{2\bar{R}T(1-t_0^+)}{F}(1+\beta)\frac{\partial ln(c_e)}{\partial x} \tag{4.13}$$

The activity coefficient β is treated as a tunable constant parameter, though in reality it depends nonlinearly on the lithium salt concentration. The current density in the liquid phase, i_e, is straightforward to determine by the uniform utilization assumption. The potential at $x = 0$ is set to zero since only potential differences are considered relevant when computing the cell voltage. Then Eq. (4.13) may be integrated directly to obtain the potential difference between $x = 0$ and $x = L_c$ after solving Eq. (4.10), since all terms are at minimum piecewise constant with respect to x.

The structure of the electrochemical model is summarized in Figure 4.3. The three diffusion PDEs predict the transfer of ionic species in the solid phase of the two electrodes and in the liquid phase. The predicted concentrations are then used to determine the half-cell open circuit potentials and the kinetic overpotentials, through a set of nonlinear algebraic equations.

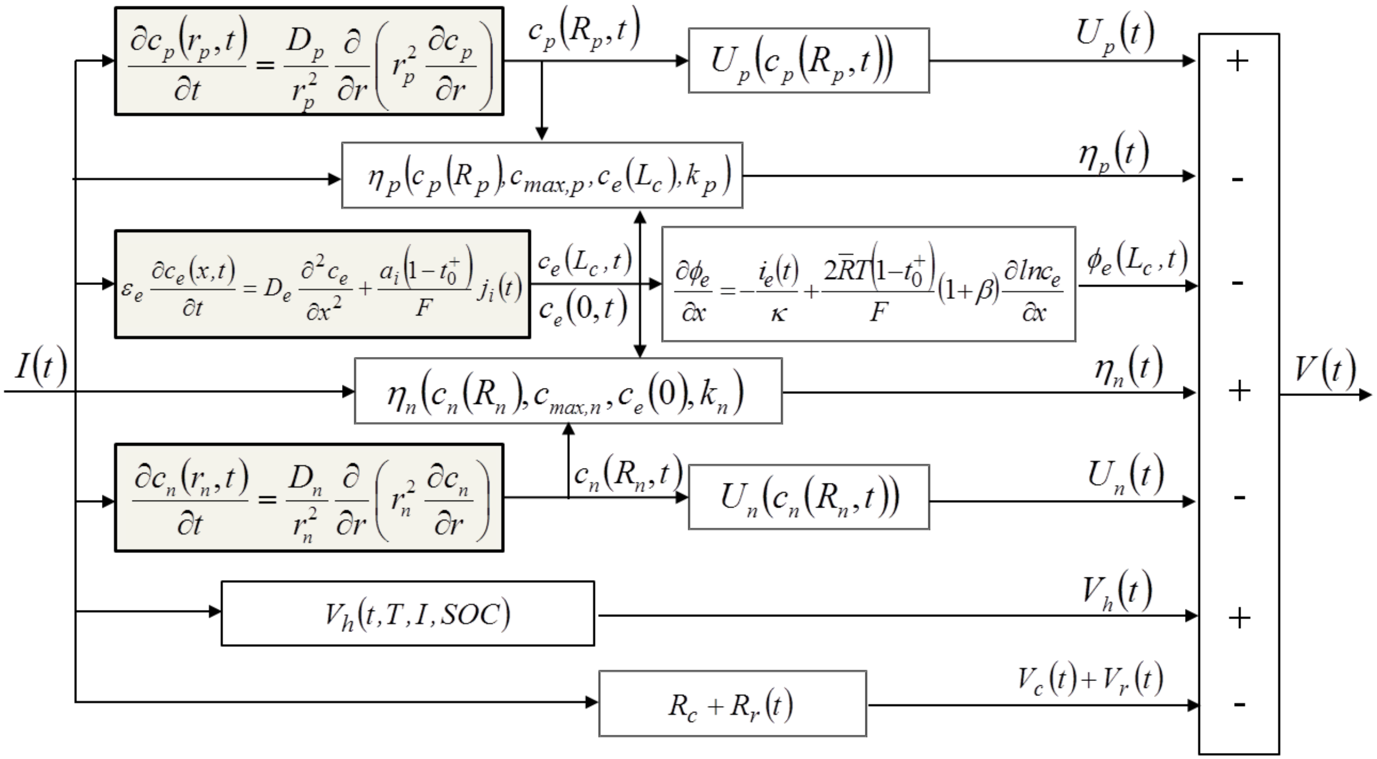

Figure 4.3: Block diagram representation of the PDE-based cell electrochemical model. Scaling factors that convert the external current input to a current density are not shown for simplicity.

As can be observed in the block diagram, the diffusion PDEs are decoupled due to the modeling assumptions introduced. Moreover, according to the inverted Butler-Volmer equation, Eq. (4.8), the kinetic overpotentials associated with charge transfer between the liquid and solid phase depend only on the concentration values at the interface, and not on the spatial distribution within the solid and liquid domains. This provides an opportunity for applying model-order reduction to obtain a computationally efficient solution.

4.4 Model Order Reduction

The Pade MOR technique discussed in Chapter 2 is now applied to Eqs. (4.5) and (4.10). The Pade approximation is a frequency-based, realization-preserving MOR method used to transform the solid and liquid diffusion PDEs into a reduced-order system of ODEs. This approach has the advantage of retaining the physical meaning of the coefficients in the reduced-order model. Though not strictly necessary for SOC estimation, it is beneficial for applications to real-time, model-based SOH estimation.

4.4.1 Approximation of the Solid Diffusion PDE

According to Eq. (4.5) the Lithium intercalation in the solid phase is described by a boundary value problem including a parabolic, constant coefficient PDE and two boundary conditions of the second kind. In the case of a constant current, both boundary conditions are steady and there is an analytical solution. In general though, one boundary condition is time-varying so an analytical solution can only be obtained by applying Duhamel's superposition integral (Doyle *et al.*, 1993; Ozisik, 2002). For estimation and control applications, a more efficient approach to obtain an approximate solution can be formulated by taking the Laplace transform (defined in Chapter 2) of Eqs. (4.5 - 4.6) (Muratori *et al.*, 2010*a*,*b*)

$$D_i \frac{d^2 C_i(s)}{dr^2} + \frac{2D_i}{r} \frac{dC_i(s)}{dr} - sC_i(s) = 0 \tag{4.14}$$

$$\left. \frac{\partial C_i(s)}{\partial r} \right|_{r=0} = 0 \quad , \quad D_i \left. \frac{\partial C_i(s)}{\partial r} \right|_{r=R_i} = -\frac{J_i(s)}{F} \tag{4.15}$$

where $s = -j\omega$ is the independent variable after executing the transform. Then introduce the substitution $W_i = C_i r$ and compute the corresponding derivatives

$$\frac{dW_i}{dr} = C_i + r\frac{dC_i}{dr} \tag{4.16}$$

$$\frac{d^2 W_i}{dr^2} = 2\frac{dC_i}{dr} + r\frac{d^2 C_i}{dr^2} \tag{4.17}$$

Dividing Eq. (4.17) by r and substituting into Eq. (4.14) gives

$$\left(\frac{d^2 W_i}{dr^2} - \frac{s}{D_i} W_i \right) = 0 \tag{4.18}$$

whose general solution is readily found as

$$W_i(r,s) = rC_i\left(r,s\right) = Aexp\left(r\sqrt{\frac{s}{D_i}} \right) + Bexp\left(-r\sqrt{\frac{s}{D_i}} \right) \tag{4.19}$$

The Lithium concentration at the surface of the particle is determined by inserting the boundary conditions defined by Eq. (4.15) into the general solution to determine the unknown coefficients A and B, and then calculating the solution at $r = R_i$. Based on this procedure, a transcendental transfer function is obtained, relating the solid phase surface concentration to the current density

$$\frac{C_i(s)}{J_i(s)} = \frac{\left(\frac{R_i^2}{3D_i^2 \epsilon_i F} \right) sinh\left(\sqrt{\frac{sR_i}{D_i}} \right)}{\sqrt{\frac{s}{D_i}} R_i cosh\left(\sqrt{\frac{s}{D_i}} R_i \right) - sinh\left(\sqrt{\frac{s}{D_i}} R_i \right)} \tag{4.20}$$

Following (Muratori *et al.*, 2010*a*,*b*; Forman *et al.*, 2011), Eq. (4.20) is related to a diffusion-based mass transport process; hence its behavior can be modeled as a low-pass filter. This facilitates the use of a Pade approximation method to obtained a linearized representation of the model

$$\frac{C_i(s)}{J_i(s)} \approx G_i(s) = \frac{m_{0,i} + m_{1,i} + m_{2,i} + ... + m_{N,i}}{s(b_{0,i} + ... + b_{N,i})} \tag{4.21}$$

The coefficients of Eq. (4.21) can be analytically obtained from the transcendental transfer function through moment matching (Antoulas, 2005; Forman *et al.*, 2011). This allows the approximated model to preserve its physical consistency, through the presence of parameters such as the solid diffusion coefficient and particle radius. The coefficients for orders one to three are documented in Table 4.3.

The frequency responses of the transcendental PDE solution and the Pade approximate transfer functions of various orders are compared in Figure 4.4. The behavior of the analytical solution is characteristic of an integrator at low frequencies, which is expected because it accumulates lithium according to the current being passed.

4.4.2 Approximation of the Liquid Diffusion PDE

According to Eq. (4.10) the Lithium transport in the electrolyte is described by a parabolic PDE with homogenous boundary conditions and a spatially piecewise constant, time-varying, source term. The Laplace transform of Eq. (4.10) is

$$sC_e(s) - D_e \frac{d^2 C_e(s)}{dx^2} - \gamma \frac{I(s)}{AL_i a_i} = 0 \tag{4.22}$$

where the substitutions $\gamma = \frac{a_i\left(1-t_0^+\right)}{F\epsilon_e}$ and $j_i = \frac{I}{AL_i a_i}$ have been made to simplify notation. The boundary conditions at the cathode and anode current collectors (Eq. (4.11)) and matching conditions at the internal boundaries of the cell (separator/anode and separator/cathode defined in Eq. (4.12)) are not repeated here because they do not change following the application of the Laplace transform. To simplify the calculation of the liquid

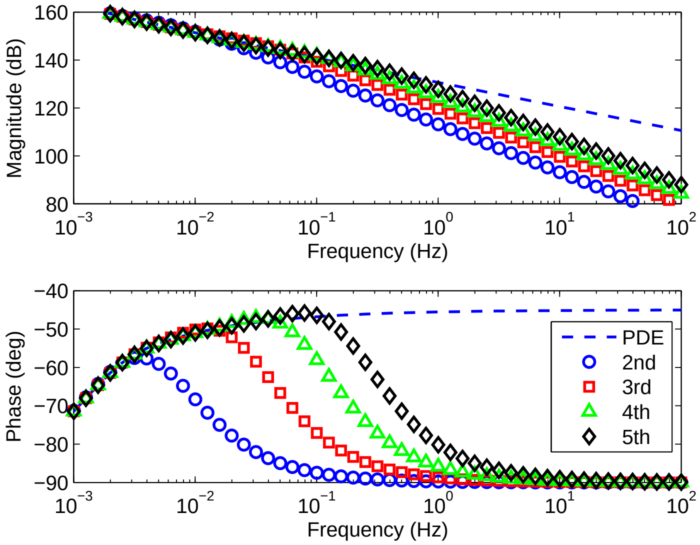

Figure 4.4: Frequency response of surface concentration, $c(R, s)$, predicted by Eq. (4.20) for the solid diffusion PDE, and Pade approximations of various truncation order.

phase transfer functions, we note that for the given cell geometry $L_n \approx \frac{1}{4}L_c$, $L_{sep} \approx \frac{3}{20}L_c$, $L_p \approx \frac{3}{5}L_c$. Then, following the computation of the analytical solution of Eq. (4.22), the transfer function for the negative electrode is found by evaluating at $x = 0$

$$\begin{aligned}\frac{C_e(s)}{\gamma I(s)} =& \frac{-12sinh\left(\frac{7}{20}\sqrt{\frac{s}{D_e}}L_c\right) - 5sinh\left(\sqrt{\frac{s}{D_e}}L_c\right)}{3sAL_csinh\left(\frac{7}{5}\sqrt{\frac{s}{D_e}}L_c\right)sinh\left(\frac{3}{5}\sqrt{\frac{s}{D_e}}L_c\right)} \\ &+ \frac{12sinh\left(\frac{3}{5}\sqrt{\frac{s}{D_e}}L_c\right) - 5sinh\left(\frac{1}{5}\sqrt{\frac{s}{D_e}}L_c\right)}{3sAL_csinh\left(\frac{7}{5}\sqrt{\frac{s}{D_e}}L_c\right)sinh\left(\frac{3}{5}\sqrt{\frac{s}{D_e}}L_c\right)} \\ &+ \frac{12sinh\left(\frac{7}{5}\sqrt{\frac{s}{D_e}}L_c\right) - 12sinh\left(\frac{23}{20}\sqrt{\frac{s}{D_e}}L_c\right)}{3sAL_csinh\left(\frac{7}{5}\sqrt{\frac{s}{D_e}}L_c\right)sinh\left(\frac{3}{5}\sqrt{\frac{s}{D_e}}L_c\right)}\end{aligned} \tag{4.23}$$

Similarly, the transfer function representing the effects of the liquid diffusion dynamics on the ion concentration at the positive electrode boundary ($x = L_c$) is given by:

$$\begin{aligned}\frac{C_e(s)}{\gamma I(s)} =& \frac{12sinh\left(\frac{1}{4}\sqrt{\frac{s}{D_e}}L_c\right) + 5sinh\left(\frac{2}{5}\sqrt{\frac{s}{D_e}}L_c\right)}{3sAL_csinh\left(\sqrt{\frac{s}{D_e}}L_c\right)} \\ &- \frac{5sinh\left(\sqrt{\frac{s}{D_e}}L_c\right)}{3sAL_csinh\left(\sqrt{\frac{s}{D_e}}L_c\right)}\end{aligned} \tag{4.24}$$

Following the same moment matching procedure discussed for the solid phase diffusion problem, a Pade approximant can be found to obtain a linear model expressing the concentration of lithium ions in the electrolyte at the current collector interface of the two electrodes, as functions of the current densities.

The frequency responses of the transcendental PDE solution and the corresponding Pade approximations are compared in Figures 4.5 and 4.6. The diffusion dynamics in the liquid phase exhibit behavior that is characteristic of a low-pass filter. The integrator behavior of the solid phase is not observed for the liquid phase, since there is no net change in the amount of lithium held in the liquid by the assumption of electroneutrality. The Pade approximate transfer functions provide better agreement for the liquid phase diffusion than for the solid up to a frequency of 10 Hz. It is not clear why the agreement is better for the liquid than for the solid, for equal approximation order, but possible reasons can be identified. First, the boundary conditions for each problem are different, and the liquid phase includes a source/sink term while the solid does not. Second, the time constant associated with transport in the solid is less than that of the liquid.

Table 4.3 summarizes the transfer functions for the liquid phase for approximations up to the third order. Again, the coefficients of the transfer functions are based on the physical parameters of the unit cell model, such as the geometry, porosity, and diffusion coefficients,

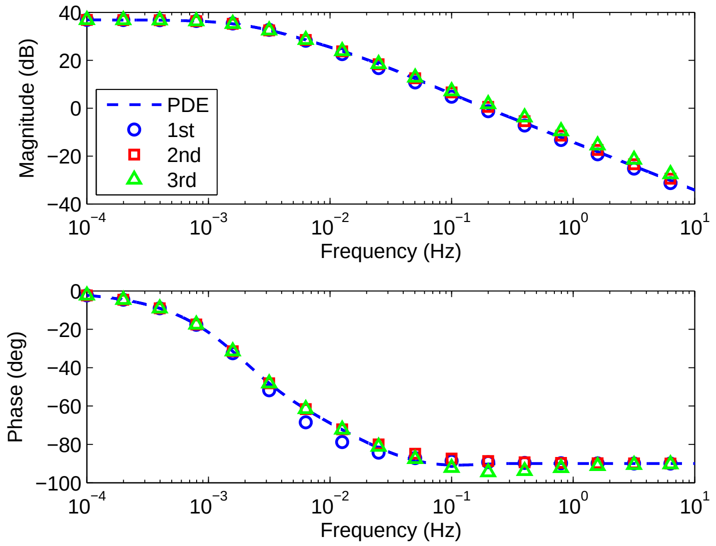

Figure 4.5: Frequency response of liquid diffusion PDE for $x = 0$ predicted by Eq. (4.23) and Pade approximations at various orders of truncation.

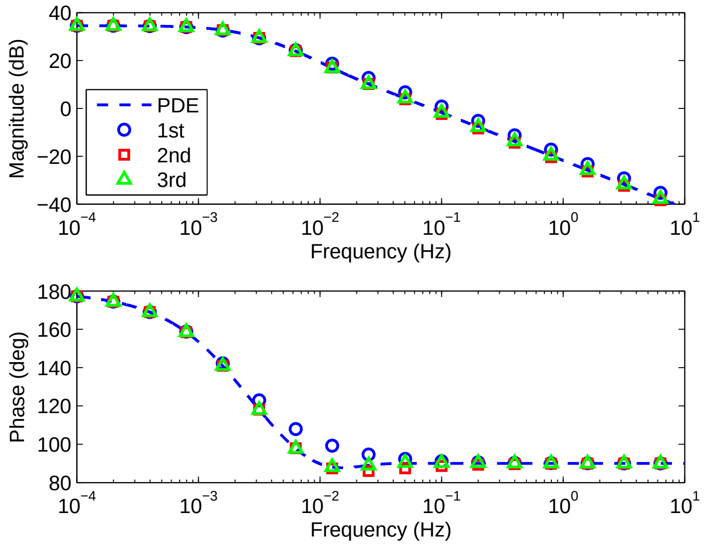

Figure 4.6: Frequency response of liquid diffusion PDE for $x = L_c$ predicted by Eq. (4.24) and Pade approximations at various orders of truncation.

and any numerical coefficients should remain constant throughout the battery's service life. For instance, a numerical substitution was used based on the relative thicknesses of the negative electrode, separator, and positive electrode, but the component thicknesses are not expected to change during aging.

Table 4.2: Pade approximate transfer functions (up to third order) for the solid diffusion dynamics.

Order	Solid
1st	$\frac{3}{sR_i}$
2nd	$\frac{\frac{3}{R_i}+\frac{2}{7}\frac{R_i}{D_i}s}{s\left(1+\frac{1}{35}\frac{R_i^2}{D_i}s\right)}$
3rd	$\frac{\frac{3}{R_i}+\frac{4}{11}\frac{R_i}{D_i}s+\frac{1}{165}\frac{R_i^3}{D_i^2}s^2}{s\left(1+\frac{3}{55}\frac{R_i^2}{D_i}s+\frac{1}{3465}\frac{R_i^4}{D_i^2}s^2\right)}$

Table 4.3: Pade approximate transfer functions (up to third order) for the liquid diffusion dynamics.

Order	Liquid, $x = L_c$	Liquid, $x = 0$
1st	$\frac{0.25\frac{L_c}{D_e}}{AF\left(1+0.112\frac{L_c^2}{D_e}s\right)}$	$\frac{0.33\frac{L_c}{D_e}}{AF\left(1+0.092\frac{L_c^2}{D_e}s\right)}$
2nd	$\frac{0.25\frac{L_c}{D_e}+0.0045\frac{L_c^3}{D_e^2}s}{AF\left(1+0.13\frac{L_c^2}{D_e}s+0.0029\frac{L_c^4}{D_e^2}s^2\right)}$	$\frac{0.33\frac{L_c}{D_e}+0.012\frac{L_c^3}{D_e^2}s}{AF\left(1+0.13\frac{L_c^2}{D_e}s+0.0029\frac{L_c^4}{D_e^2}s^2\right)}$
3rd	$\frac{0.25\frac{L_c}{D_e}+0.0065\frac{L_c^3}{D_e^2}s+4.9\times10^{-5}\frac{L_c^5}{D_e^3}s^2}{AF\left(1+0.14\frac{L_c^2}{D_e}s+0.0040\frac{L_c^4}{D_e^2}s^2+2.9\times10^{-5}\frac{L_c^5}{D_e^3}s^3\right)}$	$\frac{0.33\frac{L_c}{D_e}+0.011\frac{L_c^3}{D_e^2}s-1.5\times10^{-5}\frac{L_c^5}{D_e^3}s^2}{AF\left(1+0.13\frac{L_c^2}{D_e}s+0.0024\frac{L_c^4}{D_e^2}s^2-2.8\times10^{-6}\frac{L_c^5}{D_e^3}s^3\right)}$

4.4.3 Selection of the Model Order

The appropriate order of each transfer function can be decided based on the frequency content of the current input and by setting a trade-off between the number of states and the ability of the model to capture the frequency response of the PDE-based model. Based on

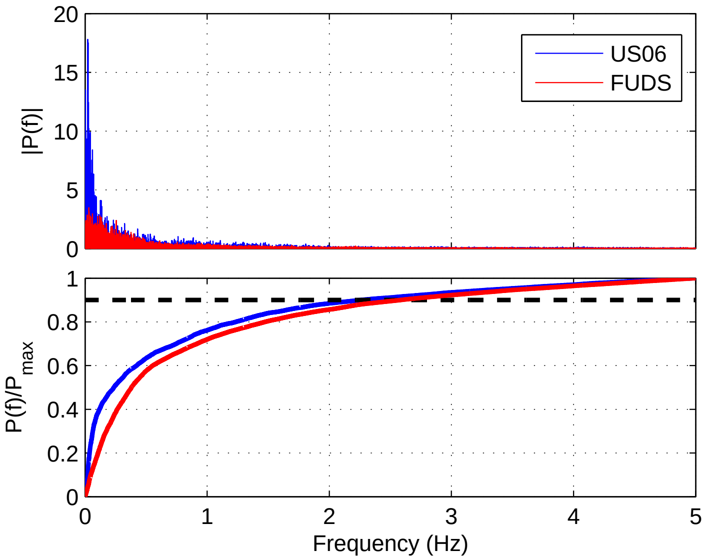

Figure 4.7: Frequency content of battery current profile for charge sustaining HEV on regulatory driving cycles.

the results shown in Figures 4.4-4.6, the approximate transfer functions present increasing error with respect to the analytical solution as the frequency content of the input signal increases. This conclusion is drawn from the divergence of the approximate transfer functions from the analytical solution with increasing frequency. In order to ascertain the highest desired frequency where accuracy should be maintained, and therefore the approximation order, a typical current profile must be obtained from the application of interest.

To this extent, Figure 4.7 shows the frequency distribution of the battery current profile obtained from a fast Fourier transform. The current profile is obtained from experimental testing on a prototype series-parallel HEV (Di Filippi *et al.*, 2010) with respect to two regulatory driving cycles, namely the US06 highway cycle and the Federal Urban Dynamometer Schedule (FUDS). By integrating the frequency spectrum, a measure of the power contained within the signal up to a given frequency is computed. The two cases presented are quite similar, in that 90% of the signal power is within frequencies less than 2.5 Hz as indicated by the dashed line. Using this information and examining the results of the Pade approximations in Figures 4.4, 4.5, and 4.6, it is possible to determine an optimal order of truncation for each transfer function. Specifically, a first order truncation is chosen to model the liquid diffusion dynamics and a third order truncation is chosen for the solid diffusion dynamics.

The resulting reduced-order model is shown in Figure 4.8, in block diagram form. The current input, converted to current density, feeds the reduced transfer functions calculating the boundary concentration dynamics within the solid and liquid phases. The outputs are then used to determine the concentration-dependent open-circuit potentials and charge transfer overpotentials, through nonlinear algebraic functions.

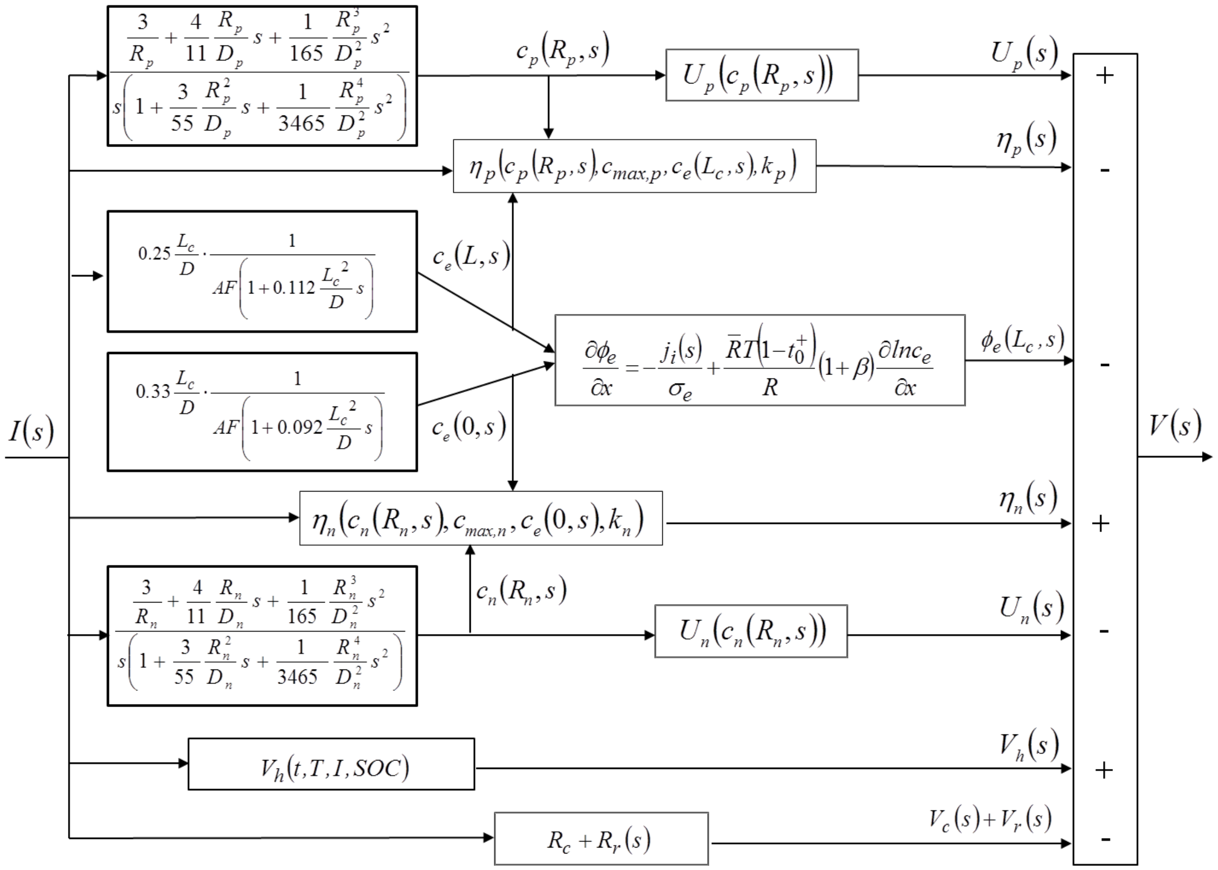

Figure 4.8: Block diagram representation of the reduced cell electrochemical model. Scaling factors that convert the external current input to a current density are not shown for simplicity.

Note that the procedure above described can be easily extended to other current profiles for electrified vehicles, based on regulatory cycles or fleet data, and that the two federal cycles considered here are only exemplary cases.

4.5 Model Parametrization Analysis

This section illustrates the procedure for defining the model parameters, based on nonlinear identification techniques. Rather than fitting all parameters purely through optimization methods, an attempt is here made to carefully exercise the system with select experimental inputs so as to limit the number of parameters that influence the output voltage, then identify that subset of parameters from experimental data. This approach has the advantage of providing a trade-off between two prevalent approaches, namely pure nonlinear identification from cell-level performance data and extensive experimental characterization using half-cell testing. Though more intuition regarding the electrochemical dynamics of the system is required as compared to a numerical approach, the procedure still relies mostly on cell-level performance data with the exception of utilizing half-cell OCV curves.

First the active volume fractions and composition ranges of the positive and negative electrodes are estimated from cell OCV data. During this process, the maximum hysteresis voltage is characterized as a function of temperature and SOC. Next, resistance parameters are estimated from cycling data over a wide range of temperatures. Lastly, the diffusion parameters are identified through a combination of literature sources and tuning to match experimental voltage relaxation data. The capacity utilization from multi-rate capacity tests are combined with an inverse model to compute the negative electrode diffusion coefficient, and current pulses are used to modify the liquid phase diffusion and activity coefficients after selecting values from literature as a useful starting point.

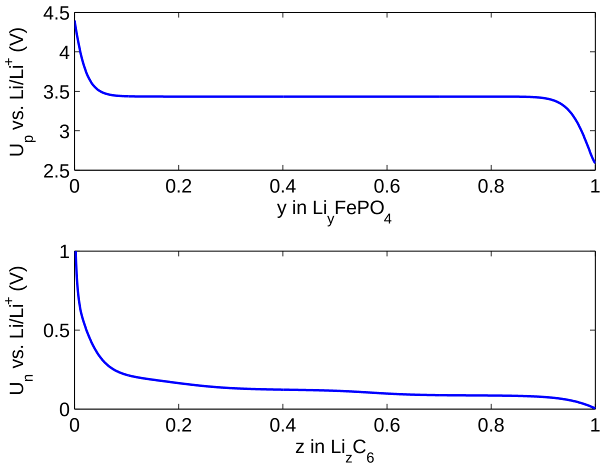

Figure 4.9: Open-circuit voltage curves for positive and negative electrode.

4.5.1 Identification of Capacity-Related Parameters

The OCV for the cell model can be found starting from the OCV curves relative to Li/Li^+ for the positive and negative electrodes, obtained experimentally from half-cell testing or from literature. In detail, the functional form of the positive OCV (Safari & Delacourt, 2011*b*) is

$$\begin{aligned} U_p(y) =& 3.432 - 0.843e^{-80.249(1-y)^{1.319}} - 3.247 \times 10^{-6}e^{20.264(1-y)^{3.800}} + \\ & 3.2482 \times 10^{-6}e^{20.264(1-y)^{3.799}} \end{aligned} \tag{4.25}$$

Similarly, the functional form of the negative OCV (Safari & Delacourt, 2011*b*) is

$$\begin{aligned} U_n(x) =& 0.638 + 0.542e^{-305.5309x} + 0.044tanh\left(-\frac{x-0.196}{0.109}\right) - \\ & 0.198tanh\left(\frac{x-1.057}{0.085}\right) - 0.686tanh\left(\frac{x+0.012}{0.053}\right) - \\ & 0.018tanh\left(\frac{x-0.569}{0.086}\right) \end{aligned} \tag{4.26}$$

Figure 4.9 shows the OCV curves for the positive and negative electrode. While the OCV of each electrode is known, the composition range determined by the initial degree of lithiation and the active volume fraction of each electrode must still be identified using full-cell OCV data. To this extent, an experimental procedure was conducted where the cell is first discharged to the manufacturer-recommended lower voltage limit of 2.0 V. Then a charge current pulse is executed to add 5-10$\%$ capacity to the cell, followed by a wait period of 1 hour to allow the cell to reach equilibrium. The cell voltage after 1 hour is recorded as the OCV for the appropriate SOC based on current integration. This procedure is repeated until the manufacturer-recommended upper voltage limit of 3.6 V is reached. The voltage data collected during this procedure is plotted in Figure 4.10 as 'Experimental Charge'. Then, the current direction is reversed and the entire process is repeated, with the voltage data plotted as 'Experimental Disharge'. The difference between these data at each SOC is used to assess the amount of hysteresis associated with the cell OCV.

The following procedure allows the identification of the model parameters related to the scaling and initial conditions of the half cell potentials while eliminating the influence of the any overpotential on the output voltage. The mean of the charge and discharge OCV data is the input to a nonlinear least square procedure to perform the estimation of the electrode composition ranges. The algorithm consists of finding the optimal set of parameters $\vec{P}^* = [x_0^*, y_0^*, \epsilon_n^*, \epsilon_p^*]$ minimizing the cost function in Eq. (4.27), where the error $\vec{e}$ is a vector of differences between the experimental OCV data and the predicted OCV ($\vec{e}(SOC) = V_{exp}(SOC) - V(SOC)$). The nonlinear least square problem is cast as follows:

$$\vec{P}^* = \underset{[x_0^*, y_0^*, \epsilon_n^*, \epsilon_p^*]}{\text{argmin}} \left(\frac{1}{2} (\Delta \vec{P})^T \frac{\partial^2 \vec{e}}{\partial \vec{P}^2} (\Delta \vec{P}) + (\Delta \vec{P})^T \frac{\partial \vec{e}}{\partial \vec{P}} \right) \tag{4.27}$$

The trust region reflective algorithm (Coleman & Li, 1994; Shi *et al.*, 2009) is used to solve Eq. (4.27). The fitted model OCV resulting from the solution of Eq. (4.27) is plotted in Figure 4.10. The maximum hysteresis voltage, plotted in the lower subplot of Figure

Table 4.4: Summary of hysteresis parameters as a function of temperature.

Temperature	h_1	h_2
5°C	-2.4×10^{-4}	6.02×10^{-2}
20°C	-4.0×10^{-4}	5.09×10^{-2}
55°C	-3.0×10^{-4}	3.95×10^{-2}

4.10, is calculated as one half the difference between the charge and discharge OCV data at each SOC. After observing the trend of the experimental data, it is fit with a linear function,

$$H(T, SOC) = h_1(T) \times SOC + h_2(T) \tag{4.28}$$

where h_1 and h_2 are identified for various temperatures to create a one-dimensional interpolation table. The resulting linear fit for the 20°C case is also plotted in Figure 4.10. There are cyclic variations from the overall linear trend that are believed to arise from experimental error associated with the current integration procedure, preventing the selection of exactly the same SOC set point when approaching from charge and discharge directions. Since these are believed to be associated with experimental error and not an actual electrochemical feature, the linear fit of maximum hysteresis voltage is considered sufficient. Other temperatures showed qualitatively similar agreement with the linear function, as the hysteresis calculation is repeated for the 5°C, and 55°C data, and a linear fit of maximum hysteresis with respect to SOC is calculated for each temperature. The fitting parameters are summarized in Table 4.4.

It is assumed that the half-cell OCV and composition ranges do not vary over the temperature range from 5°C to 55°C. Verification of this assumption is possible using extensive

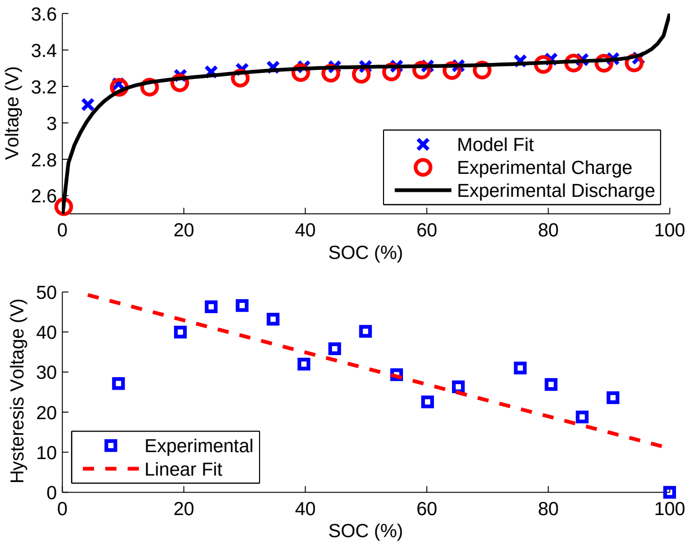

Figure 4.10: a) Experimental OCV data and model fitted to mean of charge and discharge data, where measurements taken while traversing the SOC range from 0% towards 100% are indicated as 'Experimental Charge', and those from 100% towards 0% are denoted 'Experimental Discharge'. b) Hysteresis voltage and linear fit with respect to SOC.

half-cell fabrication and testing at multiple temperatures. However, this is considered outside the scope of this paper and model agreement is acceptable without modifying the OCV or estimated composition range to consider temperature dependence within the presented range.

4.5.2 Identification of Resistance-Related Parameters

The objective of this section is to identify the temperature dependence of the parameters responsible for determining the time-varying cell resistance, including the ohmic factor R_c, the kinetic rate constants of each electrode (k_i of Eq. (4.9)), the activity coefficient of the liquid (β of Eq. (4.13)), and the diffusion coefficients, D, in each phase.

Initial Overpotential

As a current input is introduced, both ohmic and kinetic resistance contribute in determining the initial overpotential, R_0, as defined in Chapter 1, but here called R. In general it is difficult to determine each electrode rate constant and the remaining ohmic resistance without half-cell testing or literature data. Here, a method is proposed that takes advantage of the nonlinearity associated with the kinetic overpotential (Juang *et al.*, 2011) to distinguish between ohmic and kinetic resistance. This nonlinearity, when combined with careful assumptions and experimental data for a range of temperature conditions, allows one to individually identify the temperature dependence of the rate constants for each electrode and the remaining ohmic component of resistance.

For this procedure, it is assumed that the kinetic overpotential of each electrode is negligible above a certain reference temperature. This assumption takes advantage of the strong variation of the exchange current with respect to temperature that most Li-ion chemistries exhibit. Experimentally, a variation of resistance with respect to current is observed at low temperature conditions, which is assumed to be directly related to the exchange current density via the kinetic rate constant.

For the negative electrode, a reference temperature of $20°\text{C}$ is assumed, since typically the negative electrode does not contribute significantly to the cell overpotential at room temperature (Bernardi & Go, 2011). For the positive electrode the reference temperature is selected as $55°\text{C}$, and though this choice is arbitrary it reflects two key considerations. First, the kinetic overpotential of the positive electrode is non-negligible at room temperature. Second, there should be a limiting temperature where kinetic overpotential from the positive electrode is no longer a factor. An Arrhenius temperature dependence is assumed of the form

$$P = P_1 exp\left(-\left(\frac{P_2}{T} - \frac{P_2}{T_{ref}}\right)^{P_3}\right) \tag{4.29}$$

where P_1 fixes the parameter value at the reference temperature, P_2 is the activation energy that governs the temperature dependence of each parameter, and P_3 is a unitless number that is useful in obtaining agreement with experimental data in non-ideal cases. Since there has been supporting data in literature (Smart *et al.*, 2007) for a unity value of P_3 as applied to the temperature dependence of kinetic rate constants, we fix $P_3 = 1$ for both the positive and negative rate constants. However, commonly used positive electrode active materials have displayed similar electronic conductivity properties to semiconductors (Park *et al.*, 2010). Taking $P_3 \neq 1$ is useful in situations where there may be a range of activation energies for a given process, such as those associated with semiconductor-like behavior such as ion-hopping (Leon *et al.*, 1997). The ohmic fit accounts at least partially for the active material conductivity, so the ohmic fitting procedure allows for $P_3 \neq 1$. The functional form of Eq. (4.29) is also used to describe the temperature dependence of the diffusion and activity coefficients discussed in later sections.

The conducted experiments gathered resistance data for temperatures of -10, 5, 20, 35, and 55°C. For each temperature, currents from 1C to 10C are tested, except at -10°C, where current is limited to 5C due to power limitations at cold temperatures. To begin, the positive electrode characteristics are isolated by using data from each temperature above 20°C. The variation in resistance with respect to current is computed using Eq. 4.30

$$\Delta\left(R\right) = R|_{10C} - R|_{1C} = \frac{1}{I|_{10C}}\frac{\bar{R}T}{F}sinh^{-1}\left(\frac{j_p|_{10C}}{2i_{0,p}}\right) - \frac{1}{I|_{1C}}\frac{\bar{R}T}{F}sinh^{-1}\left(\frac{j_p|_{1C}}{2i_{0,p}}\right) \tag{4.30}$$

Note that the contact resistance and ohmic contributions from the liquid phase are not included. This is because they do not change with respect to current, and so they do not impact Eq. (4.30). All parameters in Eq. (4.30) are fixed except for the exchange current density, or equivalently the rate constant. Various values of the rate constant may be selected to effectively vary the exchange current density and produce different values of $\Delta\left(R\right)$. After matching the experimental $\Delta\left(R\right)$ for temperatures above 20°C, where the negative electrode kinetic overpotential is neglected, a positive electrode rate constant associated with each tested temperature is found. The resulting data are fit using Eq. (4.29) to provide a smooth interpolation and extrapolation function.

For temperatures below 20°C, the positive temperature dependence identified for temperatures above 20°C is extrapolated and included in the total overpotential. Then the variation of resistance with respect to current is fit using the negative rate constant, using a similar procedure to the positive electrode with Eq. 4.31 replacing Eq. (4.30).

$$\begin{aligned}
&\Delta\left(R\right) = R|_{10C} - R|_{1C} = \\
&\frac{1}{I|_{10C}}\left(\frac{\bar{R}T}{F}sinh^{-1}\left(\frac{j_p|_{10C}}{2i_{0,p}}\right) + \frac{\bar{R}T}{F}sinh^{-1}\left(\frac{j_n|_{10C}}{2i_{0,n}}\right)\right) - \\
&\frac{1}{I|_{1C}}\left(\frac{\bar{R}T}{F}sinh^{-1}\left(\frac{j_p|_{1C}}{2i_{0,p}}\right) + \frac{\bar{R}T}{F}sinh^{-1}\left(\frac{j_n|_{1C}}{2i_{0,n}}\right)\right)
\end{aligned} \tag{4.31}$$

The plots of resistance variation versus rate constant value for each electrode are plotted in Figure 4.11. The variation in resistance observed experimentally at each temperature is plotted as a dashed horizonatl line. The variation in resistance as a function of the rate constant is plotted as a solid line, with the positive electrode indicated on the left vertical axis and the negative electrode indicated on the right vertical axis. The three intersection points for each electrode are used to define the parameters P_1 and P_2 of Eq. (4.29), where $P = k_p$ or k_n.

Due to the superior surface area per unit volume of the iron phosphate positive electrode, the rate constant values are generally smaller than those of the negative electrode to

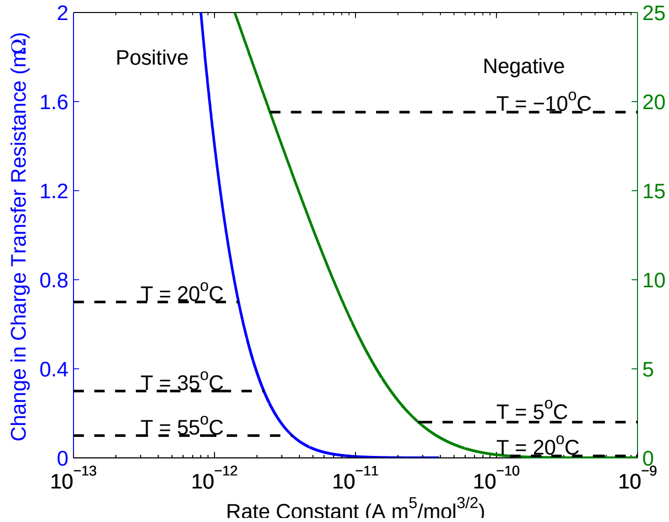

Figure 4.11: Variation of the resistance between 1C and 10C current pulses versus the required rate constant to achieve the resistance variation. Dashed lines indicate the experimentally observed level of variation at each temperature and intersect the electrode to which the variation is attributed.

achieve a similar level of resistance variation. Once the rate constant identification procedure has been completed, the kinetic component of the cell resistance is known. The temperature dependence of the ohmic resistance must account for the remaining portion of the resistance data. Here, a nonlinear least-squares problem is formulated to find the optimal parameter set for the ohmic resistance, $\vec{P}^* = [R_{c,1}, R_{c,2}, R_{c,3}]$, as

$$\vec{P}^* = \underset{[R_{c,1},R_{c,2},R_{c,3}]}{\text{argmin}} \left(R_{exp}(I,T) - R_{c,1} exp\left(-\left(\frac{R_{c,2}}{T_{ref,R_c}} - \frac{R_{c,2}}{T} \right)^{R_{c,3}} \right) - \frac{1}{I}\frac{\bar{R}T}{F} sinh^{-1}\left(\frac{I}{2i_{0,p}} \right) - \frac{1}{I}\frac{\bar{R}T}{F} sinh^{-1}\left(\frac{I}{2i_{0,n}} \right) - \left(\phi_e(L_c,0^+) - \phi_e(0,0^+) \right) \right) \tag{4.32}$$

The liquid phase ohmic contributions, represented by $(\phi_e(L_c,0^+) - \phi_e(0,0^+))$, are computed from the ohmic term of Eq. (4.13) with the notation of $t = 0^+$ indicating the result

Table 4.5: Arrhenius coefficients of parameters that vary with respect to cell temperature.

Parameter	R_1	R_2	R_3	T_{ref}
R_c	8.24 $\times 10^{-3}$	1740	1.96	328
σ_p	7.6 $\times 10^{-7}$	1740	1.96	328
k_n	1.8 $\times 10^{-6}$	7120	1.00	268
k_p	2.9 $\times 10^{-7}$	1860	1.00	328
D_n	1.9 $\times 10^{-14}$	2050	1.00	293
D_e	3.6$\times 10^{-11}$	10000	0.50	262
β	2.35	140	0.30	338

is taken immediately following the onset of current. Concentration overpotential is irrelevant since the instantaneous resistance is being considered. The conductivity properties as a function of temperature are taken directly from (Valoen & Reimers, 2005). The rest of the parameters have been identified by the preceding analyses leaving $R_{c,1}$, $R_{c,2}$, and $R_{c,3}$ for identification. Figure 4.12 shows the final comparison between experimental resistance recorded for each temperature and the model fit. The identification procedure reveals that the stretched exponential coefficient is non-zero for the contact resistance. This is required to achieve agreement with the data after identifying the Arrhenius dependence of the rate constants and has occasionally been observed for the electronic conductivity of Li-based systems (Rivera *et al.*, 2003). The variation of resistance with respect to current is captured well even for the most severe case at -10°C, where the total variation is over 20 $m\Omega$. Table 4.5 summarizes the Arrhenius coefficients for each parameter that exhibits temperature dependence.

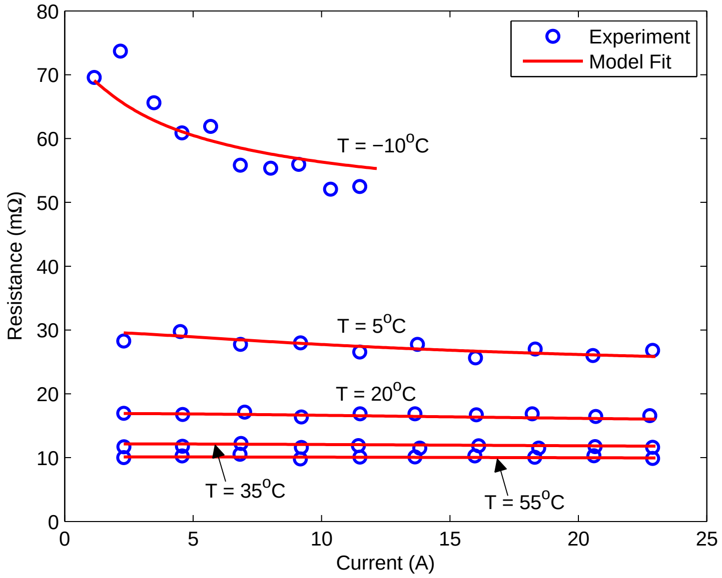

Figure 4.12: Comparison of experimental resistance data with fitted model prediction.

Time-Varying Ohmic Overpotential

As discussed during the model development of this chapter, there are increasing ohmic contributions during a charge or discharge current pulse related to the poor electronic conductivity of iron phosphate. The conductivity of the positive electrode is identified empirically, since the electrode is composed of several constituents (active material, binder, carbon) of vastly different properties making it difficult to predict without experimental data. To perform the fitting procedure, the identified capacity and intial resistance parameters are used to model a low-rate ($\leq$ 1C) galvanostatic discharge. The iron phosphate conductivity is considered constant with respect to SOC, since it has been reported previously that it does not change with composition (Chung *et al.*, 2002).

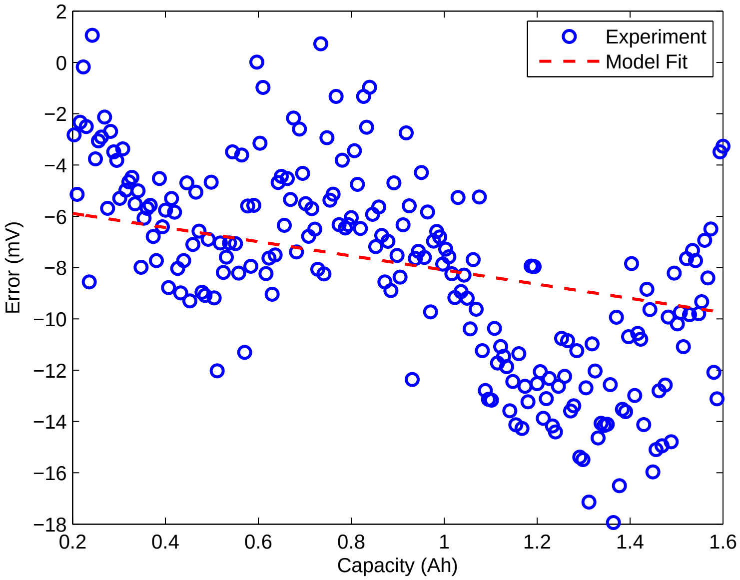

Figure 4.13: Error as a function of capacity removed during a galvanostatic discharge and model prediction of resistive reactant overpotential after identification of positive electrode conductivity.

The region for parameter identification is restricted to 0.2 to 1.6 Ah, because this region of the discharge curve is less prone to transient errors from the effects of slightly imperfect initial conditions that may cause large errors in predicted voltage at the beginning and end of the discharge process. The error between the model prediction and experimental data tends to increase linearly for a fixed current value as charge is removed from the cell. It may be fit by solving the linear least squares problem

$$V_r(t) = V_{r,0} + \frac{R_p L_{cond}(t)}{3 L_p A \epsilon_p} \frac{I}{\sigma_p} t \tag{4.33}$$

Here V_r is the overpotential error and $V_{r,0}$ is the initial unmodeled overpotential (the value at $Q = 0.2\ Ah$). When solving the least squares problem, $V_r(t)$ is a vector of values corresponding to the difference between the experimental data and model predicted voltage.

The constant term $V_{r,0}$ is subtracted from the vector $V_r(t)$ to form a vector $\tilde{V}_r(t)$, and t is a vector of time values corresponding to $\tilde{V}_r(t)$. The solution to the least squares problem is given by

$$\sigma_p = \left(\tilde{V}_r(t)(M)^T(M(M)^T)^{-1}\right)^{-1} \tag{4.34}$$

where $M = \frac{R_p^2 It}{3Fc_{max,p}(L_p A\epsilon_p)^2}$. Inserting values for the known constants gives $\sigma_p = 7.6 \times 10^{-7}\ S/m$, which is within the range of values reported in literature (Bewlay *et al.*, 2004) given that the exact amount of conductive carbon additive is unknown.

Figure 4.13 shows the error as a function of discharge capacity and the model fit to the error used to select a conductivity value. Although the identification procedure is performed only for 20°C, it is assumed that this conductivity value shares the same temperature dependence as the initial ohmic resistance, since theoretically these phenomena are related.

4.5.3 Diffusion Parameters

The solid diffusion coefficient of the negative electrode is tuned to match the experimentally observed difference in capacity between the C/3 and 1C rates, after fixing the particle size to a typical literature value. This may be approached quantitatively through the use of an inverse function, where the analytical solution of Eq. (4.5) for a constant current is related to the potential of the negative electrode at the end of discharge to ascertain the end-of-discharge Li^+ concentration, and therefore the diffusion coefficient. Following a procedure similar to the one presented in Chapter 2 for the analytical solution of Eq. (2.74), the analytical solution for the non-homogeneous, steady boundary condition case of

Eq. (4.5), where $N_0 = -D_n \frac{\partial c_n}{\partial r}\Big|_{r=R_n}$, is

$$\begin{aligned}(c_n(r,t) - c_n(r,0))\frac{D_n}{N_0 R_n} =& \frac{3D_n t}{R_n^2} + \frac{1}{2}\frac{r^2}{R_n^2} - \frac{3}{10} - \\ & 2\frac{R_n}{r}\sum_{j=1}^{N}\left(\frac{sin(\lambda_j r)}{\lambda_j^2 R_n^2 sin(\lambda_j R_n)} exp(-D_n \lambda_j^2 t)\right)\end{aligned} \tag{4.35}$$

The λ_j coefficients are given by the positive roots of

$$R_n \lambda_j cot(R_n \lambda_j) = 1 \tag{4.36}$$

where an arbitrary number of terms of the infiinte eigenvalue series may be used. Analysis of the required number of eigenvalues indicated that there are minimal accuracy gains beyond 10 terms. The goal is to use Eq. (4.35) to identify the diffusion coefficient by relating the concentration at the end of discharge and the current magnitude to the diffusion coefficient. The input to the procedure is the external current rate for the capacity test, which fixes N_0 to a constant value. Based on experimental measurement, the total time of the C/3 or 1C capacity test t_f is known. The voltage at the end of the capacity test is dictated by the lower voltage limit. Rearranging the terminal voltage expression in terms of the limiting concentration at the end of discharge, $c_n(R_n, t_f)$, gives

$$\begin{aligned}c_n(R_n,t_f) =& c_{max,n} U_n^{-1}\left(U_p(t_f) - (\phi_e(L_c,t_f) - \phi_e(0,t_f))\right. \\ & \left. -(\eta_p(t_f) - \eta_n(t_f)) - (R_r(t_f) + R_c)\, I - V_h(t_f) - V_{min}\right)\end{aligned} \tag{4.37}$$

This procedure assumes that the negative electrode OCV is invertible, which is typically a good assumption at the end of discharge away from the characteristic plateaus found for composition values approaching one. The limiting concentration values for each current are plotted as horizontal dashed lines in Figure 4.14. The limiting concentration as a function of the diffusion coefficient is also plotted by sweeping Eq. (4.35) over a range of values for D_n. The intersection of the symbols with the limiting concentration lines gives the diffusion coefficient that precisely matches the experimentally observed capacity for each rate, either C/3 or 1C.

If the model was a perfect representation of the electrochemistry occuring within the cell, the value of the diffusion coefficient predicted by this method would be constant regardless of rate. Regardless the predicted values are close and an average may be used without introducing significant model error. The agreement obtained by the diffusion coefficient tuning procedure is shown in Figure 4.15. The difference between the capacity delievered at each rate is only around 2%, but the diffusion coefficient tuning procedure has matched the experimental data well.

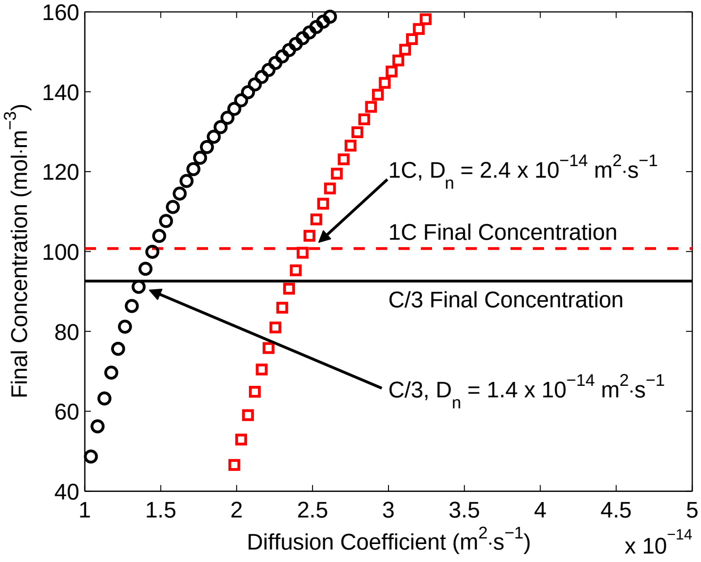

Figure 4.14: Negative electrode diffusion coefficient identification via inversion of the spherical diffusion analytical solution for a steady boundary flux. Lines indicate the final concentration for each current, defined by Eq. (4.37), and the symbols indicate the final concentration predicted by Eq. (4.35) as a function of the diffusion coefficient.

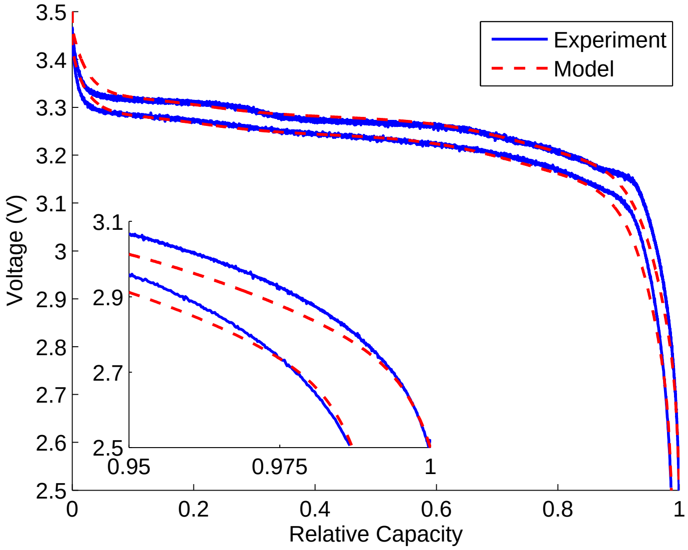

Figure 4.15: Relative capacity utilization for two examples of low rate galvanostatic discharge. The identified negative diffusion coefficient matches the capacity decrease when comparing C/3 to the 1C rate.

Once the diffusion coefficient has been identified for room temperature, the temperature dependence is estimated based upon comparisons with capacity tests conducted at the same rate, but varying temperatures. The resulting Arrhenius coefficients, to be utilized in Eq. (4.29), are documented in Table 4.5 for each parameter that depends on temperature. The positive diffusion coefficient is set to a literature value since the complex phase change process of iron phosphate is not modeled. This omission, when combined with the characteristic plateau of the iron phosphate OCV, renders the model voltage prediction somewhat insensitive to the value of the positive diffusion coefficient. However it is noted that the selected diffusion coefficient gives qualitative agreement with the behavior at various current rates in the solid solution region at high cell SOC (low positive electrode composition) near 20°C.

The diffusion coefficient, transference number, and activity coefficient of $LiPF_6$-based electrolyte have been experimentally characterized as a function of concentration and temperature for standard carbonate solvents (Valoen & Reimers, 2005). To incorporate their results into the simplified modeling approach of this work, the parameter values from the equivalent nominal concentration value of 1 mol/L are used. The reported diffusion coefficient is combined with an assumed Bruggeman coefficient of 2.8 (Patel *et al.*, 2003) and an experimentally tuned porosity value to compute the effective diffusion coefficient. Given the reported value of 1.5×10^{-10} m^2/s in (Valoen & Reimers, 2005), using a porosity value of 0.52 to calculate an effective diffusion coefficient based on the method given in Chapter 2 gives good agreement with the time constant of relaxation following interruption of current.

While the time constant is governed by the effective diffusion coefficient, the magnitude of the relaxation voltage is determined by the activity coefficient. It was found that a higher activity coefficient than reported in (Valoen & Reimers, 2005) resulted in better agreement with the experimental data through greater diffusion overpotential in the liquid phase. This could be possible for several reasons. First, the activity coefficient of the present model does not vary with concentration, and the local concentrations at either end of the cell during high current operation could be much different than the nominal value, which in turn would lead to greater potential variation if a concentration-dependent activity coefficient were used.

Another possible reason for the increased activity coefficient could be that some dynamics associated with the OCV hysteresis are being assigned to the liquid phase. For example, other authors have characterized a hysteresis effect with a time constant much smaller than the long-term effect modeled in this work (Roscher & Sauer, 2011), and the larger activity

Table 4.6: Summary of model parameters taken as independent of operating conditions.

Parameter	Definition	Value
ϵ_n	negative active volume fraction	0.35
ϵ_p	positive active volume fraction	0.35
x_0	initial negative composition	0.74
y_0	initial positive composition	0.026
t_0^+	transference number of Li^+	0.39
α	Butler-Volmer transfer coefficient	0.5
ϵ_e	liquid volume fraction	0.52
$brug$	bruggeman coefficient	2.8

coefficient could be partly accounting for the fast initial relaxation of the OCV hysteresis. Note that the solid diffusion coefficients had been previously identified and their effects are inherently included when obtaining agreement between model and experiment during voltage relaxation.

4.6 Model Validation

This section compares the model performance with experimental data to validate the preceding methodology. A variety of charge sustaining (CS) and charge depleting (CD) experiments have been performed. Charge sustaining experiments feature current pulses that are symmetric with respect to charge and discharge, so that the battery operates within a small window of SOC. Charge depleting experiments exhibit more discharge current than charge current, such that the cell SOC decreases throughout the course of the experiment. The two quantitative error metrics are the root-mean-square (RMS) error and 95th percentile error, indicating 95% of observed error is less than the reported value.

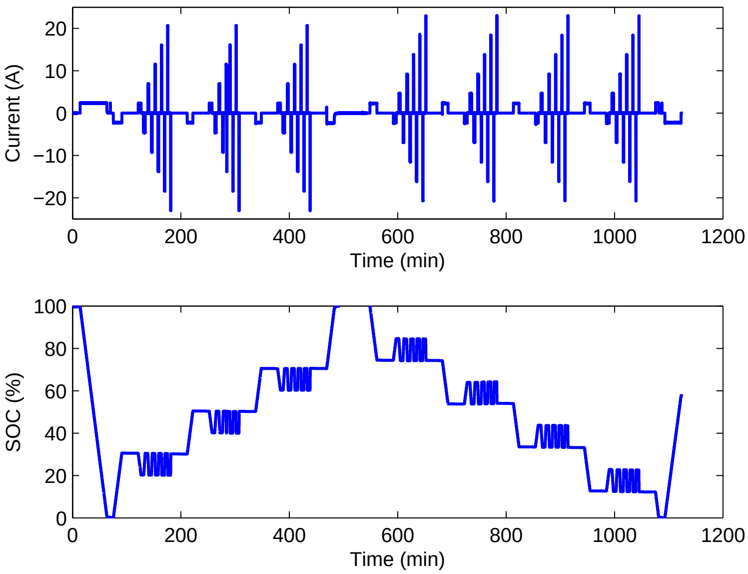

Figure 4.16: Input current profile and SOC trajectory for CS validation.

4.6.1 Charge Sustaining Operation

The first set of validation data, meant to imitate CS HEV operation, is comprised of constant current pulses of magnitudes ranging from 1C to 10C. The time duration of each pulse is set to achieve a change in SOC of 10%. Each discharge pulse is followed by a corresponding charge pulse such that the overall profile is charge neutral about a given SOC. After several charge neutral pulses about a given SOC, a 1C current is used to set SOC for the next set of current demands followed by a thirty minute rest period to ensure the system reaches equilibrium. The overall current profile and the corresponding SOC trajectory are plotted in Figure 4.16.

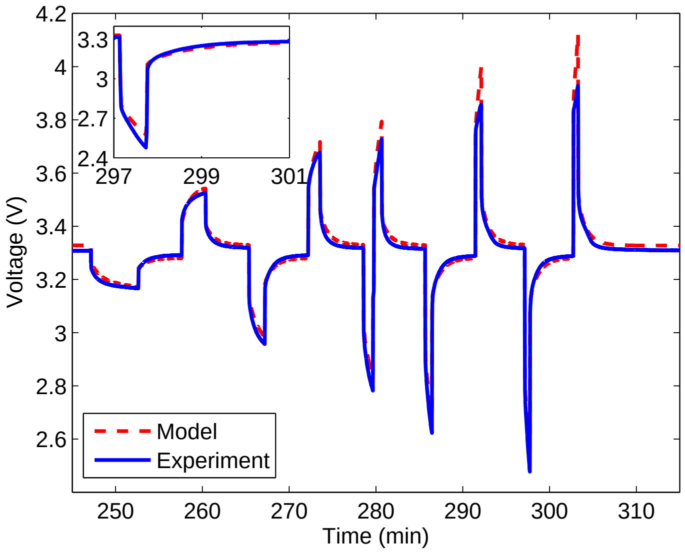

Figure 4.17: Comparison of model predictions with experimental data for charge sustaining profile and temperature of 5°C.

These inputs are applied for temperatures of 5°C, 20°C, and 55°C. Figures 4.17, 4.18, and 4.19 compare the model prediction with experimental data for these three cases respectively, for a SOC of 40%. The model accuracy for other SOC conditions is documented in Table 4.7.

Examining the voltage response in detail, it becomes apparent that the initial overpotential upon application of a current demand is predicted well for all temperatures considered. This agreement beteen model and experiment validates the resistance parameter identification procedure from a system peformance prediction standpoint, though admittedly it cannot be determined whether the extracted Arrhenius coefficients correspond to the true nature of each parameter or simply provide agreement with the experimental data. The inclusion of the liquid phase concentration and potential dynamics leads to significantly

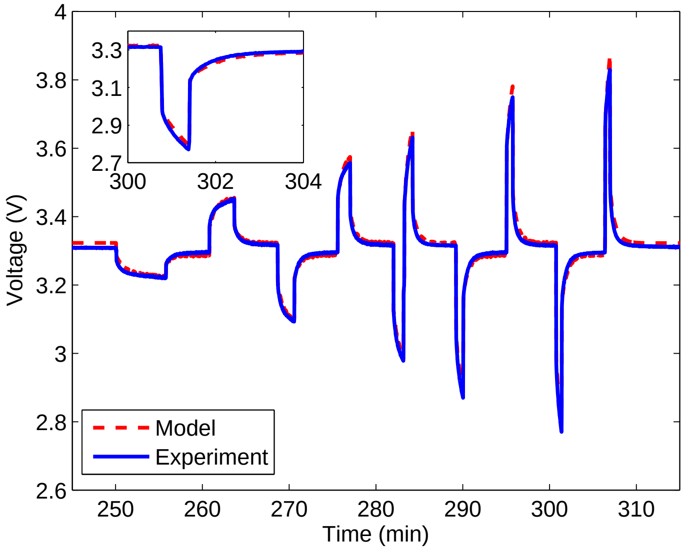

Figure 4.18: Comparison of model predictions with experimental data for charge sustaining profile and temperature of 20°C.

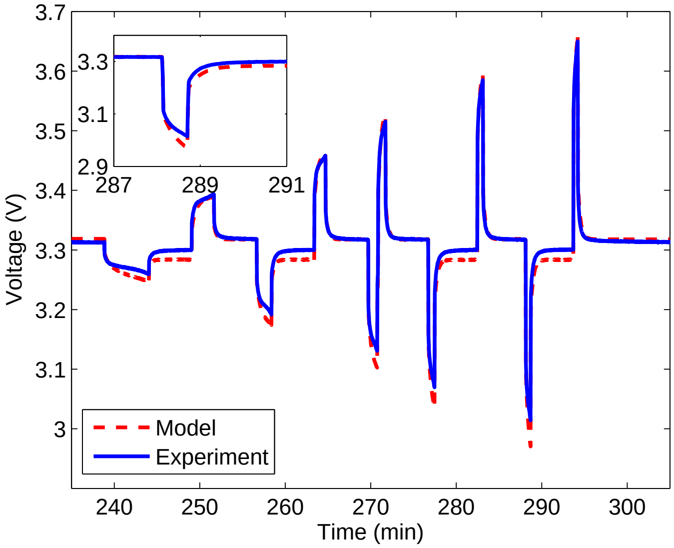

Figure 4.19: Comparison of model predictions with experimental data for charge sustaining profile and temperature of 55°C.

Table 4.7: Summary of model error for CS operation, reported as RMS/95th percentile (mV).

Temperature (^{o}C) / SOC(%)	15	20	35	40	55	60	75
5	24.7 / 55.2	27.8 / 49.3	30.9 / 61.7	27.6 / 46.6	37.1 / 69.7	29.8 / 57.4	27.3 / 55.0
20	21.7 / 42.1	17.0 / 36.3	14.9 / 31.7	13.9 / 29.0	19.3 / 39.8	14.8 / 34.8	9.8 / 21.0
55	15.7 / 26.0	9.2 / 21.4	9.5 / 20.2	13.0 / 23.7	8.1 / 17.0	7.7 / 17.8	9.7 / 20.5

more accurate prediction of the cell voltage during the relaxation phase following current interruption and for high current conditions.

Based on the results shown, it is evident that the model provides better agreement at 20°C than at the two extreme temperatures, though the results are better for 55°C than for 5°C. The reason for this may be the discrepancies between the fitted OCV, recorded at 20°C, and the experimental values begin to become more significant for extreme temperatures. The noted discrepancies could be related to changes in the thermodynamic OCV driven by entropy considerations or simply a more pronounced hysteresis phenomena. There is also a general tendency to overpredict the overpotential during charging for low-temperature operation. As a result, though the initial resistance is accurately captured at temperatures down to -10°C using the documented identification procedure, these limitations create a practical lower temperature bound around 5°C for validating the model predictions. This does not pose a serious practical concern, since most systems will be severely power limited below 5°C and it may be expected that a satisfactory thermal managament system will prevent the battery temperature from reaching such low levels.

Following authors who have examined the sources of overpotential using porous electrode models (Srinivasan & Newman, 2004*b*; Bernardi & Go, 2011), we illustrate the relative magnitude of each overpotential source during a 10C discharge beginning from 50%

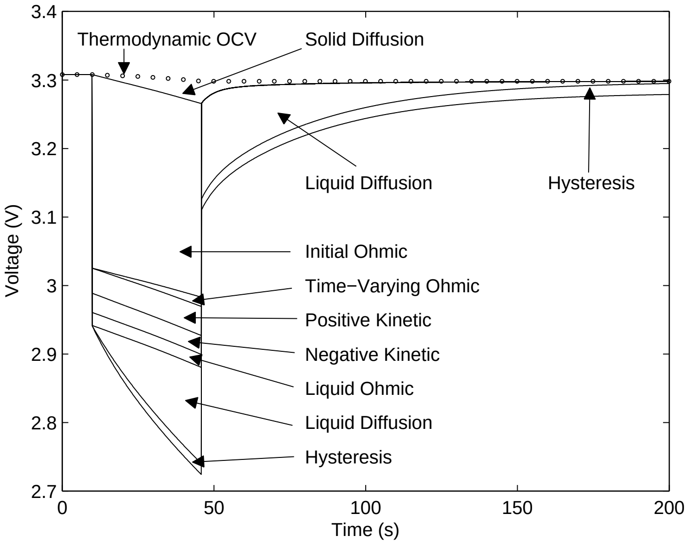

Figure 4.20: Illustration of various sources of overpotential during a 10C discharge.

SOC, at 20^{o}C, in Figure 4.20. The discharge duration is chosen to remove 10% SOC from the cell, similar to the current demands of the CS validation profile.

The dominant source of overpotential is the contact resistance, R_c, which also includes the lumped effect of the initial ohmic resistance of the solid matrix of the positive electrode in this model structure. The time-varying solid phase ohmic losses, referred to interchangeably as the resistive reactant effect, contribute a minor amount of overpotential in this case because of the short duration of the current pulse. During longer current pulses, such as the limiting case of a constant current capacity test discussed previously, the resistive reactant overpotential becomes more apparent. As expected positive kinetic losses are greater than those in the negative electrode, though neither is as large as the ohmic losses since the example is taken at 20^{o}C. Liquid ohmic losses are of the same order as the kinetic losses, and liquid phase diffusion contributes a fair amount to the total overpotential since the current rate is high. The overpotential from the liquid also tends to increase continually indicating that a steady profile is not reached by the end of the pulse duration. Finally, the solid diffusion overpotential of either electrode is surprisingly small, despite the formation of significant concentration gradients as is expected for high current rates. The lack of overpotential is due to the minimal variation of each half-cell OCV with respect to composition, and should not be interpreted as the solid phase having faster diffusion than in the liquid. There are significant concentration gradients present in the solid due to transport limitations, but the opportunities for developing overpotential are less.

Upon interruption of the current, the ohmic and kinetic contributions vanish. The subsequent relaxation phase is dominated by the decay of the liquid phase concentration gradients. The solid concentration overpotential relaxes more quickly, again due to the minimal variation of each half-cell OCV with respect to composition and not because the solid concentration gradient relaxes more quickly than in the liquid. The hysteresis effect is also visible, causing a lower voltage than predicted by the bulk SOC change of the electrode even after complete relaxation of the solid and liquid phase concentration gradients.

4.6.2 Charge Depleting Operation

Validation results are also included for a CD profile. This ensures that the model maintains sufficient performance predictions for current profiles that are not nominally charge sustaining. The profile is extracted from the United States Department of Energy battery test manual for PHEVs (Anonymous, 2010). The current and SOC trajectories are plotted in Figure 4.21. Similarly to the CS validation, these experiments are repeated at temperatures of 5°C, 20°C, and 55°C.

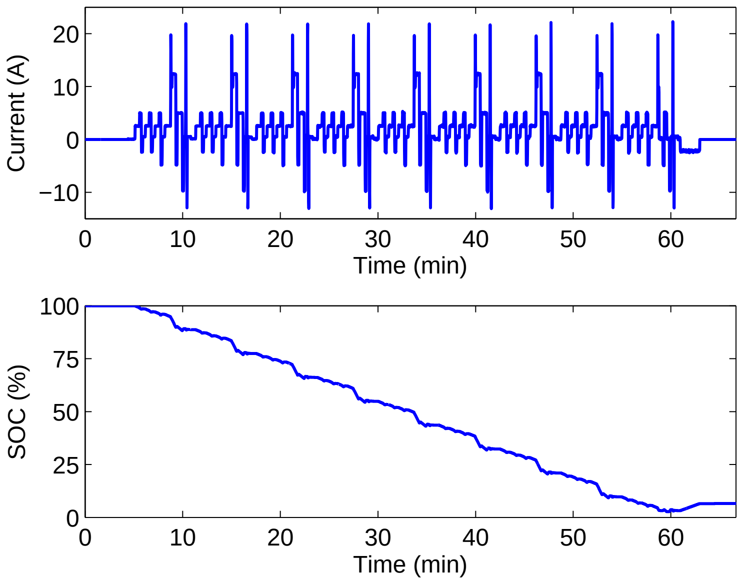

Figure 4.21: Current demand and SOC trajectory for charge depleting validation.

Figure 4.22 shows the model voltage prediction and experimental data for the CD profile at $55°\mathrm{C}$, while Figures 4.23 and 4.24 show zoomed views for sets of the repeated current cycle. The model performance is acceptable, though it is worth discussing two instances where the errors between model and experimental data are largest. In the initial portion of the profile, there are some brief transient errors at high SOC. These could be related to the neglect of the temperature dependence of the lithium diffusion coefficient for Li_yFePO_4. The second instance of notable model error is during the latter stages of the profile, where cell SOC is low. Throughout most of the profile, it appears there is a steady offset between the model prediction and experimental data, though transient overpotential is still captured well. The steady nature of the error indicates inaccurate SOC prediction in either of the two electrodes leading to inaccurate OCV, insufficient characterization of the dependence of the OCV on temperature, or insufficient hysteresis modeling.

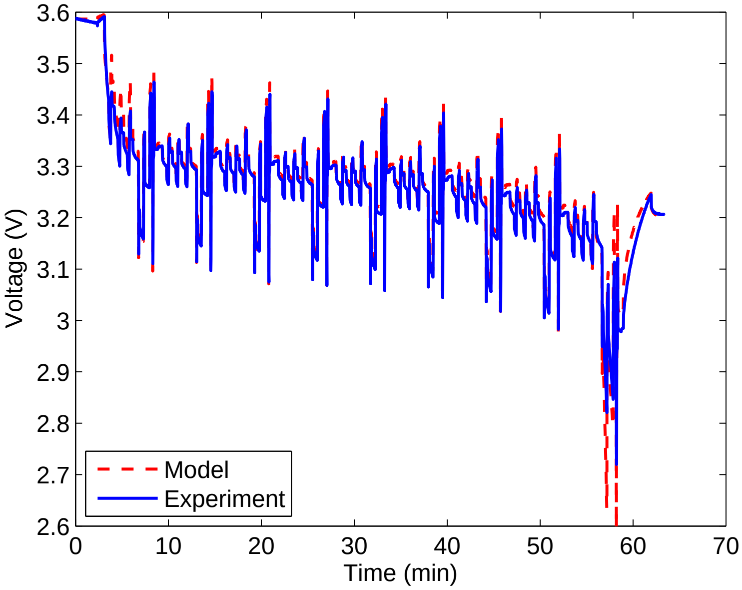

Figure 4.22: Model performance compared with experimental data for charge depleting operation at 55°C, showing the entire CD profile.

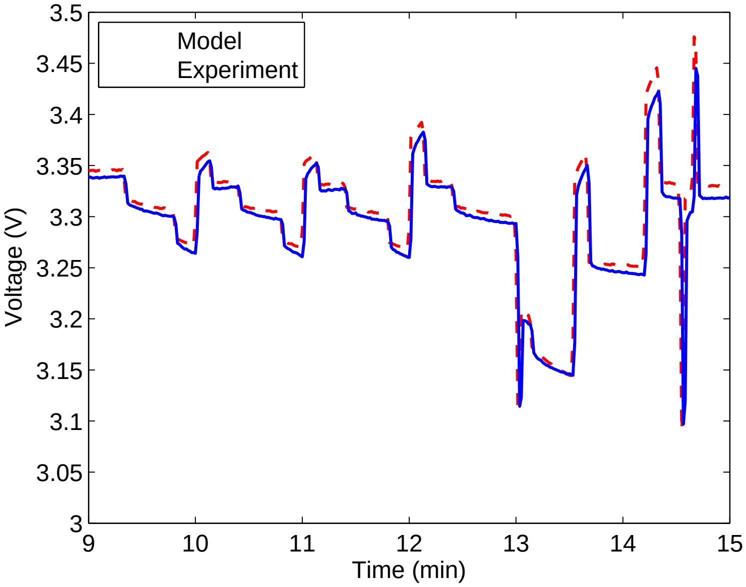

Figure 4.23: Model performance compared with experimental data for charge depleting operation at 55°C, showing the CD profile segment from 9 minutes to 15 minutes.

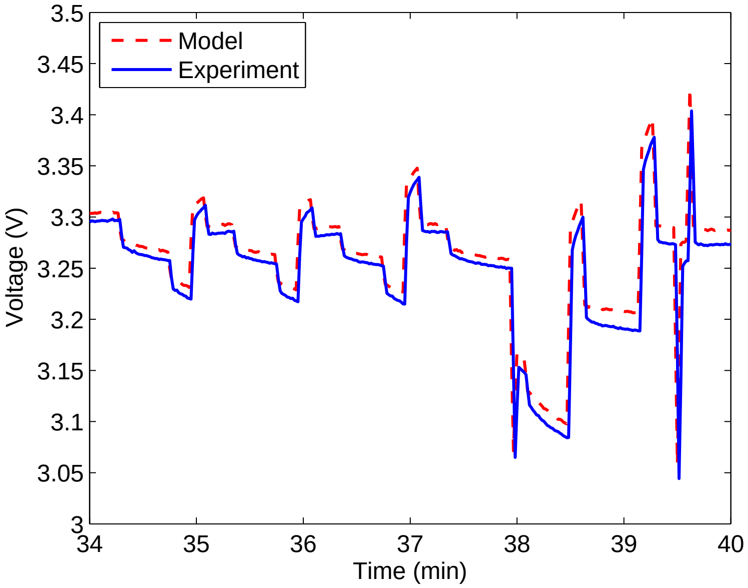

Figure 4.24: Model performance compared with experimental data for charge depleting operation at 55°C, showing the CD profile segment from 34 to 40 minutes.

The first two hypotheses can be eliminated in light of the charge sustaining operation data. If they did contribute to the model error at low SOC, it would have been revealed by the data plotted in Figures 4.17, 4.18, 4.19, and documented in Table 4.7; however, model performance is better there than exhibited during CD operation. The characterization of the hysteresis used relatively short duration current pulses that caused no greater than a 10% change in SOC. The CD profile, although not a continuous discharge, is overall charge depleting for a duration of one hour and therefore may be incurring some greater amount of hysteresis than captured by previous experiments.

In a fashion similar to the CS profile, the overall cell resistance is overpredicted during the high current demands of the profile. Additionally, the model generally overpredicts the overpotential during both discharge and charge. The most likely cause is thermal gradients

Table 4.8: Summary of model error for CD operation, reported as RMS/95th percentile (mV).

Temperature	RMS/95th percentile (mV)
5^{o}C	96.0 / 220
20^{o}C	43.6 / 86.2
55^{o}C	19.5 / 42.5

within the cylindrical cell that are not as well managed due to the larger overall rate of current throughput in this case as compared to the charge sustaining case. This would lead to a warmer bulk average temperature and thus a lower overall resistance. It should also be noted that overall this current profile represents a much more dynamic situation than the CS profile, with more step changes in the current, so there could be additional unmodeled effects contributing to model error during the rapid transitions between discharge and charge, or vice versa. The error between the model predicted voltage and the experimental result for all tested CD conditions is summarized in Table 4.8.

4.7 Sensitivity Analysis

A sensitivity study was conducted to examine the main factors and factor interactions that could contribute to capacity fade, based on the described model. The parameter subset is chosen as the active material volume fractions in the positive and negative (ϵ_p and ϵ_n, respectively), and the initial amount of cyclable lithium in the positive (y_0) and negative (x_0) normalized by the saturation value. To compute the sensitivity, the model capacity prediction is determined using the nominal parameter set and a parameter set perturbed by

Table 4.9: Discharge capacity sensitivity summary.

Parameter	$S(Q)$
x_0	1.01×10^0
y_0	0
ϵ_n	1.01×10^0
ϵ_p	2.92×10^{-4}
$x_0 \cup \epsilon_n$	1.92×10^0
$x_0 \cup y_0$	1.01×10^0
$x_0 \cup \epsilon_p$	1.01×10^0
$\epsilon_n \cup y_0$	1.01×10^0
$\epsilon_n \cup \epsilon_p$	1.01×10^0
$\epsilon_p \cup y_0$	2.92×10^{-4}
$x_0 \cup \epsilon_n \cup y_0$	1.92×10^0
$x_0 \cup \epsilon_n \cup \epsilon_p$	1.92×10^0
$x_0 \cup \epsilon_p \cup y_0$	1.01×10^0
$\epsilon_n \cup \epsilon_p \cup y_0$	1.01×10^0
$x_0 \cup y_0 \cup \epsilon_n \cup \epsilon_p$	1.92×10^0

10% (ΔP). The sensitivity of capacity with respect to each parameter is

$$S(Q) = \frac{\Delta Q/Q}{\Delta P/P} \tag{4.38}$$

All possible cases are studied, ranging from single parameter changes to four-factor interactions. For example, $x_0 \cup y_0$ represents the case where both parameters are perturbed by 10%. Table 4.9 summarizes the results of the sensitivity study when including factor interactions for discharge capacity. Based on this preliminary analysis, it appears that the discharge capacity is not correlated to the positive electrode parameters. While these parameters have a noticeable effect on the charge capacity, they are effectively unobservable during discharge due to the flat OCV curve of the Li_yFePO_4 electrode (see Figure 4.9) and the cell composition ranges. For this reason they can be removed from the parameter identification process, but devising methods for identifying the aging properties of the positive electrode will be the subject of future work.

4.8 Nonlinear Estimation of Cell Aging Parameters

A nonlinear estimation procedure was defined based on the reduced-order electrochemical model to obtain the evolution of the aging parameter set throughout the cell life. Based on the preliminary sensitivity analysis and results available in the literature (Santhanagopalan *et al.*, 2008; Liu *et al.*, 2008; Ramadass *et al.*, 2004), the normalized initial lithium concentration in the anode, x_0, and the active volume fraction ϵ_n were considered as the parameters that mostly affect the capacity degradation. In addition, the electrical conductivity σ_p of the positive electrode is included in the parameter set to account for the noticeable increase in slope of the normally flat discharge curve for the batteries used in this work. The decrease of electrical conductivity during aging is expected and most likely has a role in power fade as well.

In a similar fashion to the identification of capacity-related parameters discussed previously in this chapter, a nonlinear least square procedure is implemented based on the trust region reflective algorithm (Coleman & Li, 1994; Shi *et al.*, 2009). In this case, the algorithm consists of finding the optimal set of parameters $\vec{P}^* = [x_0^*, \epsilon_n^*, \sigma_p^*]$ minimizing the cost function in Eq.(4.39), where the error $\vec{e}$ is a vector of differences between the experimental data and the predicted voltage ($\hat{e}(t) = V_{exp}(t) - V(t)$). The nonlinear least square problem is cast as:

$$\vec{P}^* = \underset{[x_0,\epsilon_n,\sigma_p]}{\operatorname{argmin}} \left(\frac{1}{2}(\Delta\vec{P})^T \frac{\partial^2 \vec{e}}{\partial \vec{P}^2}(\Delta\vec{P}) + (\Delta\vec{P})^T \frac{\partial \vec{e}}{\partial \vec{P}} \right) \tag{4.39}$$

Table 4.10: Bounds for parameter estimation algorithm.

Parameter	Upper Bound	Lower Bound
x_0	0.5	0.9
ϵ_n	0.2	0.7
σ_p	0	0.5

The gradients of Eq. (4.39) are computed using a finite-difference approach. The trust region reflective algorithm is particularly advantageous because it allows for bounded estimation and the aging parameters in question have physical boundaries. In particular, the normalized initial lithium concentrations may range from 0 to 1, but the initial value is likely to range from 0.5 to 0.9 to ensure efficient use of available capacity, and to prevent overcharging, respectively. The active volume fraction will not be greater than 0.70 due to the porosity of the electrode and the addition of conductive agents and binders. The active volume fraction lower bound is chosen conservatively low to allow for the possibility of a large amount of active material loss during aging. The conductivity cannot be negative, and should not increase from the value estimated at BOL. The described bounds for each parameter included in the estimation scheme are summarized in Table 4.10.

Figure 4.25, compares the model voltage prediction to the capacity test data from BOL, several intermediate stages of life, and the assessment from the end of testing. As expected, the cell capacity progressively decreases as aging cycles continue towards EOL. For clarity, only results that exhibited a decrease in capacity compared to the prior lowest assessment are plotted. Every plot exhibits at least four assessments from BOL to EOL. The model agreement is generally unchanged throughout life, suggesting that the mechanisms of aging are being captured by the estimation procedure.

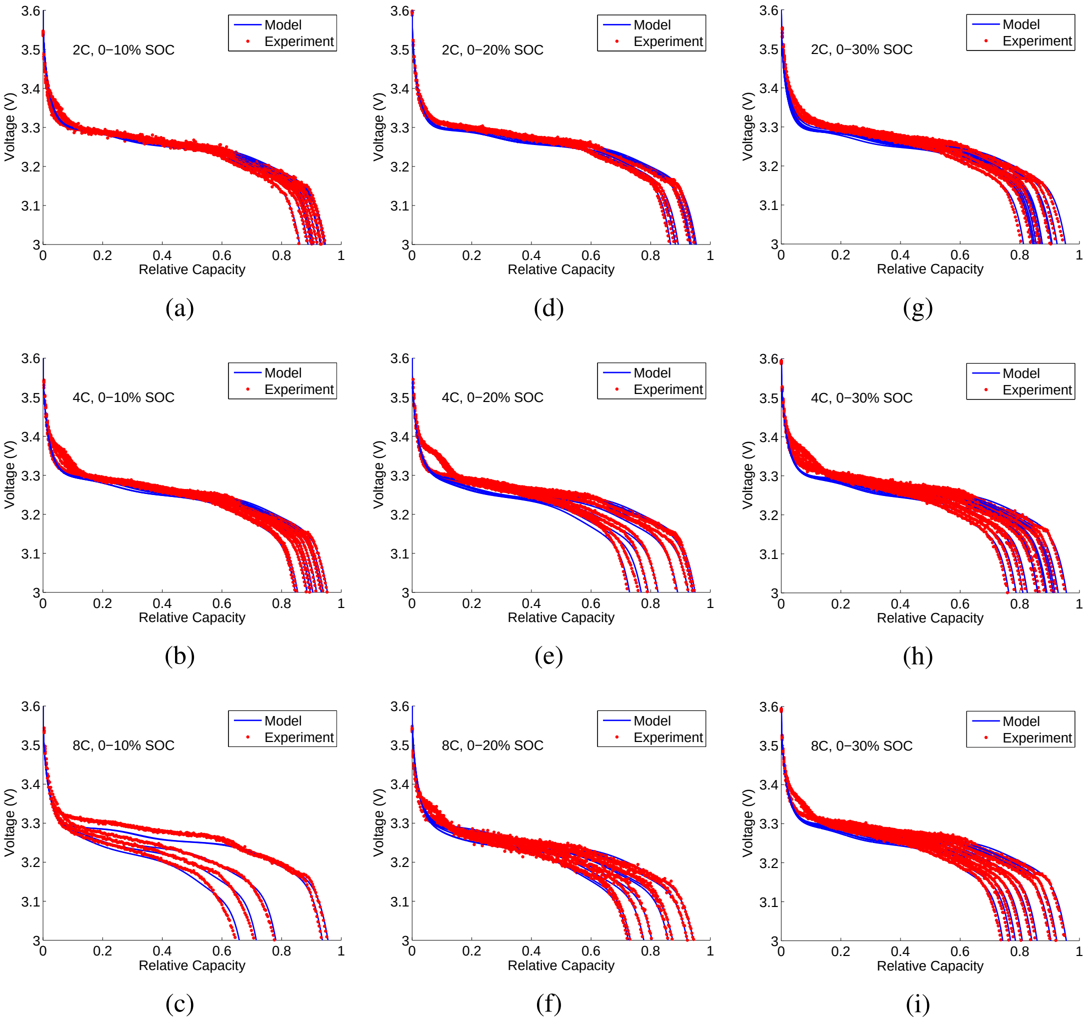

(a) (d) (g)

(b) (e) (h)

(c) (f) (i)

Figure 4.25: Model prediction of voltage based on estimated aging parameters, compared with experimental data during selected capacity assessments.

The parameter values needed to produce the agreement between the model and experimental voltage are plotted in Figure 4.26. Both the active material volume fraction and initial composition of the negative electrode show a decreasing trend. The electronic conductivity of the positive electrode also has a decreasing trend with respect to charge throughput; however, the decrease in conductivity is noticeably larger and sometimes exhibits a step change while other times it decreases in the same gradual manner as capacity. The decrease of active material is in agreement with experimental studies from literature (Liu *et al.*, 2008) which state that active material loss in the negative electrode can be a significant source of performance degradation in the Li_xC_6/Li_yFePO_4 system. Further detailed analysis is needed to identify the mechanisms underlying these trends, particularly the loss of active material which could be due to fracturing of electrode particles (Christensen & Newman, 2006).

From a system standpoint, the apparent close correlation between the active material volume fraction and the cell capacity suggested by Figure 4.26 is quite useful. A regression analysis could be performed to correlate the active volume fraction with capacity throughout battery life. Recall that the electrical conductivity of the positive electrode was included only to reduce the RMS error between experimental and model voltage prediction. Therefore, even though it does tend to decrease during aging, it is not included in the capacity regression. Further detailed analysis is needed to determine whether consideration of only the active volume fraction provides accurate capacity prediction throughout battery life for all cells, or if the loss of cyclable lithium should also be considered.

The utility of this finding lies in the fundamental significance of capacity versus that of the active material volume fraction. Capacity is a concept defining the amount of charge contained in an electrochemical energy storage device between specified voltage limits.

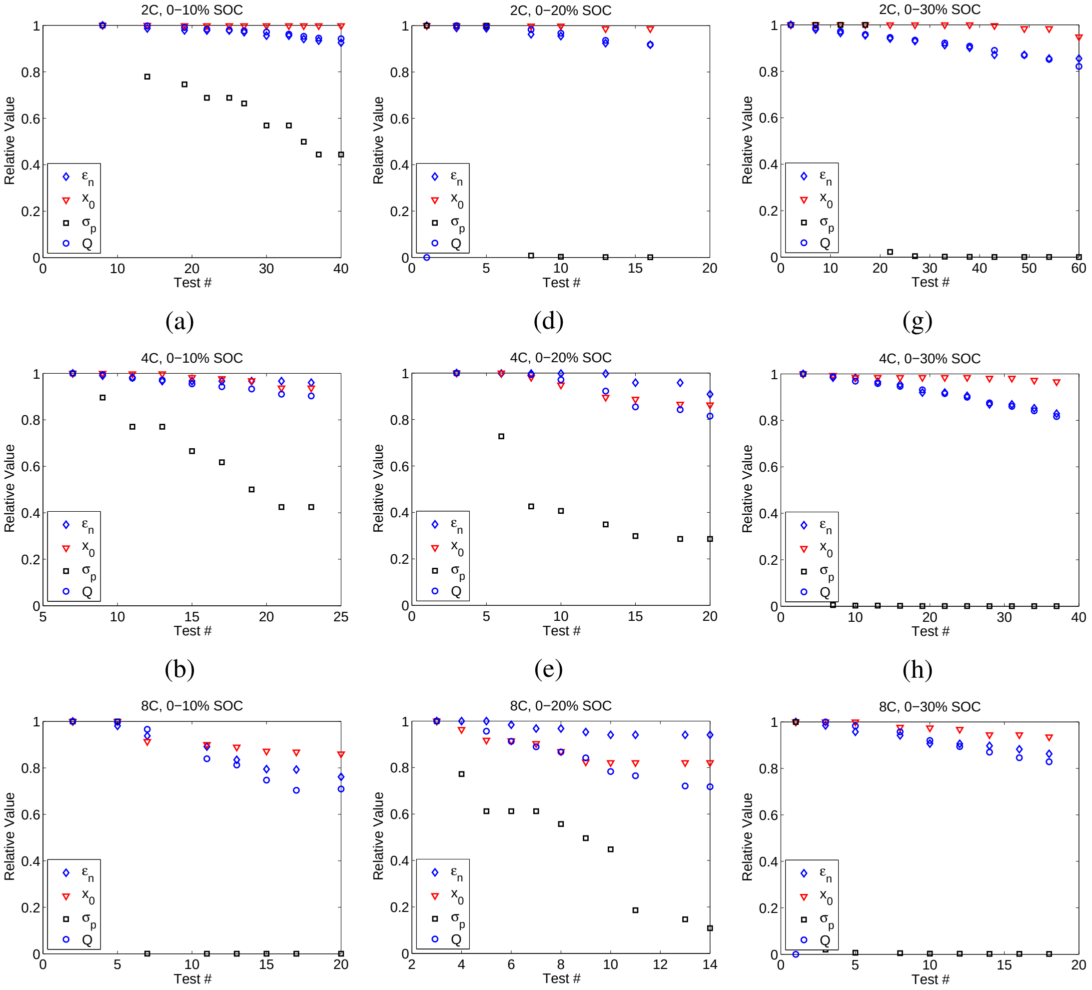

(a) (d) (g)

(b) (e) (h)

(c) (f) (i)

Figure 4.26: Parameter estimates and experimentally measured capacity from capacity assessments. Relative values are normalized by the beginning-of-life value.

The volume fraction is an actual physical parameter which effects the electrical dynamics of the cell, and as such it may be possible to estimate its value from voltage and current measurements. Combined with an open loop model for capacity fade, accurate online estimation of cell capacity may be possible.

4.9 Summary and Future Work

A reduced order model of Li_xC_6/Li_yFePO_4 cylindrical cells has been developed for large scale simulation, control, and estimation applications. The assumption of uniform utilization that is common for previously published reduced order models is used to develop a novel model extension incorporating the concentration and potential dynamics of the liquid phase. Both the solid and liquid phase diffusion dynamics exhibit nonlinear transfer functions that are approximated with the Pade method. This approach has the advantage of preserving the parameters of the parent model, and ultimately their physical meaning, which is useful for SOC and SOH estimation. Parameterization techniques that excite a confined portion of the overall cell dynamics are used to identify the required electrochemical parameters and their Arrhenius dependence on temperature. The parametrization procedure is validated with experimental data for a range of temperatures, SOC, and current rates, and the model proves to be robust.

After conducting a sensitivity analysis of the discharge capacity with respect to several model parameters, a set of capacity fade parameters associated with the negative electrode were identified, namely the active material volume fraction, and the initial amount of cyclable lithium. The result of the parameter estimation is that capacity is correlated to physical parameters that cause measurable effects on the cell output voltage. This suggests it is possible to perform estimation of capacity from the battery current-voltage dynamics without performing a distinct capacity test, a result that is significant for the estimation of battery SOC and SOH for hybrid electric vehicle applications. Future work should be focused on designing robust, real-time estimation schemes for the negative electrode capacity fade parameters.

Chapter 5: Modeling, Aging Analysis, and Capacity Fade Model for Composite Electrode Automotive Pouch Cells

5.1 Introduction

Recently researchers and battery manufacturers have developed and commercialized Li-ion cells with electrodes consisting of multiple active materials (Park *et al.*, 2007; Johnson *et al.*, 2005; Whitacre *et al.*, 2008). Specifically, composite $LiNi_{1/3}Mn_{1/3}Co_{1/3}O_2 - LiMn_2O_4$ (NMC – LMO) cells have been directed towards plug-in hybrid electric vehicles (Dubarry *et al.*, 2009*a*,*b*; Belt *et al.*, 2011; Park *et al.*, 2007; Nam *et al.*, 2009). Layered NMC cathodes have high specific capacity and good thermal stability but poor performance at high rates (Nam *et al.*, 2009). Single component LMO spinel cathodes have high rate capability and low cost (Belt *et al.*, 2011; Fergus, 2010), but suffer from poor cycle life due to Mn dissolution into the electrolyte solvent (Jang *et al.*, 1996; Xia *et al.*, 2000; Du Pasquier *et al.*, 1999). By mixing these complimentary chemistries together into a single electrode, a composite cell with high capacity and high rate capability can be achieved (Park *et al.*, 2007; Johnson *et al.*, 2005; Whitacre *et al.*, 2008). Mixing NMC with LMO also reduces Mn dissolution, improving cycle and calendar life (Dubarry *et al.*, 2009*a*,*b*; Jeong *et al.*, 1999; Yang *et al.*, 2006). A pouch cell using composite NMC–LMO positive electrode is pictured in Figure 5.1.

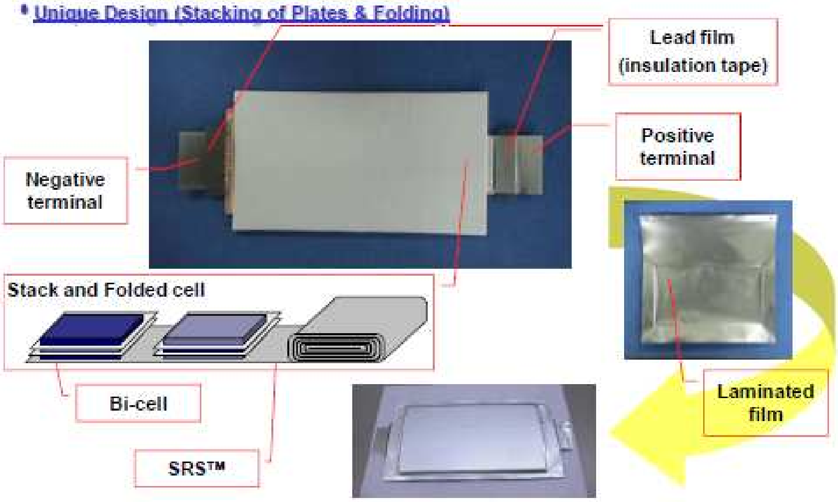

Figure 5.1: Picture of a pouch cell including aspects of the manufacturing process (Alamgir *et al.*, 2011).

While the advantages of composite electrodes are apparent, there is still the need to characterize the aging process for these cells. Many studies have been conducted to characterize the aging mechanisms of single active material electrodes composed of NMC and LMO; however the interaction between the materials within a composite structure may have non-intuitive aging consequences. Therefore, there is a need to identify and understand the predominant sources of aging in composite cells.

The aging process for cells using LMO electrodes has been examined using x-ray diffraction spectra and other *ex-situ* techniques. The dissolution of Mn into the electrolyte and subsequent deposition on the anode was confirmed, leading to capacity loss (Du Pasquier *et al.*, 1999; Liu *et al.*, 2009). Other studies have shown capacity fade and resistance rise due to Mn dissolution in the electrolyte (Jang *et al.*, 1996), and subsequent loss of contact between the spinel and carbon matrix (Xia *et al.*, 2000). The presence of the carbon matrix also aided Mn dissolution via oxidation of the electrolyte solvent on the carbon surface.

For NMC cells, multiple thermal, electrochemical, and x-ray spectral techniques have identified lithium-carbonate formation on the electrode surface in the presence of air, resulting in loss of oxygen from the active material and loss of cyclable lithium (Haik *et al.*, 2010). The NMC active material has been shown to react with standard $LiPF_6$ electrolyte salts at the surface of the electrode, a process made more severe by using smaller, nanoscale particles (Sclar *et al.*, 2009). The use of differential capacity (voltage) analysis (Smith *et al.*, 2007; Dubarry *et al.*, 2009*a*,*b*; Bloom *et al.*, 2005*b*,*a*, 2006, 2010) to detect the progression of aging has been applied to cells with NMC positive electrodes. This method associates various peaks of the dQ/dV (dV/dQ) versus cell voltage curve with reactions and phase changes of each electrode. The specific degradation mechanism is then discerned by analyzing the progression of each peak throughout aging.

The reviewed literature has characterized the aging mechanisms of electrodes composed of NMC and LMO singly; however, the aging interaction between the materials within a composite structure may be complex. Structural changes of various composite cathodes have been studied using x-ray diffraction spectra (Park *et al.*, 2007; Johnson *et al.*, 2005; Nam *et al.*, 2009; Cabana *et al.*, 2009; Du Pasquier *et al.*, 1999). Recently an aging campaign was conducted to establish the path dependence of resting and cycling for composite NMC – LMO cells, where operating temperature, resting state of charge (SOC), and rest period between cycles was varied Belt *et al.* (2011). Differential capacity analysis was used on composite NMC – LMO cells Dubarry *et al.* (2009*a*,*b*) to suggest a two stage aging process. First, cyclable lithium is consumed to initiate solid-electrolyte interphase (SEI) layer growth on the electrode surfaces. Second, continued SEI growth leads to hindered interfacial kinetics and loss of positive active material accelerates capacity fade. However, the graphical procedure usually applied to half-cell potentials in conjunction with differential capacity assessments cannot be used to understand loss of a single component of a composite electrode. Instead, a model-based approach can be useful to predict changes that result from loss of a single component.

Initial attempts have been made to model composite electrode cells. The porous electrode model (Newman & Tiedemann, 1975; Doyle *et al.*, 1993) was extended to incorporate multiple active materials (Albertus *et al.*, 2009). The model was validated with galvanostatic discharge and electrochemical impedance spectroscopy (EIS) tests of composite $LiNi_{1/3}Co_{1/3}Al_{1/3}O_2 - LiMn_2O_4$ cells. However, there have been no attempts to apply these models towards studying aging to understand the mechanisms responsible for capacity and power fade in composite cells, as has been performed on several occasions for single material electrodes.

This chapter presents experimental results for composite automotive pouch cells aged under dynamic duty cycles with periodic state of health assessments. Dependence of charge rate, minimum SOC, temperature, and charge sustaining/depleting operation on the aging process is analyzed. A reduced order, electrochemical model is developed, parametrized with half cell data, and validated with full-cell data. The model parameters are empirically scheduled to fit differential capacity as the cells age subject to hypothesized degradation mechanisms. The agreement between model and experiment is related to the likelihood and severity of proposed aging mechanisms.

After establishing the loss of cyclable lithium as the main capacity fade mechanism, an electrochemical model of solid-electrolyte interphase growth is presented. The model is used to predict lithium loss as a function of the negative electrode potential, temperature, and time. Storage and cycling cases are simulated, and the effect of the SEI film resistance on the SEI growth rate is discussed.

5.2 Experimental

In this section, experimental methods are discussed. First the method for producing aged cells with controlled experimental conditions is documented. Next, the procedure for fabricating coin cells in order to characterize each electrode of the pouch cell is discussed. The coin cells are cycled galvanostatically (constant current) to obtain the open-circuit voltage of each electrode versus a lithium reference.

5.2.1 Aging Campaign

Pouch cells with composite LMO/NMC positive electrode and graphite (C) negative electrode are used to study battery degradation for a PHEV duty cycle. They possess 15 Ah nominal capacity and 3.75 V nominal voltage. The test hardware consists of a 400 A, 25 V load and 400 A, 8 V supply individually controlled via Labview software and a personal computer. The United States Advanced Battery Consortium (USABC) PHEV charge depleting and charge sustaining profiles (Anonymous, 2010) define the aging duty cycles. These power-based profiles are plotted in Figure 5.2 after applying a battery scaling factor of 94, chosen to approximate a PHEV with 10 mile CD range.

For cells assigned to CD operation, the basic profile defined in Figure 5.2 is repeated either five, six, or seven times to cause a depth of discharge of approximately 55, 65, or 75$\%$, respectively. Then the cell is charged at either C/3, 3C/2, or 5C rate to a voltage of 4.15 V, where a constant voltage (CV) portion finishes the charge to 95$\%$ SOC and the entire cycle is repeated. The cells charging at 5C rate are meant to represent a fast charge situation, so the CV duration is set to five minutes instead of the twenty minute duration

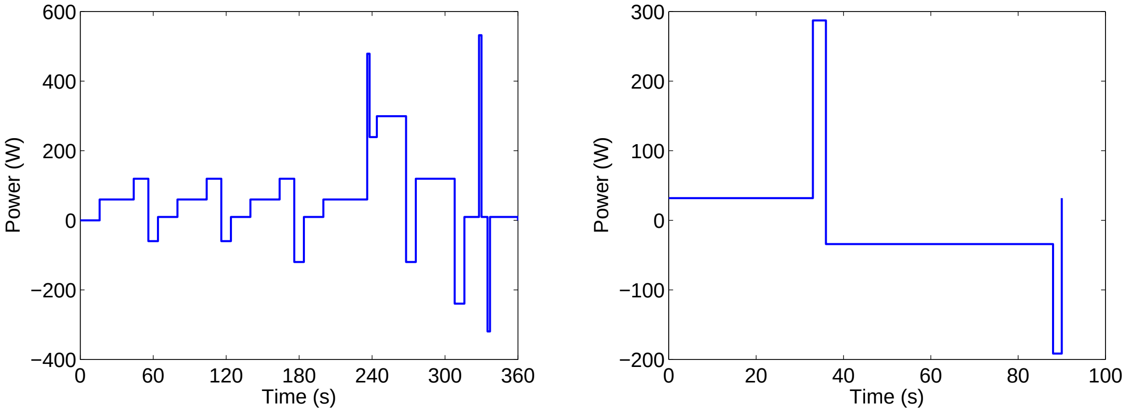

(a) (b)

Figure 5.2: a) Charge depleting duty cycle and b) charge sustaining duty cycle.

used for the other charge rates. For cells performing CS operation, the SOC is set by using the cell open-circuit voltage (OCV) versus SOC curve to select the voltage corresponding to 45%, 35%, or 25% SOC. A voltage window of $\pm$ 10 mV is enforced around the nominal setpoint, and if the OCV of the cell violates this window, a small amount of charge is used to bring the cell back within the operating window. The test conditions for all cells considered in the aging study are summarized in Tables 5.1 and 5.2.

Table 5.1: Summary of test conditions for CD aging experiments, all conducted at 30°C.

Charge Rate	C/3	C/3	C/3	3C/2	3C/2	3C/2	5C	5C	5C
SOC (%)	95 - 40	95 - 30	95 - 20	95 - 40	95 - 30	95 - 20	95 - 40	95 - 30	95 - 20

Table 5.2: Summary of test conditions for CS and mixed CD:CS aging experiments.

SOC (%)	45	35	25	35	35	35	35
Temperature (°C)	30	30	30	30	30	10	45
CD:CS Ratio	0:1	0:1	0:1	1:1	1:3	1:1	1:1

5.2.2 Half Cell Experiments

Half cell experiments are conducted to parametrize an electrochemical model for detailed analysis of the aging data. Positive and negative electrode samples are harvested by disassembling a pouch cell that had not been subjected to aging experiments. Electrode disks of 15 mm diameter are punched from the cell stack, and the electrode coating is removed from one side with 1-methyl-2-pyrolidinone solvent to expose the bare metal current collector without exposing the working side of the electrode to the solvent. All electrode materials are thoroughly dried inside a vacuum oven before being transferred to an Argonne filled glovebox with less than 0.1 ppm O_2 and H_2O for cell assembly. Coin cell cases of 20 mm diameter and 3.2 mm height (2032) are used for this study, as described in Chapter 2. Lithium metal electrodes of 17 mm diameter are used as the counter and reference electrode. A single layer of 19 mm diameter separator material (type 2400 provided by Celgard, LLC) is placed between the working and reference electrodes. The electrolyte mixture utilizes a 1:1 EC:DMC solvent with $1M\ LiPF_6$ salt. After crimping, three C/10 formation cycles are conducted followed by three C/5 cycles, where the capacity rate is determined by area-scaling the measured capacity of the fully assembled pouch cell. Following formation, capacity tests are conducted at C/20 and C/10 rates to characterize the capacity loading and OCV of each electrode.

Table 5.3: Governing equations describing the concentration and potential dynamics. Equations (5.1) - (5.4) represent the particle sub-model, while Eqs. (5.5) - (5.7) represent the liquid sub-model.

Variable	Governing Equation	
η_i	$\eta_i(t) = U_i(t) - \phi_i(t) - R_i \gamma_j I_i(t)$	(5.1)
c_i	$\frac{\partial c_i}{\partial t} = \frac{D_{s,i}}{r}\left(r^2 \frac{\partial c_i}{\partial r}\right)$, $\frac{\partial c_i}{\partial r} = 0$ at $r = 0$, $D_i \frac{\partial c_i}{\partial r} = -\frac{j_i(t)}{F}$ at $r = R_{p,i}$	(5.2)
j_i	$j_i(t) = 2 i_{0,i} sinh\left(\frac{F}{2\bar{R}T}\eta_i(t)\right) = \frac{\gamma_j I_i}{a_i A L \epsilon_i}$	(5.3)
$i_{0,i}$	$i_{0,i} = F k_i \sqrt{c_e \left(c_{max,i} - c_i(R_{p,i})\right) c_i(R_{p,i})}$	(5.4)
c_e	$\epsilon_e \frac{\partial c_e}{\partial t} = D_e \frac{\partial^2 c_e}{\partial x^2} + \frac{a_i\left(1-t_+^0\right)}{F} j_i(t)$	(5.5)
ϕ_e	$\frac{\partial \phi_e}{\partial x} = -\frac{i_e(t)}{\sigma_e} + \frac{\bar{R}T(1-t_0^+)}{F}(1+\beta)\frac{\partial ln(c_e)}{\partial x}$	(5.6)
V_e	$V_e(t) = \phi_e(L_c, t) - \phi_e(0, t)$	(5.7)
V	$V(t) = \phi_p(t) - \phi_n(t) - V_e(t) - R_c I(t)$	(5.8)

5.3 Model Development

The model presented in this chapter is intrinsically different from prior work because it is able to model electrodes composed of multiple active materials in a computationally efficient manner. The overall structure of the model builds upon the model structured presented in Chapter 4 with an important extension; two types of particles are included in each electrode. In the negative electrode, the two particles define a coarse representation of a solid-electrolyte interphase (SEI) layer thickness distribution that will be discussed in more detail in the following sections. In the positive electrode, the two particles represent each active material of the NMC – LMO composite.

The fundamental assumption is that the particles pass current while maintaining a uniform potential, in a process that is analogous to impedances operating in parallel within an electrical circuit (for electrical circuit background see (Rizzoni, 2003)). However, there are nonlinear, dynamic terms that are significant contributors to the cell overpotential. The model structure is outlined in Figure 5.3, with equations summarized in Table 5.3.

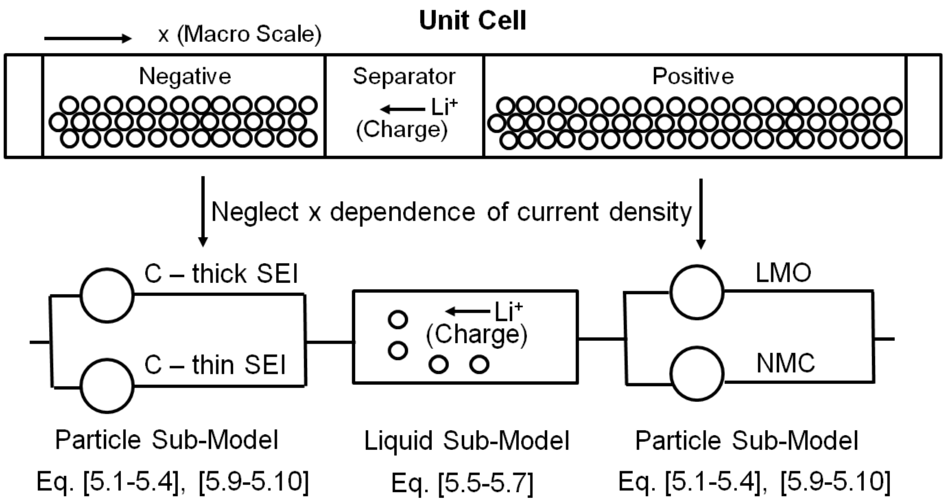

Figure 5.3: Schematic of model structure composed of liquid and particle sub-models.

Solving the nonlinear system of equations corresponding to coupling between multiple active material particles first requires an initialization criteria for the local current, denoted as the fraction parameter γ_j times the current $I(t)$. Once the initial current division is established, an iterative solution is completed as follows. The concentration of Eq. (5.2) is solved by the Pade approximation method detailed in Chapter 4, using the local current associated with each particle. The predicted concentration is used to calculated the OCV of each particle. The OCV (U_j), overpotential resulting from the non-linear contribution from the Butler-Volmer law (η_j), and overpotential due to the linear ohmic resistance R_j are computed for each particle sub-model as

$$\phi = U_j - R_j I \gamma_j - \eta_j(I\gamma_j) \tag{5.9}$$

This gives n_p equations, where n_p is the number of active material particle types in the electrode, j is the particle index. There are $n_p + 1$ unknowns corresponding to the n_p local currents and the electrode potential ϕ, so an additional equation is needed which ensures that the local currents sum to the total external current

$$\sum_{j=1}^{n_p} \gamma_j = 1 \tag{5.10}$$

The system of $n_p + 1$ nonlinear equations defined by applying Eq. (5.9) to each particle along with Eq. (5.10) is solved using an iterative nonlinear solver. After the liquid sub-model potential has been computed and the iterative solution has been completed for each electrode, the cell voltage is determined by Eq. (5.8).

5.4 Aging Analysis

The results of this section are divided into three sub-sections, beginning with the summary of the experimental aging campaign. Next, half cell results are presented and used to parametrize the model, followed by validation with full cell data for a dynamic current profile. Then the model is used to simulate prospective aging scenarios by empirically scheduling a subset of model parameters and performing a comparison between model and experimental differential capacity plots.

5.4.1 Pouch Cell Aging

To begin the aging analysis, a summary of the experimental capacity test data is presented in Figure 5.4.

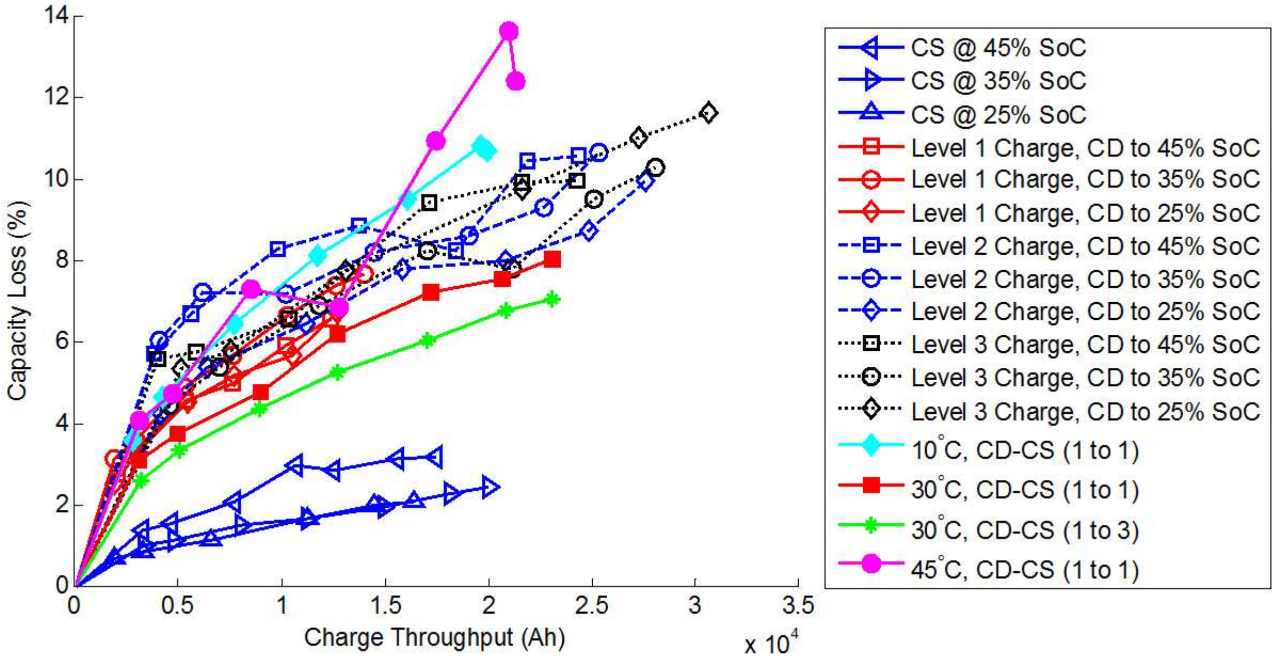

Figure 5.4: Summary of experimentally determined pouch cell capacity fade.

There is a distinct difference in the capacity fade level between cells operating in CD mode and those operating in CS mode. Cells that operated in the mixed CD:CS regime exhibited capacity fade at a weighted average rate of the two modes. Despite differences in the degradation rate, the cells tended to follow a common degradation trend of $\Delta Q = c_1(Ah)^{c_2}$, with $c_2 \approx 0.45$, $c_1 \approx 0.10$ for CD mode, and $c_1 \approx 0.025$ for CS mode. It is interesting that differences in charge rate, and minimum SOC in CD mode did not produce measurable differences in the capacity fade rate when plotted versus total capacity throughput. One potential explanation for this finding is the reduced CV time of the high charge rate reduced the total time spent at high SOC, which in turn reduced the overall rate and severity of the aging process to offset the effects of the high charge rate.

5.4.2 Aging Mechanism Assessment

Next, differential capacity is used to analyze the source of capacity fade. First, the cell OCV must be fit using half cell data so that features of the differential capacity plot can be assigned to either the negative or positive electrode. Low-rate, galvanostatic, half cell experiments were used to characterize the individual half cell OCVs. The individual electrode OCVs are scaled and shifted relative to one another to identify the capacity loading, or equivalently the active volume fraction, and the initial SOC in each electrode. A nonlinear least squares approach, similar to the approach of Chapter 4, is used rather than relying on initial half cell capacity measurements due to the complexities involved in identifying the formation cycle irreversible lithium loss. A summary of this procedure is shown in Figure 5.5.

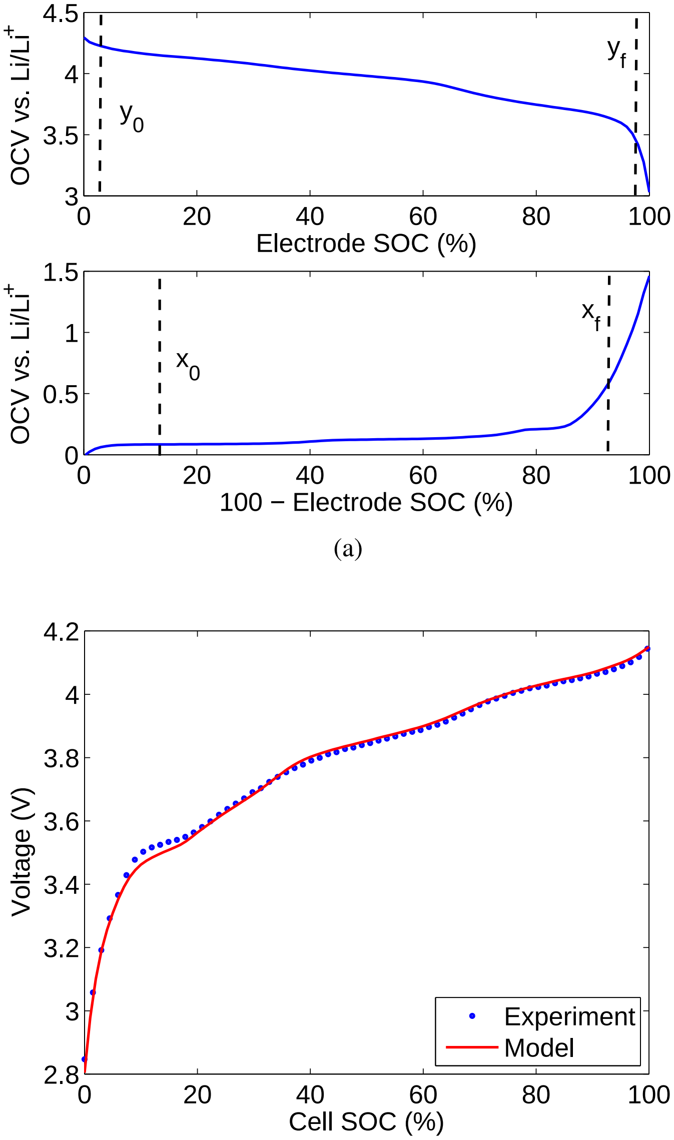

(a)

(b)

Figure 5.5: (a) Half cell OCV with identified full cell SOC range and (b) agreement with full cell OCV measurement.

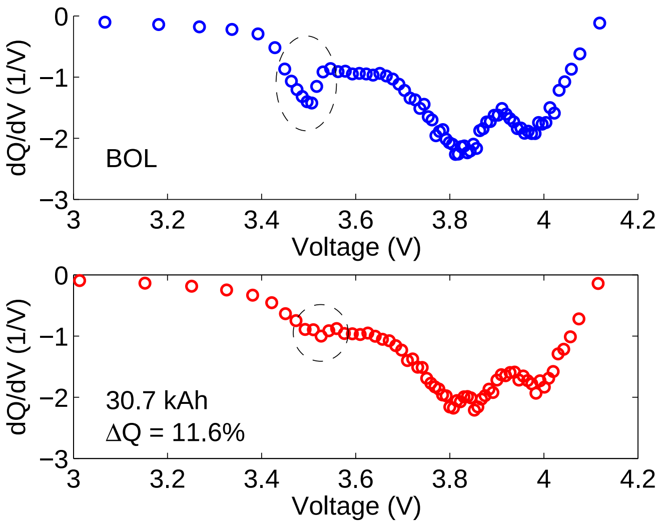

(a)

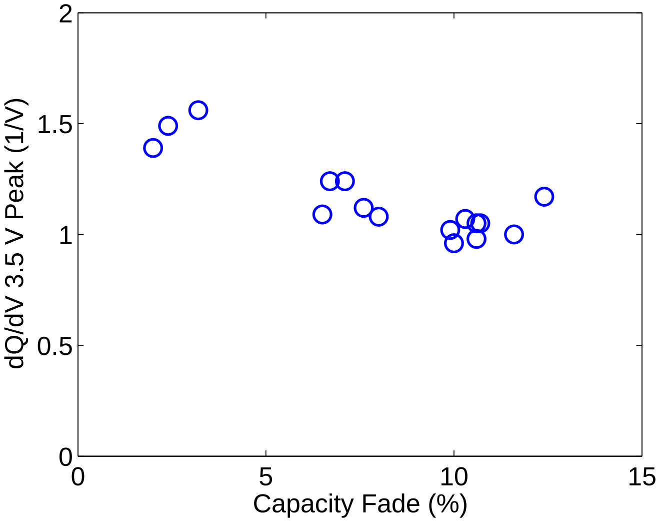

(b)

Figure 5.6: (a) Differential capacity assessment for the cell tested in charge depleting mode with 25% minimum SOC, 5C charge rate, at 30 °C. Accumulated charge throughput at the end of testing is indicated on the lower plot. (b) Relationship between 3.5 V dQ/dV peak and capacity fade magnitude for all tested cells. Operating conditions are intentionally not labeled to emphasize the general trend of the entire aging campaign rather than a specific cell result.

The identifed SOC ranges are indicated on each half cell plot of Figure 5.5a. These identified SOC ranges are used to give a prediction of the full cell OCV, and this prediction is compared with the experimental cell OCV in Figure 5.5b. Overall the half cell prediction agrees well except for a slight underprediction of the cell voltage for low SOC.

Figure 5.6a shows the differential capacity plots (as defined in Chapter 2) at beginning-of-life (BOL) and at the end of testing for the cell experiencing the highest level of capacity fade, which is the 5C charge rate, 25% minimum SOC, CD case. The main source of capacity fade is the loss of the 3.5 V peak, indicated by the dashed ellipse. Above 3.5 V, the changes are mostly negligible. Although results for only one cell are plotted, this finding is common to all cells tested as part of this aging campaign. Figure 5.6b plots the 3.5 V dQ/dV peak value versus the magnitude of capacity fade for each cell at the end of testing, which corresponds to capacity fade values ranging from 3% to over 10%. The 3.5 V peak value is linearly correlated with capacity fade regardless of the cell operating condition or capacity fade level. The common degradation trend of all cells for capacity fade versus total Ah throughput, combined with the agreement in changes of differential capacity during aging, suggests that the mechanism of capacity fade is not a function of the operating conditions explored within this work.

There are several potential mechanisms that could be responsible for the loss of the 3.5 V peak, but two main hypotheses are discussed here. First, the positive electrode capacity could be reduced during aging such that it becomes the limiting electrode. In this case, the negative electrode would not be de-lithiated to the composition that corresponds to the 3.5 V peak. Loss of positive electrode capacity could be due to loss of either LMO or NMC active material, or some combination of both. In this paper, results are presented for loss of LMO due to the dissolution phenomenon associated with this chemistry (Liu *et al.*, 2009).

The second proposed mechanism involves non-uniform solid-electrolyte interphase (SEI) layer growth that creates a distribution of SEI thickness throughout the negative electrode, which corresponds to a a distribution of film resistances. See Chapter 2 for a discussion of the classical views of SEI growth.

Prior research has proposed that different levels of lithiation throughout the electrode could cause the separation of dQ/dV peaks into separate, smaller peaks (Bloom *et al.*, 2006). Here it will be demonstrated that the same effect can be achieved with a coarse approximation of a film resistance distribution.

5.4.3 Model Parametrization and Validation

The first step of parametrizing the electrochemical model is to match the thermodynamic behavior of each electrode. In the case of the negative electrode, this requires a simple procedure that utilizes an interpolation table of the experimentally measured half cell OCV. This approach was used in place of fitting an analytical function to more accurately match the derivative of the characteristic voltage plateaus. For the positive electrode, the half cell OCV versus Li/Li^+ for LMO and NMC are cited from literature (Kim *et al.* (2012) and Shaju *et al.* (2004) respectively). Then, the model is used to predict several prospective C/10 discharge curves while treating the relative volume fraction of each material as an adjustable parameter, but matching the total active material volume identified previously. Figure 5.7a shows the prospective discharge curves for several candidate active material mixtures.

Since the comparison between model and experiment is performed at a low rate, it should be minimally impacted by the chosen resistance parameters and primarily governed

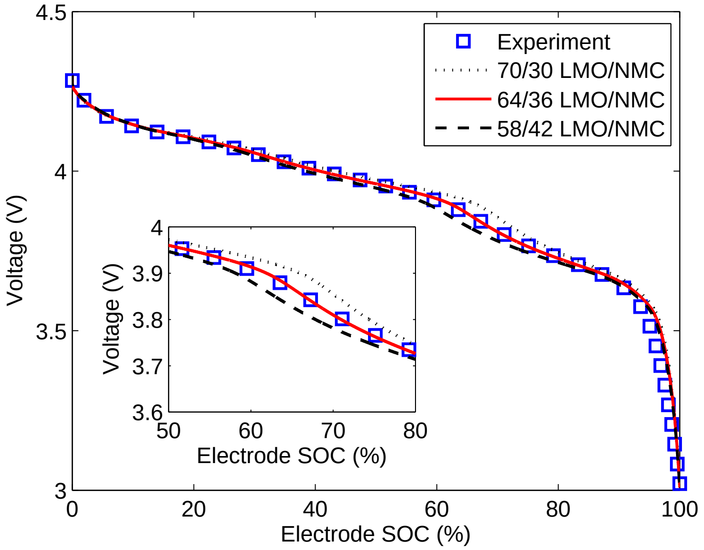

Figure 5.7: Model prediction of C/10 galvanostatic discharge for various prospective mixtures of LMO/NMC, with 64/36% LMO/NMC showing the closest agreement with the experimental data.

by the capacity contributions and OCV of the electrode components. The model agrees best with the experimental data for 64/36% LMO/NMC relative percentage. The characteristic knee that occurs upon transition from primarily using LMO to primarily using NMC is matched well for this active material mixture. A relatively small range of prospective curves is plotted even though several other simulations were conducted, because the additional simulation results continued to diverge away from the optimal result in the same direction as the plotted results. For instance, the 50/50% result exihibited an earlier onset of the transitional knee, whereas the 75/25% mixture pushes the feature further towards higher depth-of-discharge.

Due to differences in the area-specific impedance between the full cell and coin cells that arise from the fabrication process, the half cell data is not used to identify the ohmic and

Table 5.4: Summary of model parameters used for simulation results.

Parameter	Definition	Value		
		C	LMO	NMC
R_p	primary particle radius (μm)	3.5	2	2
ϵ	active material volume fraction	0.51	0.32	0.18
c_{max}	saturation concentration of Li^+ (mol/m^3)	30540	17160	35340
D_s	solid phase diffusion coefficient (m^2/s)	1.5 $\times 10^{-14}$	6.5 $\times 10^{-15}$	6.5 $\times 10^{-15}$
k	kinetic rate constant	3 $\times 10^{-8}$	1.9 $\times 10^{-9}$	2.5 $\times 10^{-10}$
q	specific capacity (mAh/g)	372	109	156
L	electrode thickness (μm)	50	70	
A	current collector area (m^2)	0.877		
D	liquid phase diffusion coefficient (m^2/s)	1.7 $\times 10^{-10}$		
c_0	electroneutral concentration (mol/m^3)	1000		
L_{sep}	separator thickness (μm)	25		
t_+^0	transference number	0.37		

kinetic resistance parameters or diffusion coefficients. Instead, literature values are used, and tuning with full cell data is applied where necessary. The full set of model parameters and their sources are summarized in Table 5.4.

Cell performance data is used to validate the model predictions. First the model is compared with galvanostatic discharge data for two separate rates in Figure 5.8a. The model voltage prediction is plotted alongside experimental data for the CD aging duty cycle in Figure 5.8b, where the data is taken shortly after the onset of the aging campaign so that the cell is still at the BOL stage.

In the galvanostatic case, although the dependence of the capacity on the discharge rate is minimal for the rates presented, the model adequately captures this effect. The model overpredicts the effects of the graphite plateaus for the 1C rate, resulting in greater variation in dV/dQ than is present in the experimental data. For the charge depleting data, agreeement is good for the entire SOC range, with 95% of the error less than 23 mV. Overall the model and experiment exhibit good agreement, which gives confidence that the model has

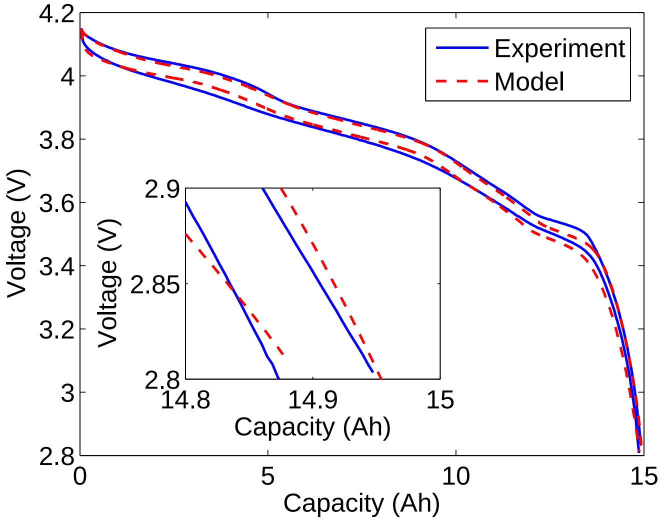

(a)

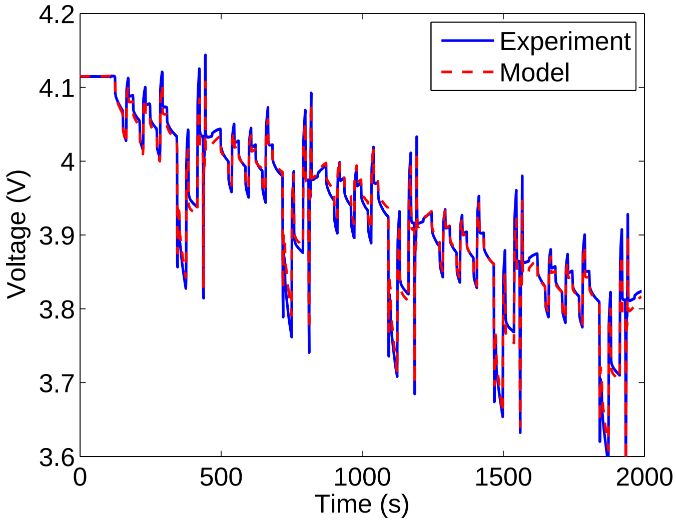

(b)

Figure 5.8: (a) Model prediction of galvanostatic discharge for low and moderate rates. (b) Model prediction for a dynamic CD profile.

captured the performance features of each electrode. Next, the model is used to interpret the previously described changes in the differential capacity plot.

5.4.4 Model-Based Aging Analysis

At this point, the model is used to simulate the effects of aging mechanisms that may produce the experimentally identified capacity fade and differential capacity data. A single cell from the aging campaign is used for this case study with CD operation, 5C charging, and 25% minimum SOC. A capacity assessment at BOL as well as two levels of capcity fade are studied in order to confirm whether the proposed aging mechanisms match the aging evolution versus total charge throughput of the experimental data.

An empirical approach is used where the model parameters are first scheduled to achieve the desired level of capacity fade, then the galvanostatic discharge is simulated. For the positive electrode case, the volume fraction of LMO is reduced to achieve the experimentally observed level of capacity fade. For the SEI growth case, the initial amount of cyclable lithium is reduced to match the experimentally observed capacity fade. Two particles of equal volume fraction are simulated in the negative electrode. One particle has a constant, small film resistance representative of the initial SEI thickness after formation, while the film resistance of the other particle increases proportionately with the loss of cyclable lithium. The additional film resistance, R_{SEI}, beyond the formation value is defined as

$$R_{SEI} = \frac{\delta_{SEI}}{\sigma_{SEI}\left(a_n R_n\right) A L_n} \quad \text{with} \quad \delta_{SEI} = \frac{\Delta x c_{max,n} M_{SEI} S}{\rho_{SEI} a_n} \tag{5.11}$$

where δ_{SEI} is the SEI thickness, σ_{SEI} is the SEI conductivity, Δx is the decrease in x_0 compared its initial value, M_{SEI} is the molecular weight of SEI, S is the stoichiometric coefficient relating moles of lithium to moles of SEI product, and ρ_{SEI} is the density of the SEI. Figure 5.9a shows the parameter values used to simulate the capacity tests and compute the associated differential capacity. The required reduction of LMO volume fraction is greater than the reduction in cell capacity. This is because the LMO has a smaller specific capacity than the NMC material, and therefore contributes less to the capacity per unit volume.

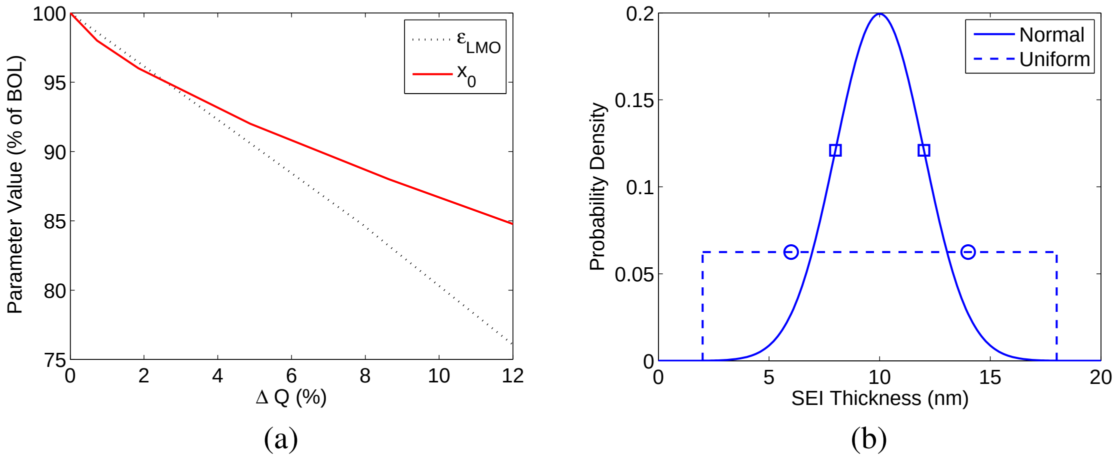

(a) (b)

Figure 5.9: (a) Relationship between relative parameter values and capactiy fade. Parameters are ϵ_{LMO} for the LMO loss case and x_0 for the SEI growth case. (b) Graphical representation of two hypothetical SEI thickness distributions with a two-point approximation of each distribution indicated by symbols.

Two examples of SEI thickness distributions are plotted in Figure 5.9b as a probability density function versus thickness. Since the exact distribution is unknown, both Gaussian and uniform density are shown. In general these thickness variations may arise from local morphological conditions that are favorable for SEI growth, or variations in the growth rate with respect to the electrode thickness due to gradients of the local electrolyte concentration and potential. A quantitative understanding of the distribution is outside the scope of this work, but the proposed concept is used in an empirical manner.

The results associated with simulating each possible degradation mechanism are given in Figure 5.10. The model output is compared with the experimental data at 5% and 10% capacity fade values.

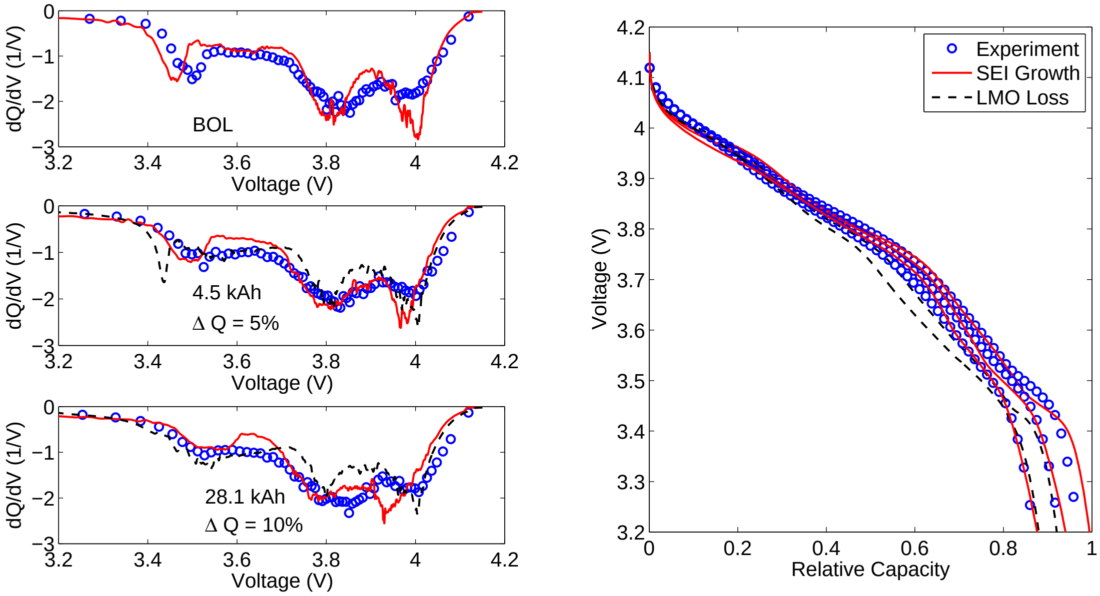

(a) (b)

Figure 5.10: (a) Differential capacity assessment at beginning of life (BOL), and at two stages of degradation. Experiment is indicated by symbols, and lines indicated model fit. Only one line is shown for the BOL stage since the cases are identical when no aging is present. (b) Constant current (1C) discharge experiment (symbols) and simulation (lines), indicating low voltage prediction by LMO loss mechanism for equivalent capacity fade values.

As discussed previously, there are minimal changes in the experimental data for the region greater than 3.8 V. The SEI growth case predicts a slight shift to lower voltages of the features in this region, as does the LMO loss case. However, the most important part of the plot is the reduction in the 3.5 V peak value cited previously. The SEI growth case predicts a gradual removal of the peak that corresponds well with the experimental data.

The LMO loss results show a reduction in the peak, but it is still present to a greater extent than the experimental data indicates for the 5% capacity fade case. For the 10% capacity fade simulation, the peak has been removed by both the SEI growth and LMO loss cases. However, the LMO loss case has significant error in the 3.75 to 3.85 V region that causes underprediction of the voltage for the 0.5 to 0.7 relative capacity range of Figure 5.10b.

It is possible that there are simultaneous contributions to capacity fade from each mechanism. In particular, it may be possible that positive electrode limitations become more apparent for long-term aging beyond the initial stages of aging analyzed here.

5.5 Development of Cyclable Lithium Loss Model for Capacity Fade

The previous analysis indicated that loss of cyclable lithium is a dominant aging effect for the presented aging campaign in this chapter. In the proposed model of SEI growth, which differs from the classical views presented in Chapter 2, it is assumed that the loss of cyclable lithium due to the SEI side reaction can follow two possible scenarios encompassing either a site-limited or kinetic-limited growth mode. It is stressed that these processes occur simultaneously, and physically they represent the distinction between increased surface area coverage and thickness evolution of the SEI respectively. It will be demonstrated that the dynamic interaction between the two reaction modes, and the inclusion of both the EC reduction reaction and the SEI product formation reaction are required to properly capture the time-dependent rate of capacity fade. Figure 5.11 further illustrates the difference between the site-limited and kinetic-limited growth regimes.

In this theory, the side reaction process begins by transport of solvent molecules from the bulk to the graphite surface in a process that is not hindered by the presence of SEI

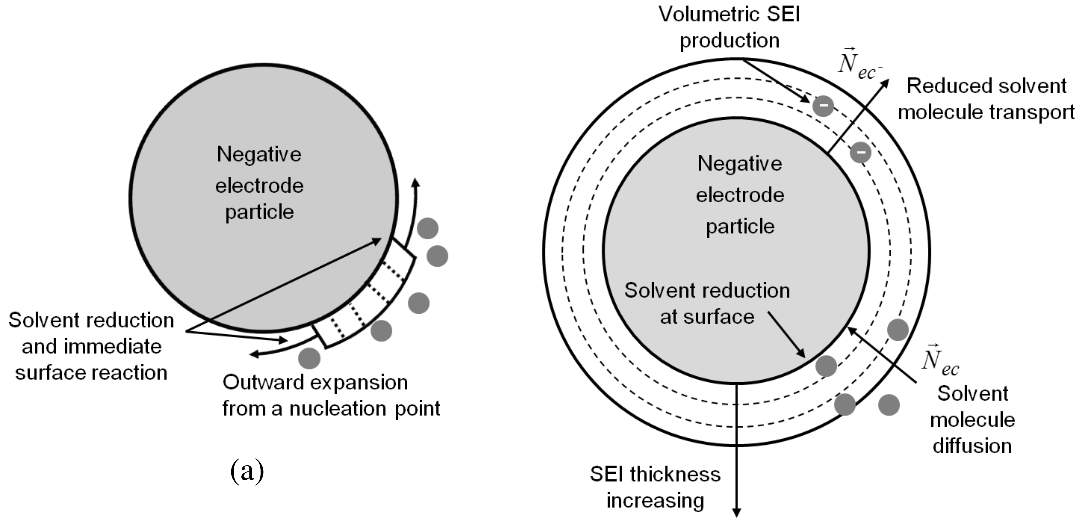

(a)

(b)

Figure 5.11: Schematic diagrams of the SEI growth process for the a) site-limited and b) kinetic-limited growth regimes (not to scale).

regardless of thickness. An electron from the graphite electrode is used to reduce the solvent molecules located at the graphite surface. The graphite electrode is now slightly less negatively charged than prior to the reaction. As a result, it loses attraction for one Li^+ ion, which de-intercalates and diffuses into the liquid phase. The site-limited model assumes outward expansion of the thin SEI layer onto previously uncovered graphite surface. Under this assumption, reactants are readily available at the reaction sites so the reduced EC molecule reacts immediately with surrounding Li^+, and it is assumed that Eq. (5.12) is not rate limiting in this process. The additional SEI molecule leads to increased area coverage of the SEI, and as the SEI reaction proceeds the number of reaction sites is reduced by SEI coverage.

Both the initial reduction reaction and the SEI product formation depend explicitly on the time-varying amount of available sites, $\theta(t)$, in moles. Beginning from Eqs. (2.103) and (2.104), the revised reactions reflecting the site dependence are

$$EC + \theta(t) + e^- \rightharpoonup EC^- \tag{5.12}$$

$$2EC^- + 2Li^+ + \theta(t) \rightharpoonup (CH_2OCO_2Li)_2 + C_2H_4 \tag{5.13}$$

The symbol $\theta(t)$ is not a participant in the reaction, but merely indicates that a reaction site is required for the reaction to proceed. The kinetic-limited regime requires the transport of solvent molecules through the pre-existing SEI to the graphite surface, but as highlighted by the previous time scale analysis, this transport step cannot be rate limiting. At the graphite surface, solvent molecules are reduced by electrons supplied by the graphite electrode surface. Since the reaction is taking place in a location where SEI has previously formed, it is assumed that there is a greatly reduced number of sites available on the graphite surface for the EC reduction reaction to continue.

This modeling convention reflects the consideration that some SEI will continuously form at the graphite surface due to breakdown of the existing layer and subsequent re-exposure of available sites, but that the rate of this process is significantly reduced compared with forming SEI on pristine graphite. The reduced EC molecule is transported away from the electrode surface into the SEI volume. Then it proceeds to form SEI as a volumetric reaction within the existing SEI to increase the thickness of the layer. Unlike the site-limited SEI production, there is no site dependence for Eq. (5.15) since it occurs volumetrically throghout the existing SEI instead of at the graphite surface. The revised reactions for this SEI growth regime are

$$EC + \chi\theta_0 + e^- \rightharpoonup EC^- \tag{5.14}$$

$$2EC^- + 2Li^+ \rightharpoonup (CH_2OCO_2Li)_2 + C_2H_4 \tag{5.15}$$

where θ_0 is the initial number of reaction sites, and $\chi \ll 1$ is a parameter that defines the small number of remaining surface sites after the graphite is covered by SEI. This represents the consideration that SEI growth does not stop completely once the graphite surface is covered, but instead continues at a reduced rate. Continued SEI growth means that EC is still being reduced at the graphite surface, but the process is hindered by the presence of existing SEI attached to the graphite.

5.5.1 Reaction Rate Modeling

The characterization of the number of sites and the effect of the number of sites on the rate of EC reduction are important contributions of this model. By inspection of Eqs. (5.12), (5.13), (5.14), (5.15), the amount of reduced EC will not be limiting if the number of sites is large. However, as the number of sites decreases, so will the rate of EC$^-$ production such that the rate of SEI product formation predicted by Eq. (5.15) will decrease. The side reaction current density, i_{SEI} is obtained for each growth regime by modeling the rate of either Eq. (5.13) or (5.15). The total rate of active lithium consumption by the side reaction, with units of g/s, is

$$\frac{dm_{Li}}{dt} = \frac{M_{Li}}{F}\left(I_{SEI,s} + I_{SEI,k}\right) \tag{5.16}$$

where $I_{SEI,s}$ is the site-limited rate, $I_{SEI,k}$ is the kinetic-limited rate, M_{Li} is the molecular weight of lithium, and m_{Li} is the mass of lithium consumed by the side reaction. It can be reported in g or converted to Ah.

The rate of the side reaction has been defined in terms of a current to stress that Li$^+$ ions are the primary reactant of interest. Next, define c_{EC} as the concentration of EC solvent, c_{EC^-} as the concentration of reduced EC, B as the number of moles of SEI product CH_2OCO_2Li, and c as the Li^+ concentration. Then the rate of formation of the SEI product, in mol/s, for the site-limited regime is found by multiplying the side reaction current density by the available area. The result is

$$\frac{dB_s}{dt} = \frac{i_{SEI,s}}{F}\frac{\theta(t)}{\rho_\theta} \tag{5.17}$$

where $i_{SEI,s}$ is the site-limited current density and ρ_θ is a surface density conversion factor, relating the number of sites to electrode surface area. The quantity ρ_θ has units of mol/m^2, and θ has units of moles. Currently ρ_θ is treated as an empirical parameter. The initial number of sites is defined as $\theta_0 = \rho_\theta a_n A_n L_n \epsilon_n$. Next the site-limited current density is defined as

$$i_{SEI,s} = i_{0,s} exp\left(-\frac{\phi_n F}{\bar{R}T}\right) \tag{5.18}$$

where $i_{0,s}$ defines the exchange current density of the side reaction and the Arrhenius exponential term characterizes the dependence of the reaction rate on the potential of the negative electrode, ϕ_n. A Tafel expression has been used since Eq. (5.12) is assumed to proceed only in one direction due to irreversibility of film formation. The exchange current density is

$$i_{0,s} = Fk_{SEI,s}c_{EC}c \tag{5.19}$$

where $k_{SEI,s}$ is the rate constant for Eq. (5.13), c_{EC} is the concentration of EC molecules, and c is lithium concentration. Combining Eqs. (5.17), (5.18), and (5.19) gives the condensed expression for the site-limited SEI production rate

$$I_{SEI,s} = \frac{Fk_{SEI,s}c_{EC}\theta(t)}{\rho_\theta} exp\left(-\frac{\phi_n F}{\bar{R}T}\right) \tag{5.20}$$

Since in most relevant cases the negative electrode potential will vary in time, Eq. (5.20) is integrated numerically.

For the kinetic-limited regime the rate, $dB_k/dt = I_{SEI,k}/F$, is

$$\frac{dB_k}{dt} = \frac{i_{SEI,k}\left(\frac{\theta_0-\theta(t)}{\rho_\theta}\right)L_{avg}(t)}{F} \tag{5.21}$$

where $i_{SEI,k}$ is the volumetric current density of the kinetic-limited side reaction, and $L_{avg}(t)$ is the average thickness of the SEI. The thickness of the SEI product formed by the described mechnism is non-uniform, since it spreads to cover the electrode surface area over a non-negligible time frame and SEI begins kinetic-limited thickness growth immediately after formation. The portions of the layer that form initially will have a longer time period for kinetic-limited growth and therefore develop a larger thickness than SEI formed at less favorable sites later in the process. The volumetric current density is characterized by an exchange current density and exponential dependence on potential

$$i_{SEI,k} = i_{0,k} exp\left(-\frac{\phi_n F}{\bar{R}T}\right) \tag{5.22}$$

The definition of the exchange current density is

$$i_{0,k} = F k_{SEI,k} c_{EC^-} c \tag{5.23}$$

where $k_{SEI,k}$ is the rate constant for Eq. (5.15) and c_{EC^-} is the concentration of reduced EC ions. Combining Eqs. (5.21), (5.22), and (5.23) gives the condensed expression for kinetic-limited SEI production

$$I_{SEI,k} = F k_{SEI,k} c_{EC^-} c \left(\frac{\theta_0 - \theta(t)}{\rho_\theta}\right) L_{avg}(t) exp\left(-\frac{\phi_n F}{\bar{R}T}\right) \tag{5.24}$$

The only remaining unknown of the preceding discussion is the concentration of reduced EC molecules, which is coupled to the kinetic-limited reaction rate.

5.5.2 Conservation Analysis for Reduced EC

A control volume analysis is used to compute the concentration of reduced EC within the SEI layer. A one-dimensional approach could be used with respect to the SEI thickness, but this would imply a non-uniform rate of SEI production throughout the existing SEI

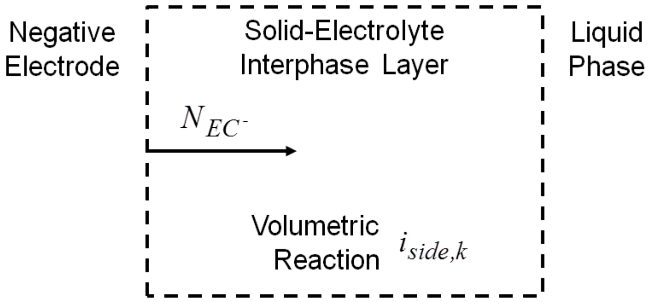

Figure 5.12: Control volume analysis for determining the mass of reduced EC within the SEI region.

layer, with consequences that make predicting cell performance much more complicated. A flux of EC^- occurs at the graphite surface due to the reduction of EC that occurs there. Throughout the SEI, a volumetric reaction consumes the EC^- molecules to increase the thickness of the exisiting SEI. The fluxes and sinks governing the mass of EC^- within the SEI layer are summarized in Figure 5.12, where it has been assumed that all EC^- is consumed by the side reaction, rather than exiting the SEI layer without reacting. The differential equation defining the mass of EC^- within the SEI is

$$\delta_{avg}(t)\frac{dc_{EC-}}{dt} = N_{EC-} - i_{SEI,k}\delta_{avg}(t) \tag{5.25}$$

Based on the disparity between the diffusion time scale and the aging time scale, the average SEI thickness is treated as constant in the above conservation equation. The flux N_{EC-} is defined by Eq. (5.18), except that the number of sites is set to a fixed fraction of the initial value so that the exchange current density becomes fixed. This reflects the fact assumption that a majority of the available reduction sites have been occupied by SEI once the graphite surface is covered, causing EC reduction to take place at a reduced rate beneath the pre-existing SEI

$$N_{EC^-} = k_{red,k} c_{EC} \chi \theta_0 exp\left(-\frac{\phi_n F}{\bar{R}T}\right) \tag{5.26}$$

Equation (5.26) defines a constant flux term with the exception of the time varying negative electrode potential. The volumetric reaction term $i_{SEI,k}$ is defined by Eq. (5.22). Since this sink term also depends on the EC^- concentration, Eq. (5.25) must be solved in a coupled fashion. Here the Crank-Nicholson implicit method is applied. This gives the average EC^- concentration within the SEI as a function of time, which is then used to compute the volumetric reaction rate and resulting loss of cyclable Li^+.

5.5.3 Consequences of SEI Growth

The relationship between the number of moles of SEI product and several important electrochemical parameters is now discussed. To begin, the number of moles produced via the site-limited mechanism is related to the electrode surface area covered by SEI film. A mass balance approach is used with an assumed value for the initial thickness of SEI upon formation as δ_0, and noting that $\delta_0 \theta_{SEI} \rho_{SEI} = B_s M_{SEI}$, which is essentially computing the site-limited SEI mass using two equivalent calculations. Then the number of available sites is computed as

$$\theta(t) = \theta_0 - \frac{B_s(t) M_{SEI} \rho_\theta}{\rho_{SEI} \delta_0} \tag{5.27}$$

Note that all the terms are constant except for $B_s(t)$, and that the number of sites is monotonically decreasing. Additionally, the relationship $\theta(t) + \theta_{SEI}(t) = \theta_0$, where $\theta_{SEI}(t)$ is the number of sites covered by SEI.

A similar mass balance procedure is followed for the kinetic-limited regime to relate the number of moles of SEI product produced to the SEI thickness. For a unit surface area of SEI formed in the time interval $t = t_i$ to $t = t_i + \Delta t$, the SEI thickness at time $t = t_f$ is found as

$$\delta(t) = \delta_0 + \int_{t_i+\Delta t}^{t_f} \frac{dB_k}{dt} \frac{M_{SEI}}{\Delta A_{SEI} \rho_{SEI}} dt \tag{5.28}$$

where the initial thickness that is created when new surface area is covered by SEI has been included. The term ΔA is the newly formed SEI surface area created within the time interval $t = t_i$ to $t = t_i + \Delta t$, given by

$$\Delta A_{SEI} = \frac{\theta_{SEI}(t_i + \Delta t) - \theta_{SEI}(t_i)}{\rho_\theta} \tag{5.29}$$

Finally, the effect of the SEI on system-level cell performance is defined. The area-specific impedance added by the SEI is defined as

$$R_{SEI}(t) = \frac{\delta(t)}{\sigma_{SEI}} \tag{5.30}$$

This is multiplied by the particle surface area covered by SEI to give a resistance. The previously described thickness distribution gives rise to a resistance distribution.

The capacity stored within the SEI layer can be computed as a function of the SEI volume by performing a material balance on the number of moles of Li stored in the SEI layer.

$$\Delta Q(t) = s_{Li} \left(B_k(t) + B_s(t)\right) \frac{F}{3600} \tag{5.31}$$

where the 3600 term is a conversion factor from coulombs to Ah, and s_{Li} denotes the number of moles of Li per mole of SEI product. This expression is written as the time-varying loss ΔQ that is removed from the initial capacity to give the capacity $Q(t) = Q(0) + \Delta Q(t)$ versus time, and it makes several assumptions. First, it assumes that the negative electrode is capacity limiting so that there is a direct correlation between cell capacity and negative electrode capacity. It also assumes that the open-circuit voltages relative to Li/Li$^+$ of each electrode satisfy the relationship $\partial U_p/\partial Q \gg \partial U_n/\partial Q$, a condition satisfied by most commonly used electrode materials. Finally, it assumes that loss of cyclable lithium is the dominant mode of capacity fade experienced by the cell.

The assumption of $\partial U_p/\partial Q \gg \partial U_n/\partial Q$ is supported by the electrode OCV data plotted in Figure 5.13. In order to simplify the problem and ease understanding, the constant voltage storage case at 100% SOC is used in the following discussion, but the same principles apply for any cycling case followed by a standard constant current/constant voltage (CC/CV) charge to the cell upper voltage limit. The critical point of the discussion is that the cell is charged to the same upper voltage limit each time, which may actually correspond to different amounts of cyclable lithium in each lithium as long as their voltage difference remains the same. This upper voltage limit defines the initial condition of each electrode. Figure 5.13 shows an illustration of the composition range of each electrode and the effects of capacity fade governed by loss of cyclable lithium from the negative electrode.

At the beginning of life, the pouch cell analyzed in prior sections of this chapter exhibits 15 Ah of capacity. For discussion purposes, assume that the SEI layer side reaction consumes 3 Ah of cyclable lithium, equivalent to 0.0634 mol, 0.44 g, or 20% of the initial cell capacity. This causes a shift to the right of the initial condition in the negative electrode, such that the new initial condition begins at the point defined by 3 Ah, 89.9 mV. This 5 mV increase in the negative electrode initial condition requires a corresponding increase in the positive electrode voltage to achieve the upper voltage limit upon charging to 100% SOC. However, the shift along the x-axis needed to achieve this 5 mV increase of the OCV is much smaller in the positive electrode than in the negative electrode since

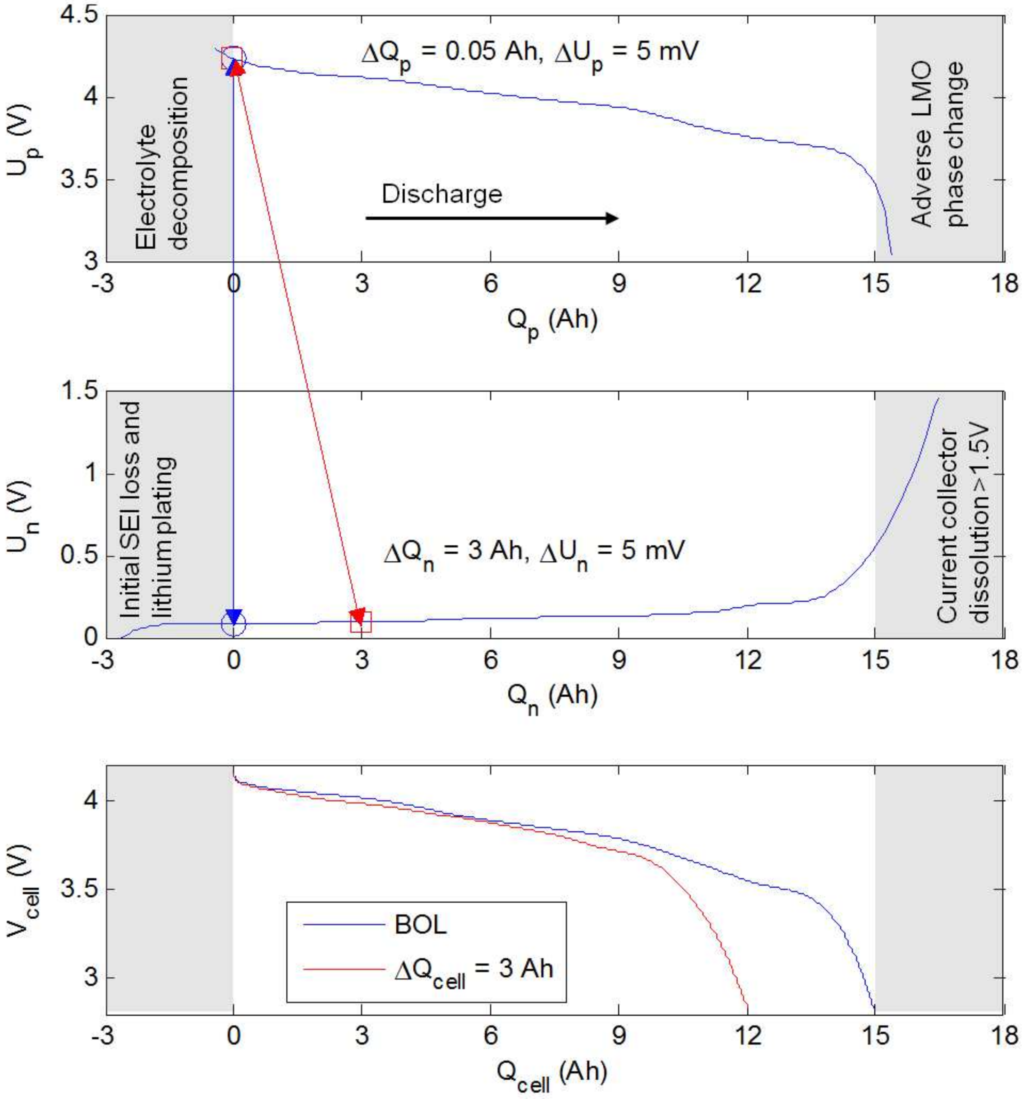

Figure 5.13: Change in electrode operating points introduced by loss of cyclable lithium from the negative electrode, and resulting loss of cell capacity.

$\partial U_p/\partial Q \gg \partial U_n/\partial Q$. Therefore, the capacity fade of the negative electrode directly impacts the cell capacity, and the cell capacity is roughly the same as the negative electrode capacity for significant losses of cyclable lithium.

Further loss of cyclable lithium beyond the 3 Ah (20%) degradation level will have similar effects, since $\partial U_p/\partial Q \gg \partial U_n/\partial Q$ is satisfied by the positive electrode until roughly 4.5 V. At this point, the cell has experienced severer levels of capacity fade that are outside the scope of this model. Furthermore, at 4.5 V electrolyte breakdown increases rapidly at the positive electrode and the assumptions of this model are no longer valid.

5.5.4 Capacity Fade Prediction

The SEI growth and subsequent capacity fade during storage is modeled, since this condition does not require integration with a model of the battery dynamics. The initial state of charge is set to either 100%, 80%, 60%, or 40% and constant voltage is maintained, presumably through a trickle charge that is of the correct magnitude to counteract self-discharge of the cell. Figure 5.14a shows the side reaction current versus time for the simulation, as well as the individual contributions from the site-limited and kinetic-limited regimes. It is evident that initially the side reaction rate due to expansion of the SEI across the available electrode surface area dominates.

However, the rate decreases as the available sites are consumed. The kinetic-limited rate is initially zero, then begins to rise as the surface area covered by SEI expands. Eventually, the kinetic-limited rate surpasses the site-limited rate as the available sites trends toward zero, indicating nearly all of the graphite surface is covered with SEI at the end of the simulation. Then, the kinetic-limited regime continues at a steady pace for the remainder

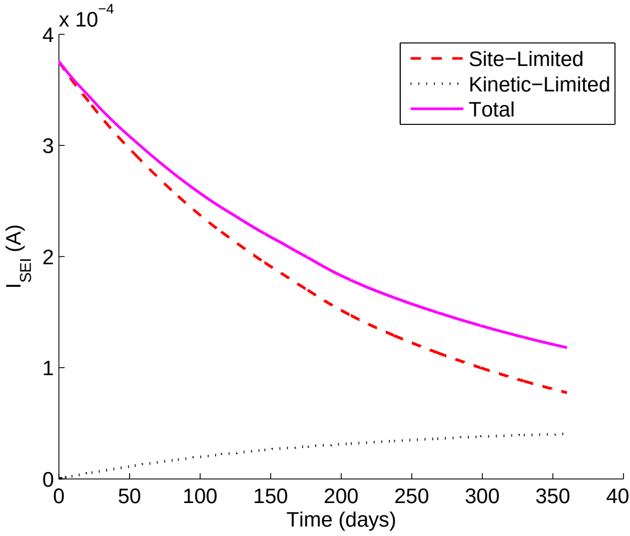

(a)

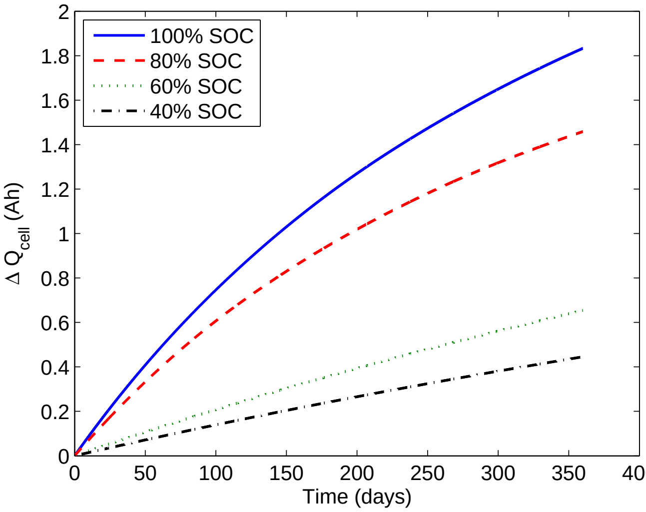

(b)

Figure 5.14: (a) Total side reaction current as the sum of contributions from site-limited (Eq. (5.20)) and kinetic-limited (Eq. (5.24)) regimes for the 100% SOC aging condition. (b) Capacity fade calculation from Eq. (5.31) for storage at various storage SOC values.

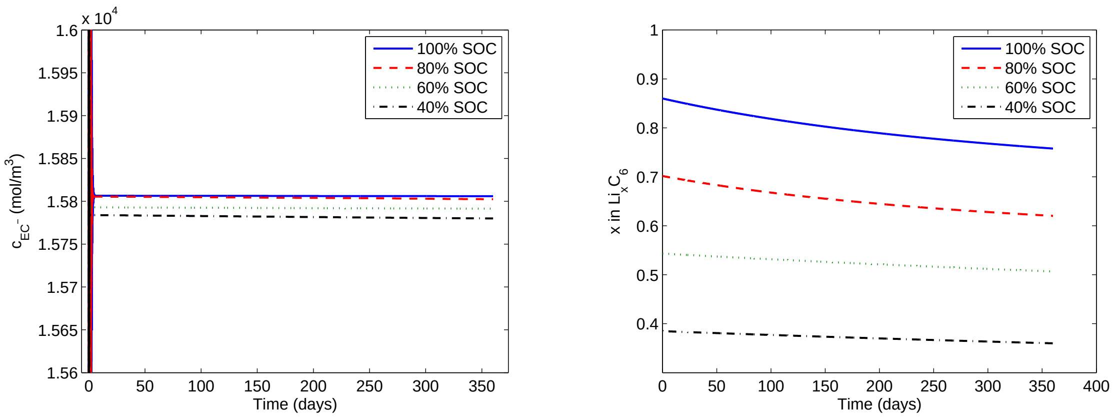

(a) (b)

Figure 5.15: a) Concentration of EC$^-$ within the SEI region and b) trend of negative electrode SOC during aging.

of battery life, indicating that the concentration of EC$^-$ reaches a steady state within the SEI layer.

Figure 5.14b displays the capacity fade prediction for the 100%, 80%, 60%, and 40% SOC storage conditions showing decreasing levels of capacity fade as SOC decreases, though each prediction follows a similar trend. The time dependence is initially an exponential decay caused by the loss of nucleation sites, and the resulting effect on the site-limited reaction rate. This exponential followed by a linear trend produces a result that is similar to power law empirical predictions that are often employed. Degradation trends that are linear can also be represented by the model as the overall capacity fade trend is determined by the relative magnitudes of each reaction rate constant, which are fitting parameters at this stage of model maturity.

Figure 5.15a plots the concentration of EC^- within the SEI layer as a function of time for the 100% SOC condition. Since this is a storage simulation instead of cycling, the concentration of EC^- reaches a steady value rapidly. However, the magnitude of the steady state concentration is dependent upon the volumetric SEI reaction rate, which changes for each SOC storage condition. The results show that the relative change in the volumetric reaction rate is of the same order of magnitude as the relative change ini the surface reduction flux, causing the concentration to exhibit minimal dependence on the storage SOC. Initial "ringing" of the solution is due to taking large time steps in order to simulate months of storage in a minimal computing time, and are sometimes observed for the Crank-Nicholson method despite being a stable numerical approach.

Figure 5.15b plots the decreasing trend of SOC of the negative electrode for each SOC aging condition. This decrease in the cyclable lithium of the negative electrode is the same phenomena that causes the shift towards lower capacity with aging discussed in relation to Figure 5.13. Essentially, the change in x of Li_xC_6 is proportional to the capacity fade level, but this gives a visual representation of how Li^+ is consumed causing the negative electrode SOC to shift relative to the positive electrode SOC and disrupt the intended cell balance. The initial value, rate of decline, and final value decrease with decreasing cell storage SOC.

5.6 Summary and Future Work

An aging campaign has been conducted to establish the degradation trend of composite cathode pouch cells. An assessment of differential capacity data at various points of life has established that the reduction in charge storage at 3.5 V is the primary cause of capacity fade. A model-based analysis has been used to examine various electrochemical mechanisms for the capacity loss, and it was found that a distribution of SEI thicknesses accompanied by corresponding loss of cyclable lithium agrees well with experimental data. Future work will investigate the possibility of positive electrode contributions to capacity fade as aging becomes more severe. Long-term aging predictions require knowledge of whether factors that limit the growth of SEI will cause positive electrode capacity reduction to become significant over time.

The mechanistic knowledge gained by this aging analysis has been used to develop an electrochemical model of SEI layer growth. The SEI product formation reaction occurs volumetrically within the SEI layer and the EC reduction occurs at the graphite surface, requiring open sites. Capacity fade results have been presented for the storage case, where it is assumed that a charging current is present to counteract the discharge effect of the side reaction current. Future work will focus on calibrating this model to predict the capacity fade trends of the pouch cell aging campaign, including cycling results for charge depleting and charge sustaining conditions.

Chapter 6: Summary

6.1 Introduction

In this dissertation, the aging process of Li-ion batteries has been investigated through the use of novel modeling techniques combined with parameter estimation and experimental diagnostics. Theoretical modeling tools have been developed ranging from a first principles, localized approach to system-oriented models based on volume-averaged quantities. These models have been validated for two chemistries that are relevant to electrified vehicle powertrains. Aging has been analyzed via parameter estimation, experimental diagnostics, and first-principles modeling of the side reactions that consume cyclable lithium.

6.2 Mathematical Modeling of Li-Ion Batteries

There are many techniques that are capable of modeling lithium-ion battery performance, where performance modeling is defined as predicting the battery voltage in response to current and temperature inputs. The field of electrochemical modeling combines the contributions of thermodynamics, kinetics, and transport to predict the time-varying voltage of an electrochemical cell. The battery modeling literature does not account for electrical double layer effects, and there is a lack of reduced order modeling methods for predicting cell voltage for automotive operating conditions that feature large (compared to cell capacity), dynamic currents.

Aging mechanisms and their sytem-level effects must be included in high fidelity performance models. To assist with the identification of aging effects, diagnostic techniques have been presented including power, energy, and differential capacity assessments.

6.3 Electrical Double Layer Effects in Li-Ion Batteries

A simplified model structure that uses analytical expressions for the electroneutral liquid concentration and potential in the separator, kinetic overpotential caused by the electrical double layers, and solid lithium concentration in each electrode has been presented. The primary conclusion is that the presence of diffuse charge in the electrical double layer causes greater initial overpotential and greater variation of overpotential with respect to battery state of charge when modeled in an intercalation battery. The resistive effects of the cathode solid matrix have been added to the theoretical current-voltage relationship of the EDL and electroneutral liquid. It has been shown that a single resistance value that increases with depth of discharge improves the agreement with experimental data for a range of galvanostatic discharge experiments from C/3 to 4.8C.

Future work can investigate the relationship between SEI growth rate and the variation in potential that is predicted by including the effects of the electrical double layer. Classical porous electrode models correspond to the Helmholtz limit of the double layer, but using the Gouy–Chapman limit may modify the aging rate and cause a propensity for the SEI to exhibit variations in density throughout the layer thickness, since local growth rates are highly dependent on the local potential value.

6.4 Graphite/LiFePO$_4$ Cell Modeling and Aging Analysis

A reduced order model of Li_xC_6/Li_yFePO_4 cylindrical cells has been developed for large scale simulation, control, and estimation applications. The liquid phase diffusion dynamics have been included to more accurately model battery performance for high currents. Both the solid and liquid phase diffusion dynamics exhibit nonlinear transfer functions that are approximated with the Pade method to provide a computationally efficient solution. This approach has the advantage of preserving the parameters of the parent model, and ultimately their physical meaning, which is useful for SOC and SOH estimation. Parameterization techniques that excite a confined portion of the overall cell dynamics are used to identify the required electrochemical parameters and their temperature dependence. The parametrization procedure is validated with experimental data for a range of temperatures, SOC, and current rates, and the model structure proves to be robust.

After establishing that the model represents battery performance, a sensitivity analysis was conducted for the discharge capacity with respect to several model parameters. A set of aging parameters were identified, namely the active material volume fraction and the initial amount of cyclable lithium of the negative electrode. The result of the parameter estimation is that capacity is correlated to a physical parameter set that has noticeable effects on the cell output voltage. This suggests it is possible to perform estimation of capacity from the battery current-voltage dynamics without performing a distinct capacity test, a result that is significant for the estimation of battery SOC and SOH for hybrid electric vehicle applications. Future work will focus on developing estimation algorithms for SOH and investigating prognostics methods. Additionally the knowledge of parameter trends versus charge throughput can be combined with a cumulative damage model to form a semi-empirical, predictive model of capacity fade.

6.5 Composite Electrode Cell Modeling, Aging Analysis, and SEI Growth Modeling

An aging campaign has been conducted to establish the capacity fade of composite cathode pouch cells based on minimum SOC, charge rate, and operating mode (charge depleting or charge sustaining). Half cell experiments were performed in order to obtain the OCV vs. Li/Li^{+} for each electrode of the pouch cell individually, which leads to the assignment of differential capacity features to each electrode. An assessment of differential capacity data at various points of life has established that the reduction in charge storage at 3.5 V correlates well with the measured capacity fade, a feature that corresponds to the negative electrode. A model-based analysis that models explicitly the dual materials within the composite cathode has been used to examine various electrochemical mechanisms for the capacity loss, including LMO dissolution, and it was found that a distribution of SEI thicknesses accompanied by corresponding loss of cyclable lithium agrees well with experimental data. Future work will investigate the possibility of positive electrode contributions to capacity fade due to LMO dissolution as aging becomes more severe. Long-term aging predictions require knowledge of whether factors that limit the growth of SEI will cause positive electrode capacity reduction to become significant over time.

The mechanistic knowledge gained by this aging analysis has been used to develop an electrochemical model of SEI layer growth. The SEI product formation reaction occurs volumetrically within the SEI layer and the EC reduction occurs at the graphite surface, requiring open sites. This growth mechanism differs from classical views and does not require unrealistically small transport parameters to reproduce experimentally observed capacity fade rates. Capacity fade results have been presented for the storage case, where it is assumed that a charging current is present to counteract the discharge effect of the side reaction current. Future work will focus on calibrating this model to predict the capacity fade trends of the pouch cell aging campaign, including long-term cycling results for charge depleting and charge sustaining conditions. Also, the relationship between the site-limited growth rate and the distribution of SEI thickness will be studied in conjunction with the SEI resistance distribution that reproduces experimental differential capacity data.

Bibliography

ALAMGIR, M., KETKAR, S. & YOO, K. 2011 Recent Progresses of LG Chem's Large-Format Li ion polymer batteries. In *Power and Energy Society General Meeting*. IEEE, Detroit, MI.

ALBERTUS, P., CHRISTENSEN, J. & NEWMAN, J. 2009 Experiments on and Modeling of Positive Electrodes with Multiple Active Materials for Lithium-Ion Batteries. *Journal of the Electrochemical Society* **156** (7), A606–A618.

AMATUCCI, G., PASQUIER, A. D., BLYR, A., ZHENG, T. & TARASCON, J. 1999 The elevated temperature performance of the $LiMn_2O_4$/C system: failure and solutions. *Electrochimica Acta* **45**, 255–271.

AMINE, K., LIU, J., KANG, S., BELHAROUAK, I., HYUNG, Y., VISSERS, D. & HENRIKSEN, G. 2004 Improved lithium manganese oxide spinel/graphite cells for high-power applications. *Journal of Power Sources* **129**, 14–19.

ANONYMOUS 2002 Power Assist HEV Battery Goals. *Tech. Rep.*. U.S. Advanced Battery Consortium, see URL http://www.uscar.org/guest/news.php.

ANONYMOUS 2010 United States Department of Energy Battery Test Manual for Plug-In Hybrid Electric Vehicles, Revision 1. *Tech. Rep.*. U.S. Advanced Battery Consortium, see URL http://www.uscar.org/guest/news.php.

ANONYMOUS 2011 Celgard High Performance Battery Separators. *Tech. Rep.*. Celgard, LLC, see http://www.celgard.com/.

ANONYMOUS 2012*a* Goals for Advanced Batteries for EVs. *Tech. Rep.*. U.S. Advanced Battery Consortium, see URL http://www.uscar.org/guest/news.php.

ANONYMOUS 2012*b* Lithium Battery Separator Goals. *Tech. Rep.*. U.S. Advanced Battery Consortium, see URL http://www.uscar.org/guest/news.php.

ANONYMOUS 2012*c* Plug-in HEV Battery Goals. *Tech. Rep.*. U.S. Advanced Battery Consortium, see URL http://www.uscar.org/guest/news.php.

ANTOULAS, A. 2005 *Approximation of Large-Scale Dynamical Systems*. Society for Industrial and Applied Mathematics.

ARORA, P. & WHITE, R. 1998 Capacity Fade Mechanisms and Side Reactions in Lithium-Ion Batteries. *Journal of the Electrochemical Society* **145**, 3647–3667.

ATKINS, P. 1993 *Elements of Physical Chemistry*. New York, NY: Oxford University Press.

BARD, A. & FAULKNER, L. 2001 *Electrochemical Methods: Fundamentals and Applications*. New York, NY: John Wiley and Sons, Inc.

BARSOUKOV, E. & MACDONALD, J. 2005 *Impedance Spectroscophy Theory, Experiment, and Applications*. Hoboken, NJ: John Wiley & Sons.

BAUMANN, B., WASHINGTON, G., GLENN, B. & RIZZONI, G. 2000 Mechatronic design and control of hybrid electric vehicles. *IEEE/ASME Transactions on Mechatronics* **5** (1), 58 – 72.

BAZANT, M., CHU, K. & BAYLY, B. 2005 Current-Voltage Relations for Electrochemical Thin Films. *SIAM Journal of Applied Mathematics* **65** (5), 1463–1484.

BEDROV, D., SMITH, G. & VAN DUIN, A. 2012 Reactions of Singly-Reduced Ethylene Carbonate in Lithium Battery Electrolytes: A Molecular Dynamics Simulation Study Using the ReaxFF. *Journal of Physical Chemistry A* **116**, 2978 – 2985.

BELT, J., UTGIKAR, V. & BLOOM, I. 2011 Calendar and PHEV cycle life aging of high-energy, lithium-ion cells containing blended spinel and layered-oxide cathodes. *Journal of Power Sources* **196**, 10213 – 10221.

BERNARDI, D. & GO, J.-Y. 2011 Analysis of pulse and relaxation behavior in lithium-ion batteries. *Journal of Power Sources* **196**, 412–427.

BERNARDI, D., PAWLIKOWSKI, E. & NEWMAN, J. 1985 A General Energy Balance for Battery Systems. *Journal of the Electrochemical Society* **132**, 5–12.

BEWLAY, S., KONSTANTINOV, K., WANG, G., DOU, S. & LIU, H. 2004 Conductivity improvements to spray-produced $LiFePO_4$ by addition of a carbon source. *Materials Letters* **58**, 1788 – 1791.

BIESHEUVEL, P., VAN SOESTBERGEN, M. & BAZANT, M. 2005 Imposed currents in galvanic cells. *Electrochimica Acta* **54**, 4857–4871.

BLOOM, I., CHRISTOPHERSEN, J., ABRAHAM, D. & GERING, K. 2006 Differential voltage analyses of high-power lithium-ion cells 3. Another anode phenomenon. *Journal of Power Sources* **157**, 537 – 542.

BLOOM, I., CHRISTOPHERSEN, J., ABRAHAM, D. & GERING, K. 2010 Differential voltage analyses of high-power lithium-ion cells 4. Cells containing NMC. *Journal of Power Sources* **195**, 877 – 882.

BLOOM, I., CHRISTOPHERSEN, J. & GERING, K. 2005*a* Differential voltage analyses of high-power lithium-ion cells 2. Applications. *Journal of Power Sources* **139**, 304 – 313.

BLOOM, I., JANSEN, A., ABRAHAM, D., KNUTH, J., JONES, S., BATTAGLIA, V. & HENRIKSEN, G. 2005*b* Differential voltage analyses of high-power lithium-ion cells 1. Technique and application. *Journal of Power Sources* **139**, 295 – 303.

BOOVARAGAVAN, V., HARINIPRIYA, S. & SUBRAMANIAN, V. 2008 Towards real-time (milliseconds) parameter estimation of lithium-ion batteries using reformulated physics-based models. *Journal of Power Sources* **183**, 361 – 365.

BOTTE, G., RITTER, J. & WHITE, R. 2000 Comparison of finite differences and control volume method for solving differential equations. *Computers and Chemical Engineering* **24**, 2633 – 2654.

BOYCE, W. & DIPRIMA, R. 2009 *Elementary Differential Equations and Boundary Value Problems*. Hoboken, NJ: John Wiley and Sons, Inc.

BROUSSELY, M., BIENSAN, P., BONHOMME, F., BLANCHARD, P., HERREYRE, S., NECHEV, K. & STANIEWICZ, R. 2005 Main aging mechanisms in Li ion batteries. *Journal of Power Sources* **146**, 90–96.

BROUSSELY, M., HERREYRE, S., BIENSAN, P., KASZTEJNA, P., NECHEV, K. & STANIEWICZ, R. 2001 Aging mechanism in Li ion cells and calendar life predictions. *Journal of Power Sources* **97**, 13–21.

BURSTEIN, G. 2005 A hundred years of tafel's equation: 1905–2005. *Corrosion Science* **47** (12), 2858 – 2870.

CABANA, J., KANG, S.-H. & JOHNSON, C. 2009 Structural and Electrochemical Characterization of Composite Layered-Spinel Electrodes Containing Ni and Mn for Li-Ion Batteries. *Journal of the Electrochemical Society* **156** (9), A730 – A736.

CAI, L., DAI, Y., NICHOLSON, M., WHITE, R., JAGANNATHAN, K. & BHATIA, G. 2013 Life modeling of a lithium ion cell with a spinel–based cathode. *Journal of Power Sources* **221**, 191 – 200.

CAI, L. & WHITE, R. 2009 Reduction of Model Order Based on Proper Orthogonal Decomposition for Lithium-Ion Battery Simulations. *Journal of the Electrochemical Society* **156** (3), A154–A161.

CAI, L. & WHITE, R. 2010 An Efficient Electrochemical–Thermal Model for a Lithium-Ion Cell by Using the Proper Orthogonal Decomposition Method. *Journal of the Electrochemical Society* **157** (11), A1188–A1195.

CHENG, Y. & VERBRUGGE, M. 2010*a* Application of Hasselman's Crack Propagation Model to Insertion Electrodes. *Electrochemical and Solid State Letters* **13** (9), A128.

CHENG, Y. & VERBRUGGE, M. 2010*b* Diffusion-Induced Stress, Iinterfacial Charge Transfer, and Criteria for Avoiding Crack Initiation of Electrode Particles. *Journal of the Electrochemical Society* **157** (4), A508–A516.

CHO, I., KIM, S., SHIN, S. & CHOI, N. 2010 Effect of SEI on Capacity Losses of Spinel Lithium Manganese Oxide/Graphite Batteries Stored at 60°C. *Electrochemical and Solid State Letters* **13** (11), A168–A172.

CHRISTENSEN, J. & NEWMAN, J. 2006 Stress generation and fracture in lithium insertion materials. *Journal of Solid State Electrochemistry* **10**, 293–319.

CHRISTENSEN, J., SRINIVASAN, V. & NEWMAN, J. 2006 Optimization of Lithium Titanate Electrodes for High-Power Cells. *Journal of the Electrochemical Society* **153** (3), A560–A565.

CHU, K. & BAZANT, M. 2005 Electrochemical Thin Films At and Above the Classical Limiting Current. *SIAM Journal of Applied Mathematics* **65** (5), 1485–1505.

CHUNG, S., BLOKING, J. & CHIANG, Y. 2002 Electronically conductive phospho-olivines as lithium storage electrodes. *Nature Materials* **1**, 123 – 128.

CIARLET, P. & LIONS, J. 1990 *Handbook of Numerical Analysis*. New York, NY: Elsevier.

COLEMAN, T. & LI, Y. 1994 On the convergence of interior-reflective newton methods for nonlinear minimization subject to bounds. *Mathematical Programming* **67** (1), 189 – 224.

CONLISK, A. 2011 *Essentials of Micro and Nanofluidics with Applications to the Biological and Chemical Sciences*. New York, NY: Cambridge University Press.

CRANK, J. 1975 *The Mathematics of Diffusion*. New York, NY: Oxford University Press.

DARLING, R. & NEWMAN, J. 1997 Modeling a Porous Intercalation Electrode with Two Characteristic Particle Sizes. *Journal of the Electrochemical Society* **144** (12), 4201–4208.

DEISS, E., HARINGER, D., NOVAK, P. & HAAS, O. 2001 Modeling of the charge–discharge dynamics of lithium manganese oxide electrodes for lithium–ion batteries. *Electrochimica Acta* **46**, 4185 – 4196.

DESHPANDE, R., CHENG, Y., VERBRUGGE, M. & TIMMONS, A. 2011 Diffusion Induced Stresses and Strain Energy in a Phase-Transforming Spherical Electrode Particle. *Journal of the Electrochemical Society* **158** (6), A718.

DESHPANDE, R., VERBRUGGE, M., CHENG, Y., WANG, J. & LIU, P. 2012 Battery Cycle Life Prediction with Coupled Chemical Degradation and Fatigue Mechanics. *Journal of the Electrochemical Society* **159** (10), A1730–A1738.

DI DOMENICO, D., FIENGO, G. & STEFANOPOULOU, A. 2008*a* Lithium-ion battery state of charge estimation with a Kalman filter based on a electrochemical model. In *Proceedings of 2008 IEEE Conference on Control Applications*. Shanghai, P.R. China, 702–707.

DI DOMENICO, D., FIENGO, G. & STEFANOPOULOU, A. 2008*b* Reduced order lithium-ion battery electrochemical model and extended Kalman filter state of charge estimation. *J. Dyn. Syst. Meas. Control - Special Issue on Physical System Modeling* **132**.

DI FILIPPI, A., STOCKAR, S., ONORI, S., CANOVA, M. & GUEZENNEC, Y. 2010 Model-based aging characterization of lithium-ion batteries in PHEVs using large scale monte-carlo vehicle simulations. In *Proceedings of the 2010 IEEE Vehicle Power and Propulsion Conference*. IEEE, Lille, France.

DOYLE, M., FULLER, T. & NEWMAN, J. 1993 Modeling of Galvanostatic Charge and Discharge of the Lithium/Polymer/Insertion Cell. *Journal of the Electrochemical Society* **140** (6), 1526–1533.

DU PASQUIER, A., BLYR, A., COURJAL, P., LARCHER, D., AMATUCCI, G., GERAND, B. & TARASCON, J.-M. 1999 Mechanism for Limited 55°C Storage Performance of $Li_{1.05}Mn_{1.95}$. *Journal of the Electrochemical Society* **146** (2), 428 – 436.

DUBARRY, M., TRUCHOT, C., CUGNET, M., LIAW, B., GERING, K., SAZHIN, S., JAMISON, D. & MICHELBACHER, C. 2009*a* Evaluation of commercial lithium-ion cells based on composite positive electrode for plug-in hybrid electric vehicle applications. Part I: Initial characterizations. *Journal of Computational and Applied Mathematics* **231** (1), 365 – 377.

DUBARRY, M., TRUCHOT, C., LIAW, B., GERING, K., SAZHIN, S., JAMISON, D. & MICHELBACHER, C. 2009*b* Evaluation of commercial lithium-ion cells based on composite positive electrode for plug-in hybrid electric vehicle applications. Part II: Degradation mechanism under 2C cycle aging. *Journal of Computational and Applied Mathematics* **231** (1), 365 – 377.

DUKHIN, A., DUKHIN, S. & GOETZ, P. 2005 Electrokinetics at high ionic strength and hypotheses of the Double Layer with Zero Surface Charge. *Langmuir* **21** (22), 9990–9997.

FANG, W., KWAN, O. J., WANG, C. & ISHIKAWA, Y. 2009 Modeling of Li-ion Battery Performance in Hybrid Electric Vehicles. *SAE Technical Paper 2009-01-1388* .

FANG, W., KWON, O. & WANG, C. 2010 Electrochemical-thermal modeling of automotive Li-ion batteries and experimental validation using a three-electrode cell. *International Journal of Energy Research* **34** (2), 107–115.

FERGUS, J. 2010 Recent developments in cathode materials for lithium ion batteries. *Journal of Power Sources* **195**, 939 – 954.

FLEISCH, D. 2008 *A Student's Guide to Maxwell's Equations*. New York, NY: Cambridge University Press.

FORMAN, J., BASHASH, S., STEIN, J. & FATHY, H. 2011 Reduction of an Electrochemistry-Based Li-Ion Battery Model via Quasi-Linearization and Pade Approximation. *Journal of the Electrochemical Society* **158** (2), A93–A101.

GOERS, D., SPAHR, M., LEONE, A., MARKLE, W. & NOVAK, P. 2011 The influence of the local current density on the exfoliation of graphite in lithium-ion battery negative electrodes. *Electrochimica Acta* **56**, 3799 – 3808.

GUMMOW, R., DE KOCK, A. & THACKERAY, M. 1994 Improved capacity retention in rechargeable 4 v lithium/lithium-manganese oxide (spinel) cells. *Solid State Ionics* **69**, 59–67.

HAIK, O., LEIFER, N., SAMUK-FROMOVICH, Z., ZINIGRAD, E., MARKOVSKY, B., LARUSH, L., GOFFER, Y., GOOBES, G. & AURBACH, D. 2010 On the Surface Chemistry of $LiMO_2$ Cathode Materials (M=[MnNi] and [MnNiCo]): Electrochemical, Spectroscopic, and Calorimetric Studies. *Journal of the Electrochemical Society* **157** (10), A1099 – A1107.

HARAN, B., POPOV, B. & WHITE, R. 1998 Theoretical analysis of metal hydride electrodes. *Journal of The Electrochemical Society* **145** (12), 4082–4090.

HARRIS, S., TIMMONS, A., BAKER, D. & MONROE, C. 2010 Direct *in situ* measurements of Li transport in Li–ion battery negative electrodes. *Chemical Physics Letters* **485**, 265 – 274.

HAYAMIZU, K. 2012 Temperature Dependence of Self-Diffusion Coefficients of Ions and Solvents in Ethylene Carbonate, Propylene Carbonate, and Diethyl Carbonate Single Solutions and Ethylene Carbonate + Diethyl Carbonate Binary Solutions of $LiPF_6$ Studied by NMR. *Journal of Chemical & Engineering Data* **57**, 2012 – 2017.

HOWELL, D. 2012 Overview of Battery R & D Activities. *Tech. Rep.*. U.S. Department of Energy, Washington, D.C., see URL http://www1.eere.energy.gov/vehiclesandfuels/.

HU, Y. & YURKOVICH, S. 2011 Linear parameter varying battery model identification using subspace methods. *Control Engineering Practice* **196**, 2913–2923.

HU, Y., YURKOVICH, S., GUEZENNEC, Y. & YURKOVICH, B. 2009 A technique for dynamic battery model identification in automotive applications using linear parameter varying structures. *Journal of Power Sources* **17**, 1190–1201.

HU, Y., YURKOVICH, S., GUEZENNEC, Y. & YURKOVICH, B. 2011 Electro-thermal battery model identification for automotive applications. *Journal of Power Sources* **196**, 449–457.

HUANG, H., VINCENT, C. & BRUCE, P. 1999 Correlating Capacity Loss of Stoichiometric and Nonstoichiometric Lithium Manganese Oxide Spinel Electrodes with Their Structural Integrity. *Journal of the Electrochemical Society* **146**, 3649 – 3654.

ILTCHEY, N., CHEN, Y., OKADA, S. & YAMAKI, J. 2003 $LiFePO_4$ storage at room and elevated temperatures. *Journal of Power Sources* **119–121**, 749–754.

JANG, D., SHIN, Y. & OH, S. 1996 Dissolution of Spinel Oxides and Capacity Losses in 4 v $Li/Li_xMn_2O_4$ cells. *Journal of the Electrochemical Society* **143** (7), 2204–2210.

JENN, A., AZEVEDO, I. & FERREIRA, P. 2012 Impact of Federal Incentives on the Adoption of Hybrid Electric Vehicles. In *IEEE International Symposium on Sustainable Systems and Technology*. IEEE, Boston, MA.

JEONG, S., SHIN, J., NAHM, K., PREM KUMAR, T. & STEPHAN, A. 1999 Electrochemical studies on cathode blends of $LiMn_2O_4$ and $Li[Li_{1/15}Ni_{1/5}C_{2/5}Mn_{1/3}O_2]$. *Journal of the Electrochemical Society* **146** (2), 428 – 436.

JOHNSON, C., LI, N., VAUGHEY, J., HACKNEY, S. & THACKERAY, M. 2005 Lithium-manganese oxide electrodes with layered-spinel composite structures $x\mathrm{Li_2MnO_3}\cdot(1-x)\mathrm{Li_{1+y}Mn_{2-y}O_4}$. *Electrochemistry Communications* **7**, 528 – 536.

JUANG, L., KOLLMEYER, P., JAHNS, T. & LORENZ, R. 2011 Improved nonlinear model for electrode voltage-current relationship for more consistent online battery system identification. In *Proceedings of the 2011 IEEE Energy Conversion Congress and Exposition*, pp. 2628 – 2634. IEEE, Phoenix, AZ.

KARDEN, E., PLOUMEN, S., FRICKE, B., MILLER, T. & SNYDER, K. 2007 Energy storage devices for future hybrid electric vehicles. *Journal of Power Sources* **168**, 2–11.

KIM, D., PARK, S., CHAE, O., RYU, J., IM, Y.-U., YIN, R.-Z. & OH, S. 2012 Re-Deposition of Manganese Species on Spinel $LiMn_2O_4$ Electrode after Mn Dissolution. *Journal of the Electrochemical Society* **159** (3), A193 – A197.

Kim, G., Smith, K., Lee, K., Santhanagopalan, S. & Pesaran, A. 2011 Multi-Domain Modeling of Lithium-Ion Batteries Encompassing Multi-Physics in Varied Length Scales. *Journal of the Electrochemical Society* **158** (8), A955–A969.

Lee, S., Kim, Y. & Chun, H. 2002 Modeling on lithium insertion of porous carbon electrodes. *Electrochimica Acta* **47**, 1055 – 1067.

Leon, C., Santamaria, J., Paris, M., Sanz, J., Ibarra, J. & Torres, L. 1997 Non-Arrhenius conductivity in the fast ionic conductor $Li_{0.5}La_{0.5}TiO_3$: Reconciling spin-lattice and electrical conductivity relaxations. *Physical Review B* **56** (9), 5302 – 5305.

Levi, M. & Aurbach, D. 1997 Simultaneous Measurements and Modeling of the Electrochemical Impedance and the Cyclic Voltammetric Characteristics of Graphite Electrodes Doped with Lithium. *Journal of Physical Chemistry B* **101**, 4630 – 4640.

Liu, P., Wang, J., Hicks-Garner, J., Sherman, E., Soukiazian, S., Verbrugge, M., Tataria, H., Musser, J. & Finamore, P. 2008 Aging Mechanisms of $LiFePO_4$ Batteries Deduced by Electrochemical and Structural Analyses. *Journal of the Electrochemical Society* **157** (4), A499 – A507.

Liu, Y., Li, X., Guo, H., Wang, Z., Hu, Q., Peng, W. & Yang, Y. 2009 Electrochemical performance and capacity fading reason of $LiMn_2O_4$/graphite batteries stored at room temperature. *Journal of Power Sources* **189**, 721 – 725.

Markle, W., Lu, C. & Novak, P. 2011 Morphology of the Solid Electrolyte Interphase on Graphite in Dependency on the Formation Current. *Electrochimica Acta* **56**, 3799 – 3808.

MORAN, M. & SHAPIRO, H. 2004 *Fundamentals of Engineering Thermodynamics, Third Edition*. Hoboken, NJ: John Wiley and Sons, Inc.

MURATORI, M., MA, N., CANOVA, M. & GUEZENNEC, Y. 2010*a* A Model-Order Reduction Method for the Temperature Estimation in a Cylindrical Li-Ion Battery Cell. In *Proceedings of the 2010 ASME Dynamic Systems and Control Conference*. Boston, MA.

MURATORI, M., MA, N., CANOVA, M. & GUEZENNEC, Y. 2010*b* A Reduced-Order Model for the Thermal Dynamics of Li-Ion Battery Cells. In *Proceedings of the 2010 IFAC Symposium on Advances in Automotive Control*. Munich, Germany.

NAGPURE, S., DINWIDDIE, R., BABU, S., RIZZONI, G., BHUSHAN, B. & FRECH, T. 2010 Thermal diffusivity study of aged Li-ion batteries using flash method. *Journal of Power Sources* **195**, 872–876.

NAKAHARA, K., NAKAJIMA, R., MATSUSHIMA, T. & MAJIMA, H. 2003 Preparation of particulate $Li_4Ti_5o_{12}$ having excellent characteristics as an electrode active material for power storage cells. *Journal of Power Sources* **117** (1–2), 131 – 136.

NAM, K., YOON, W., SHIN, H., CHUNG, K., CHOI, S. & YANG, X. 2009 In-Situ X-ray diffraction studies of mixed $LiMn_2O_4$ - $LiNi_{1/3}Mn_{1/3}Co_{1/3}O_2$ composite cathode in Li-ion cells during charge-discharge cycling. *Journal of Power Sources* **192**, 652–659.

NEWMAN, J. 1965 The polarized diffuse double layer. *Transactions of the Faraday Society* **61**, 2229–2237.

NEWMAN, J. & CHAPMAN, T. 1973 Restricted Diffusion in Binary Solutions. *American Institute of Chemical Engineers Journal* **19**, 343 –348.

NEWMAN, J. & THOMAS-ALYEA, K. 2004 *Electrochemical Systems, 3rd Edition*. Hoboken, NJ: John Wiley and Sons, Inc.

NEWMAN, J. & TIEDEMANN, W. 1975 Porous-Electrode Theory with Battery Applications. *American Institute of Chemical Engineers Journal* **21**, 25–41.

NING, G., WHITE, R. & POPOV, B. 2006 A generalized cycle life model of rechargeable Li-ion batteries. *Electrochimica Acta* **51**, 2012–2022.

NORTHROP, P., RAMADESIGAN, V., DE, S. & DIWAKAR, V. 2011 Coordinate Transformation, Orthogonal Collocation, Model Reformulation and Simulation of Electrochemical-Thermal Behavior of Lithium-Ion Battery Stacks. *Journal of the Electrochemical Society* **158**, A1461 – A1477.

OHZUKU, T. & BRODD, R. 2007 An overview of positive–electrode materials for advanced lithium–ion batteries. *Journal of Power Sources* **174**, 449 – 456.

OHZUKU, T., IWAKOSHI, Y. & SAWAI, K. 1993 Formation of Lithium–Graphite Intercalation Compounds in Nonaqueous Electrolytes and Their Application as a Negative Electrode for a Lithium Ion (Shuttlecock) Cell. *Journal of the Electrochemical Society* **140**, 2490 – 2498.

ONG, I. & NEWMAN, J. 1999 Double-Layer Capacitance in a Dual Lithium Ion Insertion Cell. *Journal of the Electrochemical Society* **146** (12), 2229–2237.

OZISIK, M. 2002 *Boundary Value Problems of Heat Conduction*. Mineola, NY: Dover Publications.

PARK, J., SEO, J., PLETT, G., LU, W. & SASTRY, A. 2011 Numerical Simulation of the Effect of the Dissolution of $LiMn_2O_4$ Particles on Li-Ion Battery Performance. *Journal of the Electrochemical Society* **14** (2), A14–A18.

PARK, M., ZHANG, X., CHUNG, M., LESS, G. & SASTRY, A. 2010 A review of conduction phenomena in Li-ion batteries. *J. Power Sources* **195**, 7904 – 7929.

PARK, S.-H., KANG, S.-H. & JOHNSON, C. 2007 Lithium-manganese-nickel-oxide electrodes with integrated layered-spinel structures for lithium batteries. *Electrochemistry Communications* **9** (2), 262 – 268.

PARKER, G., SCHMALZ, T. & LIGHT, J. 1980 A variable interval variable step method for the solution of linear second order coupled differential equations. *Journal of Chemical Physics* **73** (4), 1757 – 1764.

PATEL, K., PAULSEN, J. & DESILVESTRO, J. 2003 Numerical simulation of porous networks in relation to battery electrodes and separators. *Journal of Power Sources* **122**, 144 – 152.

PLETT, G. 2004*a* Extended Kalman filtering for battery management systems of LiPB-based HEV battery packs: Part 1. Background. *Journal of Power Sources* **134** (2), 252–261.

PLETT, G. 2004*b* Extended Kalman filtering for battery management systems of LiPB-based HEV battery packs: Part 2. Modeling and identification. *Journal of Power Sources* **134** (2), 262–276.

PLETT, G. 2004*c* Extended Kalman filtering for battery management systems of LiPB-based HEV battery packs: Part 3. State and parameter estimation. *Journal of Power Sources* **134** (2), 277–292.

RAMADASS, P., HARAN, B., GOMADAM, P., WHITE, R. & POPOV, B. 2004 Development of first principles capacity fade model for li-ion cells. *Journal of the Electrochemical Society* **151** (2), A196 – A203.

RAMADESIGAN, V., BOOVARAGAVAN, V., JR., J. P. & SUBRAMANIAN, V. 2010 Efficient Reformulation of Solid-Phase Diffusion in Physics-Based Lithium-Ion Battery Models. *Journal of the Electrochemical Society* **157**, A854 – A860.

RAO, L. & NEWMAN, J. 1997 Heat-Generation Rate and General Energy Balance for Insertion Battery Systems. *Journal of the Electrochemical Society* **144**, 2697–2704.

RENGANATHAN, S., SIKHA, G., SANTHANAGOPALAN, S. & WHITE, R. 2010 Theoretical Analysis of Stresses in a Lithium Ion Cell. *Journal of the Electrochemical Society* **157** (2), A155–A163.

RIVERA, A., SANTAMARIA, J., LEON, C., BLOCHOWICZ, T., GAINARU, C. & ROSSLER, E. 2003 Temperature dependence of the ionic conductivity in $\mathrm{Li}_{3x}\mathrm{La}_{2/3-x}\mathrm{TiO}_3$: Arrhenius versus non-arrhenius. *Applied Physics Letters* **82** (15), 2425 – 2427.

RIZZONI, G. 2003 *Principles and Applications of Electrical Engineering*. New York, NY: McGraw-Hill.

ROSCHER, M. & SAUER, D. 2011 Dynamic electric behavior and open-circuit-voltage modeling of $LiFePO_4$-based lithium ion secondary batteries. *Journal of Power Sources* **196**, 331 – 336.

SAFARI, M. & DELACOURT, C. 2011*a* Mathematical modeling of lithium iron phosphate electrode: Galvanostatic charge/discharge and path dependence. *Journal of the Electrochemical Society* **158** (2), A63–A73.

SAFARI, M. & DELACOURT, C. 2011*b* Modeling of a Commercial Graphite/$LiFePO_4$ Cell. *Journal of the Electrochemical Society* **158** (5), A562–A571.

SAFARI, M. & DELACOURT, C. 2011*c* Simulation-Based Analysis of Aging Phenomena in a Commercial Graphite/$LiFePO_4$ Cell. *Journal of the Electrochemical Society* **158** (12), A1436–A1447.

SAFARI, M. & DELACOURT, C. 2012 Life Simulation of a Graphite/$LiFePO_4$ Cell under Cycling and Storage. *Journal of the Electrochemical Society* **159** (8), A1283–A1291.

SAFARI, M., MORCRETTE, M., TEYSSOT, A. & DELACOURT, C. 2009 Multimodal Physics-Based Aging Model for Life Prediction of Li-Ion Batteries. *Journal of The Electrochemical Society* **156** (3), A145–A153.

SANTHANAGOPALAN, S., GUO, Q., RAMADASS, P. & WHITE, R. 2006 Review of models for predicting the cycling performance of lithium ion batteries. *Journal of Power Sources* **156**, 620–628.

SANTHANAGOPALAN, S. & WHITE, R. 2006 Online estimation of the state of charge of a lithium ion cell. *Journal of Power Sources* **161**, 1346–1355.

SANTHANAGOPALAN, S. & WHITE, R. 2008 Capacity Fade Analysis of a Lithium Ion Cell. *Journal of Power Sources* **179**, 793–798.

SANTHANAGOPALAN, S., ZHANG, Q., KUMARESAN, K. & WHITE, R. 2008 Parameter Estimation and Life Modeling of Lithium-Ion Cells. *Journal of The Electrochemical Society* **155** (4), A345–A353.

VAN SCHALKWIJK, W. & SCROSATI, B. 2002 *Advances in Lithium-Ion Batteries*. New York, NY: Kluwer Academic Publishers.

SCHMIDT, A., BITZER, M., IMRE, A. & GUZZELLA, L. 2010*a* Experiment-driven electrochemical modeling and systematic parameterization for a lithium-ion battery cell. *Journal of Power Sources* **195**, 5071–5080.

SCHMIDT, A., BITZER, M., IMRE, A. & GUZZELLA, L. 2010*b* Model-based distinction and quantification of capacity loss and rate capability fade in Li-ion batteries. *Journal of Power Sources* **195** (22), 7634–7638.

SCLAR, H., KOVACHEVA, D. & ZHECHEVA, D. 2009 On the Performance of $LiNiMnCoO_2$ Nanoparticles as a Cathode Material for Lithium-Ion Batteries. *Journal of the Electrochemical Society* **156** (11), A938–A948.

SHAJU, K., SUBBA RAO, G. & CHOWDARI, B. 2004 Influence of Li-Ion Kinetics in the Cathodic Performance of Layered Li $(Ni_{1/3}Co_{1/3}Mn_{1/3})O_2$. *Journal of the Electrochemical Society* **151** (9), A1324 – A1332.

SHEARING, P., HOWARD, L., JORGENSEN, P., BRANDON, N. & HARRIS, S. 2010 Characterization of the 3-dimensional microstructure of a graphite negative electrode from a Li-ion battery. *Electrochemistry Communications* **12**, 374 – 377.

SHI, Z., XU, Z. & CO, J. 2009 The convergence of subspace trust region methods. *Journal of Computational and Applied Mathematics* **231** (1), 365 – 377.

SINGH, G., CEDER, G. & BAZANT, M. 2008 Intercalation dynamics in rechargeable battery materials: General theory and phase-transformation waves in $\mathrm{LiFePO_4}$. *Electrochimica Acta* **53**, 8599–7613.

SIOSHANSI, R. & DENHOLM, P. 2009 Emissions Impacts and Benefits of Plug-In Hybrid Electric Vehicles and Vehicle-to-Grid services. *Environmental Science and Technology* **43**, 1199–1204.

SMART, M., WHITACRE, J., RATNAKUMAR, B. & AMINE, K. 2007 Electrochemical performance and kinetics of $\mathrm{Li_{1+x}(Co_{1/3}Ni_{1/3}Mn_{1/3})_{1-x}O_2}$ cathodes and graphite anodes in low-temperature electrolytes. *Journal of Power Sources* **168**, 501 – 508.

SMITH, K., RAHN, C. & WANG, C. 2007 Control oriented 1D electrochemical model of lithium ion battery. *Energy Conversion and Management* **48**, 2565 – 2578.

SMITH, K., RAHN, C. & WANG, C. 2008 Model Order Reduction of 1D Diffusion Systems Via Residue Grouping. *Journal of Dynamic Systems, Measurement, and Control* **130**.

SMITH, K., RAHN, C. & WANG, C. 2010 Model-Based Electrochemical Estimation and Constraint Management for Pulse Operation of Lithium Ion Batteries. *IEEE Transactions on Control Systems Technology* **18**, 654 – 663.

SMITH, K. & WANG, C. 2006*a* Power and thermal characterization of a lithium-ion battery pack for hybrid-electric vehicles. *Journal of Power Sources* **160**, 662–673.

SMITH, K. & WANG, C. 2006*b* Solid-state diffusion limitations on pulse operation of a lithium ion cell for hybrid electric vehicles. *Journal of Power Sources* **161**, 628–639.

SMYRL, W. & NEWMAN, J. 1967 Double layer structure at the limiting current. *Transactions of the Faraday Society* **63** (207), 1463–1484.

SNYDER, K., YANG, X. & MILLER, T. 2009 Hybrid Vehicle Battery Technology – The Transition From NiMH to Li-Ion. *SAE Technical Paper 2009-01-1385* .

SPELTINO, C., DI DOMENICO, D., FIENGO, G. & STEFANOPOULOU, A. 2009 Experimental identification and validation of an electrochemical model of a lithium-ion battery. In *Proceedings of the 2009 IEEE European Control Conference*. Budapest, Hungary.

SRINIVASAN, V. 2008 Batteries for Vehicular Applications. In *Physics of Sustainable Energy: Using Energy Efficiently and Producing It Renewably*. American Institute of Physics, Berkeley, CA.

SRINIVASAN, V. & NEWMAN, J. 2004*a* Design and Optimization of a Natural Graphite/Iron Phosphate Lithium-Ion Cell. *Journal of the Electrochemical Society* **151** (10), A1530–A1538.

SRINIVASAN, V. & NEWMAN, J. 2004*b* Discharge Model for the Lithium Iron-Phosphate Electrode. *Journal of the Electrochemical Society* **151** (10), A1517–A1529.

SRINIVASAN, V. & WANG, C. 2002 Computational battery dynamics (CBD) – electrochemical/thermal coupled modeling and multi-scale modeling. *Journal of Power Sources* **110**, 364–376.

STEPHENSON, D., HARTMAN, E., HARB, J. & WHEELER, D. 2007 Modeling of Particle-Particle Interactions in Porous Cathodes for Lithium-Ion Batteries. *Journal of the Electrochemical Society* **154** (12), A1146 – A1155.

SUBRAMANIAN, V., BOOVARAGAVAN, V. & DIWAKAR, V. 2007 Towards Real-Time Simulation of Physics-Based Lithium-Ion Battery Models. *Electrochemical and Solid-State Letters* **10**, A255 – A260.

SUBRAMANIAN, V., BOOVARAGAVAN, V., RAMADESIGAN, V. & ARABANDI, M. 2009 Mathematical Model Reformulation for Lithium-Ion Battery Simulations: Galvanostatic Boundary Conditions. *Journal of the Electrochemical Society* **156**, A260 – A271.

SUBRAMANIAN, V., DIWAKAR, V. & TAPRIYAL, D. 2005 Efficient Macro-Micro Scale Coupled Modeling of Batteries. *Journal of Power Sources* **152** (10), A2002 – A2008.

SUBRAMANIAN, V., RITTER, J. & WHITE, R. 2001 Approximate Solutions for Galvanostatic Discharge of Spherical Particles. *Journal of the Electrochemical Society* **148** (11), E444–E449.

SUBRAMANIAN, V., TAPRIYAL, D. & WHITE, R. 2004 A Boundary Condition for Porous Electrodes. *Electrochemical and Solid State Letters* **7** (9), A259 – A263.

TAYLOR, R. & KOOIJMAN, H. 1991 Composition Derivatives of Activity Coefficient Models for the Estimation of Thermodynamic Factors in Diffusion. *Chemical Engineering Communications* **102** (1), 87 – 106.

TAYLOR, R. & KRISHNA, R. 1993 *Multicomponent Mass Transfer*. Hoboken, NJ: John Wiley and Sons, Inc.

THOMAS-ALYEA, K. 2008 Modeling Resistive-Reactant and Phase-Change Materials in Battery Electrodes. *ECS Transactions* **16** (13), 155–165.

TROFFKIN, H., BURTON, M., SPOTNITZ, R., GIOVANNONI, R. & GUO, Y. 1993 U.S. Patent Number 5240655.

TSUJIKAWA, T., YABUTA, K., MATSUSHITA, T., ARAKAWA, M. & HAYASHI, K. 2011 A Study on the Cause of Deterioration in Float-Charged Lithium-Ion Batteries Using $LiMn_2O_4$ as a Cathode Active Material. *Journal of the Electrochemical Society* **158** (3), A322–A325.

TSUNEKAWA, H., TANIMOTO, S., MARUBAYASHI, R., FUJITA, M., KIFUNE, K. & SANO, M. 2002 Capacity Fading of Graphite Electrodes Due to the Deposition of Manganese Ions on Them in Li-Ion Batteries. *Journal of the Electrochemical Society* **149**, A1326–A1331.

VALOEN, L. & REIMERS, J. 2005 Transport Properties of $LiPF_6$-Based Li-Ion Battery Electrolytes. *Journal of the Electrochemical Society* **152** (5), A882–A891.

VAN MIERLO, J., MAGGETTO, G. & LATAIRE, P. 2006 Which energy source for road transport in the future? A comparison of battery, hybrid, and fuel cell vehicles. *Energy Conversion and Management* **47** (17), 2748 – 2760.

VENUGOPAL, G., MOORE, J., HOWARD, J. & PENDALWAR, S. 1999 Characterization of microporous separators for lithium–ion batteries. *Journal of Power Sources* **77** (1), 34–41.

VERBRUGGE, M. & CHENG, Y. 2008 Stress Distribution within Spherical Particles Undergoing Electrochemical Insertion and Extraction. *ECS Transactions* **16** (13), 155–165.

VERBRUGGE, M. & KOCH, B. 1996 Modeling Lithium Intercalation of Single-Fiber Carbon Microelectrodes. *Journal of the Electrochemical Society* **143** (2), 600–608.

VETTER, J., NOVAK, P., WAGNER, M., VEIT, C., MOLLER, K., BESENHARD, J., WINTER, M., WOHLFAHRT-MEHRENS, M., VOGLER, C. & HAMMOUCHE, A. 2005 Ageing mechanisms in lithium-ion batteries. *Journal of Power Sources* **147**, 269–281.

WEST, A. & FULLER, T. 1996 Influence of rib spacing in proton-exchange membrane electrode assemblies. *Journal of Applied Electrochemistry* **26**, 557 – 565.

WHITACRE, J., ZAGHIB, K., WEST, W. & RATNAKUMAR, B. 2008 Dual active material composite cathode structures for Li-ion batteries. *Journal of Power Sources* **177**, 528 – 536.

WOHL, K. 2004 *Transactions of the American Institute of Chemical Engineers* **42** (215).

WOHLFAHRT-MEHRENS, M., VOGLER, C. & GARCHE, J. 2004 Aging mechanisms of lithium cathode materials. *Journal of Power Sources* **127**, 58–64.

XIA, Y., KUMADA, N. & YOSHIO, M. 2000 Enhancing the elevated temperature performance of Li/LiMn$_2$O$_4$ cells by reducing LiMn$_2$O$_4$ surface area. *Journal of Power Sources* **90**, 135–138.

YANG, C., LAI, H., LIU, Z. & MA, P. 2006 Density and Viscosity of Binary Mixtures of Diethyl Carbonate with Alcohols at (293.15 to 363.15) k and Predictive Results by UNIFAC-VISCO Group Contribution Method. *Journal of Chemical and Engineering Data* **51** (4), 1345–1351.

ZHANG, S. 2007 A review on the separators of liquid electrolyte Li-ion batteries. *Journal of Power Sources* **164**, 351–364.

ZHANG, X., SHYY, W. & SASTRY, A. 2007 Numerical Simulation of Intercalation-Induced Stress in Li-ion Battery Electrode Particles. *Journal of the Electrochemical Society* **154** (10), A910.

ZHAO, K., PHARR, M., VLASSAK, J. & SUO, Z. 2010 Fracture of electrodes in lithium-ion batteries caused by fast charging. *Journal of Applied Physics* **108**.